Crustal Deformation During Co- and Postseismic Phases of the Earthquake Cycle Inferred from Geodetic and Seismic Data

by

Mong-Han Huang

A dissertation submitted in partial satisfaction of the
requirements for the degree of
Doctor of Philosophy

in

Earth and Planetary Science

in the

Graduate Division

of the

University of California, Berkeley

Committee in charge:

Professor Roland Bürgmann, Chair
Professor Douglas S. Dreger
Professor David Steigmann

Spring 2014

Crustal Deformation During Co- and Postseismic Phases of the Earthquake Cycle Inferred from Geodetic and Seismic Data

Abstract

Crustal Deformation During Co- and Postseismic Phases of the Earthquake Cycle Inferred from Geodetic and Seismic Data

by

Mong-Han Huang

Doctor of Philosophy in Earth and Planetary Science

University of California, Berkeley

Professor Roland Bürgmann, Chair

The work presented in my dissertation focuses on the crustal deformation during the co- and postseismic periods in earthquake cycles. I use geodetic and seismic data to constrain and better understand the behavior of the earthquake source during the coseismic period. For the postseismic period, I use geodetic data to observe the surface displacements from centimeter-scale to millimeter-scale from an M_w 7.9 and M_w 6.9 event, respectively. I model different mechanisms to explain the postseismic deformation and to further constrain the crustal and upper mantle rheology.

For the coseismic earthquake source study, I explore the source of the 2010 M_w 6.3 Jia-Shian, Taiwan earthquake. I develop finite-source models using a combination of seismic data (strong motion and broadband) and geodetic data (InSAR and GPS) to understand the rupture process and slip distribution of this event. The main shock is a thrust event with a small left-lateral component. Both the main shock and aftershocks are located in a transition zone where the depth of seismicity and an inferred regional basal detachment increases from central to southern Taiwan. The depth of this event and the orientation of its compressional axis suggest that this event involves the reactivation of a deep and weak pre-existing NW-SE geological structure.

The 1989 M_w 6.9 Loma Prieta earthquake provides the first opportunity since the 1906 San Francisco (M_w 7.9) earthquake to study postseismic relaxation processes and estimate rheological parameters in the region with modern space geodetic tools. The first five years postseismic displacements can be interpreted to be due to aseismic right-oblique fault slip on or near the coseismic rupture, as well as thrusting up-dip of the rupture within the Foothills thrust belt. However, continuing transient surface displacements ($\leq$ 5 mm/yr) until 2002 revealed by PSInSAR and GPS in the northern Santa Cruz Mountains may indicate a longer-term postseismic deformation. I model the viscoelastic relaxation of the lower crust

and upper mantle following the Loma Prieta earthquake to explain the surface displacement. A 14-km-thick lower crust (16 – 30 km depth) viscosity of $> 10^{19}$ Pa s and an upper mantle viscosity of $\sim 10^{18}$ Pa s best explain the geodetic data. The weak upper mantle viscosity in this area is in good agreement with upper mantle rheology in southern California (0.46 – 5 $\times$ 10^{19} Pa s) using a similar approach from studying the postseismic deformation following the 1999 (M_w 7.1) Hector Mine earthquake.

Periods of accelerated postseismic deformation following large earthquakes reflect the response of the Earth's lithosphere to sudden coseismic stress changes. I investigate postseismic displacements following the 2008 Wenchuan (M_w 7.9), China earthquake in eastern Tibet and probe the differences in rheological properties across the edge of the Tibetan Plateau. Based on nearly two years of GPS and InSAR measurements, I find that the shallow afterslip on the Beichuan Fault can explain the near-field displacements, and the far-field displacements can be explained by a viscoelastic lower crust beneath Tibet with an initial effective viscosity of 4.4×10^{17} Pa s and a long-term viscosity of 10^{18} Pa s. On the other hand, the Sichuan Basin block has a high-viscosity upper mantle ($\geq 10^{20}$ Pa s) underlying an elastic 35-km-thick crust. The inferred strong contrast in lithospheric rheologies between the Tibetan Plateau and the Sichuan Basin is consistent with models of ductile lower crustal flow that predict maximum topographic gradients across the Plateau margins where viscosity differences are greatest.

With additional 6-year-long continuous GPS measurements deployed in the eastern Tibetan Plateau and the Sichuan Basin, viscoelastic relaxation models with the same geometry setups suggests Tibetan lower crust with an initial effective viscosity of 9×10^{17} Pa s and steady-state viscosity of 10^{19} Pa s. I also use the laboratory experiments derived power law flow model to fit the postseismic deformation. The viscosity estimated from this model varies with material parameters (e.g. grain size, water content, etc.) as well as environmental parameters (temperature, pressure, background strain rate, etc.). The diffusion creep refers to the power law flow mainly controlled by the mineral grain size, and the dislocation creep refers to it mainly controlled by the background stress level. For a diffusion creep type of power law flow, a Tibetan crust composed of wet feldspar (water content = 1000 H/10^6Si; grain size = 1 – 4 mm) and upper mantle composed of wet olivine (water content = 200 H/10^6Si; grain size = $\sim$2 mm) can predict the 6-year-long poseismic time series well. This result roughly agrees with rock mechanics laboratory experiments. The channel flow model predicts the plateau margins are steepest where the viscosity of the surrounding blocks are highest. The low viscosity in the Tibetan lower crust and the contrasting rheology across the plateau margin derived from postseismic deformation are consistent with the channel flow model.

"Divide each difficulty into as many parts as is feasible and necessary to resolve it."

René Descartes

Contents

List of Figures

List of Tables

Acknowledgments

Living in Bay Area has been a wonderful life experience. The cool weather, the bay, the mountains, there are thousands of reasons why you want to go outside and breathe some fresh air! Berkeley is great, but it won't be that great without so many great people living here!

I would like to thank prof. Roland Bürgmann, my PhD advisor. We didn't know what my PhD project would lead us to because we were not even sure if geodesy would work for this project. Roland is always optimistic and gives me the highest degree of freedom to explore different ways to approach problems. In addition, he always knows where to find the right person and resource to solve the difficulties. In the group meetings, he shows he zeal for science and constantly stimulates us to take a step forward. Five years have passed and somehow it works, so I hope I will always keep in my mind to be eager in what I like and stay optimistic.

Thanks to the EPS PhD program, so I could have the opportunity to have prof. Douglas Dreger as my secondary advisor. As a seismologist, Doug can tell us stories about an earthquake just from reading a seismogram; as a friend he has not run out of great stories! Every time when I have any kind of questions he is always approachable and helpful. Besides, his geology background also leads me into some new direction.

I would like to thank my qualify exam committee prof. Michael Manga and prof. David Steigmann. Michael has the ability to find the most crucial part of a story, and use most understandable words and equations to explain a complicate system. I learnt continuous mechanics from David. After taking his class, vector or tensor calculation is so much easier. It is all because of the training in the Mechanical Engineering department.

I was prof. Chi-Yuen Wang's GSI for the EPS 50 class. His enthusiasm for research and science encourages us to pursuit what we really want to do in a lifetime scale. Prof. Bill Dietrich leads me into a whole new world - geomorphology. Now I not only sketch landscapes, I also think about surface processes that would form to unique landscapes on Earth or different planets.

My officemates, Qingkai Kong, William Hawley, and Chris Johnson are great accompanies in McCone 289. I really enjoy doing different activities all together! Sierra Boyd and Pamela Kaercher gave me enormous help in late 2012 after I broke my jaw from a bike accident. It was the first time I realized how important friends are when you are in a foreign country. Thank you both for being so eager to help me through all of my difficult time. Without your help I wouldn't have recovered so quickly. My housemate, Marissa Tremblay, you are such a wonderful person to live with! I appreciate what you have helped me, and I hope we will have more and more stories to share with each other.

Five years in graduate school is so enjoyable because of all of my friends. I would like to thank all of the fifth year EPS graduate students. I will not forget the time we share at McCone! Kelly Wiseman, Amanda Thomas, Max Rudolph, Shan Dou, Aurélie Guilhem, Rob Porritt, Sonne Cottaar, Tyler Arbour, Scott French, Jennifer Frederick, Ian Rose, Percy Link, Andrea Chiang, Heidi Fuqua, Shuai Zhang, Brent Delbridge, Courtney Sprain, Katie Wooddell, Avinash Nayak, Noah Randolph-Flagg, Seth Saltiel, Hannah Bourne, Kristen Fauria, Liz Mitnick, Alex Bryk, and Voon Lai, I am so lucky to know all of you and learn from you during my PhD live. I will always remember the moments we prepare our qualify exam, having parties, camping, hiking, rock climbing, and swimming together.

Postdocs and BSL staff including Isabelle, Pascal, Collin, Ingrid, Seung Hoon, Taka'aki, Peggy, Clay, Jennifer, Ronni, Kim, Manoo, Estelle, and Yan help me on coding, computer problems, and provide critical insights into my research. Charley and Stephen do a great job on maintaining our BSL system. Margie is more like a friend than our graduate student officer to me. EPS undergrads gave me the chance to be their GSI several times and help me improve communication and teaching.

Finally I would like to thank my parents and my sister who are always supportive, no matter what my decision was. Thank you for understanding my decision pursuing a PhD degree oversees. You three are always in my mind.

Chapter 1

Introduction

Most of the crustal earthquakes are associated with activities on faults. Inside a fault zone, earthquakes occur at the same or different parts of the fault repeadly. During an earthquake event, slip on the fault generates seismic waves and causes ground motions in a very short time period. Between two earthquake events in the same fault zone area, however, much smaller amount of crustal deformation is observed. The earthquake (or seismic) cycle describes the crustal deformation of one fault zone in four different periods: *preseismic*, *co-seismic*, *postseismic*, and *interseismic*. The coseismic displacement refers to the deformation during an earthquake event within seconds to minutes, depending on the size of the earthquake. The postseismic displacement refers to the deformation process after an earthquake until it falls back to the background level as before the earthquake. The interseismic deformation describes the long-term crustal movement between earthquake events in the same fault zone. The preseismic deformation describes the crustal deformation just prior to an earthquake event. The amount and the spatial distribution of coseismic deformation relay on the magnitude and depth of the event as well as the geologic setting of the area. Similarly, for postseismic deformation it is dependent on the magnitude of coseismic slip on the fault as well as the regional rheology. The interval of earthquake cycles is largely controlled by the fault zone properties, regional tectonic loading, influence from the change of loading stress, etc. To understand the process of fault zone activies in earthquake cycle as well as the connection to the long-term tectonic loadings, we rely on precise and dense observations of crustal deformation in space and time.

In this thesis, I study three crustal deformation cases during co- and postseismic periods in plate boundries such as Taiwan (Eurasian Plate and Philippine Sea Plate), San Francisco Bay Area (Pacific Sea Plate and North American Plate), and eastern Tibetan Plateau (Eurasian Plate and Yangze craton). For coseismic, I study an M_w 6.3 earthquake in SW Taiwan to understand earthquake source based on seismic and geodetic observations. For postseismic, I study crustal deformatin after an M_w 6.9 in San Francisco Bay Area and an M_w 7.9 earthquake in eastern Tibetan Plateau, and compare postseismic deformation with different magnitude of earthquakes. For example, even it is more than four decades since the M_w 9.5 Chile earthquke in 1960, the coastal and inland GPS stations still shows opposite direction of motion that indicates the still on-going postseismic displacement in the region [Wang et al., 2012]. On the other hand, 6 years of GPS measurements following the 2004 M_w Parkfield, California, earthquake show ∼1.2 cm postseismic displacement between 2004 and 2008, but do not show significant postseismic deformation after 2008 [Bruhat et al., 2011].

Modern technology in seismology and remote sensing allows us to record the deformation history during and after earthquakes. In seismology, strong motion and broadband seismic sensors can detect acceleration and velocity in a very wide range of frequency. In remote sensing, the global positioning system (GPS) measurements are used to observe the surface displacement in 3-D with centimeter-scale accuracy. Overall, the uncertainty of GPS is generally less than 1 cm in horizontal and about three times higher in vertical. For active tectonic studies, GPS is used for coseismic static displacement, postseismic deformation measurement with time, interseismic deformation, and plate motions (i.e. secular motion). Another technique, interferometric synthetic aperature radar (InSAR), has been developed since early 1990s [Bürgmann et al., 2000]. A SAR interferogram can detect a map of surface displacement in line of sight (LOS) with tens of meters resolution and sub-centimeter accuracy between two SAR image acquisitions. InSAR has been widely used for observing crustal deformation including co-, post-, and interseismic displacement, volcanic deformation, land subsidence, and glacial movement.

Understanding the earthquake source process is one of the most important topic in seismology. The earthquake source describes the dimension, depth, and the mechanism of the earthquake. To obtain the detail and accurate source process would rely on good velocity struction and good surface observations. In Chapter 2, I focus on the 2010 M_w 6.4 Jia-Shian, Taiwan, earthquake. I use seismic and geodetic measurements for this earthquake event separately and jointly to understand the source and the source process. I perform a series of moment tensor solution tests to constrain the source depth. In order to improve the regional velocity structure, I use an M_w 5.0 aftershock which occurred at similar location but with a simpler source to optimize the velocity structure. For the main shock event, I invert for finite-source models using geodetic (GPS and InSAR) and seismic waveform (strong motion and broadband stations) data independently and jointly, in order to compare th esensitivities of each dataset and the proper smoothing parameters and data weighting for a joint inversion. In addition, I compare the inversion result with region tectonic setting. The Jia-Shian event occurred along the boundary between the western Foothills and the Central Rnage to the north and east and the sedimentary Pingtung Basin in the south. This event and its aftershocks are at the transition zone separating regions of distinctly different depth extent of seismicity and seismic velocity, and this event and its aftershocks seem to fill the seismic gap at this transition zone. In the second part of this chapter, I explore the implications for the rgional seismo-tectonic environment of south Taiwan from this event. I further compare the mechanism of this event with regional geology, paleo-stress measurements, and the background seismicity in order to gain further insight into the tectonics of south Taiwan. This work has been published in *Geophysical Journal International* in 2013 [Huang et al., 2013].

Postseismic deformation refers to the deformation after an earthquake event. Postseismic mechanisms include aseismic afterslip, aftershocks, viscoelastic relaxation in middle-to-lower crust and/or upper mantle, and poroelastically induced fluid flow. However, the contributions from these mechanisms to observed postseismic deformation is difficult to separate, so a major challenge lies in resolving the contributions of various postseismic processes to the observed transient surface deformation [Hearn, 2003]. Viscoelastic relaxation describes the coseismic stress changes to the viscous middle-to-lower crust and/or upper mantle, and the response of these viscous layers would cause surface deformation with time in terms of viscoelastic deformation. Afterslip describes the process when predominantly aseismic fault slip occurs on or beneath the rupture zone, in the days to years after the main shock. Poroelastic rebound happens when the coseismic pressure changes drive fluid flow in the crust, and it usually would affect the regions near the fault surface rupture within months after the earthquake. From Chapters 3 to 5, I use geodetic measurements to study postseismic deformation after a median (M_w 6.9) and a large (M_w 7.9) magnitude earthquakes.

In Chapter 3, I study the 1989 M_w 6.9 Loma Prieta earthquake postseismic deformation. I collect over 20 years of geodetic measurements, so I can use the long-term surface deformation time series to test for different possible postseimic mechanisms. In addition, I also use two decades of trilateration network survey in the San Francisco Bay area prior to the Loma Prieta earthquake, to estimate the interseismic secular motion. I combine GPS measurements during 1989.8 – 1998 and 1994 – 2013 by different groups, which represent the early and late periods of the Loma Prieta postseismic displacement. I process about 400 SAR interferograms between 1992 and 2010 and generate a 18-year-long surface displacement time series for the San Francisco Bay Area. Previous work (e.g. Bürgmann et al., 1997; Segall et al., 2000) shows that shallow afterslip on the Loma Prieta earthquake fault and a shallowly dipping fault planes dominates the early period of the Loma Prieta postseismic deformation until 1994. However, both GPS and InSAR results indicate continuous surface deformation in the Santa Clara Valley close to the earthquake epicenter 10 years after the event. In this study I use the viscoelastic relaxation model to predict surface deformation during the late period. Viscoelastic relaxation forward models indicate that a weaker upper mantle with lower viscosity below 30 km depth and a stronger lower curst with higher viscosity above the upper mantle can better explain the postseismic surface deformation in late period (1994 – 2013). In order to descriminate the viscoelastic relaxation and the afterslip contributions to surface deformation during early period, I use the best fitting viscoelastic relaxation model to predict the early viscoelastic relaxation during 1989.8 – 1994, and I remove the relxation component from the original GPS measurements in the same period. Dislocation models calculate the afterslip distribution on the fault to explain these residual displacements, so I can compare ths new afterslip model with previous work without removing the early postseismic relaxation. In the last part of the chapter I compare the decay rate of the viscoelastic relaxation from the Loma Prieta earthquake with repeating earthquakes on the nearby San Andreas Fault. I argue the viscoelastic relaxation as the driving force to the repeating earthquakes.

For higher magnitude earthquakes, coseismic stress changes could influence wider and deeper region and potentially produce higher postseismic amplitude in space and longer duration in time. At this sense, we can actually probe the lithospheric properties from postseismic deformation. In Chapter 4, I study the 2008 M_w 7.9 Wenchuan, China earthquake postseismic deformation. I process InSAR data and generate a time series that describes the surface deformation 1.5 years after the Wenchuan event. The tectonic evolution and geodynamics of the Tibetan Plateau, with its average elevation of ~5 km and 60-to-80-km-thick crust, continue to be topics of debate. In east side of the plateau, the May 12, 2008 M_w 7.9 Wenchuan earthquake occurred along the eastern Longmen Shan and ruptured ~235 km of the Beichuan Fault (BCF) and the enitre Pengguan Fault (PGF) [Shen et al., 2009]. In this chapter, I calculate the coseismic dislocations on the BCF and PGF using coseismic GPS measurements, and I use this coseismoc dislocations as the input source for viscoelastic relaxation. In order to obtain reliable rheologic structure underneath the Tibetan Plateau and the Sichuan Basin, I apply 3-D finite element model (FEM) to construct contrasting elastic and viscoelastic layer geometries across the plateau margin according to geophysical observations such as ambient noise surface wave tomography and receiver functions. To test for possible afterslip and its depth range, I use the same dislocation inversion method to estimate afterslip distribution based on a down-dip extensional fault model and an alternative shallow west dipping fault detachment model. Lastly, I test for the poroelastic rebound model to examine possible surface deformation driven by the porefluid flow. All of the models are based on the 1.5-year InSAR time series and the GPS measurements in the first few months. Knowing the main Wenchuan postseismic mechanism can help examine different end-member hyphotheses: The viscoelastic relaxation model would require a lower viscosity layer in the lithosphere which might agree with the ductile lower crustal flow model; the afterslip model describes fault dislocations at certain depth range that might agree with the idea of crustal imbrications and localized deformation along major faults. This work has been published in *Earth and Planetary Science Letter* in 2014 [Huang et al., 2014].

In Chapter 5, I incorporate 18 GPS stations that continuously recorded 6 years of displacement since the Wenchuan earthquake. In this chapter, I calculate viscoelastic relaxation using bi-viscous Burgers rheology as well as power law flow rheology including dislocation and diffusion creeps. For the bi-viscous model, I use the same viscoelastic model as in Chapter 4 to estimate the transient and long-term viscosities based on longer period of geodetic observations. For the power law flow rheology, I review the theory and test the sensitivity of viscosity with different material parameters (e.g. mineral type, grain size, water content, etc.) and the environmental parameters (e.g. temperature, pressure, background strain rate, etc.). According to regional geology, geochronology, and geophysical studies, I can infer certain minerals to represent the Tibetan crust and upper mantle. Next I incorporate different geothermal gradients to represent temperature profile at the plateau margin or ∼100 km away from the margin, and compute viscosity profiles according to different temperature profiles and types of creep (dislocation or diffusion). I construct the rheologic structure unerneath eastern Tibet based on power law flow models with different material and environmental parameters, and then forward calculate the postseismic deformation in the surface. By comparing with the 6-year-long GPS time series, I am able to test for different minerals as well as material parameters such as grain size and water content, and compare with laboratory experiment results. Consequently, my results show different long-term effective viscosity using short (∼1.5 years) and long (6 years) periods of geodetic measurements, and the rheologic structure with considering power law flow models provide comparable results with laboratory experiemnts and with regional geodynamic models.

In Chapter 6, I summarize the co- and postseismic studies in the three different tectonic regions and suggestions for future work.

Bibliography

[1] Bruhat, L., Barbot, S. and Avouac, J.-P. Evidence for postseismic deformation of the lower crust following the 2004 M_w 6.0 Parkfield earthquake. *J. Geophys. Res.*, 116, B08401 (2011).

[2] Bürgmann, R., Segall, P., Lisowski, M. and Svarc, J. Postseismic strain following the 1989 Loma Prieta earthquake from GPS and leveling measurements. *J. Geophys. Res.*, 102, 4933-4955 (1997).

[3] Bürgmann, R., Rosen, P. A. and Fielding, E. J. Synthetic aperture radar interferometry to measure Earth's surface topography and its deformation. *Annu. Rev. Earth Planet. Sci.*, 28, 169-209 (2000).

[4] Hearn, L. H. What can GPS data tell us about the dynamics of post-seismic deformation? *Geophys. J. Int.*, 155, 753-777 (2003).

[5] Huang, M.-H., Dreger, D., Bürgmann, R., Yoo, S.-H. and Hashimoto, M. Joint inversion of seismic and geodetic data for the source of the 2010 March 4, M_w 6.3 Jia-Shian, SW Taiwan, earthquake. *Geophys. J. Int.*, 193, 1608-1626 (2013).

[6] Huang, M.-H., Bürgmann, R., Freed, A. M. Probing the lithospheric rheology across the eastern margin of the Tibetan Plateau. *Earth Planet. Sci. Lett.*, 396, 88-96 (2014).

[7] Segall, P., Bürgmann, R. and Matthews, M. Time-dependent triggered afterslip following the 1989 Loma Prieta earthquake. *J. Geophys. Res.*, 105, 5615-5634 (2000).

[8] Shen et al. Slip maxima at fault junctions and rupturing of barriers during the 2008 Wenchuan earthquake. *Nat. Geo.*, 2, 718-724 (2009).

[9] Wang, K., Hu, Y. and He, J. Deformation cycles of subduction earthquakes in a viscoelastic Earth. *Nature*, 484, 327-332 (2012).

Part I

Coseismic Deformation

Chapter 2

Joint Inversion of Seismic and Geodetic Data for the Source of the 4th March 2010 M_w 6.3 Jia-Shian, SW Taiwan, Earthquake

2.1 Abstract

The 4th March 2010 Jia-Shian (M_w 6.3) earthquake in SW Taiwan caused moderate damage and no surface rupture was observed, reflecting a deep source that is relatively rare in western Taiwan. We develop finite-source models using a combination of seismic waveform (strong motion and broadband), Global Positioning System (GPS), and synthetic aperture radar interferometry (InSAR) data to understand the rupture process and slip distribution of this event. The rupture centroid source depth is 19 km based on a series of moment tensor solution tests with improved 1D Green's functions. The preferred fault model strikes 322° and dips 27° to the NE and the mainshock is a thrust event with a small left-lateral component. The finite-source model shows a primary slip asperity that is about 20 km in diameter at a depth range from 22 to 13 km, with peak slip of 42.5 cm, a total scalar seismic moment of 3.25×10^{18} N m (M_w 6.34), and with an average static stress drop of 0.24 MPa. The rupture velocity of this event is faster than the mid-crustal shear wave velocity in Taiwan, which suggests the possibility of a supershear event which has not been previously observed in Taiwan. Systematic resolution and sensitivity tests are performed to confirm the slip distribution, rupture velocity, the choice of weighting and smoothing for the joint inversions, and the consistency of the slip distribution. The first 24 hours of aftershocks appeared along the upper periphery of the main coseismic slip asperity. Both the mainshock and aftershocks are located in a transition zone where the depth of seismicity and an inferred regional basal décollement increases from central to southern Taiwan. The difference between the current orientation of plate convergence in Taiwan (120°) and the P axis of this event (052°) and nearby measurements of recent crustal strain directions (050° to 080°), as well as the relatively low static stress drop, suggest that the Jia-Shian event involves the reactivation of a deep and weak pre-existing NW-SE geological structure.

Key words: finite source inversion; joint inversion; south Taiwan Tectonics; Jia-Shian earthquake; Taiwan earthquakes; InSAR

2.2 Introduction

The current tectonic framework of Taiwan is the result of the oblique collision of the Eurasian Plate and the Philippine Sea Plate. The Philippine Sea Plate moves toward the northwest with respect to Eurasia at 8.2 cm/yr [Yu et al., 1997; Lin et al., 2010], and this oblique collision has resulted in a series of N-S trending fold-and-thrust belts in the western Taiwan Foothills (Fig. 2.1b). In SW Taiwan, a Plio-Pleistocene foreland basin developed in response to lithospheric flexure due to the tectonic loading of the Central Range orogenic belt [Lin and Watts, 2002], resulting in a geographic boundary separating the internally deforming Western Foothills and Central Range in the NE from the Pingtung Plain to the SW (Fig. 2.1) [Lacombe et al., 2001; Ching et al., 2011]. Deffontaines et al. [1997] proposed that the Chishan Transfer Fault Zone (CTFZ) following this boundary (Fig. 2.1a) represents a NW-SE trending structural and kinematic transition zone resulting from oblique plate collision. The fold-and-thrust belt in western Taiwan has been interpreted to follow a thin-skinned model, i.e. a thin, deforming wedge above a low angle detachment fault [Suppe, 1981] or as a thick-skinned system where earthquakes and faults reach deep into crustal basement rocks [Wu et al., 1997].

The 4^{th} March 2010 Jia-Shian (M_w 6.3) earthquake occurred in southwestern Taiwan near the SE end of the CTFZ and caused moderate damage. Ground fractures are found near Meinong (Fig. 2.1b for location), but there is no direct evidence that the observed surface deformations are related to the fault plane, which implies an unusually deep source. The focal depth reported by the Central Weather Bureau (CWB) is about 23 km, below the proposed basal detachment of the fold and thrust belt of Taiwan [Ching et al., 2011]. The coseismic GPS measurements (Hsu et al., 2011) show a fan shaped pattern with azimuths from SW to NW (Fig. 2.2a). The greatest horizontal displacement observed with GPS is 37 mm towards N80°W and was measured about 20 km to the west of the epicenter. There are several published models for this event (e.g., Ching et al., 2011; Hsu et al., 2011; Lee et al., 2012), which propose a north-dipping rupture with peak fault slip of 12-35 cm based on GPS or GPS and seismic inversions.

Joint inversion techniques for kinematic earthquake models have been developed, since about two decades ago (e.g., Yoshida and Koketsu, 1990; Wald et al., 1996; Wald and Somerville, 1995; Wald and Heaton, 1994; Kim and Dreger, 2008). These methods combine the available seismic and geodetic data (e.g. GPS and InSAR) for an event into a joint inversion for both temporal and spatial slip variations. Generally, only the seismic data

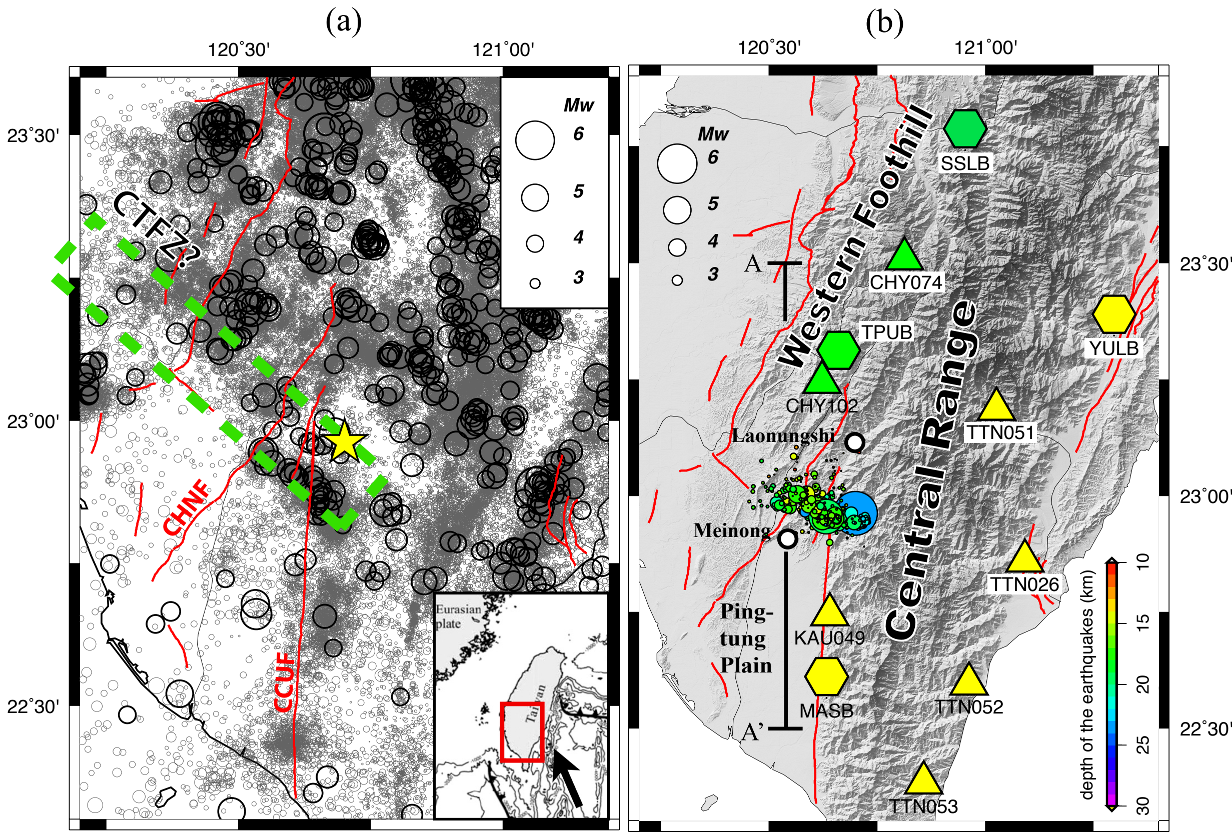

Figure 2.1: (a) Background seismicity of Taiwan from 1990 to 2010 (data from Wu et al., 2009). Earthquakes smaller and larger than M 3 are shown as gray and black circles, respectively. The red lines are the active faults (data from Central Geological Survey of Taiwan) and the dashed green rectangle is the inferred CTFZ [Deffontaines et al., 1997]. The star indicates the Jia-Shian main shock. (b) Selected strong motion stations (triangles) and broadband stations (hexagons). Data from the green and yellow stations are modeled using velocity models for west and east Taiwan, respectively. The Jia-Shian main shock and aftershocks are color coded with depth. AA' is seismic profile for Fig. 2.16.

can provide information about the time history of slip, whereas the geodetic data are more sensitive to the fault geometry and the finite slip pattern. Combining both seismic and geodetic data sets allows us not only to obtain a more reliable solution but also to improve understanding of the complexity of an event. In this study, we invert for finite-source models using geodetic (GPS and InSAR) and seismic waveform (strong motion and broadband stations) data independently and jointly, in order to compare the sensitivities of each data set and the proper smoothing parameters and data weighting for a joint inversion. We examine the rupture velocity with refined Green's functions obtained by fitting the largest Jia-Shian aftershock using the method suggested by Cohee and Beroza [1994]. In addition, we also perform station sensitivity and synthetic data resolution tests to explore the reliability of the inversions.

The aim of this study is to thoroughly investigate the source characteristics of the Jia-Shian earthquake by applying the joint inversion technique, and to explore the implications for the regional seismo-tectonic environment of south Taiwan from this event. The result of the joint inversion is then put into the context of the regional geology, paleo-stress measurements, and the background seismicity in order to gain further insight into the tectonic setting of the Jia-Shian event.

2.3 Seismic and Geodetic Data

The Jia-Shian earthquake was recorded by two network systems operated in Taiwan, the Taiwan Strong-Motion Instrumentation Program (TSMIP) operated by the CWB of Taiwan and the Broadband Array in Taiwan for Seismology (BATS) operated by the Institute of Earth Sciences (IES), Academia Sinica of Taiwan and CWB. More than 700 TSMIP stations and more than 20 BATS stations recorded this event. In order to avoid complex three-component wave propagation problems we select stations located within 100 km of the epicenter. In order to minimize the amplification effects when waves travel through sedimentary basins, we only select seismic stations located on bedrock, while maintaining good azimuthal coverage (7 TSMIP stations and 3 BATS stations, locations see Fig. 2.1b). The three-component TSMIP stations record acceleration in horizontal and vertical directions with sample rates of 200 samples per second. We removed the mean offset of the seismograms and integrated twice from acceleration to displacement. Each BATS station records the velocity in east, north, and vertical directions with a sample rate of 10 samples per second. We removed the instrument response and the mean offset, and integrated once from velocity to displacement. All of the seismograms are bandpass filtered between 0.03 and 0.3 Hz with a two-pole acausal Butterworth filter before resampling the data to 10 samples per second.

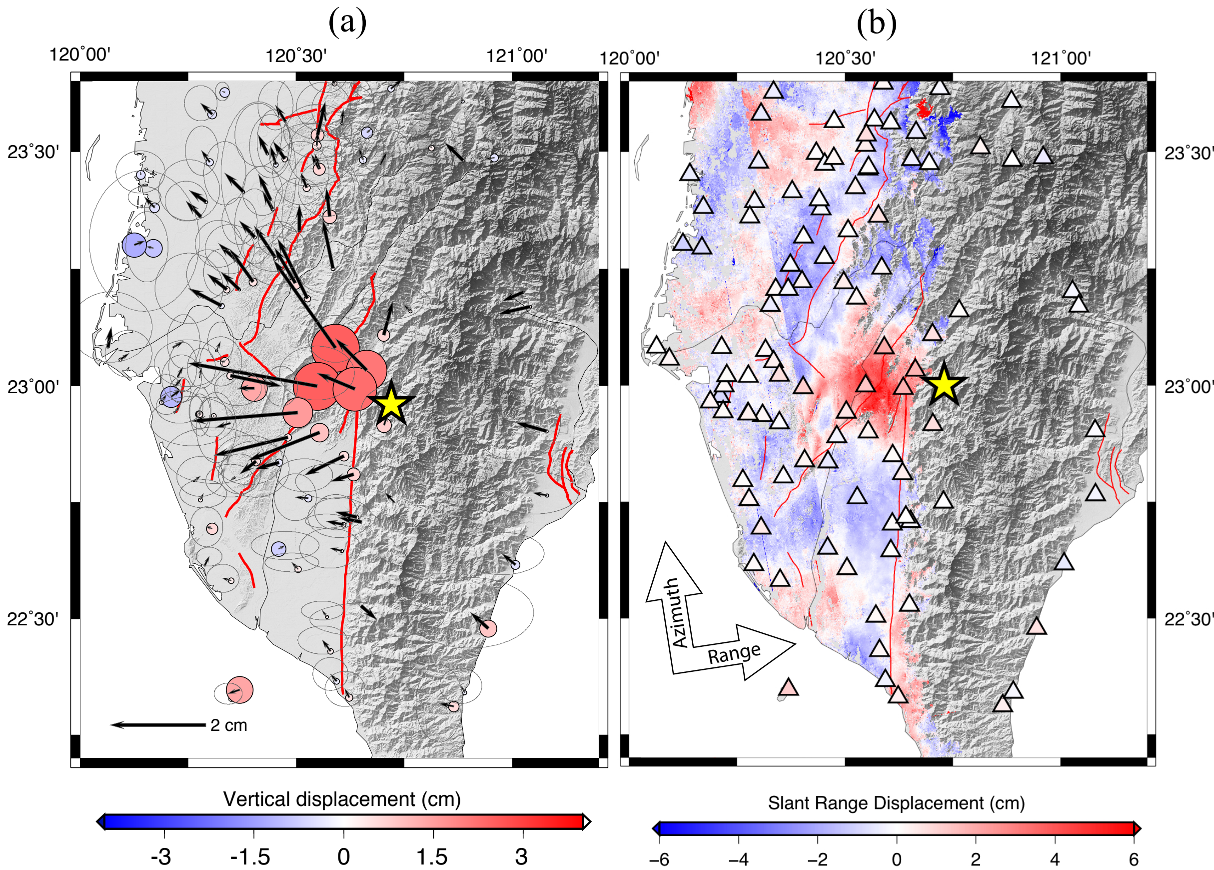

Figure 2.2: (a) The GPS coseismic measurements in southern Taiwan. The black arrows show the horizontal displacements with 95 % confidence ellipses, and the color of the circles around the stations indicate vertical displacement. The size of the circles is scaled with the magnitude of vertical displacement. (b) ALOS coseismic interferograms. Tracks 447 and 446 are both plotted in this map. The colors represent the coseismic slant range displacement (SRD), and the triangles are the GPS estimated SRD. Note that the GPS estimated SRD and the InSAR range changes are shown with the same color scale.

There are more than 350 continuous GPS (CGPS) stations deployed in Taiwan by different institutions [Yu et al., 2003]. Most of the stations are maintained by IES of the Academia Sinica of Taiwan and data are downloadable from their website (`http://gps.earth.sinica.edu.tw`). The choice of CGPS stations used in our inversion is adopted from Hsu et al. [2011], including data from 108 CGPS stations located within a radial distance of about 80 km from the epicenter of the Jia-Shian earthquake (Fig. 2.2a). The data were processed with the Bernese software v.4.2 to obtain the precise daily station coordinates, and the coseismic displacements were estimated from the difference between averages of 4 days of GPS site positions before and after the mainshock [Hsu et al., 2011]. The GPS measurements show coseismic horizontal displacements of up to 3.7 cm close to the hypocenter moving toward the SW and NW, whereas no eastward displacement was observed. Up to 3 cm of uplift is observed at stations to the west of the epicenter.

Five ALOS ascending SAR images collected along path 446 and two from path 447 were used to generate coseismic interferograms. All data were processed with the open source *ROI PAC 3.0* software developed and maintained at Caltech/JPL [Rosen et al., 2004]. The 90 m Shuttle Radar Topography Mission (SRTM) DEM is used to correct the phase due to topography. Phase unwrapping relied on the branch cut algorithm in *ROI PAC 3.0*. The ALOS PALSAR signal has a relatively long wavelength (L band, about 24 cm) and obtains reliable phase-change measurements even in densely vegetated areas and mountains. We processed four coseismic interferograms in two ascending-orbit paths. However, some of the interferograms are highly perturbed by ionosphere-correlated noise that can bias the result of the geodetic inversion, so only two interferograms are used. The coseismic pairs for both paths 446 and 447 (Fig. 2.2b) show range displacement towards the satellite west of the hypocenter, which indicates that the fault plane is located west of the hypocenter. The coseismic deformation area is about 400 km^2. On the other hand, some increasing range changes in the south and north of the coseismic deformation could be due to tropospheric artifacts. Near-field GPS measurements are converted into slant range displacement and show good agreement with the InSAR results (triangles in Fig. 2.2b). Note that the InSAR dataset contains about 4 months of postseismic deformation. Given the agreement between the GPS and InSAR results, it is reasonable to assume that the contribution of postseismic deformation to the InSAR measurement is negligible.

2.4 Taiwan Velocity Structure, Source Depth, and the Moment Tensor Solution

Severaleismic velocity structure from western to eastern Taiwan observed in tomographic studies has a strong lateral heterogeneity (e.g. Wu et al., 2007), which is correlated with a change of the topography (Fig. 2.1b). Hence, a simple 1D velocity model may not allow for fitting all the seismic station data. In order to increase the accuracy of the seismic inversion, we construct two 1D velocity structures to represent western and eastern Taiwan, which we use for stations in either region. To obtain the two velocity models, we rely on data from the largest aftershock with known focal mechanisms and similar distance. Cohee and Beroza [1994] pointed out that aftershocks from similar distances as the mainshock can be modeled to find the velocity model and frequency range over which theoretical Green's functions are most accurate. Hence, we use the improved velocity structures, and determine the pass band frequencies for the mainshock waveforms based on the pass band frequencies applied for the aftershock inversion. The largest aftershock (M_w 5.0) occurred about 8 hours after the mainshock and is located about 8 km west of the epicenter. The reported location and depth (from CWB and Huang et al., 2011) are similar to the mainshock, and the CWB focal mechanism is also similar to the mainshock (strike: 323°, dip: 33°, rake: 77°). To improve the velocity structure, we use an initial 1D velocity model proposed by Chi and Dreger [2002] as a reference model, and vary the Vp and Vs values and the number of layers to fit the aftershock seismograms given the known focal mechanism. We apply full waveform inversion using the quasi Newton method [Tarantola, 2005] to find optimum 1D velocity structures for western and eastern Taiwan. In the inversion, we compute the partial derivative Green's function wavefields with respect to P and S wave velocity of each layer and their Frchet derivatives using the finite difference method. The Green's functions were computed with forward frequency wavenumber integration (e.g. Wang and Herrmann, 1980; Saikia, 1994). The gradient vector is scaled by the inverse of the pseudo-Hessian matrix, which is the diagonal component of the approximated Hessian matrix [Shin et al., 2001]. For additional stability of the inversion, a small amount of damping is added to the pseudo-Hessian matrix as 1-3 % of the maximum value of the diagonal elements in the pseudo-Hessian matrix. We fix the band pass filter at 0.03-0.3 Hz because this pass band maintains a relatively higher variance reduction (VR) of the aftershocks. Given the fact that the source of the mainshock generally has lower frequency due to longer rise time and finite-source rupture durations, 0.3 Hz is an adequate choice for the upper frequency limit for the mainshock. Additionally, frequencies greater than 0.3 Hz are sensitive to structural complexity between the stations and the source that is not captured by the two simple 1-D velocity models for western and eastern Taiwan.

The fitting to the aftershock waveforms obtained at stations in western and eastern Taiwan is shown in Fig. 2.3. According to the best-fitting model, the Moho depth is 35 and 40 km in western and eastern Taiwan, respectively. The P- and S wave velocities in western Taiwan are slower above 15 km depth, which is probably due to the thicker sedimentary layers. However, the west-Taiwan velocities become slightly faster in the 15 - 40 km depth range. This feature is also apparent in the tomographic 3D velocity model of Wu et al. [2007]. The values of the western and eastern Taiwan velocity models are listed in Table 2.1.

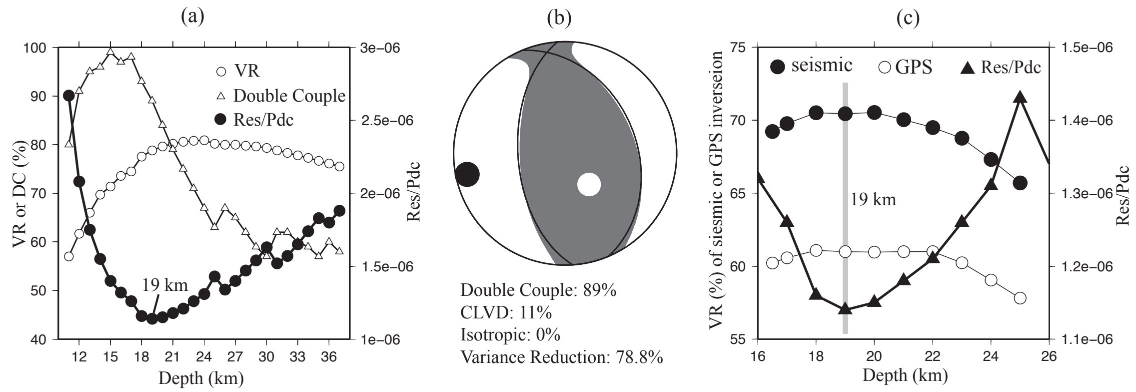

Figure 2.3: Waveform fitting of the largest aftershock using the velocity models for western and eastern Taiwan. TPUB and YULB (locations shown in Fig. 2.1b) are representative broadband stations in west and east Taiwan. R, T, and Z represent the radial, transverse, and vertical components. The waveforms are bandpass filtered to 0.03 - 0.3 Hz.

To determine the depth of the mainshock, we apply a moment tensor inversion method [Pasyanos et al., 1998; Minson and Dreger, 2008] to estimate the deviatoric moment tensor solution including the strike, dip, rake, and the percentage of double-couple (DC) and CLVD (compensated linear vector dipole) components. We used data from 6 BATS broadband stations for the inversion. The residual (L2-norm) and the double couple component percentage (Pdc) can be evaluated with depth and can provide a better estimate of the source depth by examining the ratio of the residual over the Pdc for different depths. The best depth in this case has the smallest residual and largest percent double couple. All of the waveforms are bandpass filtered into the 0.02-0.05 Hz frequency range. The eastern Taiwan 1D velocity structure derived using the method described in the previous paragraph is used to generate the Green's functions for the moment tensor inversion. The result shows that the highest VR (80.8 %) is obtained when the source depth is 23 km, which is close to the inferred source depths of Ching et al. [2011] and Huang et al. [2011]. However, the moment tensor solution at this depth has only 65 % of double couple component (Fig. 2.4a), which is below the expectation for a subduction/collision tectonic setting such as in western Taiwan. On the other hand, the solution with the highest double-couple component (99 %) is located at 15 km depth, with only 71 % VR. In order to better balance the trade-off between VR and Pdc, we estimate the ratio of the residual and Pdc. The most reliable solution lies where the residual/Pdc is a minimum. As shown in Fig. 2.4a, the lowest residual/Pdc value is at 19 km in depth, about 3 km shallower than found in previous studies of this event (e.g. Ching et al., 2011; Huang et al., 2011). The focal mechanism (Fig. 2.4b) based on this source depth shows 89 % DC component with the NE-dipping nodal plane having strike, dip and rake

Table 2.1: The one-dimensional velocity model used in this study.

Thickness (km)	V_p	V_s	**Density**	Q_p	Q_s
West Taiwan					
10	4.9	2.9	2680	600	300
15	6	3.7	2680	600	300
5	6.9	4.1	2680	600	300
100	7.8	4.5	3300	600	300
East Taiwan					
2.5	4.3	2.5	2400	300	100
12.5	5.7	3.3	2400	600	300
15	5.8	3.4	2680	600	300
10	6.4	3.6	2680	600	300
100	7.8	4.5	3300	600	300
Chi and Dreger [2004] 1D model					
2.5	4.5	2.6	1800	300	100
2.2	4.85	2.8	2050	600	300
2.2	5.3	3.06	2250	600	300
2.2	5.6	3.23	2390	600	300
4.5	5.84	3.37	2500	600	300
4.5	6.13	3.54	2640	600	300
7.5	6.28	3.63	2700	600	300
8.5	6.6	3.81	2850	600	300
5	6.87	3.97	2970	600	300
21.5	7.43	4.29	3300	600	300
25	7.8	4.5	3300	600	300

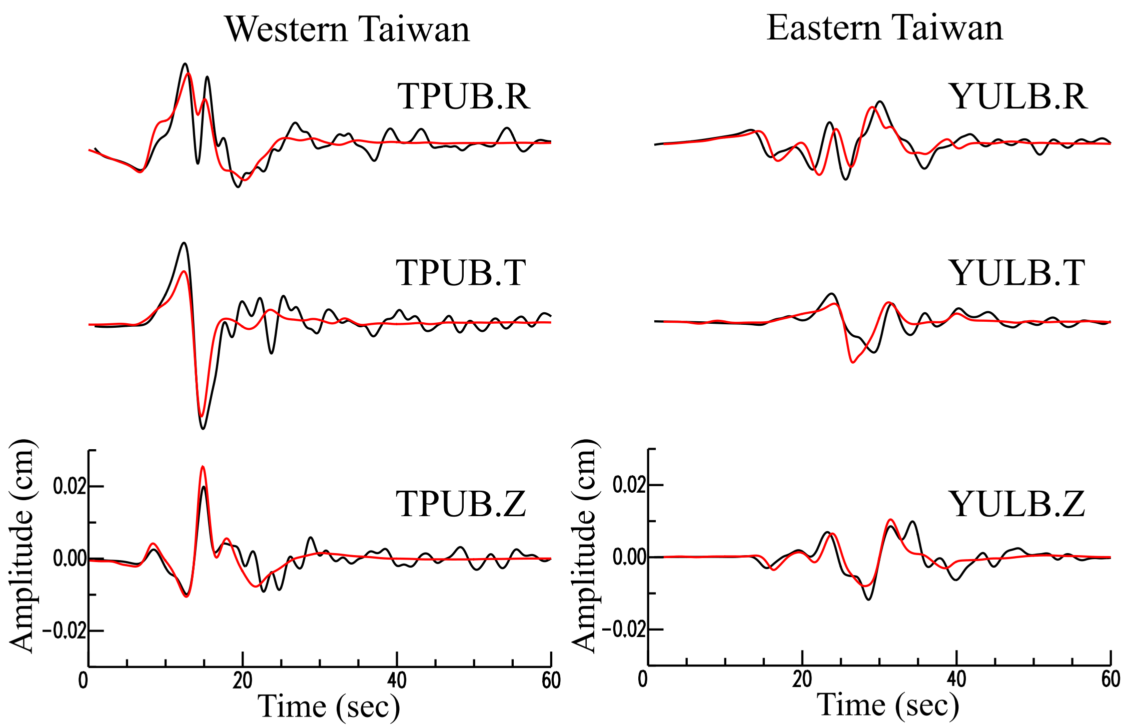

Figure 2.4: The determination of the moment tensor solution of the Jia-Shian event. (a) The variance reduction (VR), Double Couple (DC) component, and residual/DC (Res/Pdc) curves versus source depth. The lowest Res/Pdc value is at 19 km depth. (b) The focal mechanism at 19 km depth using the moment tensor inversion based on Pasyanos et al. [1996] and Minson and Dreger [2008]. (c) Plot of centroid depth versus VR and Res/Pdc. Both seismic and GPS finite source inversions (circles) have higher VR when the source is in the depth range of 18-20km. The Res/Pdc (triangles) from Fig. 2.4a is lowest when the source depth is 19 km shown by the gray line.

values of 322°, 28° and 60°, respectively. This strike and dip of the double couple component of the moment tensor solution and the centroid depth of the source are then used for the finite source inversions. The seismic moment obtained from the moment tensor inversion is 1.69 $\times 10^{18}$ N m corresponding to M_w 6.1.

2.5 Inversion Method and Result

We rely on a linear least squares inversion code based on the method of Hartzell and Heaton (1983) in which the finite source is discretized with a finite distribution of point sources in both space and time. We use a damped, linear least squares inversion with a slip positivity constraint to determine the spatiotemporally distributed slip. The waveforms are bandpass filtered to 0.03 to 0.3 Hz, which is determined from the aftershock fitting described in section 3. Based on an empirical relationship between the rise time (T_R) and the seismic moment [Somerville et al., 1999; modified for SI units Dreger and Kaverina, 2000], $T_R = 4.37 \times 10^{-7} \times M_o^{1/3}$ (SI units). Thus, given our seismic moment from the moment tensor inversion, $M_o = 1.69 \times 10^{18}$ N m, the rise time is $T_R = 0.5086$ s. As a result, we use a single time window with a fixed rise time of 0.5s. Although we use the rise time from the empirical relationship, the frequency band determined from the velocity structure modeling of the aftershock data precludes the resolution of rise time for values less than 3 seconds. This implies that we cannot resolve the rise time we apply it to account for the phase delay. The choice of rupture velocity will be tested and discussed in Section 2.4.4. Spatial smoothing with linear equations minimizing differences in slip between subfaults is applied to stabilize the seismic and geodetic inversion. Different weighting and smoothing parameters are applied to the simultaneous inversion using the method proposed by Kaverina and Dreger [2002]. The Green's functions for western and eastern Taiwan are obtained from fitting the largest aftershock as described in section 3. The seismic Green's functions were computed every 2 km from a distance of 20 to 100 km and every 1 km from a depth of 13 to 25 km using a frequency wavenumber integration code by Saikia [1994] based on the method of Wang and Herrmann [1980].

Absolute time shifts between the Green's functions and the observed data may be caused by the use of the simplified velocity model (Kim and Dreger, 2008). To reduce this problem, we first perform forward modeling based on a point source focal mechanism with a moment equivalent to a M_w 6.3. The starting time of this point source is based on the CWB solution, so we can then line up the first shear wave arrival between the predicted and observed waveforms by shifting the predicted waveforms. We note that the applied time-shift correction of the three components should be the same at a single seismic station, but can differ between stations. The reason of the time shift is mainly due to lateral velocity variations and depends on the distance from the source to the seismic station. We determine the time shift corrections for both TSMIP and BATS stations, as listed in Table 2.2.

For the geodetic inversion, the geodetic Green's functions are computed using the programs EDGRN/EDCMP [Wang et al., 2003]. This allows for the calculation of the Green's functions relating unit slip on each source subfault dislocation to surface displacements in a layered elastic model over a half-space. However, this calculation does not consider lateral variations of elastic structure. Thus we use the east Taiwan model derived from fitting the waveforms described earlier to compute the Green's functions for Taiwan (Table 2.2), since the hypocenter and most of the coseismic slip are located in the Central Range that belongs to the east Taiwan velocity model.

We construct a 50×50 km NE dipping fault plane with 625 (25×25) subfaults for the finite source inversions. The initial location of the fault center is set to be the hypocenter, and the fault geometry is the same as the 322° striking, 28° dipping nodal plane of the DC component of the preferred moment tensor inversion result described in section 3. We first run multiple GPS finite source inversions to obtain a more accurate fault location. We vary the horizontal location of the fault plane by a few kilometers in EW and NS components until the highest VR is reached in the GPS inversion. The depth of the fault plane is also re-estimated to reach the highest VR in either GPS or seismic inversion. The result (Fig. 2.4c) shows that both seismic and GPS inversions have higher VR in the depth range of 18-20 km. This range contains the depth resolved from lowest Residual/Pdc ratio of the moment tensor inversion (triangles in Fig. 2.4c).

The finite source inversions are first obtained using the seismic, GPS, and InSAR datasets individually to compare results and determine common features. Due to the different characteristics of data and the number of data points, each inversion requires different smoothing parameters to reach the highest VR. As a higher spatial smoothing factor is applied to the inversion, a smoother result will be obtained, but the fitting to the data (VR) will be lower as well. We can depict the smoothing by plotting the smoothing factor versus VR curve, and then choose the smoothing factor beyond which the model if does not significantly decrease. We first determine the preferred degree of smoothing and obtain the peak coseismic slip for the seismic inversion. We then choose the smoothing factor for the GPS and InSAR inversions to produce a model with a comparable peak slip as the seismic inversion. In the seismic-only inversion, the chosen smoothing factor is 4×10^{-7} resulting in VR = 72 % (Fig. 2.5a). The smoothing curves versus VR for GPS and InSAR are shown in Figs 5b and 5c. We can see that the smoothing values are 10^{-7} and 2×10^{-6} for GPS (VR: 68 %) and InSAR (VR: 75 %), respectively. By this method of choosing the degree of smoothing, we find that all three inversions obtain similar total slip area (Fig. 2.6). The detail of the inversion results and the joint inversion will be discussed below.

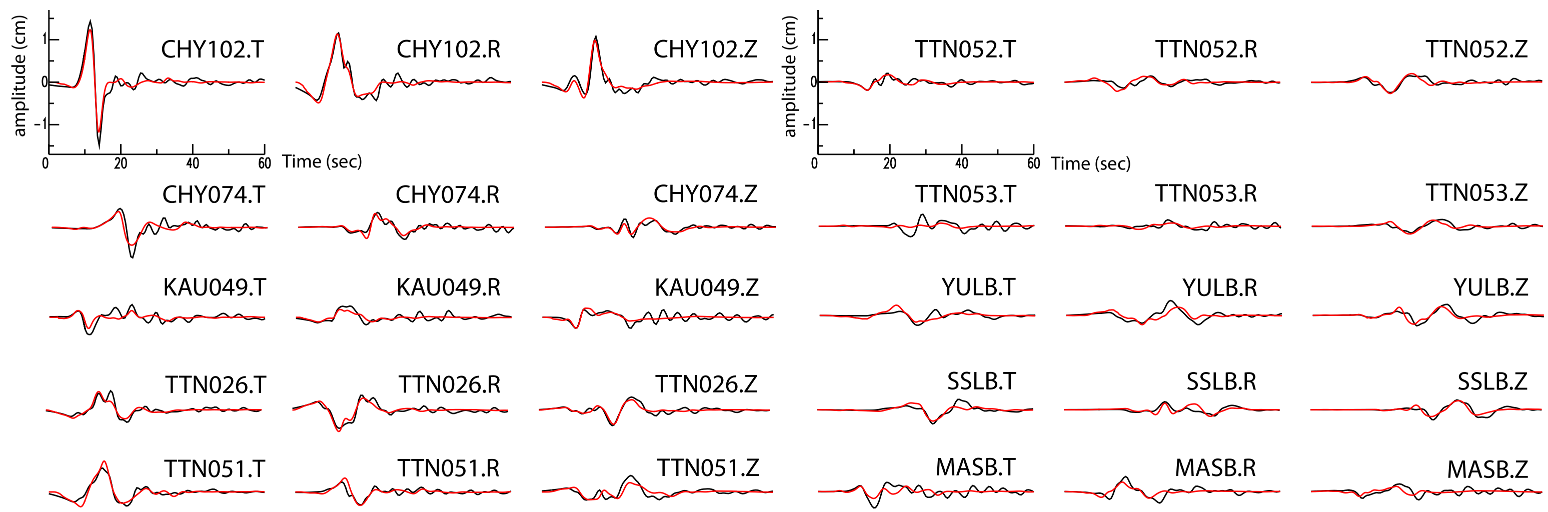

Figure 2.5: Variance reduction as a function of smoothing factors applied to individual (a) seismic, (b) GPS, and (c) InSAR inversions.

Table 2.2: Station locations and time shifts

Station	**Latitude (°)**	**Longitude (°)**	**Time Shift (s)**	**West or East Taiwan**	**Strong Motion or Broadband**
TTN026	22.8597	121.0916	0.0	East	Strong Motion
TTN052	22.5956	120.9620	-0.5	East	Strong Motion
TTN051	23.1864	121.0253	1.0	East	Strong Motion
CHY102	23.2442	120.6226	0.0	West	Strong Motion
KAU049	22.7442	120.6399	0.5	East	Strong Motion
CHY074	23.5087	120.8131	0.0	West	Strong Motion
TTN053	22.3814	120.8569	0.6	East	Strong Motion
MASB	22.6109	120.6326	-0.5	East	Broadband
YULB	22.3900	121.2970	-0.8	East	Broadband
SSLB	23.7870	120.9540	0.0	West	Broadband

2.5.1 Seismic inversion

The seismic data are from broadband stations of the BATS network and from strong motion stations (TSMIP). Only stations located on bedrock are selected for the inversion to prevent model artifacts due to site effects for stations located on sedimentary basins. We choose 7 strong motion stations providing near field observations and 3 BATS stations for the far field. The E-W, N-S, and vertical waveforms are all used in the seismic inversion; thus we have 30 components of seismic data. We apply the same bandpass filter (0.03 - 0.3 Hz) to both datasets prior to the seismic inversion. As described before, we correct the time shift based on point source forward modeling, and use two different 1D velocity models for the stations located in west and east Taiwan. The depth of the hypocenter is determined by the moment tensor solution (see section 3 and Fig 2.4). The rise time is fixed to 0.5 second (see section 4), and determination of the rupture velocity is described in section 2.4.4.

The model obtained in the seismic inversion fits both the strong motion data and the broadband data very well (Fig. 2.7). The result of the seismic inversion shows the main slip asperity is located near and mostly above the earthquake hypocenter. The primary coseismic slip area is about 15 $\times$ 20 km^2 (the light yellow to dark red area near the star in Fig. 2.6a), and there are two peak slip regions in this area, with about 34 cm and 24 cm of slip, respectively. In addition to the main asperity at the source depth ($\sim$20 km), there is an additional asperity near the upper part of the fault plane that has coseismic slip of less than 10 cm at about 4 km depth. There are some other minor slip areas located on the edge of the fault plane that might be due to the uneven distribution of seismic stations. The stability of the minor slip asperities in the model is tested in the station sensitivity and resolution tests in Section 2.5, and is found to be more stable near the hypocenter and the near surface. The rake is variable on the each sub fault and ranged from 15° to 105°, but most of the sub faults, and those with significant slip, have a rake angle of about 60°. The total moment obtained from the seismic inversion is 3.46 $\times$ 10^{18} N m, which is equivalent to a M_w 6.3 earthquake. The VR of the best fitting inversion is 72 % with a smoothing factor of 4×10^{-5} (Fig. 2.5a).

2.5.2 Geodetic Inversion

Individual GPS and InSAR Inversions

In the geodetic inversions we do not need to specify the hypocenter, rise time and rupture velocity, since both GPS and InSAR data reflect the final static surface displacement and are independent of the source time history. The result of the GPS inversion based on 3D displacements at the 108 continuous GPS stations is shown in Fig. 2.6b. The total moment is 3.29×10^{18} N m, which is also equivalent to a M_w 6.34 event. As described above, the smoothing factor for the geodetic inversion is chosen to obtain the same peak slip as the seismic-only inversion. The smoothing factor versus VR plot is shown in Fig. 2.5b. The main slip asperity is located northwest of the epicenter, and the slip area is about 13×15 km^2. The seismic and GPS inversions result in very similar models in terms of the primary slip asperity and the total moment. However, the GPS inversion also shows an additional slip asperity on the shallower part of the fault plane that is similar to the seismic inversion. This provides supporting evidence for this minor asperity, because it is indicated by two completely independent datasets.

Fig. 2.8 shows the result of the predicted coseismic displacements based on the GPS only inversion model. The GPS residuals are 2.7, 1.8, and 4.5 mm in the east, north, and vertical components, respectively (Fig. 2.8c). The misfit in the far-field is generally smaller than 5 mm which is within the uncertainty of the GPS data. In the vertical, larger residuals are observed in the coastal area that might be due to land subsidence that is independent of the earthquake, even though the misfit is still within the vertical uncertainties (6.8 mm, estimated from Hsu et al., 2011). Since the coseismic GPS observation is the difference of the 4-day average positions before and after the mainshock, the coseismic observation may be contaminated with early postseismic transients [Hsu et al., 2011]. However, since the coseismic slip distribution from the GPS inversion is very similar to that revealed by the seismic inversion, the postseismic surface displacements during the first 4 days must have been very small.

For the InSAR inversion (Fig. 2.9), the InSAR coseismic measurement is taken from the average of two coseismic interferograms (one from track 447 and one from track 446, see Fig. 2.2b, Table 2.3). In order to reduce the effects of atmospheric or topography related noise, and to focus on the coseismic change, we only consider the area where the InSAR coseismic surface displacements are significant. We also down-sample the interferogram into about one pixel per square kilometer to reduce the calculation time. We consider the InSAR signal

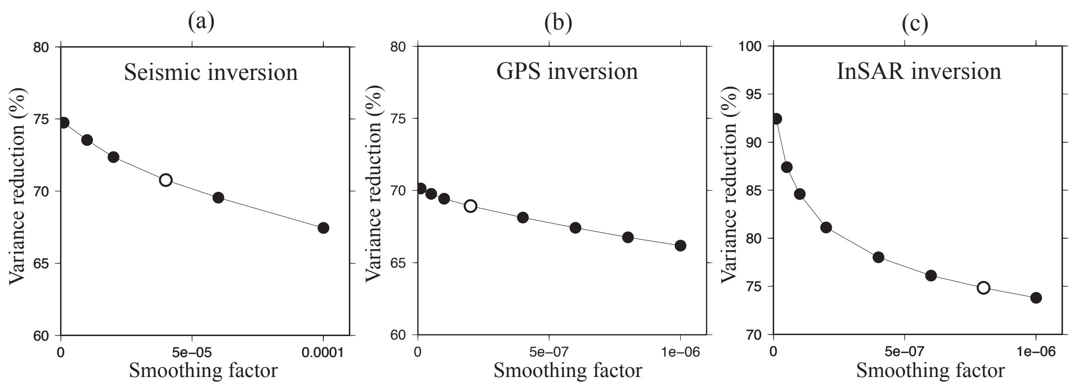

Figure 2.6: Coseismic slip model obtained from (a) 10 seismic stations (peak slip: 33.5 cm; total moment: 3.46×10^{18} N m; VR: 76%), (b) GPS (peak slip: 34.7 cm; total moment: 3.29×10^{18} N m; VR: 69%), (c) InSAR (peak slip: 30.4 cm; total moment: 3.35×10^{18} N m; VR: 71%). The black arrows represent the slip direction and amplitude of each subfault. Note that the inversions from different datasets have different spatial distribution, but they all have a 15 km $\times$ 15 km coseismic slip zone northwest of the epicenter (gray star).

in an area of about 25 × 25 km^2 with 601 InSAR data points in total (Fig. 2.9a). The InSAR-only inversion result (Fig. 2.7c) also shows one main asperity NW of the hypocenter with a circular area of about 6 km radius. The peak slip is 30.3 cm and the rake of the slip is generally 60°, consistent with the seismic and GPS inversions. The InSAR-derived coseismic slip is smoother than the other inversions because of a smaller spatial data coverage and a median filter with 1.2 × 1.2 km window size applied to the InSAR data. However, due to the denser data spacing of InSAR in the given area, the detail of the surface displacement is well preserved (some localized surface change in Fig. 2.9a). Hence, even though the slip distribution is smoother than in the other inversions, the slip asperities are more reliable. The InSAR inversion also shows a minor slip asperity in the shallower part, but the location of this small slip area is about 2 km deeper than in the other inversions. The zone of InSAR surface displacement corresponding to this minor asperity occurred along the Lungchuang anticline (Fig. 2.9a). If this minor asperity is the same as the one inferred from seismic inversion, we can conclude that this shallow slip is coseismic and the Jia-Shian earthquake ruptured to shallow depths of about 5 km in the southwest below this geologic structure.

GPS and InSAR Combined Inversion

For the geodetic inversion, we need to invert both GPS and InSAR data with proper weighting and smoothing parameters for both. We first fix the GPS weighting as one and change the InSAR weighting from 0 to 2 to find a higher VR for both datasets. The result (Fig. 2.10a) shows a decrease of GPS VR while increasing InSAR weighting. However, the increase of InSAR VR is less significant when InSAR weighting is higher than 0.2. The InSAR weighting is chosen as 0.1 because there is a substantial increase of the VR for InSAR as the weight increases from 0 to 0.1 but only a little decrease of GPS VR. We test InSAR weighting as 0.1 or 0.2, and vary the smoothing of the geodetic inversion from 10^{-8} to 10^{-6} (Fig. 2.10b), but we keep the InSAR weighting as 0.1 because it doesn't significantly decrease the GPS VR as when 0.2 does. The smoothing factor is determined by finding the smoothest model that does not decrease VR significantly [Kaverina et al., 2002]. From this criteria we determine the smoothing factor as 2 $\times 10^{-7}$, so the geodetic joint inversion (Fig. 2.11a) has a similar pattern as the individual inversions (Fig. 2.6). The total moment estimated from the geodetic inversion is 3.3 × 10^{18} N m and the peak slip is 39.8 cm. The pattern of the slip model is similar to the GPS inversion.

One main difference between GPS and InSAR inversion results is that the main slip area in the InSAR inversion is shifted by 2 km to the west, even though both obtain a similar area for the main slip asperity. However, according to the trade-off curve in Fig. 2.10b, shifting the main slip asperity, i.e. changing the InSAR weighting from 0 to 0.1 or 0.1 to 0.2 only increases the VR of InSAR by 6 % or 3 %, so the InSAR inversion is not very sensitive to the location of main asperity within the range of the 1-2 km shift. Thus, the geodetic

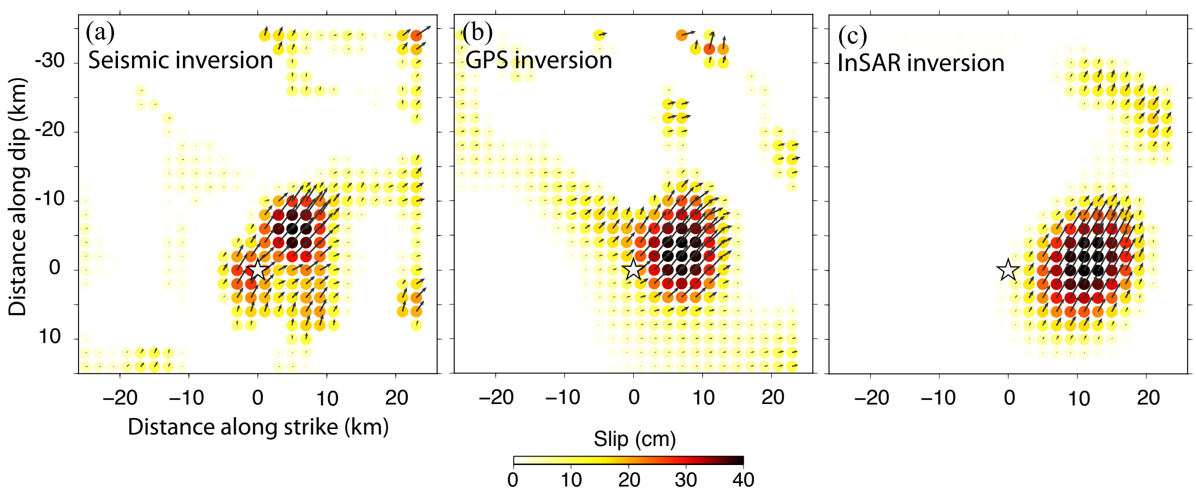

Figure 2.7: Comparison of synthetic waveforms (red) and the data (black) using only seismic inversion. CHY102, CHY074, KAU049, TTN026, TTN051, TTN052, and TTN053 are strong motion stations. YULB, SSLB, and MASB are broadband stations. All of the waveforms are bandpass filtered to 0.03 - 0.3 Hz. For the locations of all stations see Fig. 2.1b. Note that station TPUB is not used here because the data are clipped in the main shock.

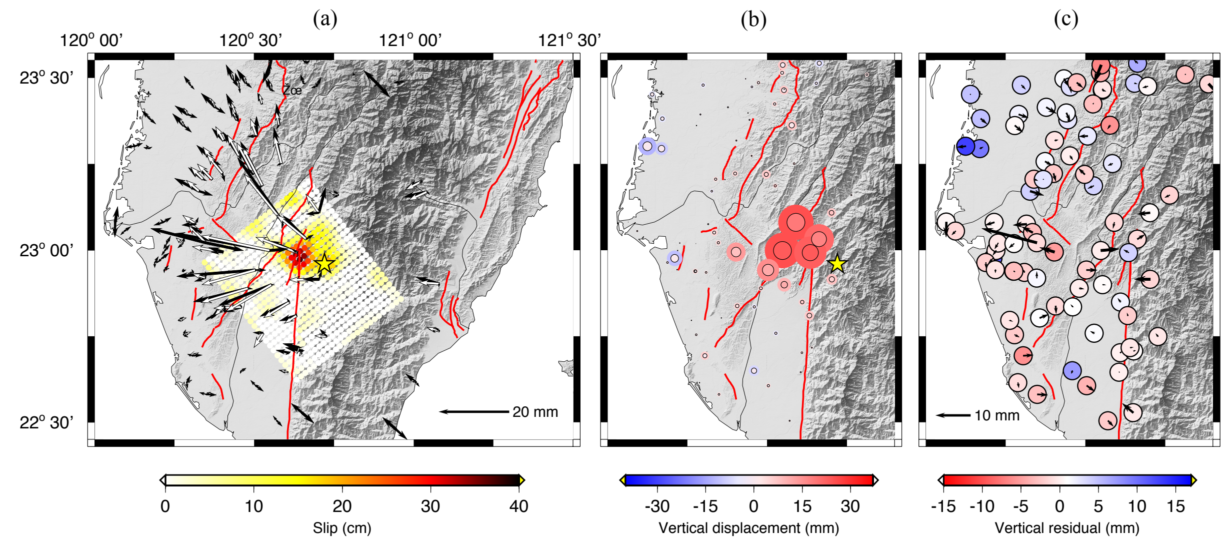

Figure 2.8: GPS-only inversion. (a) The black and white arrows represent the horizontal data and predictions, respectively. The color-contoured grid represents the coseismic slip model projected to the surface. (b) The color of the circles represent the vertical coseismic displacement. The circles without outlines and the circles with black outlines are the data and predictions, respectively. (c) The arrows and circle colors show the residuals between the GPS data and model predictions.

inversion finds the main asperity close to that of the GPS-only inversion.

2.5.3 Joint Inversion

For the joint inversion, we keep the same weighting ratio between GPS and InSAR (GPS weight = 10 $\times$ InSAR weight) as in the geodetic inversion, we then change the weighting of geodetic data from 0.5 to 5 with a constant weighting the of seismic data (weight = 1). As shown in Fig. 2.10c, the VR for the geodetic data increases rapidly as the weight of the geodetic data increases from 0.5 to 5.0, whereas the VR of the seismic data decreases from 70 % to about 50 %. We choose a weight of the geodetic data of 2.0 from visual inspection of the tradeoff in fitting the respective datasets. Consequently, the VR for the seismic, GPS, and InSAR data in the joint inversion are 74.8 %, 64.9 %, and 77.0 %, respectively (Fig. 2.10c).

The result of the joint inversion is shown in Fig. 2.11b. Not surprisingly, we find a similar main slip asperity as in the individual and geodetic inversions (Figs 6a to 6c, 11a). The peak slip and the area of the main asperity are 42.5 cm and about 200 km^2, respectively. The total moment of the joint inversion is 3.25 $\times 10^{18}$ N m, which is equivalent to a M_w 6.34 event. Given the mean slip of 15 cm on a 20 $\times$ 25 km^2 main asperity (Fig. 2.11b), the static stress drop of the Jia-Shian event is 0.24 MPa. This value of stress drop is at least ten times smaller than the 1999 Chi-Chi earthquake (6.5 or 22.5 MPa, Huang et al., 2001; Ma et al., 2001) and its aftershocks [Chi and Dreger, 2004], and in the low range of global average stress drops for reverse events [Allmann and Shearer, 2009; Mai and Beroza, 2000]. Some minor asperities are seen in the shallower part, but also in the western and bottom edges. The first 24 hours aftershocks are plotted onto the geodetic and the joint inversions. Most of them lie along the upper periphery of the main asperity, which implies that the aftershocks occurred along the margin of the coseismic rupture. Most of the aftershocks shown in Fig. 2.11 occurred in the first 12 hours.

2.5.4 Rupture Velocity From Seismic Data

The rupture velocity is examined for seismic-only and the joint inversions in order to evaluate the stability of the inversion associated with the combined data. As shown in Fig. 2.12, the rupture velocities producing higher VR are in the range of 3.8 – 4.4 km/sec for seismic VR for both seismic only and joint inversions. The preferred rupture velocity is somewhat higher in the joint inversion than in the seismic inversion, but the fitting curves are quite similar (Fig. 2.12). This shows that considering the geodetic data, which do not contain time dependent information of the earthquake source, does not change the inferred rupture velocity much. The preferred rupture velocity range is higher than the shear wave velocity

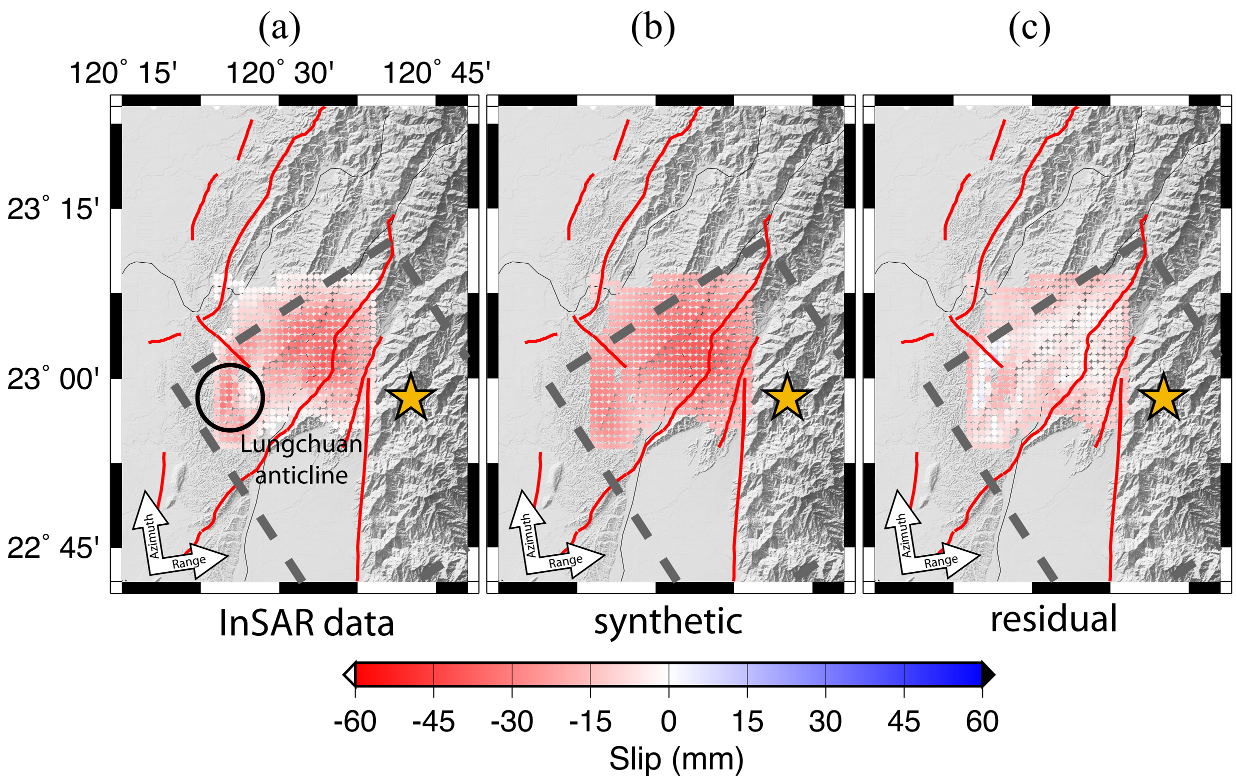

Figure 2.9: Observed, predicted and residual InSAR displacements from InSAR-only inversion. (a) Coseismic InSAR measurements after downsampling and noise reduction (see text). The spatial resolution is about one pixel per km^2. (b) InSAR model prediction with the same color scale. (c) Difference between the observed and predicted InSAR observations. The orange star represents the epicenter of the earthquake, and the gray dashed lines represent the outline of the fault model.

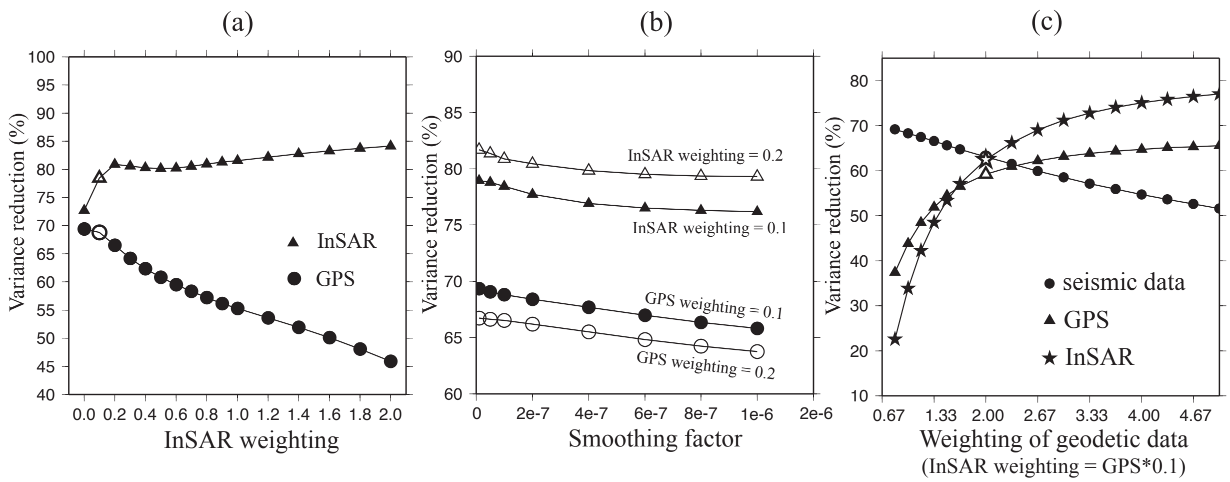

Figure 2.10: Tests of weighting and smoothing for geodetic and joint inversions. (a) Different InSAR weighting with GPS weighting fixed to one versus VR. The white triangles and circles represent the range of preferred weights of the InSAR data. (b) Tests for the smoothing factor to the geodetic inversion. Triangles and circles show VR of InSAR and GPS data, respectively. White and Black symbols represent InSAR weighting of 0.2 and 0.1, respectively. (c) Weighting of each data set versus VR. The weighting of seismic data is fixed to 1, and the InSAR weight is 10% of the GPS weighting.

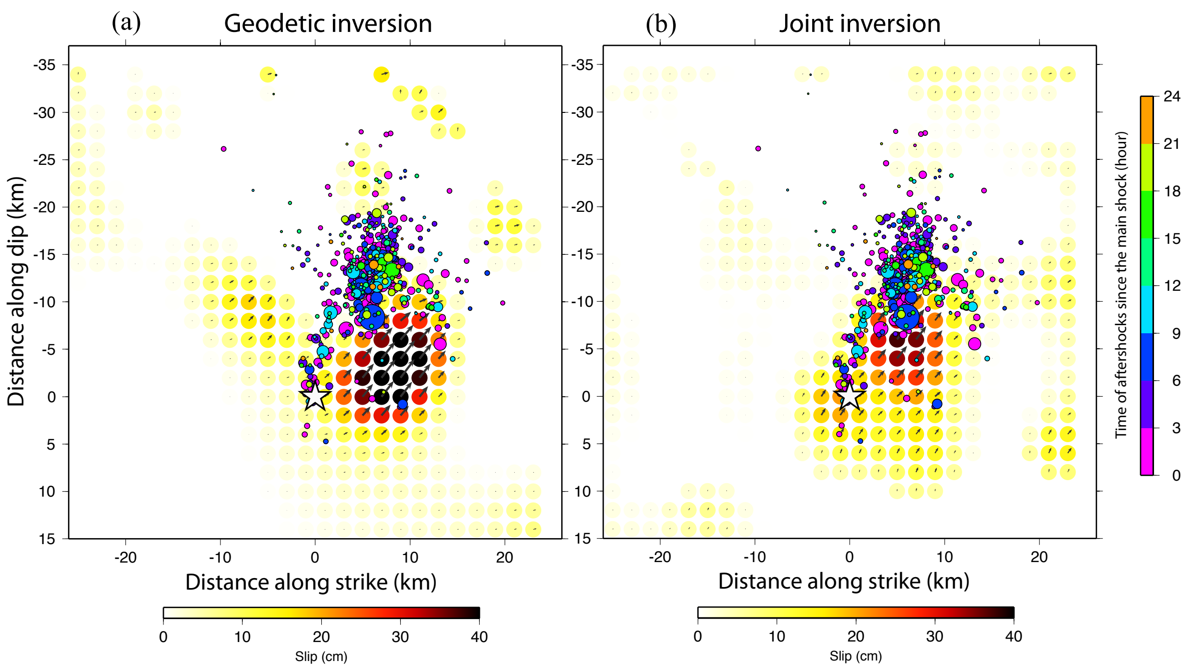

Figure 2.11: Coseismic slip model obtained from (a) geodetic inversion (peak slip: 39.8 cm; total moment: 3.30×10^{18} N m; GPS VR: 68.8%, InSAR VR: 78.4%), (b) Joint inversion (peak slip: 42.5 cm; total moment: 3.25×10^{18} N m; seismic VR: 74.8%, GPS VR: 64.9%, InSAR VR: 77.0%). The black arrows represent the slip direction and amplitude of each subfault. The colored circles are the aftershocks since the main shock in hours.

in either west or east Taiwan (3.7 and 3.4 km/sec, respectively). A rupture velocity between the shear wave and P wave velocity can be interpreted as a supershear event [Walker and Shearer, 2009]. In comparison, the rupture velocity obtained for other recent earthquakes in Taiwan such as the 1999 M_w 7.6 Chi-Chi earthquake in Central Taiwan and its larger aftershocks is much lower. The rupture velocity of the Chi-Chi mainshock is about 2.0 km/s [Ji et al., 2003] and 1.5 – 3.2 km/s for the larger aftershocks (M_w 5.8 to 6.3) that occurred in the month following the mainshock [Chi and Dreger, 2004]. Most of the Chi-Chi aftershocks are shallow events with source depth less than 16 km, except one at 18 km [Chi and Dreger, 2004]. The Jia-Shian event is located deeper than the earthquakes in Central Taiwan, so the larger rupture velocity and deeper location of this event may reflect a different geological setting.

Supershear ruptures are quite rare. At least two supershear cases are found in the 2001 M_w 7.8 Kokoxili [Bouchon and Vallée, 2003] and the 2002 M_w 7.9 Denali events [Ellsworth et al., 2004; Dunham and Archuleta, 2004; Dunham, 2007]. Walker and Shearer (2009) found a rupture velocity close to the P wave velocity (~5.6 km/s) for these two events. The supershear rupture velocity for these events is between $\sqrt{2} \times$ Vs and Vp, whereas the rupture velocity for the Jia-Shian event is only 1.23 $\times$ Vs. One interpretation is that supershear rupture velocity requires propagation for a certain distance up to which which the rupture velocity is still about 0.8 $\times$ Vs, and it will jump to $\sqrt{2} \times$ Vs or higher velocities after this initial distance (Walker and Shearer, 2009). In other words, the rupture velocity history is not a constant and can be quite complex. In our inversion we assume a constant rupture velocity resulting in a value between the Rayleigh wave velocity (2.72 km/sec) and 2 $\times$ Vs (4.8 km/sec), which may decrease the maximum rupture velocity. We also test the inversion with Rayleigh wave velocity as the rupture velocity and find a rougher slip distribution and smaller slip area given the same smoothing (Fig. 2.S4). The total VR in this model is reduced by 2.2 % from the best fitting model.

2.6 Resolution and sensitivity tests using synthetic data

We test the sensitivity and the model resolution in order to evaluate the validity of our joint inversion result and the influence on the inversion from incomplete data or inversion parameterization (e.g. incorrect rupture velocity). For the station sensitivity analysis we perform the inversion with incomplete datasets in order to investigate the solution with different distributions of stations. For the resolution test we generate an artificial rupture model similar to the Jia-Shian event to obtain synthetic waveforms and geodetic data. Different smoothing and noise, and incorrect rupture velocity are added to the synthetic data to test the resolution of the inversion results.

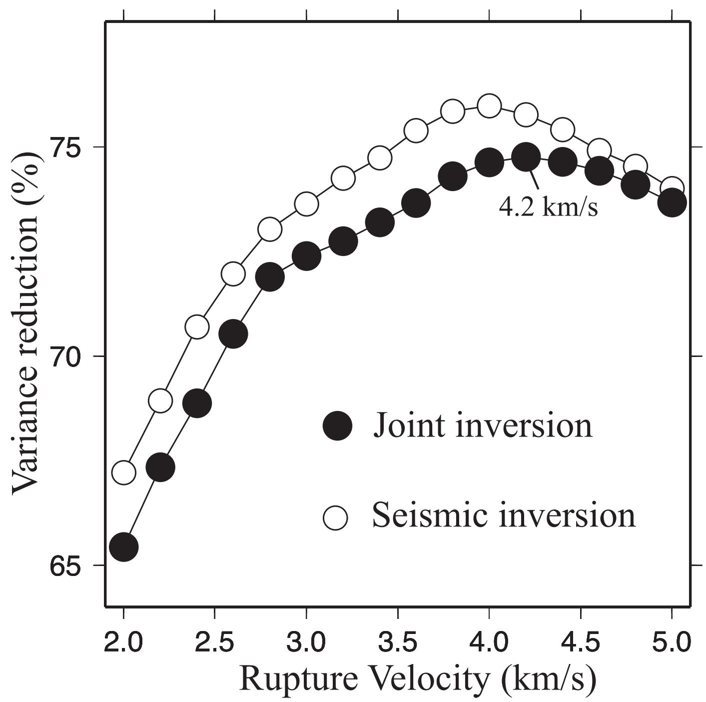

Figure 2.12: The variance reduction versus rupture velocity. The white circles are the seismic only inversion and the black circles are the VR of seismic data in the joint inversion. The rupture velocity used in this study is 4.2 km/sec.

2.6.1 Stations and Solution Sensitivities

In south Taiwan, the seismic and GPS stations are deployed in mountain, foothill, and plain areas (Figs 1b and 2a), and the InSAR data points are restricted to the relatively flat area (Fig. 2.2b). As a result, the topography and the geologic structure underneath the stations may add propagation complexity and affect the finite-source inversion result. Timing errors, site, and 3D propagation effects in the seismic data contribute additional sources of uncertainty to the model [Kim and Dreger, 2008]. In order to test the effect of the spatial distribution of data and the uncertainties of the seismic data, we randomly remove 20 % of the seismic, GPS, and InSAR data and repeat this process 20 times to see how much the resampled seismic and geodetic data can vary the inferred coseismic slip distribution. The average slip, standard deviation, and the coefficient of variation of the slip on the fault plane from the 20 inversions are shown in Fig. 2.13. The slip distribution obtained from all data and the 80 % data subsets are very similar. The obtained standard deviation of slip of the subfaults (Fig. 2.13b) is generally 10 times smaller than the slip on each subfault but is larger along the bottom and west edges of the fault plane. The coefficient of variation is the standard deviation divided by the average slip, which indicates a more stable solution when the coefficient is lower. The coefficient of variation of each subfault (Fig. 2.13c) shows that the coefficient is less than 30 % in the main asperities (the asperity near the hypocenter and the upper right of the fault plane), which indicates that these asperities represent stable features of the slip models.

The average total moment obtained from the 20 subsampled datasets is 3.22×10^{18} N m with a standard deviation of 1.18×10^{17} N m, and the coefficient of variation is equal to 3.67%. The total moment based on the 80% data subsets is very close to that based on the joint inversion (3.29×10^{18} N m). The VR of the 80% data are 71.7% (standard deviation, std: 2.23%), 66.4% (std: 4.72%), and 76.2% (std: 1.27%) for the seismic, GPS, and InSAR data, respectively. These values are very close to the joint inversion with all of the data (74.8%, 64.9%, and 77.0% for seismic, GPS, and InSAR, respectively, Fig. 2.10c). However, it is notable that the coefficient of variation of slip for the GPS data (7.11%) is much higher than that for the seismic (3.11%) or the InSAR data (1.68%), so it appears that the GPS data have less sensitivity to slip than the other two datasets. Indeed, given the uncertainties of the GPS about 0.25 cm in horizontal and 0.7 cm in vertical based on the GPS data of Hsu et al. [2011], the coseismic displacement in the far-field stations may be lower than their noise level. So the random removal of 20% GPS data (including both far- and near-field stations) can increase the GPS model variance more than in either of the seismic or InSAR tests. For InSAR data, since we down-sample the interferogram and take the average line of sight displacement from two interferograms, the data are relatively smoother than GPS or seismic data. For the seismic data, it seems that the solution is well constrained with the different station subsets, and thus station coverage does not appear to introduce a bias in the solution.

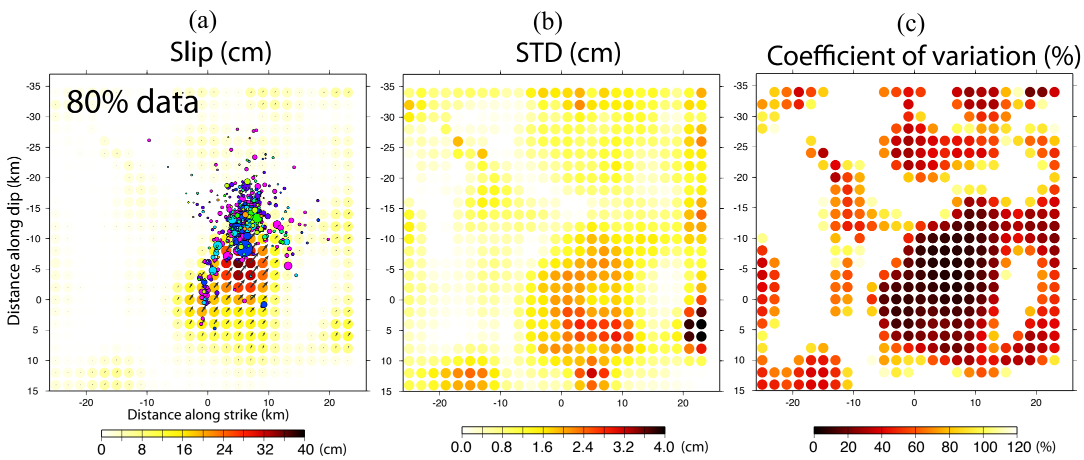

Figure 2.13: Sensitivity test of inversions using 20 repeated samples of 80% of seismic, GPS, and InSAR data. (a) average slip, (b) standard deviation, and (c) coefficient of variation. The mean total moment is 5% larger than the total moment obtained in the inversion of all of the data (Figure 11b).

2.6.2 Resolution Test

The resolution test investigates the sensitivity of the source model to the spatial distribution of the seismic and geodetic data. In addition, we also test how data smoothing, weighting, and the noise level affect the model resolution. In this test, we use a forward slip model on the same 50 km $\times$ 50 km fault plane with 625 subfaults and a synthetic slip distribution (Fig. 2.14e). The rupture velocity is set to be 4.2 km/sec. We use the forward model to obtain the synthetic seismic waveforms and geodetic measurements. In order to keep the same condition as in our data inversion, we keep the same weight between seismic and geodetic data as in our previous joint inversion, and then add the smoothing to the inversion and/or add random noise of 20% of peak amplitude to the seismic waveforms as well as the geodetic data.

Fig. 2.14a shows the result without smoothing and noise. The variance reduction is more than 99% for the three datasets, and the number of the slip asperities and the area are the same as the input model, even though the amplitude of the slip in the asperities is not fully recovered. Another test with seismic only inversion shows 100% variance reduction and identical slip distribution as the input model (Fig. 2.S5). In fact, one seismic station has 65 (sec) $\times$ 10 (sample/sec) $\times$ 3 (components) = 1,950 samples, so we have 1,950 $\times$ 10 (stations) = 19,500 data points for the inversion, with only 625 unknown subfaults $\times$ 2 degree-of-freedom for rake = 1,250. Besides, we do not change the rise time, rupture velocity, and the Green's functions, so an identical result could be obtained in the absence of noise. However, the total number of GPS or InSAR data points is less than the unknowns, so the joint inversion that requires weighting of seismic, GPS, and InSAR cannot reproduce an identical inversion result. In the first test there is no smoothing applied to the inversion, so the slip on the subfaults will be assigned in order to obtain highest VR without considering any correlation on the adjacent subfaults (Fig. 2.14a). In addition, the seismic data represent finite wavelengths in the data [Kim and Dreger, 2008], so the constraining equations (smoothing between the adjacent subfaults) are needed to prevent the model from over fitting the given data. As a result, some amount of smoothing needs to be applied to the inversion, even though it will decrease the fit to data. The inversion with the same smoothing as we apply in the joint inversion is shown in Fig. 2.14c. The variance reduction is still very high ($>$ 99% for three datasets), but now the inversion result shows the correct number of asperities and the amplitude of the slip is much closer to the input model compared to the inversion without smoothing.

Furthermore, we apply random noise scaled at 20% of the peak amplitude of each synthetic waveforms and synthetic geodetic displacements (GPS and InSAR) obtained from the input model, in order to simulate the condition that the waveforms are affected by the regional heterogeneity or other site-effects. Without applying any smoothing (no constraining equations between subfaults), the result (Fig. 2.14b) shows a very scattered slip distribution,

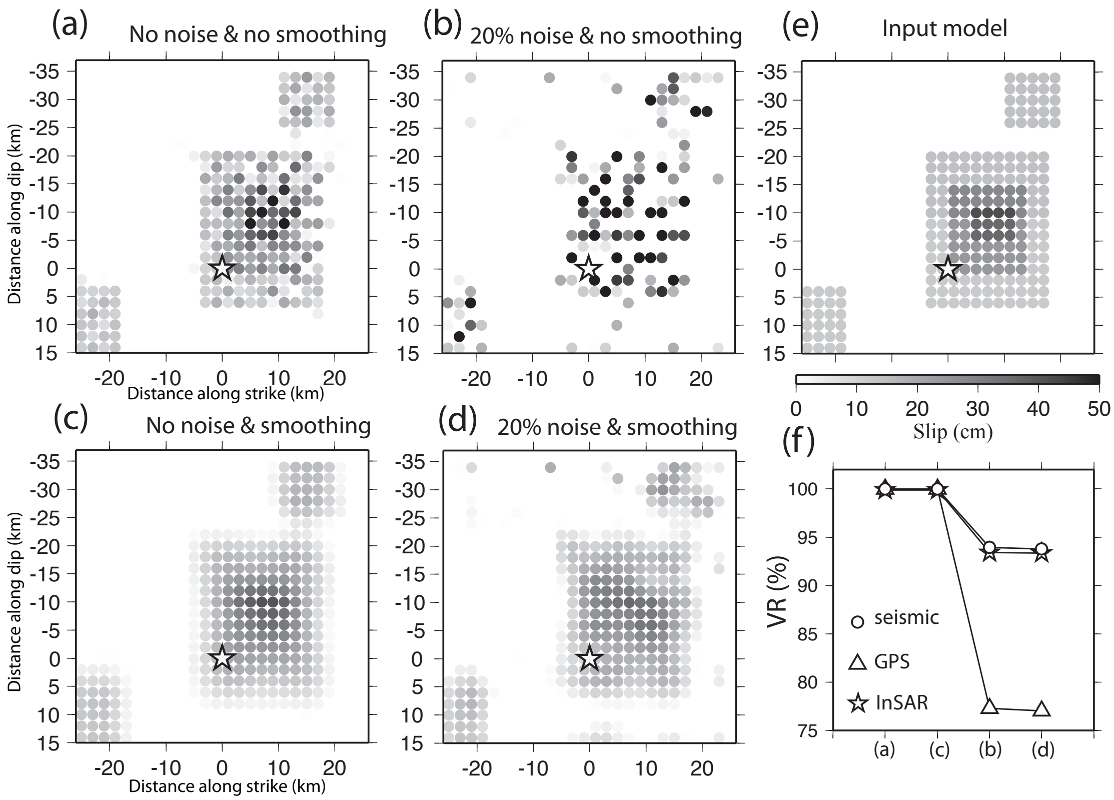

Figure 2.14: Synthetic resolution tests. (a) Inversion result without smoothing (constraining equations). (b) Inversion result with the smoothing. (c) Inversion result with random noise (20% of the peak amplitude of seismic data, GPS, and InSAR) without smoothing. (d) Inversion result with noise and smoothing. (e) Input slip model. The velocity models, rake, rise time, and rupture velocity are the same as used in the joint inversion of the Jia-Shian event. (f) Variance reduction of each dataset and different resolution tests.

even though the slip areas are similar to the input model and the variance reduction is still high (98.57%, 99.98%, and 99.87% for seismic, GPS, and InSAR data respectively). With 20% noise and smoothing applied (Fig. 14d), the slip asperities are smeared out, but the peak slip is similar to the input model. This suggests that even with certain amounts of uncertainty in the seismic and geodetic data, the inversion result does not deviate from the input model. The result of this test differs from a previous study on the 2004 Parkfield, California, strike-slip rupture using the same method [Kim and Dreger, 2008]. They found that they cannot recover the slip distribution deeper than 13 km, but our resolution test shows that the inversion can resolve the slip even at the depth of 25 km, which is likely due to our use of more distant seismic and GPS stations that provide coverage in both the near- and far-field, and because we include the vertical component of seismic and GPS data.

In order to investigate the effect of the choice of rupture velocity on the inversion result, we test the inversion of the synthetic data (produced with a rupture velocity of 4.2 km/sec) with rupture velocities from 2.0 to 5.0 km/sec. We find that the VR drops to 70.5% for the low (2.6 km/sec) rupture velocity that is generally obtained for other earthquakes in central Taiwan (e.g., Ji et al., 2001; Chi and Dreger, 2004). It is also notable that the inversion cannot resolve the deeper portion of the slip distribution given a much slower rupture velocity, and the depth of the slip asperities changes as rupture velocities are varied (see the different rupture velocities in Fig. 2.15). However, no matter the variation of the rupture velocity, the variance reduction does not change much for the synthetic GPS or InSAR datasets (all above 96% for all rupture velocities). This suggests that the geodetic data are not very sensitive to the details of the slip distribution at greater depths, and therefore the temporal constraint on the earthquake source from the seismic data is very important to resolve the slip distribution on the fault plane.

2.7 Discussion

2.7.1 Comparison with other studies

The geodetic and joint inversions show the total moment of the Jia-Shian event as 3.30×10^{18} and 3.25×10^{18} N m, which both equal M_w 6.34. Fig. 2.11 shows the inversion results of the geodetic and the joint inversions. The colored circles represent the aftershocks in the first 24 hours following the mainshock [Huang et al., 2011]. From this figure, the main difference between the geodetic and the joint inversions is the slip area. The main slip area of the joint inversion is more compact and surrounded by the aftershocks, whereas the slip area of the geodetic inversion is observed inside and outside of the aftershocks (e.g., the smaller slip asperity on the left hand side of the epicenter in Fig. 2.11a). The difference might be due to additional postseismic displacement that may be observed by the GPS and InSAR data. As

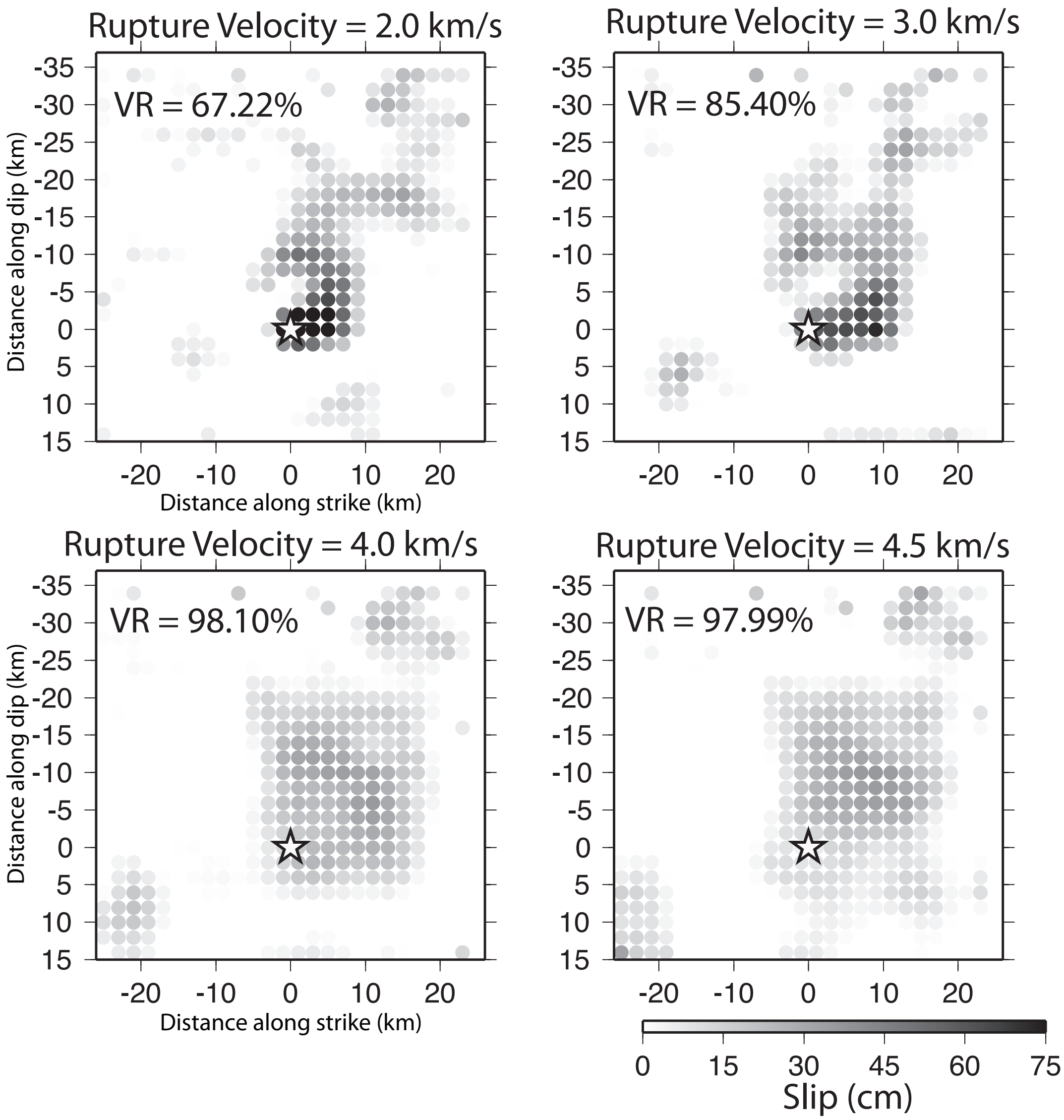

Figure 2.15: Joint inversion using synthetic input from forward model shown in Fig 14e. The forward model has a rupture velocity of 4.2 km/s and inversions are tested with a range of rupture velocities. Note that even though the incorrect rupture velocity can significantly decrease the fit to the seismic data, it does not significantly change the fit to the geodetic data (VR of the geodetic data are above 96% for all models shown).

a result, the geodetic inversion would also include some afterslip, whereas the joint inversion has weighting from seismic data and would be more restricted to the mainshock. Thus, the joint inversion better represents the coseismic slip distribution due to the mainshock. We can clearly see that most of the aftershocks are located along the upper peripheries of both inversions, which indicates that the aftershocks lie along the highly stressed coseismic slip margin. Both the slip area and the aftershock distribution indicate that the main slip asperity is about 226 km^2 with about 43 cm peak slip obtained in the joint inversion. The difference in total moment between the geodetic and the joint inversions is about 5 $\times$ 10^{16} N m, which is equivalent to a M_w 5.1 earthquake. Since the largest aftershock of this event is M_w 5.0 (3.54 $\times$ 10^{16} N m) that occurred about 8 hours later, the difference between the geodetic and joint inversions could largely be due to this and other aftershocks.

Similar work has been done by [Ching et al., 2011] (GPS inversion), Hsu et al. [2011] (GPS inversion), and Lee et al. [2012] (seismic and GPS combined inversion). Both Ching et al. [2011] and Hsu et al. [2011] inferred about 12 cm peak coseismic slip, whereas Lee et al. [2012] found 35 cm. The total moment obtained in previous studies differs, but is of the same order (2.92 $\times$ 10^{18} from Ching et al.; 4.95 $\times$ 10^{18} from Hsu et al.; 6.53 $\times$ 10^{18} from Lee et al., units in N m). The GPS data we use are the same as Hsu et al. [2011] and similar to the data used by Ching et al. [2011] and Lee et al. [2011], so the main differences could be the result of different model parameterizations (, subfault discretization and smoothing), or the velocity structure applied (half-space geodetic inversion for Ching et al., 2011 and Hsu et al., 2012; CWB 1D velocity for Lee et al., 2011; two refined 1D velocity structures represented for west- and east Taiwan for seismic inversion and layered model for geodetic inversion in this study).

Mai and Beroza [2000] develop source-scaling properties based on finite-source rupture models. They estimate the empirical relations between the seismic moment and fault length, fault width, and mean slip for dip-slip and strike-slip events. According to their empirical relations, a $M_o = 3.25 \times 10^{18}$ N m event would have a fault area = 105 km^2 with length = 10.8 km and width = 9.7 km, and mean slip = 104.7 cm. Our joint inversion result suggests a fault area = 286 km^2 and mean slip $\approx$ 20 cm. In other word, the slip area of Jia-Shian event is 2.7 times larger than the average, and the mean slip is only 1/5 of that expected for a M_w 6.3 event. Nevertheless, while the values of fault length, width, and mean slip of Jia-Shian deviate from the average, they are still within the standard errors (i.e. the a and b values in Mai and Beroza, 2000). This lower mean slip value also suggests that the Jia-Shian event was a low stress-drop event. Given the mean slip of 15 cm on a 20 $\times$ 25 km^2 main asperity (Fig. 2.11b), the static stress drop of the Jia-Shian event is 0.24 MPa. This value of stress drop is at least ten times smaller than the 1999 Chi-Chi earthquake (6.5 or 22.5 MPa, Huang et al., 2001; Ma et al., 2001) and its aftershocks (Chi and Dreger, 2004), and in the low range of global average stress drops for reverse events (Allmann and Shearer, 2009; Mai and Beroza, 2000).

2.7.2 The Relation with the CTFZ and regional seismicity

The NW-SE strike-slip Chishan Transfer Fault Zone (CTFZ) was proposed by Deffontaines et al. [1997] based on morphological evidence and field mapping (Fig. 2.1a). Mapped shear bands in the surrounding mudstones in this region indicate a left-lateral sense of shear that has a minimum 12 $\pm$ 4 mm/yr slip-rate based on offset geologic markers and sparse GPS data [Deffontaines et al., 1997]. Ching et al. [2011] argued that based on this long-term slip rate and the coseismic peak slip of about 19 cm from their geodetic inversion, an earthquake with a magnitude similar to the Jia-Shian event would occur every 12-24 years. This rapid recurrence rate is inconsistent with the observed low strain rate and low background seismicity in the source area [Ching et al., 2011], it assumes that all CTFZ displacement is accommodated by the fault on which the Jia-Shian event occurred, and the slip rate on the fault plane at 20 km deep is unknown. In addition, the peak coseismic slip is quite uncertain and depends on the smoothing and rupture velocity applied to the inversion, as we showed in the synthetic tests.

A recent study by Rau et al. [2012] indicates that the NW-trending Jia-Shian earthquake sequence and the upward extension of the rupture to the surface correspond to the CTFZ. However, based on the result of our individual and joint inversions (Fig. 2.6), there is a minor slip asperity in the western shallower part of the fault. The surface projection of this minor patch coincides with the Lungchuan anticline (location see Fig. 2.9a), which is about 13 km south of the CTFZ. Hence, the Jia-Shian fault plane does not extend to the inferred CTFZ unless the dip changes with depth on the fault [Ching et al., 2011].

The Jia-Shian earthquake occurred in a transition zone separating regions of distinctly different depth extent of seismicity and seismic velocity. A S-to-N profile of the regional seismicity and Vp tomography (seismicity and velocity tomography data from Wu et al., 2007, 2009) of SW Taiwan is shown in Fig. 2.16. The seismicity data clearly show a change in depth to the base of the seismogenic zone from about 15 km in the north to about 25 km in the south, near latitude $22.8° - 23°$N. A corresponding change is observed in tomographic Vp velocity models, with a 5-km-thick near-surface low velocity layer (Vp $<$ 4.5 km/s) in the north increasing to about 10 km depth in the south. There is an apparent gap in seismicity at 22.9°N that seems to be filled by the Jia-Shian mainshock and aftershocks (Figs 2.1 and 2.16). However, the north dipping Jia-Shian earthquake clearly did not involve faulting parallel to this south dipping seismicity transition zone. Nevertheless, both the Jia-Shian event and the transition zone represent ESE-WNW striking structures in SW Taiwan that may correspond to Miocene structures formed during the extension of the south China Sea [Teng, 1990] and were reactivated during the latest orogeny. The change in crustal strain orientations across this area described in the next section may also relate to the effect of such deep-seated pre-existing structures.

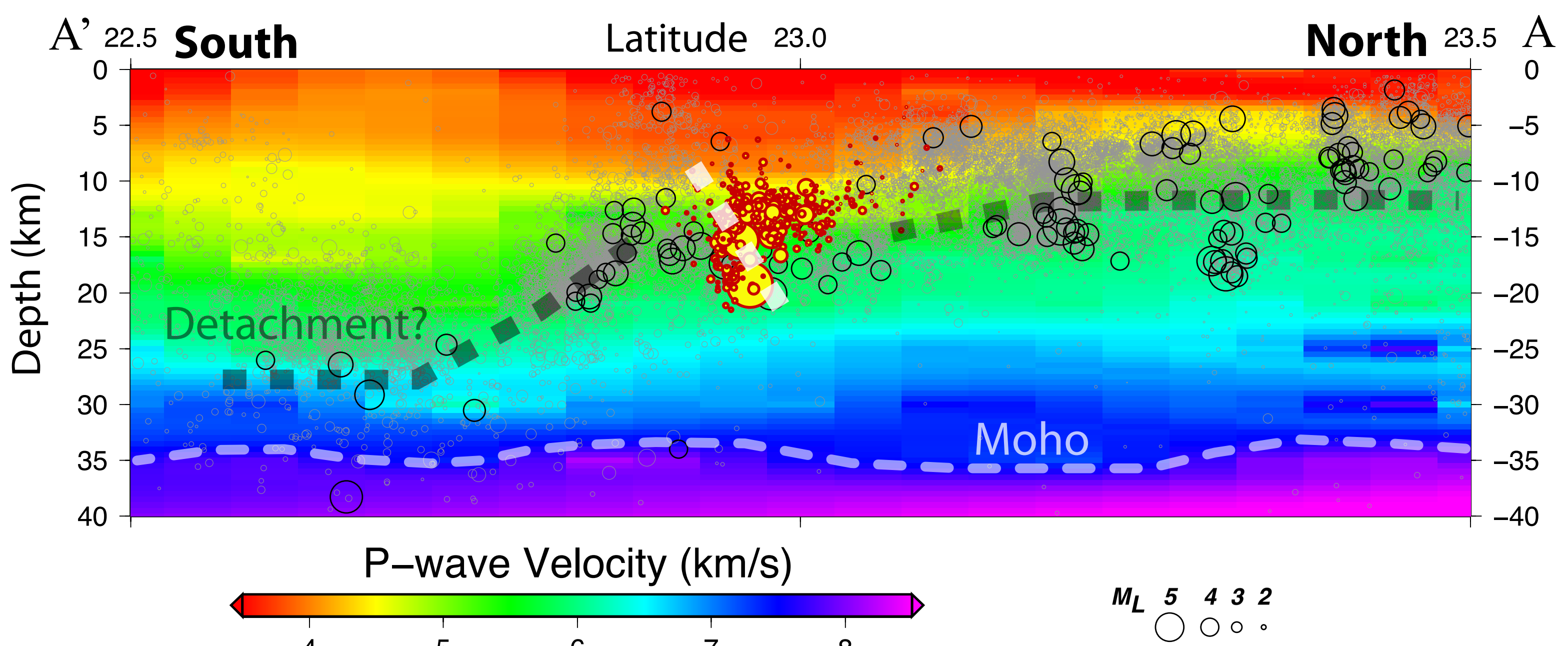

Figure 2.16: Distribution of seismicity from 1991 to 2009 (data from Wu et al., 2009) along S-to-N profile AA' in Fig. 1a. The grey circles are the seismicity lower than M_w 4.0; the black circles are those larger than M_w 4.0. The red circles show the Jia-Shian main shock and its aftershocks [Huang et al., 2011]. The background colors show the regional P-wave tomography model of Wu et al. [2007] along the same profile.

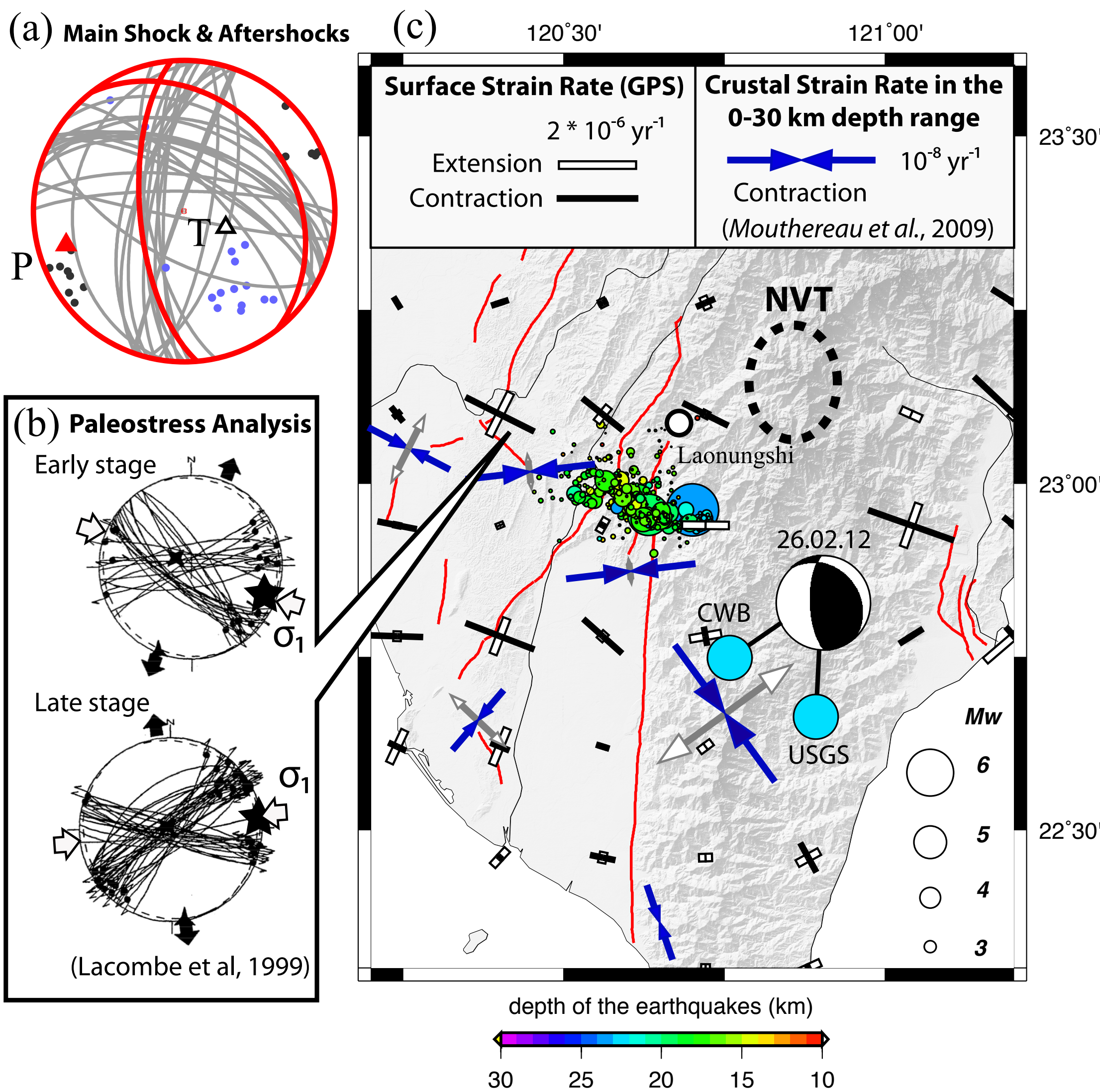

Figure 2.17: (a) Focal mechanisms of the Jia-Shian main shock (red) and its aftershocks (grey). The red and white triangles represent the P- and T-axes of the main shock; the black and blue dots represent the P- and T-axes of the aftershocks. (b) Paleostress reconstruction based on fault slip analysis of the Chishan Transfer Fault Zone in SW Taiwan (after Lacombe et al., 1999). (c) Surface (bars) and crustal (arrows) two-dimensional strain rate tensor measurements in SW Taiwan obtained from GPS and seismicity data, respectively. A cluster of non-volcanic tremor (NVT) identified by Chao et al. (2012) is outlined with dashed ellipse. The beach ball diagram shows the 26th February, 2012 event and its epicenter located by CWB and USGS.

2.7.3 Paleostress Analysis and Crustal Scale Strain

Lacombe et al. [1999] analyze the paleostress inferred from regional fault orientations and slip vectors and find two Quaternary stress regimes: an early period of NW-SE (140°) compression followed by more recent E-W (080°) compression (Fig. 2.17). The earlier direction of compression appears to reflect the current direction of plate convergence, whereas the second direction prevailed only in the latest stage of folding. Recently, a study by Huang et al. [2010] on the paleostress orientations near Laonungshi to the north of the Jia-Shian earthquake (location see Figs 2.1b and 2.17c) resolved two primary NW-SE and WNW-ESE, and one NE-SW compressional directions. The NE-SW compression represents the youngest stage based on cross-cutting relationships, but the age is not well constrained. While the orientation of inferred stress axes in SW Taiwan is quite heterogeneous (Fig. 2.17c), the paleostress studies provide some evidence for recent initiation of an E-W compressional stress regime near the Jia-Shian earthquake.

Geodetic measurements can be used to determine interseismic strain rate fields and the orientation of the principal strain axes across Taiwan. We consider GPS measurements of the horizontal strain rate tensor and the orientation and rate of regional horizontal principal strains inferred from earthquake focal mechanisms. The surface strain rate estimated by GPS measurements between 2000 and 2005 (Fig. 2.S6, GPS data from Kuo, 2008) indicates E-W to SE-NW directed contraction in SW Taiwan. The orientation of maximum shortening is close to the current direction of plate collision [Lin et al., 2010]. In the area of the Jia-Shian event, there seems to be a transition from shortening to extension between the Western Foothills and the Central Range. This is in contrast to the strain field based on focal mechanism inversions (dark blue arrows in Fig. 2.17; after Mouthereau et al., 2009), which shows ENE-WSW contraction in the northern Pingtung plain and the Western Foothill near the Jia-Shian event, but SE-NW oriented contraction in the southern Central Range. This ENE-WSW shortening has the same orientation as the P axis of the mainshock (this study) and most of the aftershocks [Huang et al., 2011]. Thus, the major compression axis of the Jia-Shian event agrees with the ambient strain distribution at source depth (21 km) but not the geodetic strain field observed at the surface.

2.7.4 Latest Aftershock and Nearby Tremors

On 26^{th} February, 2012, an M_w 5.7 earthquake occurred about 25 km (USGS solution) or 40 km (CWB location) southeast of the Jia-Shian sequence (Fig. 2.17). Both the focal mechanism and the source depth (22.5km) of this earthquake are similar to the Jia-Shian mainshock. This recent earthquake can be considered as an aftershock of the Jia-Shian event due to the similar focal mechanism and source depth, and may have involved slip on the same geological structure. The appearance of this recent event may indicate that this

NW-SE structure (Fig. 2.1a) extends further to the southeast beneath the Central Range of Taiwan, but whether or not this represents a SE continuation of the CTFZ is unclear.

A recent study of non-volcanic tremor (NVT) by Chao et al. [2012] finds deep triggered tremors located beneath the Central Range at 15-25 km depth, about 20 km north of the Jia-Shian sequence. The tremors were triggered by several M_w 7.5+ earthquakes at distances of more than 1000 km. These triggered tremors are bursts of high frequency (2-8 Hz), non-impulsive and long-duration seismic energy modulated by surface waves. Chao et al. [2012] explain the triggered tremors as Coulomb failure involving NS-striking, left-lateral shear on a low-angle detachment fault at the base of the seismogenic zone of the Central Range, but the steeply E-dipping Chaochou-Lishan Fault has also been suggested as a possible source structure of tremor activity in S Taiwan [Tang et al., 2010]. It may be worth exploring the triggering potential of deep-seated receiver faults with a Jia-Shian type orientation. The repeated teleseismic triggering of tremor suggests the existence of weak fault structures in the lower crust below the Central Range and SW Taiwan. Future studies of this tremor activity may improve our understanding of the deep roots of the deformation zone associated with the Jia-Shian earthquake.

2.7.5 Thick or Thin Skinned Model

The depth of the nucleation of this event seems to support a thick-skinned model for SW Taiwan [Ching et al., 2011], even though there is some inconsistency in the depth between the previous studies (e.g. 23 km from CWB, 23-24 km from Ching et al. [2011] and Huang et al. [2011] and our finite source inversion (18-19 km). The earthquake occurred within a NW-SE oriented transition zone across which the depth to the base of seismicity increases by about 10 km to the south, possibly associated with the CTFZ proposed by Deffontaines et al. [1997]. The latest M_w 5.7 aftershock implies that this NW-SE structure may extend at least 50 km into the south Central Range. This structure may also involve pre-existing normal faults that are associated with the opening of the South China Sea during Miocene pre-collision stage [Lin and Watts, 2002; Rau et al., 2012]. However, the actual geometry of these preexisting structures and their relationship with the CTFZ, the source fault of the Jia-Shian earthquake, the orientation of active shortening, and the topographic expression of the active Tectonics in this area are not well understood. Hence, models considering more complex fault geometry, and an improved velocity structure model may be needed to gain further insight about the structure and setting of the Jia-Shian event, and provide more information on this long lasting debate.

2.8 Conclusion

In this study we apply finite source inversion techniques relying on seismic, GPS, and InSAR data individually, as well as in a joint inversion to obtain rupture models of the 2010 Jia-Shian earthquake. Contrary to previous studies of this event, we generate separate Green's functions for seismic stations in west and east Taiwan by fitting the waveforms of the largest aftershock to calibrate the velocity structure and Green's functions. We also find the proper frequency band for fitting the largest aftershock to apply for the inversion of mainshock data for finite-source parameters. In addition, we use a layered elastic model for the geodetic inversions to help with obtaining a more reliable slip distribution. These efforts result in high consistency between the models obtained independently from the different data sets. A comprehensive test of the model smoothing of each dataset and the weighting between different datasets for the joint inversion represents an objective way to investigate the model parameters and solutions, and to find the best weighting relation between the different datasets. The station sensitivity test done by the random removal of 20% data shows the main features of the inversion result are stable. The resolution test with added noise also informs on the confidence of the shallower slip, and the effect of the smoothing we applied on the solution. The individual inversions using seismic or geodetic data show consistent peak slip, slip area, and magnitude of the Jia-Shian mainshock. The total moment of this event obtained in the joint inversion is 3.25×10^{18} N m, which is equivalent to an M_w 6.3 event. Rupture velocity tests suggest that this event was a supershear event propagating at about 1.23 of the regional shear-wave velocity.

The Jia-Shian event in SW Taiwan occurred along the boundary between the western Foothills and the Central Range to the north and east and the sedimentary Pingtung Basin in the south. This boundary coincides with a transition zone from shallower (north) to deeper (south) seismicity and the previously proposed CTFZ at the surface. However, since the up-dip extension of the coseismic slip is located south of the CTFZ, whether or not the Jia-Shian event is within the CTFZ at depth remains unclear. The youngest paleostress orientations and compression axes from seismic data are consistent with the kinematics of the Jia-Shian earthquake. Around the region of the Jia-Shian sequence, the stress orientation in the upper crust inferred from focal mechanism data is not consistent with the directions of the surface strain rate field derived from GPS or the current plate collision. The location of the most recent large aftershock (M_w 5.7) reveals that the deep structure extends further to the SE below the Central Range. Consequently, the Jia-Shian event may represent the reactivation of pre-existing deep structures, and the orientation of stress locally deviates from the current orientation of plate collision.

2.9 Supplementary figures

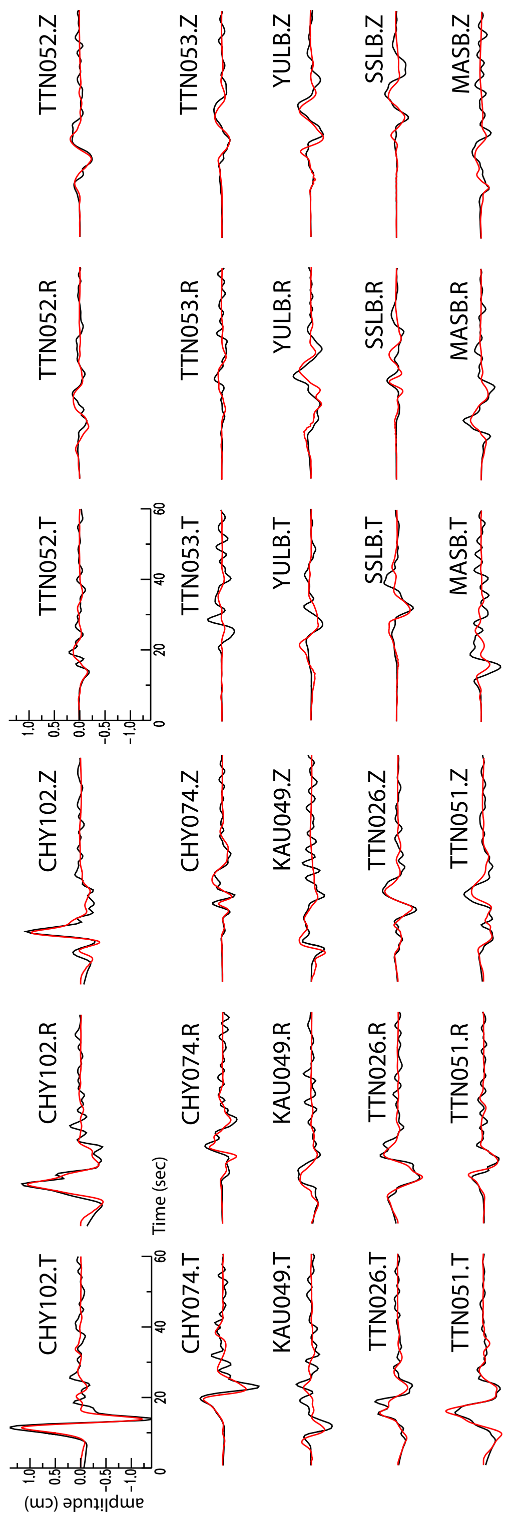

Figure 2.18: The comparison of synthetic (red) and the data (black) by using joint inversion. CHY102, CHY074, KAU049, TTN026, TTN051, TTN052 and TTN053 are strong motion stations. YULB, SSLB and MASB are broadband stations. All of the waveforms are bandpassed to 0.030.3 Hz. The locations of all stations see in Fig. 2.1(b).

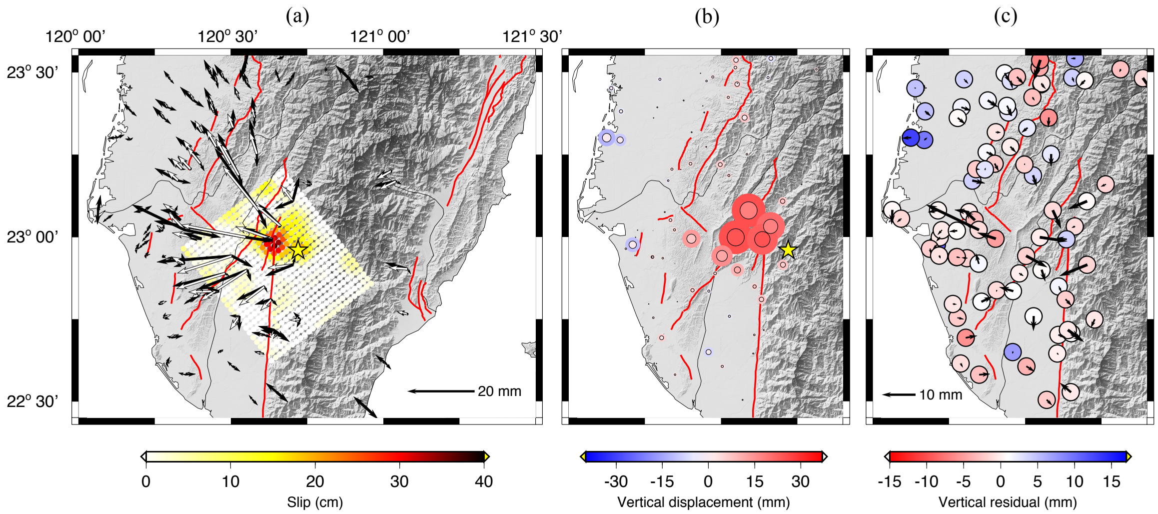

Figure 2.19: The predicted GPS displacement based on joint inversion and the residual. (a) The black and white arrows represent the data and predictions of horizontal motions, respectively. The rectangular grids represent the coseismic slip projected onto the surface. (b) The colour and size of the circle represents the GPS vertical coseismic displacement. The circles without outlines and the circleswith black outlines are the data and predictions, respectively. (c) The arrows and colours in the circles are the residuals between the GPS data and predictions.

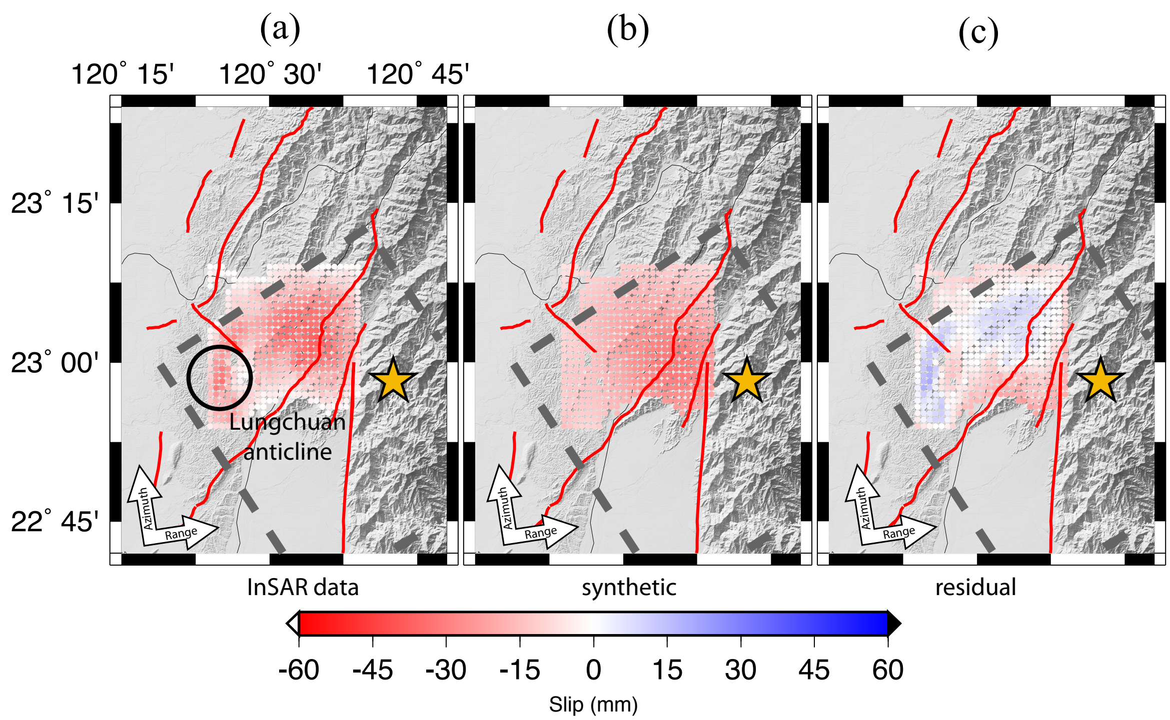

Figure 2.20: The predicted InSAR displacement based on joint inversion and the residual. (a) Coseismic InSAR measurements after downsampling and noise reduction (see text). The spatial resolution is about one pixel per km^2. (b) InSAR prediction with the same colour scale. (c) Difference between the observed and predicted In- SAR observations. The orange star represents the epicentre of the earthquake, and the grey dashed lines represent the fault model.

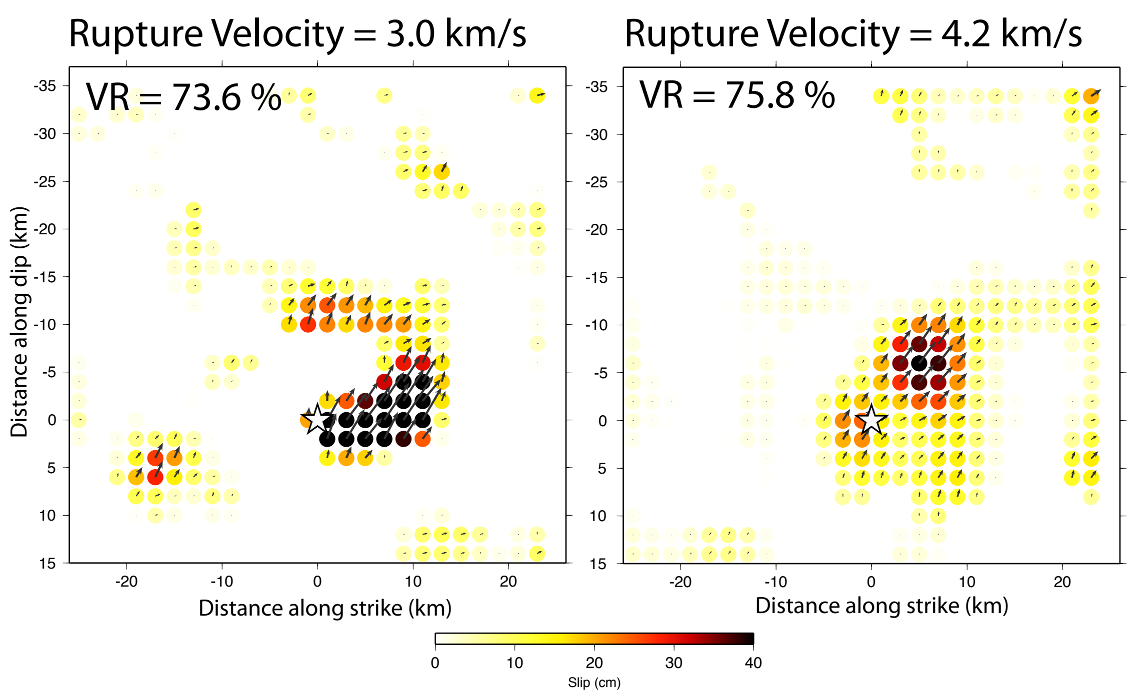

Figure 2.21: Joint inversion with different rupture velocities. Rupture velocity = 3.0 km s[1] is equivalent to the Rayleigh velocity in this region.

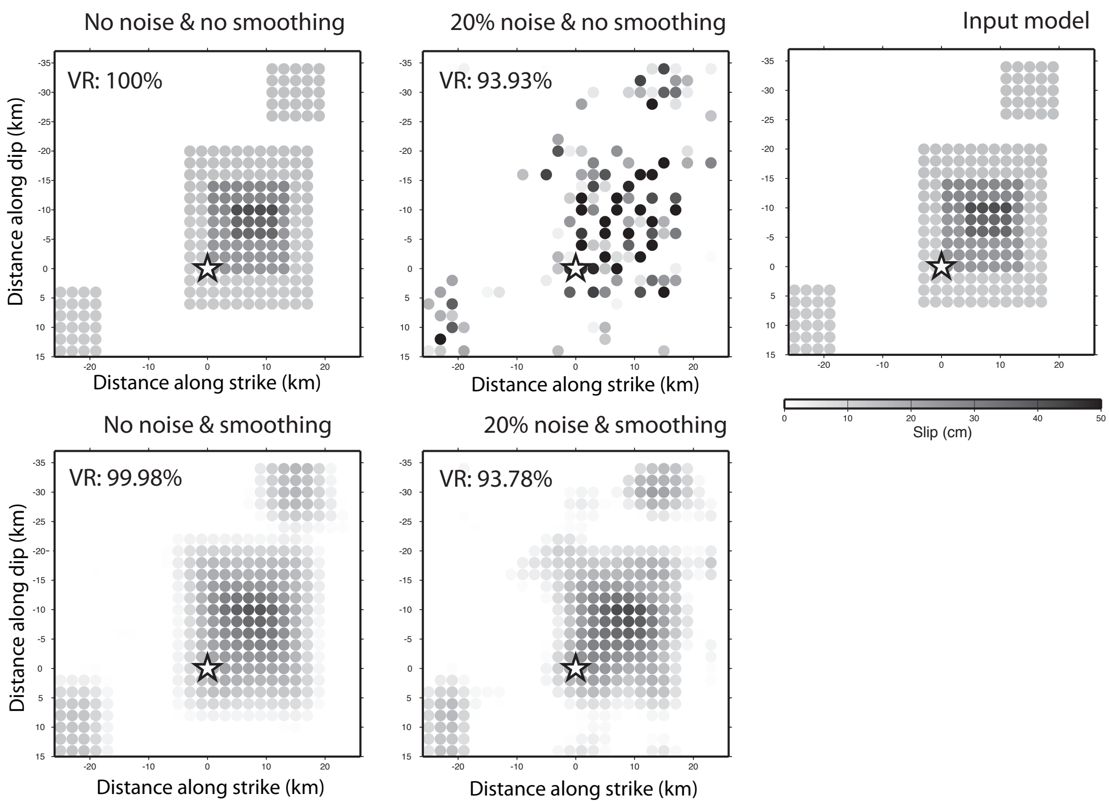

Figure 2.22: Synthetic resolution tests with seismic only inversion.

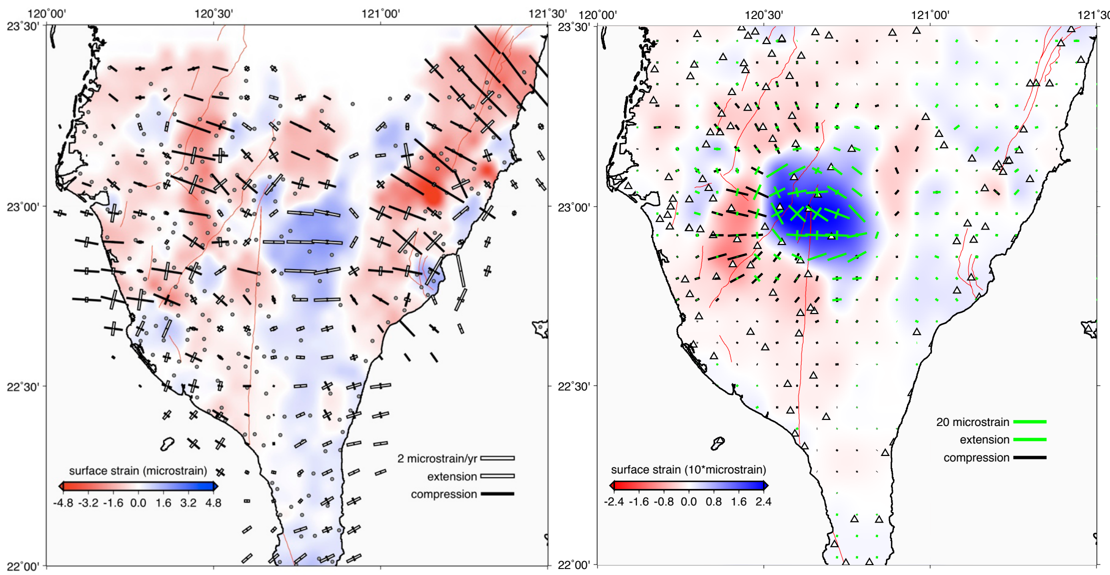

Figure 2.23: (a) Surface strain rate from 2002 to 2007 (GPS data from Kuo 2008). (b) Strain change obtained from GPS station offsets due to the Jia-Shian earthquake.

Bibliography

[1] Allmann, B. P., and P. M. Shearer, 1991, Global variations of stress drop for moderate to large earthquake, *J. Geophys. Res.*, *114*, B01310.

[2] Bouchon, M., and M. Valle, 2003, Observation of long supershear rupture during the magnitude 8.1 Kunlunshan earthquake, *Science*, 301, 824-826, doi:10.1126/*Science*.1086832.

[3] Chao, K., Z. Peng, C. Wu, C.-C. Tang, and C.-H. Lin, 2012, Remote triggering of non-volcanic tremor around Taiwan, *Geophys. J. Int.*, 188, 301-324, doi:10.1111/j.1365-246X.2011.05261.x.

[4] Chi, W.-C. and Dreger, D., 2002, Finite fault inversion of the September 25, 1999 (Mw=6.4) Taiwan earthquake: Implications for GPS displacements of Chi-Chi, Taiwan earthquake sequence, *Geophy. Res. Lett.*, 29, 1694, doi:10.1029/2002GL015237.

[5] Chi, W.-C., and D. Dreger, 2004, Crustal deformation in Taiwan: Results from finite source inversions of six Mw ¿ 5.8 Chi-Chi aftershocks, *J. Geophys. Res.*, 109, B07305, doi:10.1029/2003JB002606.

[6] Ching, K.-E., K. M. Johnson, R.-J. Rau, R. Y. Chuang, L.-C. Kuo, and P.-L. Leu, Inferred fault geometry and slip distribution of the 2010 Jiashian, Taiwan, earthquake is consistent with a thick-skinned deformation model, 2011, *Earth Planet. Sci. Lett.*.

[7] Cohee, B. P. and Beroza, G. C., 1994, Slip distribution of the 1992 Landers Earthquake and Its Implications for Earthquake Source Mechanics, *Bull. Seismol. Soc. Am.*, 84, 692-712.

[8] Deffontaines, B., Lacombe, O., Angelier, J., Chu, H.T., Mouthereau, F., Lee, C.T., Deramond, J., Lee, J.F., Yu, M.S., Liew, P.M., 1997, Quaternary transfer faulting in the Taiwan Foothills: evidence from a multisource approach, *Tectonophysics*, 274, 61-82.

[9] Dreger, D. and A. Kaverina, 2000, Seismic Remote Sensing for the Earthquake Source Process and Near-Source Strong Shaking: A Case Study of the October 16, 1999 Hector Mine Earthquake, *Geophy. Res. Lett.*, 27, 1941-1944.

[10] Dunham, E. M., 2007, Conditions governing the occurrence of supershear ruptures under slip-weakening friction, *J. Geophys. Res.*, 112, B07302, doi:10.1029/2006JB004717.

[11] Dunham, E. M., and R. J. Archuleta, 2004, Evidence for a supershear transient During the 2002 Denali fault earthquake, *Bull. Seismol. Soc. Am.*, 94(6B), S256-S268, doi:10.1785/0120040616.

[12] Ellsworth, W. L., M. Celebi, J. R. Dvans, E. G. Jensen, R. Kayen, M. C. Metz, D. J. Nyman, J. W. Roddick, P. Spudich, and C. D. Stephens, 2004, Near-field ground motion of the 2002 Denali fault, Alaska, earthquake recorded at pump station 10, *Earthquake Spectra*, 20, 597-615, doi:10.1193/1.1778172.

[13] Hartzell, S. H., and T. H. Heaton, 1983, Inversion of strong ground motion and teleseismic waveform data for the fault rupture history of the 1979 Imperial Valley, California, earthquake, *Bull. Seismol. Soc. Am.*, 73, 1553-1583.

[14] Hsu, Y.-J., S.-B., Yu, L.-C., Kuo, Y.-C., Tsai, and H.-Y., Chen, 2011. Coseismic deformation of the 2010 Jiashian, Taiwan earthquake and implications for fault activities in southwestern Taiwan, *Tectonophys.*, 502, 328-335, doi:10.10^{16}/j.tecto.2011.02.005.

[15] Hu, J.-C., C.-S. Hou, L.-C. Shen, Y.-C. Chan, R.-F. Chen, C. Huang, R.-J. Rau, K. H. Chen, C.-W. Lin, M.-H. Huang, and P.-F. Nien, 2007, Fault activity and lateral extrusion inferred from velocity field revealed by GPS measurements in the Pingtung area of southwestern Taiwan, *J. Asian Earth Sci.*, 31, 287-302.

[16] Huang C., T. Byrne, and D. Mirakian, 2010. Geologic Setting of the 2010 Jiasian earthquake, southern Taiwan, abstract T23D-03 presented at 2010 Fall Meeting, AGU, San Francisco, Calif., 13-17 Dec.

[17] Huang, H.-H., Y.-M. Wu, T.-L. Lin, W.-A. Chao, J. B. H. Shyu, C.-H. Chan, and C.-H. Chang, 2011, The preliminary Study of the 2010 Mw 6.3 Jiasian, Taiwan, Earthquake Sequence, Terr. Atmos. Ocean. Sci., 22(3), 283-290, doi:10.3319/TAO.2010.12.13.01(T).

[18] Huang, W.-G., J.-H. Wang, B.-S. Huang, K.-C. Chen, T.-M. Chang, R.-D. Hwang, H.-C. Chiu, and C.-C. P. Tsai, 2001, Estimates of Source Parameters for the 1999 Chi-Chi, Taiwan, Earthquake Based on Brunes Source Model, *Bull. Seism. Soc. Am.*, 91(5), 1190-1198.

[19] Kim, A., and D. S. Dreger, 2008, Rupture process of the 2004 Parkfield earthquake from near-fault siesmic waveform and geodetic records, *J. Geophys. Res.*, 113, B07308, doi:10.1029/2007JB005115.

[20] Kuo S.-M., 2008, Earthquake potential of SW Taiwan inferred from GPS and seismic data. Master thesis, National Cheng Kung University, pp. 66.

[21] Lacombe, O., F. Mouthereau, B. Deffontaines, J. Angelier, H.-T. Chu, and C.-T. Lee, 1999, Geometry and Quaternary kinematics of fold-and-thrust units of southwestern Taiwan, *Tectonics*, 18, 1198-1223.

[22] Lacombe, O., F. Mouthereau, J. Angelier, and B. Deffontaines, 2001, Structural, geodetic and seismological evidence for tectonic escape in SW Taiwan, *Tectonophys.*, 333, 323-345, doi:10.10^{16}/S0040-1951(00)00281-X.

[23] Lee, S.-J., L. Mozziconacci, W.-T. Liang, Y.-J. Hsu, W.-G. Huang and B.-S. Huang. Source complexity of the 4 March 2010 Jiashian, Taiwan, Earthquake determined by joint inversion of teleseismic and near field data, *J. Asian Earth Sci.*, doi:10.10^{16}/j.jseaes.2012.11.018.

[24] Lin, A.-T., and A. B. Watts, 2002, Origin of the West Taiwan basin by orogenic loading and flexure of a rifted continental margin, *J. Geophys. Res.*, 107(B9), 2185, doi:10.1029/2001JB000669.

[25] Lin, K.-C., J.-C. Hu, K.-E. Ching, J. Angelier, R.-J. Rau, S.-B. Yu, C.-H. Tsai, T.-C. Shin, and M.-H. Huang, 2010, GPS crustal deformation, strain rate, and seismic activity after the 1999 Chi-Chi earthquake in Taiwan, *J. Geophys. R.*, 115, B07404, doi:10.1029/2009JB006417.

[26] Ma, K.-F., J. Mori, S.-H. Lee, and S.-B. Yu, 2001, Spatial and Temporal Distribution of Slip for the 1999 Chi-Chi, Taiwan, Earthquake, *Bull. Seism. Soc. Am.*, 91(5), 1069-1087.

[27] Mai, P. M. and G. C. Beroza, 2000, Source Scaling Properties from Finite-Fault-Rupture Models, *Bull. Seismol. Soc. Am.*, 90, 604-615.

[28] Minson, S. E. and D. S. Dreger, 2008, Stable inversions for complete moment tensors, *Geophys. J. Int.*, 174, 585-592, doi:10.1111/j.1365-246X.2008.03797.x.

[29] Mouthereau, F., C., Fillon, and K.-F., Ma, 2009. Distribution of strain rates in the Taiwan orogenic wedge, *Earth Planet. Sci. Lett.*, 284, 361-385.

[30] Pasyanos, M. E., D. S. Dreger, and B. Romanowicz, 1996, Toward real-time estimation of regional moment tensors, *Bull. Seism. Soc. Am.*, 86(5), 1255-1269.

[31] Rau, R.-J., and F. Wu, 1995, Tomographic imaging of lithospheric structures under Taiwan, *Earth Planet. Sci. Lett.*, 133, 517-532.

[32] Rau, R.-J., and J.-C., Lee, K.-E., Ching, Y.-H., Lee, T. B. Byrne, and R.-Y., Chen, 2012. Subduction-continent collision in southwestern Taiwan and the 2010 Jiashian earthquake sequence, *Tectonophysics.*, 578, 107-116, doi:10.10^{16}/j.tecto.2011.09.013.

[33] Rosen, P. A., S. Hensley, et al., 2004, Updated Repeat Orbit Interferometry Package Released. *Eos Trans. AGU*, 85(5), 35.

[34] Saikia, C. K., 1994, Modified frequency-wave-number algorihm for regional seismograms using Filons quadrature-modeling of L(g) waves in eastern North America, *Geophys. J. Int.*, 118, 142-158.

[35] Shin, C., K. Yoon, K. J. Marfurt, K. Park, D. Yang, H. Y. Lim, S. Chung, and S. Shin, 2001, Efficient calculation of a partial-derivative wavefield using reciprocity for seismic imaging and inversion, *Geophys.*, 66, 1856-1863.

[36] Somerville, P. G., K. Irikura, R. Graves, S. Sawada, D. Wald, N. Abrahamson, Y. Iwasaki, T. Kagawa, N.

[37] Smith, and A. Kowada, 1999, Characterizing crustal earthquake slip models for the prediction of strong ground motion, *Seismo. Res. Lett.*, 70, 59-80.

[38] Suppe, J., 1981, Mechanics of mountain building and metamorphism in Taiwan. *Mem. Geol. Soc. China*, 4, 67-89.

[39] Suppe, J., C.-T. Hu, and Y.-J. Chen, 1985, Present-Day stress directions in western Taiwan inferred from borehole elongation, *Petr. Geol. Taiwan*, 21, 1-12.

[40] Tarantola, A., 2005, Inverse Problem Theory and Model Parameter Estimation, Society for Industrial and Applied Mathematics, Philadelphia.

[41] Tang C.-C., Z. Peng, K. Chao, and C.-H. Lin, 2010, Detecting low-frequency earthquakes within non-volcanic tremor in southern Taiwan triggered by the 2005 Mw 8.6 Nias earthquake, *Geophy. Res. Lett.*, 37, L16307, doi:10.1029/2010GL043918.

[42] Teng, L., 1990, Geotectonic evolution of late Cenozoic arc-continent collision in Taiwan, *Tectonophys.*, 183, 57-76.

[43] Wald, D. J. and P. G. Somerville (1995). Variable-slip rupture model of the great 1923 Kanto, Japan earthquake: geodetic and body-waveform analysis, *Bull. Seism. Soc. Am.*, 85, 159-177.

[44] Wald, D. J. and T. H. Heaton (1994). Spatial and temporal distribution of slip for the 1992 Landers, California earthquake, *Bull. Seism. Soc. Am.*, 84, 668-691.

[45] Wald, D. J., and T. H. Heaton, and K. W. Hudnut (1996). Rupture history of the 1994 Northridge, California earthquake from strong-motion, GPS, and leveling data, *Bull. Seism. Soc. Am.*, 86, S49-S70.

[46] Wang, C. Y. and R. B. Herrmann, 1980, A numerical study of P-, SV-, and SH-wave generation in a plane layered medium, *Bull. Seism. Soc. Am.*, 70(4), 1015-1036.

[47] Wang, R., F. Martin, and F. Roth, 2003, Computation of deformation induced by earthquakes in multi-layered elastic crust: FORTRAN programs EDGRN/EDCMP, *Comput. Geosci.*, 29, 195-207.

[48] Wessel, P., and W. H. F. Smith, 1995, New version of the generic mapping tools released, *Eos Trans. AGU*, 76(29), 329.

[49] Wu, F. T., Rau, R. J., and Salzberg, D. H., 1997. Taiwan orogeny: thin-skinned or lithospheric collision? *Earth Planet. Sci. Lett.*, 133, 517-532.

[50] Wu, Y.-M., C.-H. Chang, L. Zhao, J. B. H. Shyu, Y.-G. Chen,, K. Sieh, and J. P. Avouac, 2007, Seismic tomography of Taiwan: Improved constraints from a dense network of strong-motion station, *J. Geophys. Res.*, 112, B08312, doi:10.1029/2007JB004983.

[51] Wu, Y.-M., J. B. H. Shyu, C. H. Chang,, L. Zhao, M. Nakamura, and S.-K. Hsu, 2009, Improved seismic tomography offshore northeastern Taiwan: Implications for subduction and collision processes between Taiwan and the southernmost Ryukyu, *Geophys. J. Int.*, 178, 1042-1054, doi:10.1111/j.1365-246X.2009.04180.x.

[52] Yeh, Y.-H., Barrier, E., Lin, C.-H., and Angelier, J., 1991. Stress tensor analysis in the Taiwan area from focal mechanisms of earthquakes, *Tectonophysics*, 200, 267-280.

[53] Yoo, S.-H., J. Rhie, H. Choi, and K. Mayeda, 2010. Evidence for non-self-similarity and transitional increment of scaled energy in the 2005 west off Fukuoka seismic sequence, *J. Geophys. Res.*, 115, B08308, doi:10.1029/2009JB007169.

[54] Yoshida, S. and Koketsu, K., 1990. Simultaneous inversion of wave-form and geodetic data for the rupture process of the 1984 Naganoken Seibu, Japan, earthquake, *Geophys. J. Int.*, 103, 355-362, doi:10.1111/j.1365-246X.1990.tb01776.x.

[55] Yu, S.-B., H.-Y. Chen, and L.-C. Kuo, 1997. Velocity field of GPS stations in the Taiwan area, *Teconophysics*, 274, 41-59, doi:10.10[16]/S0040-1951(96)00297-1.

[56] Yu, S.-B., Y.-J. Hsu, L.-C., Kuo, H.-Y., Chen, C.-C. Liu, 2003. GPS measurement of postseismic deformation following the 1999 Chi-Chi, Taiwan, earthquake. *J. Geophys. Res.*, 108, doi:10.1029/2003JB002396.

Part II

Postseismic Deformation

Chapter 3

Viscous Post 1989 M_W 6.9 Loma Prieta earthquake relaxation revealed from GPS and InSAR Data

3.1 Abstract

The 1989 M_w 6.9 Loma Prieta earthquake provided an opportunity of probing the crustal and upper mantle rheology of Bay Area since the 1906 M_w 7.9 San Francisco earthquake. Insights into lithospheric rheology can be gained from observations of postseismic deformation, which represents the response of the Earths interior to coseismic stress changes. Here we use geodetic observations including GPS and InSAR to reveal the 1989 M_w 6.9 Loma Prieta earthquake postseismic displacement from 1989.8 to 2013. We observe 1-4 mm/yr GPS horizontal displacement toward the Loma Prieta epicenter, and ~2 mm/yr land subsidence in southern Santa Clara Valley between 1992 and 2002 followed by ~1 mm/yr uplift until 2013. We model the viscoelastic relaxation by assuming a 30-km-thick crust (19-30 km is viscoelastic) with a viscoelastic upper mantle. The best fitting model is composed of an elastic upper crust, a viscous lower crust ($\eta = 10^{19}$ Pa s), and a bi-viscous upper mantle ($\eta_M = 10^{18}$ Pa s; $\eta_K = 10^{17}$ Pa s), which is consistent with rheologic studies in South California. Repeating earthquake activities following the Loma Prieta event seem to correlate with surface displacement, both driven by the viscoelastic relaxation from upper mantle.

Keywords: Loma Prieta earthquake, postseismic displacement, lithospheric rheology, viscoelastic relaxation, San Francisco Bay Area

3.2 Introduction

Periods of accelerated postseismic deformation following large earthquakes reflect the response of the Earth's lithosphere to sudden coseismic stress changes. Thus, detailed geodetic measurements of postseismic relaxation effectively probe the rheology off rocks and faults at depth [Bürgmann and Dresen, 2008]. Transient post-earthquake relaxation includes contributions from (1) fault afterslip above [Bürgmann, et al., 1997; Johnson, et al., 2006; Marone, et al., 1991; Freed, 2004] and below [Bürgmann, et al., 2002; Tse and Rice, 1986] the base of the seismogenic zone, (2) viscous flow in the lower crust and upper mantle [Pollitz, et al., 2001], and (3) poroelastic rebound in the upper crust due to fluid flow in response to coseismic pressure changes [Jónsson, et al., 2003; Peltzer, et al., 1996]. For relatively small earthquakes, shallow afterslip and poroelastic relaxation dominate the observed postseismic transients and contributions from below the seismogenic zone are difficult to resolve [Jónsson, et al., 2003; Pollitz, et al., 1998; Freed et al., 2007]. Depending on the magnitude of the source earthquake and the viscosity structure of the lithosphere, viscous relaxation at depth dominates transient deformation, especially at larger distances from the coseismic rupture [Freed et al., 2010].

Much of our knowledge of the earthquake cycle and the rheology of the deep SAF system in central California is based on interpretation of geodetic measurements collected in the decades following the 1906 San Francisco earthquake that ruptured a $\sim$ 400-km-long section of the SAF [Kenner and Segall, 2003; Thatcher, 1983]. Kenner and Segall [2003] consider data collected between 1906 and 1995 in a systematic evaluation of various first-order models of lower-crustal structure and rheology. They find that models incorporating vertical viscous shear zones in the lower crust provide a good fit to the geodetic data and are consistent with seismic studies that suggest that narrow fault zones extend through the entire crust [Parsons, 1998; Henstock et al., 1997]. The occurrence of the M_w 6.9 Loma Prieta earthquake provides the first opportunity since 1906 to study postseismic relaxation processes and estimate rheological parameters in the region with modern space geodetic tools.

The deformation measured with GPS immediately following the Loma Prieta earthquake revealed significant postseismic contraction and right-lateral shear across the southern Santa Cruz Mountains northeast of the SAF [Bürgmann, et al., 1997; Savage et al., 1994; Savage and Svarc, 2010]. The localized nature of the transient displacement field indicates relatively shallow deformation sources. The measurements of the first five years can be interpreted to be due to aseismic right-oblique fault slip on or near the coseismic rupture, as well as thrusting up-dip of the rupture within the Foothills thrust belt [Bürgmann, et al., 1997]. Analysis of the time-varying nature of the deformation signal suggests that the shallow transient thrusting ceased in 1992 while resolvable oblique shear at seismogenic depths may have persisted through 1994 [Segall, et al., 2000]. The total moment of the modeled 1989 – 1994 afterslip on the two sources was $\sim 5\times10^{18}$ N m, about 15 % of the coseismic moment release [Segall et al., 2000]. Analysis of the GPS measurements did not resolve a significant contribution of lower-crustal, or upper-mantle relaxation processes during the first 5 years following the event [Pollitz et al., 1998]. Longer-term geodetic measurements can help us resolve continued transient strain accumulation in the region.

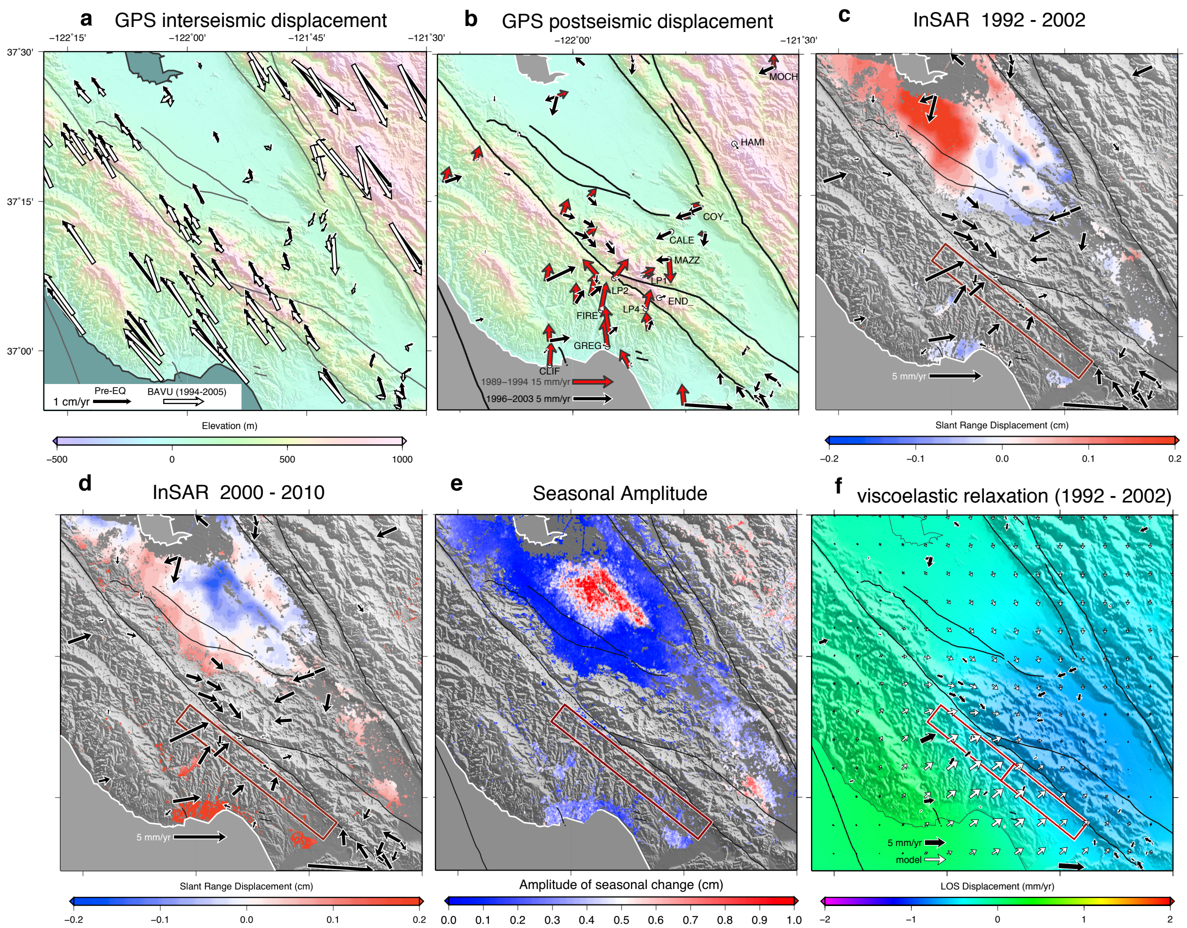

Figure 3.1: (a) The horizontal displacement in South Bay and the Santa Cruz area in different time periods. The circles represent the GPS stations with yearly survey. The red arrows are the EDM measurements before the Loma Prieta earthquake; the black arrows are the GPS measurements between 1996 and 2005; the white arrows are the predicted interseismic displacement based on Johanson and Bürgmann, 2005. (b) The Loma Prieta postseismic GPS displacment in early (1989-1998; red arrows) and late (1994-2005; black arrows) periods. (c) Mean annual InSAR LOS velocity during 1992-1997 and (d) 1997-2003. Note the red rectangle is the Loma Prieta earthquake fault. (e) Amplitude of InSAR seasonal change during 1992-2010. (f) Best fitting viscoelastic relaxation model (white arrows) predicting the Loma Prieta postseismic displacement during 1992-1997.

Since the Loma Prieta earthquake, several studies have focused on the interseismic deformation in the Bay Area that accommodates the secular motion between the North American plate and the Pacific plate. d'Alessio et al. [2005], Johanson and Bürgmann [2005], and Bürgmann et al. [2006] estimate the Bay Area interseismic displacement model based on campaign and continuous GPS measurements after 1994 (Figs 3.1a and 3.8). Even though the model-predicted displacement generally agrees with most of the GPS measurements, a systematic misfit exists around Santa Cruz Mountains in all studies (Fig. 3.1b). This result indicates a mechanism that cannot be predicted by regional fault system. In addition, Bürgmann et al. [2006] found similar model residual restricted in northern and eastern Santa Cruz mountains from PSInSAR measurement. We argue that this systematic residual is due to viscoelastic relaxation following the Loma Prieta coseismic stress change still acting on this area after 1994. In this study, we use GPS and InSAR time series data to investigate the viscoelastic relaxation following Loma Prieta earthquake. To do this, we combine different GPS campaigns during 1989 – 1998 [Segall et al., 2000] and 1994 – 2013 [USGS, 2014] to obtain a 24-year-long surface observation. We also generate an 18-year-long InSAR time series with sub-cm resolution between 1992 and 2010 based on both ERS-1/2 and Envisat satellites. We try to distinguish the postseismic displacement contributed by afterslip and viscoelastic relaxation, and therefore we can probe the lithospheric rheology based on surface displacement.

3.3 Geodetic Data

Before the Loma Prieta earthquake, the U. S. Geological Survey (USGS) has surveyed trilateration networks in the San Francisco Bay area since 1973 [Lisowski et al., 1990, 1991]. This measurement can detect temporal changes of the deformation rate between stations, and further provide the secular motion between the North American Plate and the Pacific Sea Plate prior to the Loma Prieta earthquake. Bürgmann et al. [1997] used the trilateration stations data to solve for the horizontal interseismic velocity field in the southern San Francisco Bay area. In addition, they developed a dislocation model of the San Francisco Bay area inverted based on the interseismic velocity field. This fault model is composed of 78 individual fault segments, and each fault segment has a uniform-slip dislocation in elastic, homogenous, and isotropic half-space. In this study we adopt the same fault dislocations and perform a forward modeling using the same boundary conditions, so we can estimate the velocity before the Loma Prieta earthquake that is mainly due to plate motions for each GPS station. The purpose of this is to remove the secular motion from the GPS measurements during the postseismic deformation period.

Segall et al. [2000] analyzed 173 daily GPS solutions at 62 stations collected from 1989.8 to 1998.3, and used the Network Inversion Filter (NIF) to investigate time dependent slip. They modeled relative baseline vectors by subtracting the position of an arbitrary site from the other simultaneously observed positions, in order to minimize the higher errors in the absolute position determinations due to translational biases in the reference frame. Later on, d'Alessio et al. [2005] published the Bay Area velocity unification (BAVU) solutions based on more than 200 campaign and continuous GPS measurements ranged between 1993 and 2003. All of the GPS benchmarks used in Segall et al. [2000] are continuously surveyed in BAVU, and most of them are currently updated to the 2010 campaigns (BAVU 3.0). Besides, USGS also resurveyed most of the GPS stations in early 2013 (`http://earthquake.usgs.gov/monitoring/gps/SFBayArea_SGPS/`), so we could potentially have 24 years of GPS postseismic time series data. Note the GPS measurement uncertainty is generally higher (about 10 mm in horizontal) in the earlier surveys (before 1994). Besides, we only rely on the horizontal GPS solutions because the uncertainty of the vertical component is higher (about 15 mm) than the postseismic signal.

To generate a long period of postseismic displacement time series, we combine GPS measurements from Segall et al. [2000], BAVU [d'Alessio et al., 2005], and the USGS 2013 survey data to obtain the time series of each GPS station. Also, we use the pre-Loma Prieta San Francisco Bay Area fault dislocation model [Bürgmann et al., 1997] to remove the secular motions. The main challenge of combing different GPS data sets is that each data set has different start time of measurements and different uncertainties (generally higher in Segall et al., 2000). We consider assigning early 1994 as the reference time because all GPS data sets covered measurements between 1994 and 1995, so we can obtain GPS measurements from 1989.8 to 2013. Another challenge is that Segall et al. [2000] considered vector positions of GPS rather than displacements, so they needed an arbitrary station for the reference site. In this sense, we need to find a reference site that has lower uncertainty and is continuously surveyed in both early and late periods. We follow Segall et al. [2000] and also choose their preferred site LP1 as the reference station as it has denser survey times since the Loma Prieta earthquake.

We use 52 ERS-1/2 SAR descending acquisitions (Track: 70) of the European Space Agency (ESA) between 1992 and 2006 and 46 Envisat ASAR descending acquisitions (Track: 70) of ESA between 2005 and 2010 (see Table 3.1 which list the detail of the SAR acquisitions). All interferograms are generated using ROI PAC 3.0 (Rosen et al., 2004). The 90 m Shuttle Radar Topography Mission (SRTM) DEM is used to correct the phase due to topography. Snaphu 1.4.2 [Chen and Zebker, 2002] is used for the phase unwrapping.

Persistent Scatterer InSAR (PSInSAR) is a method to detect stable signals from a series of interferograms that we can carry out the displacement from the stable scatterer points [Ferretti et al., 2001; Berardino et al., 2002; Hooper et al., 2008]. We find the stable point scatterers by setting a threshold in a stack of the coherence map of each SAR pair. In general, smaller spatial or temporal baseline has higher coherence that makes the interfero-

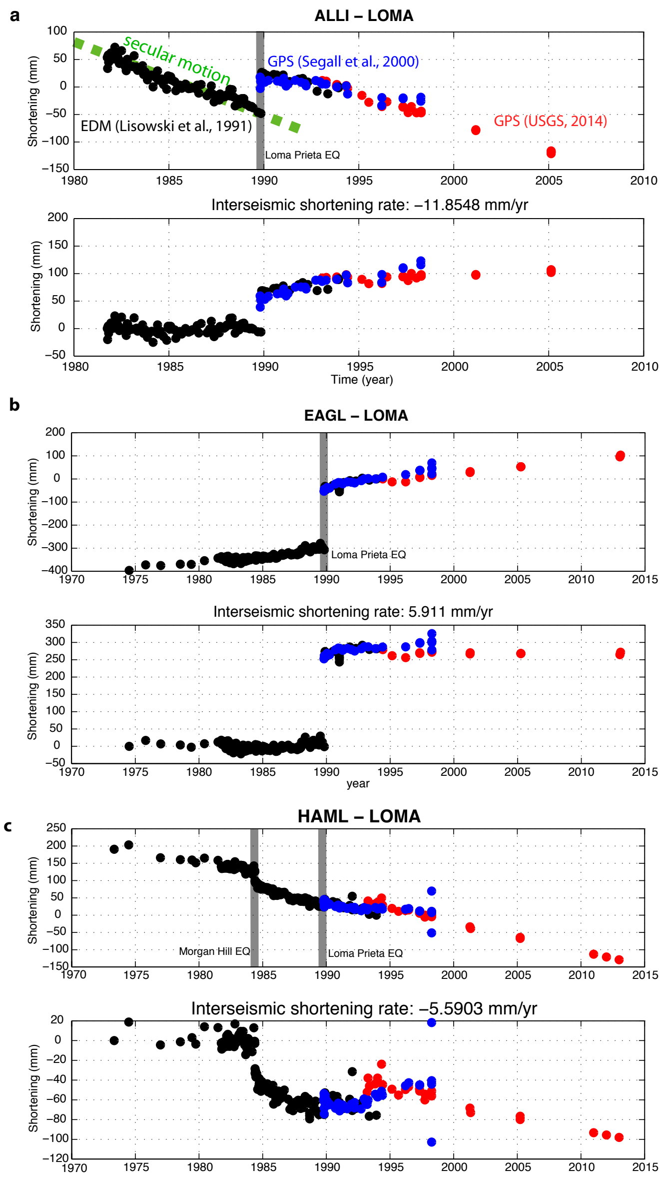

Figure 3.2: Twenty-five-year-long time series of length change between stations ALLI and LOMA (locations see Fig. 3.1b). (a) The EDM data (black dots, data from Lisowski et al., 1991) mainly show the preseismic period; the GPS data show the early (blue dots, data from Segall et al., 2000) and late (red dots, data from USGS, 2014) periods. Note the slope across whole observation period is due to secular motion between the Pacific plate and North American plate. The step in 1989.8 is due to Loma Prieta earthquake. (b) The same time series after removing the preseismic secular motion. The change of slope after Loma Prieta earthquake is due to postseismic displacement.

gram more reliable. The small baseline (SBAS, see Berardino et al., 2002) method generates interferograms that have small spatial baseline, and inverts for the displacement between each scene from interferograms. In our study we process all of the interferograms that have spatial baselines less than 350 m and temporal baselines less than 4.5 years, and generate 392 interferograms (200 in ERS-1/2 and 192 in Envisat) for inverting LOS displacement for 94 acquisitions.

3.4 Postseismic deformation

3.4.1 Compare with preseismic EDM data

We combine EDM data with GPS data by Segall et al. [2000] and BAVU to verify pre-, co-, and postseismic displacement with time between stations that have continuous recordings since the 1970s. Fig. 3.2a shows the shortening since 1980s for station pair Alliston Loma. We estimate the shortening due to secular motion based on the records before Loma Prieta. After removing this value (-11.8 mm/yr), we obtain the co- and postseismic shortening time series (Fig. 3.2b). This result shows a rapid coseismic displacement and a change of shortening rate in the early postseismic period. The shortening rate gradually falls back to the preseismic level implying that the secular motion has not changed by the Loma Prieta earthquake. Fig. 3.2 shows two more station pairs: Eagle Rock Loma and Hamilton Loma with shortening time series more than 10 years before Loma Prieta earthquake. For pair Eagle Rock Loma, the shortening rate from secular motion is about 5.9 mm/yr and returns to the same value 10 years after the Loma Prieta earthquake. However, for station pair Hamilton Loma (Fig. 3.2), there is a change of shortening rate in 1984 due to the M 6.2 Morgan Hall earthquake. This earthquake affected the shortening rate and has increased the rate from -5.6 mm/yr before 1984 to -6.1 mm/yr after the Morgan Hall earthquake. The 1989 Loma Prieta earthquake contributed relatively lower coseismic shortening (less than 20 mm) than the Morgan Hall earthquake ($\sim$30 mm). Besides, the Morgan Hall postseismic period has rapider shortening than it after the Loma Prieta earthquake. Nevertheless, the 1989-2013 GPS time series indicates that the current shortening rate stays about the same level as it after the Morgan Hall earthquake and before the Loma Prieta earthquake, and is slightly lower than the pre-Morgan Hall level.

3.4.2 GPS data

The red and black arrows in Fig. 3.1b show respectively early (1989-1994) and late (1995-2013) periods of GPS postseismic displacement, both relative to LP1. Similar to early period, the later period displacement also shows NE-SW convergence with strike-slip component, but the amplitude is about three times smaller than in the early period. Across the southern Santa Cruz Mountains NW of the Foothills thrust belt, all GPS measurements show a convergent sense of motion with right-lateral strike-slip component, and the postseismic displacement is generally less than 3 mm/yr. To further investigate the displacement with time, we combine 10 GPS stations that have been surveyed by Segall et al. [2000] during 1989 1998 (red dots in the insets of Fig. 3.3) and BAVU and USGS measurements during 1994 2010 (blue dots in the insets of Fig. 3.3) as described in section 2, and generate horizontal time series of 11 stations. All of the displacements in time are relative to a reference station LP1, and we use the preseismic EDM data to exclude secular motion. However, for postseismic modeling we do not consider stations east of Calaveras Fault (stations HAML and MOCH) because for these stations the displacement rate has changed since the 1984 Morgan Hill earthquake (Fig. 3.2c). This would add the difficulty on estimating the later period of postseismic displacement in this region because of the perturbation of the Morgan Hill earthquake, and we are unable to discriminate the contribution of postseismic displacement from the change of slip on the Calaveras Fault.

3.4.3 InSAR data

Fig. 3.1c and d show the InSAR LOS displacement relative to a reference pixel near GPS station LUTZ during 1992 - 2002 and 2002 - 2010, respectively. We remove the secular motion based on the interseismic model derived from EDM (the red arrows in Fig. 3.1b; Bürgmann et al., 1997; also see section 2). In eastern Santa Clara Valley (Fig. 3.1c) there is a change of displacement across the Silver Creek fault indicating deformation due to groundwater level changes [Schmidt and Bürgmann, 2003]. Near Palo Alto, there is a $\sim$2 mm/yr uplift during 1992 - 2000 but nearly 0 mm/yr afterward. In part of the Santa Clara Valley we see seasonal uplift/subsidence in time series (Supplementary Fig. 3.10b), which does not have a significant long term change, but starts subsiding after 2006. We use one-year sine and cosine functions to model the seasonal uplift/subsidence to the entire time series (see Supplementary Information S1 for the approach). Fig. 3.1e shows the amplitude of the seasonal change based on this method. There is stronger seasonal amplitude in northern Santa Clara Valley throughout the entire period with the peak amplitude $\sim$2 cm, which agrees with a recent study by Chaussard et al. [in preparation]. The time series of a point in this region (Supplementary Fig. 10a) shows the peak seasonal change correlated with high precipitation every year as well as the groundwater head. Besides, this region is roughly coincided with the observed land subsidence from 1934 to 1960 (Poland and Ireland, 1988). We thus consider the surface displacement in this region is not related with regional tectonics, so we exclude this region for postseismic modeling.

However, there is long-term range increase in line of sight (LOS) in southern Santa Clara Valley and Gilroy (Fig. 3.4a-b). In southern Santa Clara Valley, the time series is not significantly seasonal (Fig. 3.1e), but we observed subsidence from $\sim$1.3 mm/yr during 1992

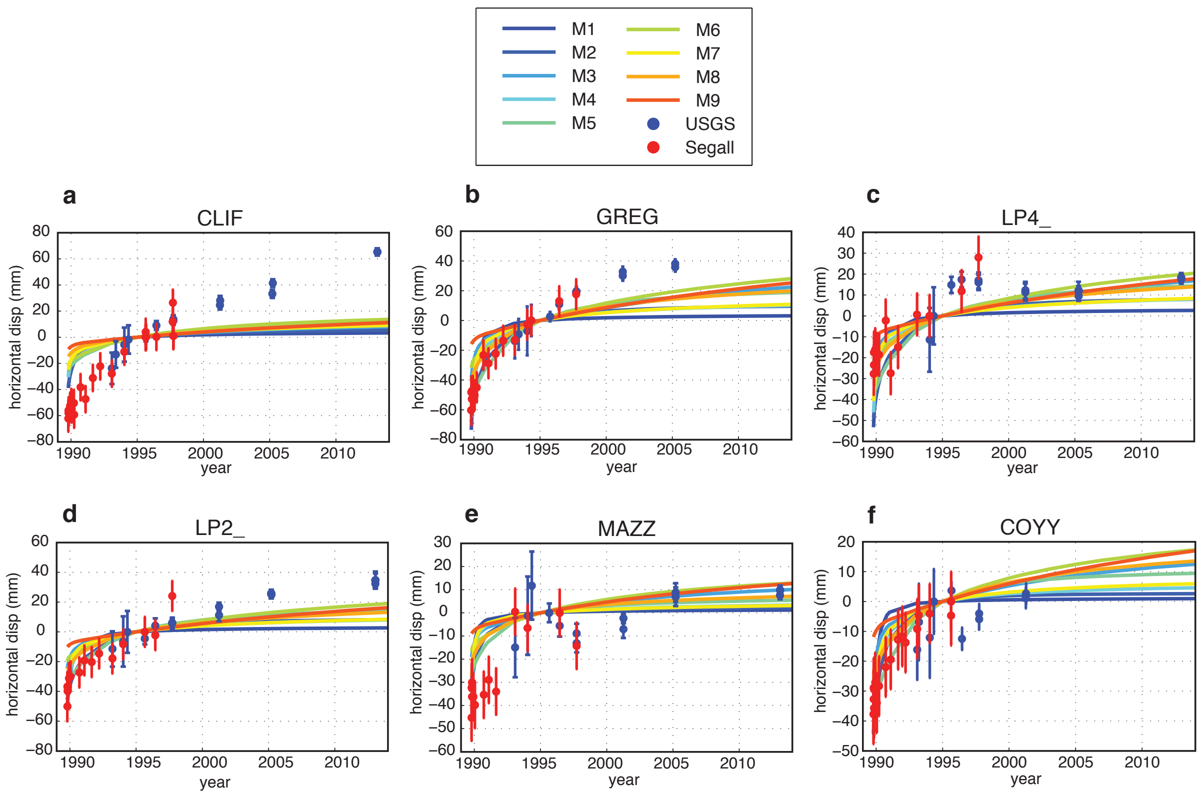

Figure 3.3: Selected GPS time series of total horizontal displacements from 1989.8 to 2013 shown in circles (red: Segall et al., 2000; blue: USGS, 2014) and the viscoelastic relaxation predictions shown in colored lines (locations see Fig. 3.1b). Note that the secular motion (Fig. 3.1a) has been removed and all horizontal displacement time series is relative to station CLIF (data after Bürgmann et al., 1997, Segall et al., 2000, and USGS, 2014).

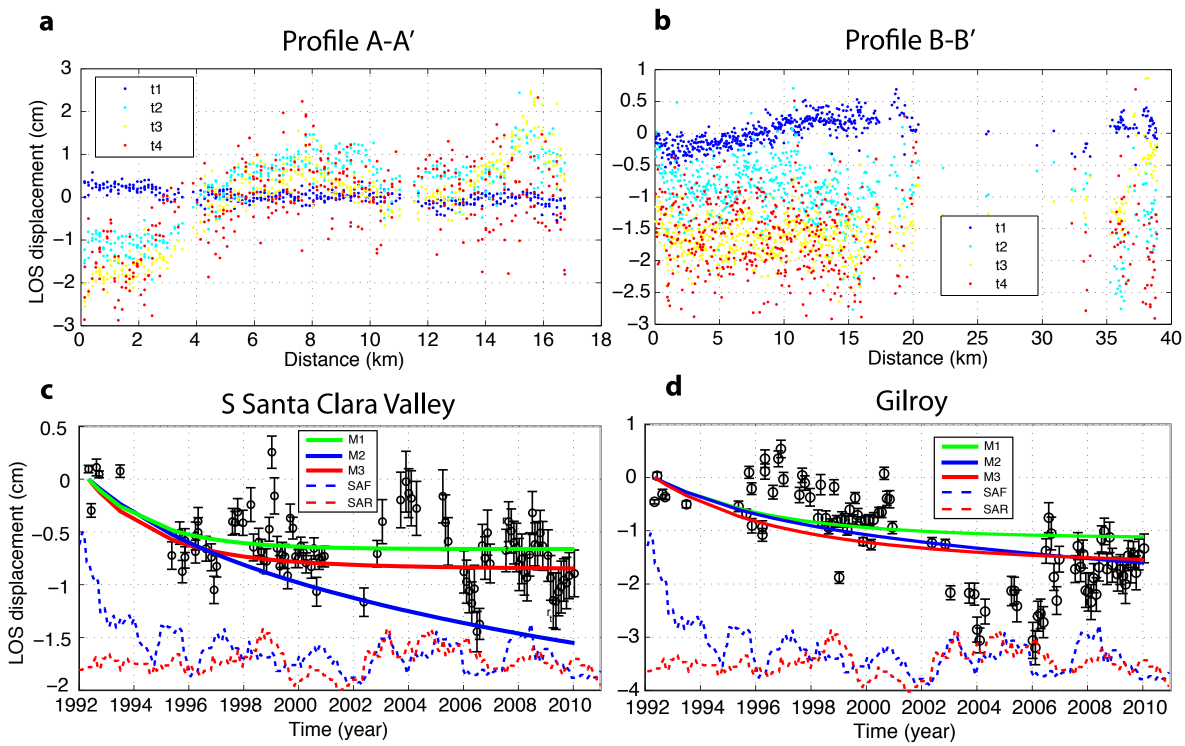

Figure 3.4: (a) Profile A-A shows LOS displacement along southern Santa Clara Valley at different time shown in different colors. (b) Profile B-B shows LOS displacement from southern Santa Clara Valley to Gilroy. (c) InSAR time series at a point at southern Santa Clara Valley. The three colored lines represent three relaxation predictions. The red and blue dashed lines show the slip rate at San Juan Bautista and Gilroy, respectively. (d) InSAR time series at a point at Gilroy. The location of the profiles and points is located in Fig. 3.1b. Note that the secular motion has been removed.

– 2002 to ∼1 mm/yr uplift during 2002 - 2010 (Fig. 3.4c). This long-term land subsidence region is similar to the area where Bürgmann et al. [2006] find a systematic PSInSAR misfit from their preferred interseismic model prediction. In Gilroy (Fig. 3.3d), there is also land subsidence observed during 1992 – 2010, and the subsidence rate goes from about -1 mm/yr to about 1 mm/yr between 2001 and 2004. This observed subsidence is only in the periphery of the Santa Cruz Mountains and also the subsidence rate decreases with time, so we infer that it is related to the Loma Prieta postseismic displacement.

3.5 Postseismic deformation modeling

In this section we first focus on viscoelastic relaxation model for GPS time series data between 1994 and 2013 and InSAR data between 1992 and 2010. We apply Maxwell fluid and bi-viscous Burgers rheologic models [Bürgmann and Dresen, 2008] to represent the lower crust and the upper mantle, respectively. We then predict the contribution from viscoelastic relaxation during the early period (1989.8 – 1994), and subtract the viscoelastic relaxation components from the early GPS measurements by Segall et al. [2000]. Finally, we invert the afterslip on the fault plane using dislocation models.

3.5.1 Viscoelastic relaxation

For the viscoelastic relaxation model, we consider simple elastic dislocation models of the coseismic rupture and stress changes and models of postseismic relaxation in a layered viscoelastic representation of the Earths lithosphere to evaluate the nature of the inferred transient deformation. By specifying the coseismic fault geometry and slip, and the depth dependent elastic and viscous parameters, we can predict the surface displacement with time due to the stress relaxation. We consider the coseismic fault geometry of Marshall et al. [1991] and Arnadottir and Segall [1994], both derived from geodetic measurements and estimate coseismic stress change based on this model (Table 3.1). We recomputed the slip distribution into a two sub-fault system to represent a rake transition in slip from nearly right-lateral (163°) in the southeast to oblique right-reverse in the northwest (116°). There is a discrepancy of source depth between seismic and geodetic inversions (e.g. 10-18 km based on body waves studies and 8 km based on geodetic study; see comparison in Marshall et al., 1991). By considering the aftershock distribution and the layered model for a geodetic inversion study, we set the source depth as 13 km, as proposed in Arnadottir and Segall [1994]. The coseismic slip extended from 4.5 to 12.4 km in depth on the main fault geometry, and strike-slip movement dominates in the south and oblique reverse movement in the north (Table 3.1). The layered rheologic model consists of an elastic upper crust underlain by a Maxwell fluid layer to represent the lower crust, and a bi-viscous Burgers half-spaced upper

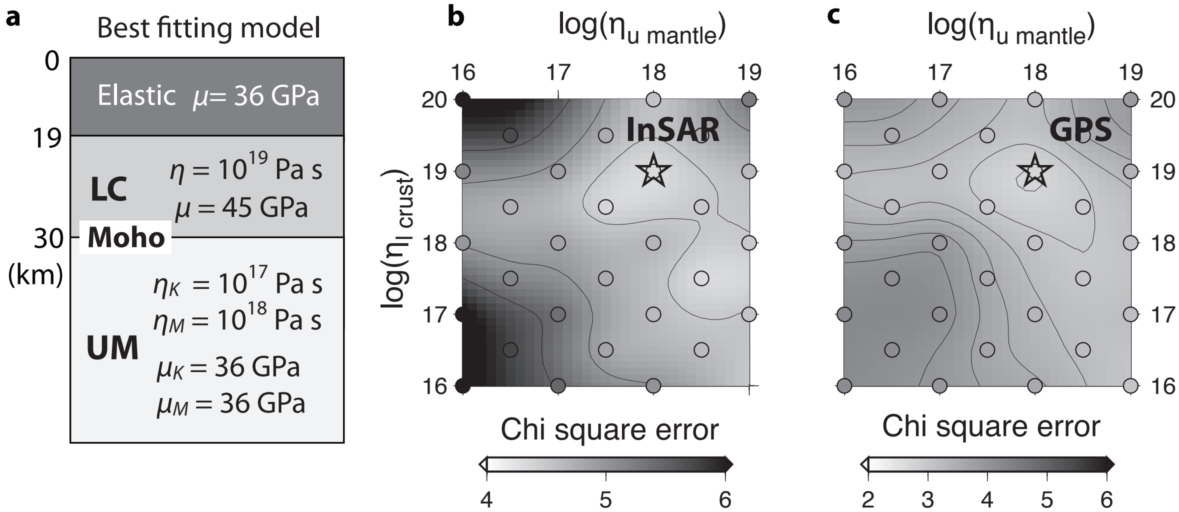

Figure 3.5: (a) The rheologic structure model for Bay Area. Note the lower crust is composed of a Maxwell fluid layer and the upper mantle is composed of a bi-viscous Burgers layer. The values of the viscosities are based on the best-fitting model. LC: lower crust; UM: upper mantle. (b) and (c) show respectively the residual misfit of InSAR and GPS with respect to the viscoelastic relaxation model.

Table 3.1: Coseismic fault parameters (after Marshell et al., 1991)

Fault	Length (km)	Width (km)	Strike (°)	Dip (°)	Rake (°)	Slip (m)	Depth (km)	Moment (N m)
Plane 1 (NW)	17	9.1	128	60	116	2.1	4.5 – 12.4	1.62×10^{19}
Plane 2 (SE)	17	9.1	128	60	163	1.0	4.5 – 12.4	7.7×10^{18}

mantle (Fig. 3.5a). The purpose of using a Burgers model for upper mantle is to describe the earlier transient following the Loma Prieta earthquake [Pollitz, 2003].

The bi-viscous Burgers model is composed of a Kelvin solid (η_K) and a Maxwell fluid (η_M) to explain the two-stage displacements [Pollitz, 2003; Bürgmann and Dresen, 2008; Wang et al., 2012]. In the Burgers model, we do not try to explore the ratio between Kelvin solid and Maxwell because we only compare the viscoelastic relaxation model with data after 1994, the year afterslip no longer dominated the postseismic displacement [Segall et al., 2000]. As a result, we keep the ratio between Maxwell fluid and Kelvin solid as 10 (i.e., $\eta_M/\eta_K = 10$), which is about the same order of postseismic studies [Hearn et al., 2009; Freed et al., 2012; Meade et al., 2013].

Table 3.2: Fault parameters for afterslip model (after Bürgmann et al., 1997)

Fault	**Length (km)**	**Bottom depth (km)**	**Top depth (km)**	**Strike (°)**	**Dip (°)**	**Rake (°)**	**Longitude**	**Latitude**
Plane 1 (Loma Prieta)	53.82	15.57	1.48	130	70	90	-121.55	36.80
Plane 2 (shallower fault)	61.40	6.11	1.62	132	30	90	-121.59	36.86

The program VISCO1D [Pollitz, 1997] is carried out to calculate deformation using spheroidal and toroidal motion modes of the spherically stratified elastic-viscoelastic medium. The thickness of the upper- and lower crust is respectively 19 and 11 km, based on previous studies by Pollitz et al. [1998, 2004]. In order to distinguish the contribution of relaxation from either lower crust or upper mantle, we test the viscosity of both layers by varying the steady-state (Maxwell element) viscosity of the Burgers body in the range of 10^{18} to 10^{20} Pa s for lower crust, and 10^{17} to 10^{20} Pa s for upper mantle extending from 30 km to 500 km depth.

3.5.2 Afterslip

Segall et al. [2000] used GPS measurements between 1989 and 1998 and concluded that the afterslip dominated the postseismic displacement until 1994, so we also consider the possible localized shallow or deep afterslip distributed in the earlier postseismic period (e.g. Bürgmann et al., 1997; Segall et al., 2000; Savage and Svarc, 2010). To evaluate the contribution, we first compare the viscoelastic relaxation with geodetic observation after 1994, and then predict the relaxation between 1989 and 1994 based on the best fitting viscoelastic relaxation model. We then take both GPS and InSAR misfit residual between 1989 and 1994 for dislocation inversions. The geodetic Greens functions are computed using the programs EDGRN/EDCMP [Wang et al., 2006] for dislocation inversions. This allows for the calculation of the Greens functions relating unit slip on each sub-fault dislocation to surface displacement in a layered elastic model over a half-space. The weight between GPS and InSAR is chosen so that both datasets have similar variance reduction (see Huang et al., 2013 for detail about data weighting and smoothing factors). We set up the fault geometry based on Bürgmann et al. [1997], which is composed of two fault planes: one coincided with the Loma Prieta earthquake, and the other shallower dipping (30°) fault that was proposed in their paper that is based on the aftershocks relocation (see Table 3.2 for the fault parameters). For this two-fault-system, each fault plane is composed of 20 × 10 subfaults, so the size of each subfault is roughly $3 \times 2\ km^2$. Each subfault is able to slip freely along the fault surface but no off-fault component is allowed (i.e. no volume change in the fault).

3.6 Model Result

3.6.1 Viscoelastic relaxation

To explore the rheologic structure, we perform a grid search for the lower crustal viscosity and the ration between the viscosities of lower crust and upper mantle. Figs 3 and 4 show GPS and InSAR time series with different model predictions based on different combinations of lower crust and upper mantle viscosities. The color of the lines in Figs 3 and 4 represent the viscoelastic relaxation with different viscosity combinations relative to 1994 and 1992, respectively. For GPS data, we compare the horizontal displacement in order to simplify the data and model comparison. In comparing with InSAR time series, Fig. 3.4a and b show the range change at different time period along profiles A-A and B-B (location of the profiles see Fig. 3.1c). Fig. 3.4c and d show two time series plots from stable scatterers respectively in southern Santa Clara Valley and Gilroy and compare with viscoelastic relaxation predictions. In map view, Fig. 3.1f shows the best-fitting postseismic relaxation model in the early period.

Fig. 3.5b and c respectively show the residual misfits of GPS and InSAR in conditions with different lower crust (10^{16-20} Pa s) and upper mantle (10^{16-19} Pa s) viscosity combinations. Here we use Chi-square error to calculate the residual misfit. The Chi-error is defined as, $\chi^2 = \frac{1}{MNP}\sum_{k=1}^{M}\sum_{i=1}^{N}\sum_{j=1}^{P}\frac{(o_{k_{i,j}}-m_{k_{i,j}})^2}{\sigma^2_{i,j,k}}$, where $o_{k,i,j}$ is the jth component of the ith time step for the kth GPS observation, and $m_{k,i,j}$ is the j^{th} component of the ith time step for the k^{th} model prediction. $\sigma_{i,j,k}$ is the standard deviation of the j^{th} component of the ith time step for the k^{th} GPS observation. In individual GPS and InSAR fitting, the models for both data sets favor a lower crustal viscosity that is $\sim$10 times higher than that for upper mantle (i.e. $\eta_{lc} \approx 10 \times \eta_{um}$), and this viscosity combination can describe both earlier and later postseismic periods even though we only compare with the data during later period (Figs 3.1f, 3.2, and 3.4). The best fitting model (stars in Figs 3.5b and c) is composed of a lower crust with viscosity of 10^{19} Pa s and a mantle with long term viscosity of 10^{18} Pa s, assuming the transient viscosity is an order lower than the long term viscosity. Fig. 3.5a represents the configuration of the best fitting model.

3.6.2 Afterslip inversion

For afterslip inversions, we first consider the postseismic GPS measurements during 1989.8 1994. We perform dislocation inversions using the two-fault system proposed by Bürgmann et al. [1997]. The result (red dots in Fig. 3.6a) shows that afterslips are dominated in the shallower part of both faults and the peak afterslip is about 3 cm/yr on the main Loma Prieta fault plane. There are two main afterslip asperities on the main Loma Prieta fault, and three asperities on the shallower dipping fault. The predicted surface deformation based on this inversion result (white arrows in Fig. 3.6a) shows that this model fits the

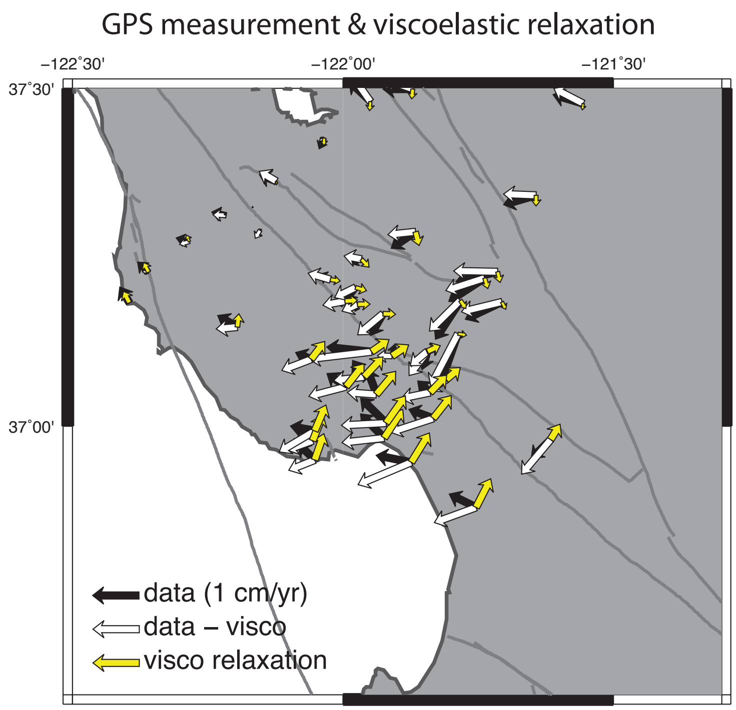

Figure 3.6: Comparison of early GPS measurements (black arrows) and the predicted viscoelastic relaxation (yellow arrows) in the early period. The GPS measurements are based on Bürgmann et al. [1997] and note the measurements are shown in rate (cm/yr). The residual velocity (white arrows) is the difference between the GPS measurements and the predicted viscoelastic relaxation.

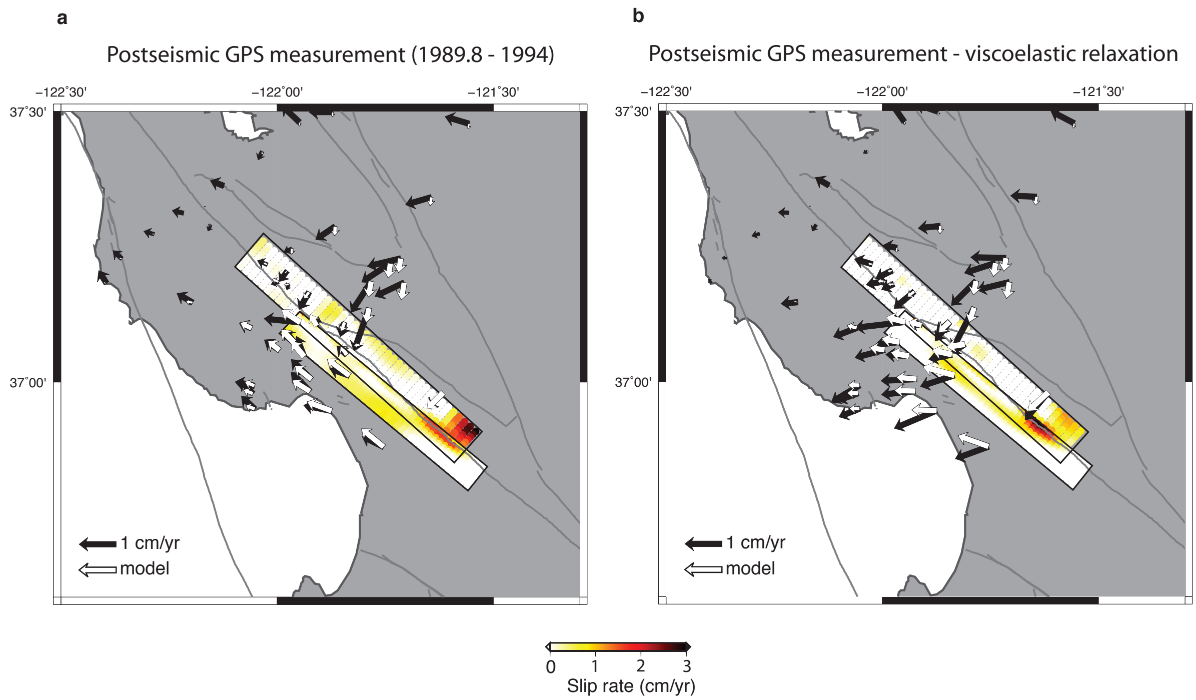

Figure 3.7: Afterslip distribution on the two-fault system [Bürgmann et al., 1997] based on the first 5-year GPS measurements. (a) With original GPS measurement. The red dots are the afterslip distribution on the two-fault system. The black and white arrows are data and the predicted displacement based on the afterslip distribution. The color bar shows the amplitude of the slip for (a) and (b). (b) With subtraction of early viscoelastic relaxation from the same GPS measurements in (a).

western side (Santa Cruz Mountains) better, and for eastern side (Santa Clara Valley) the dislocation model cannot predict the more westward movement in the GPS measurements.

On the other hand, we subtract the viscoelastic relaxation component calculated in Section 5.1 from the GPS measurements, and then use the residual velocity as the data input for the dislocation inversions using the same two-fault system. Compare with the original GPS measurements, the residual velocity (black arrows in Fig. 3.6b) is generally is generally more westward, and the amount of postseismic displacement rate is about 1 cm/yr in the Loma Prieta faults. Fig. 3.6b shows the afterslip distribution (red dots) and the predicted surface deformation based on the afterslip (white arrows). The afterslip distribution is similar with considering GPS total measurements (Fig. 3.6a), and the peak afterslip is about 3 cm/yr. This dislocation model can predict the amplitude of the data near the earthquake region, but there is a higher azimuthal misfit in both sides of the Loma Prieta fault system.

3.7 Discussion

3.7.1 Constraining lithospheric rheology

The residual misfit of both GPS and InSAR suggests a relatively high viscosity lower crust (η_{lc}) and a low viscosity upper mantle (η_{um}). This finding is consistent with another study of Loma Prieta early postseismic displacement (Pollitz et al., 1998), as well as postseismic studies in southern California (e.g., Pollitz et al., 2001; Freed et al., 2007; 2010; 2012). In southern California, Freed et al. (2007) inferred lower crustal viscosity as 4.6×10^{18} Pa s and 4×10^{17} Pa s for the upper mantle. This result is similar to Pollitz et al. (2001), which found about 10^{19} Pa s for lower crust and 6 - 8×10^{17} Pa s for the upper mantle. In the later period (after 1994), the best-fitting model can predict GPS horizontal displacement in southwestern and northwestern Santa Cruz Mountains, but is unable to explain the convergent GPS displacement in northeastern part of Santa Cruz Mountains near Gilroy (Fig. 3.1f). In GPS time series, the viscoelastic relaxation model can predict most of the later period postseismic displacement, and even agrees well for stations MAZZ, GREG, and CLIF (Fig. 3.3). For stations LP1 and LP2, none of the viscoelastic model can predict the early transient, which is arguably due to the early afterslip in the shallower part of the fault (Bürgmann et al., 1997). In InSAR time series, the viscoelastic relaxation model with similar crustal and upper mantle rheology as GPS can predict the trend of land subsidence in spatial and temporal (Figs 3.3 and 3.4c). However, since there is no InSAR data prior to 1992, we are unable to resolve the early transient.

In general, the predicted postseismic displacement agrees well with the geodetic observations (Figs 3.1f, 3.3, and 3.4). However, higher uncertainty in the earlier GPS survey and combining with BAVU 3.0 data would decrease the data quality in the GPS time series. In addition, the total amount of viscoelastic relaxation can be produced from a M_w 6.9 earthquake is up to $\sim$10 cm scale, and most of the relaxation occurred in the early postseismic period that is difficult to discriminate from early shallow afterslip. The later period postseismic relaxation is generally less than 0.5 mm/yr, hence significantly limits the sensitivity of the choice of viscosities in lower crust and upper mantle. Similar problem exists in InSAR time series. The first SAR acquisition is about 3 years after the main shock and the early acquisitions are limited (only 5 acquisitions before 1995; see Table 3.1), so the geodetic data cannot well constrain the rheology into a fine scale. Due to this limitation, we are unable to probe the crustal/mantle rheology into a fine scale, but the viscosity in the scale between 10^{19-20} Pa s in lower crust and between 10^{17-18} Pa s in the upper mantle at least can explain GPS and InSAR data sets in both early and late periods (Figs 3.2 and 3.3) and agree with studies for southern California.

3.7.2 Afterslip models

Savage et al. [1994] postulated most of the first 3 years of postseismic displacement can be attributed to a 1.5 m right-lateral and 0.9 m reverse afterslip on a 5-km-wide downdip extension (depth range 16 to 21 km) of the Loma Prieta earthquake fault based on dislocation models. In addition, it seems to be a 0.1 m postseismic fault zone collapse in the direction perpendicular to the plane of the rupture. Bürgmann et al. [1997] combined 5 years of GPS and leveling measurements and suggested about 2.9 cm/yr uniform reverse afterslip on the Loma Prieta fault plane and 2.4 cm/yr uniform reverse afterslip on a buried fault within the Foothills thrust belt. We first use the same two-fault geometry and the same 5 years GPS measurements for dislocation inversions. In our model, each fault plane is composed by 20 $\times$ 10 subfaults so we are able to outline the afterslip distribution on both faults. In our model, most of the afterslip asperities are above 10 km. This result is also similar with Pollitz et al. [1998], which they found 3-5 cm/yr reverse afterslip on the coseismic fault plane and a shallowly dipping reverse fault plane.

In this study, we estimate the viscoelastic relaxation based on InSAR and GPS measurements, so we can calculate the early viscoelastic relaxation between 1989.8 and 1994 based on the preferred rheologic structure. We then subtract the early viscoelastic relaxation components from the 1989.8 - 1994 GPS measurements, and perform the afterslip inversion based on the same two-fault system. Compare with the viscoelastic relaxation estimated by Pollitz et al. [1998], our estimation (yellow arrows in Fig. 3.6) is about 5 times larger ($\sim$5 mm/yr in this study versus $\sim$1 mm/yr in Pollitz et al., 1998). The main reason of the difference is because we consider a bi-viscous Burgers model that can predict a transient relaxation in the early period. However, the azimuth of the relaxation is generally different from the observed displacement (black arrows in Fig. 3.7b), so the residual between observation and viscoelastic relaxation does not decrease. Nevertheless, the dislocation model inverted from the residual velocity is similar with the afterslip model with consideration of original GPS measurements, but the fitting of viscoelastic relaxation-free postseismic displacement is poorer than the one of the original measurements.

3.7.3 Repeating earthquake along San Andreas Fault and Sargent Fault

Turner et al. (2013) documented the repeating earthquake activities along the San Andreas and Sargent faults near San Juan Bautista. They found that these repeating earthquakes were excited by the Loma Prieta earthquake and stayed active for more than 15 years (Fig. 3.3b). They estimated the slip rate of both faults based on the repeater activity and found that the San Andreas creep rate fell back close to the interseismic rate and the variations in creep became coherent in time with the Sargent fault. Since these high repeater activities lasted for more than 5 years after the end of the afterslip on Sargent fault, the driving force of the repeater activities may mainly contribute from viscoelastic relaxation at depth.

To further examine this, we compare the time series of slip rates on San Andreas Fault near San Juan Bautista and Sargent Fault inverted from repeaters with PSInSAR time series at southern Santa Clara Valley and Gilroy. The result (Fig. 3.4c and d) shows that both surface displacement and the repeaters have higher subsiding rates during 1992 2002, but during 2002 2004, there is a gradual uplift up to 1 cm on the surface at southern Santa Clara Valley and up to 1.5 cm slip on both San Juan Bautista and Sargent faults (Fig. 3.3b). After this temporal peak value, both surface and slip rate decrease until the end of the observation. Besides, it seems like both surface displacement and slip activities on the faults are correlated with a period term, but this period is not an annual cycle and is not correlated with annual precipitation.

Most of the repeating earthquakes are more than 20 km far away from the Loma Prieta epicenter. Our best fitting viscoelastic relaxation model can produce from $\sim$5 mm/yr of relaxation at 5 – 15 km epth between 1989.8 and 1994 to $\sim$1.4 mm/yr between 1994 and 2002. This result is smaller than $\sim$16 mm/yr in 1994 or $\sim$9 mm/yr on the San Andreas Fault, but provides some comparable source for the repeating earthquakes. However, we are unclear about the coupled gradual increase of surface and creep on the two faults, but this may indicate a mutual driving force in the system that requires further work to understand. Nevertheless, both the surface displacement and the deep slip rate seem to gradually falling back to the pre-seismic period, so the contribution of viscoelastic relaxation is withering.

3.8 Conclusion

The 1989 Loma Prieta earthquake showed a two-period postseismic displacement: A faster (postseismic transient) displacement during 1989.8 - 1994 and slower (mainly viscoelastic relaxation) during 1994 - 2004. The afterslip in the deeper part of the fault (between 14 and 20 km) dominated the first 5 years of postseismic displacement and can explain the geodetic measurements, whereas the viscoelastic relaxation from the upper mantle contributed the postseismic displacement until 2002. Based on the 1D viscoelastic layered model, a weak upper mantle composed of a Burgers body ($\eta_K = 10^{17}$ Pa s; $\eta_M = 10^{18}$ Pa s) and a ten times stronger lower crust composed of a Maxwell fluid ($\eta_M = 10^{19}$ Pa s) can explain both GPS and PSInSAR time series during this 13-year-long late period. The rheologic structure of our best-fitting forward model is at the same range as previous studies found in Southern

California using postseismic displacement [Pollitz et al., 2001; Pollitz, 2003; Freed et al., 2007, 2010, 2012], even though our geodetic measurements cannot resolve the exact values of lower crust and upper mantle viscosities due to lower amplitude postseismic displacement. This is because the total amount of Loma Prieta postseismic relaxation is limited by the lower moment magnitude of the main shock (M_w 6.9), comparing with other postseismic studies (e.g., M_w 7.1 Hector Mine earthquake for southern California by Pollitz et al., 2001; M_w 7.9 Denali earthquake for Alaska by Freed et al., 2006). The pattern of postseismic land subsidence in southern Santa Clara Valley and Gilroy is similar to the deep slip rates derived from repeaters on San Andreas Fault and Sargent Fault near San Juan Bautista. The high repeating earthquake activities lasts for more than 5 years after the end of the afterslip, and is still higher than pre-Loma Prieta earthquake level in 2011. The similarity of the repeater activity and surface displacement around Santa Cruz Mountains in time imply that both are driven by the Loma Prieta postseismic viscoelastic relaxation.

3.9 Supplementary information and figures

3.9.1 Seasonal change in InSAR time series

The seasonal change in time series can be described as, $a(i,j) \times sin(2\pi t) + b(i,j) \times cos(2\pi t)$, where a and b are constants that describe the coefficients of the sine/cosines functions and (i,j) is the location of a given pixel. The amplitude of the seasonal effect is $(a^2 + b^2)^{0.5}$, and the phase shift (i.e. when is the peak of seasonal effect) is $2\pi \times tan^{-1}$(a/b).

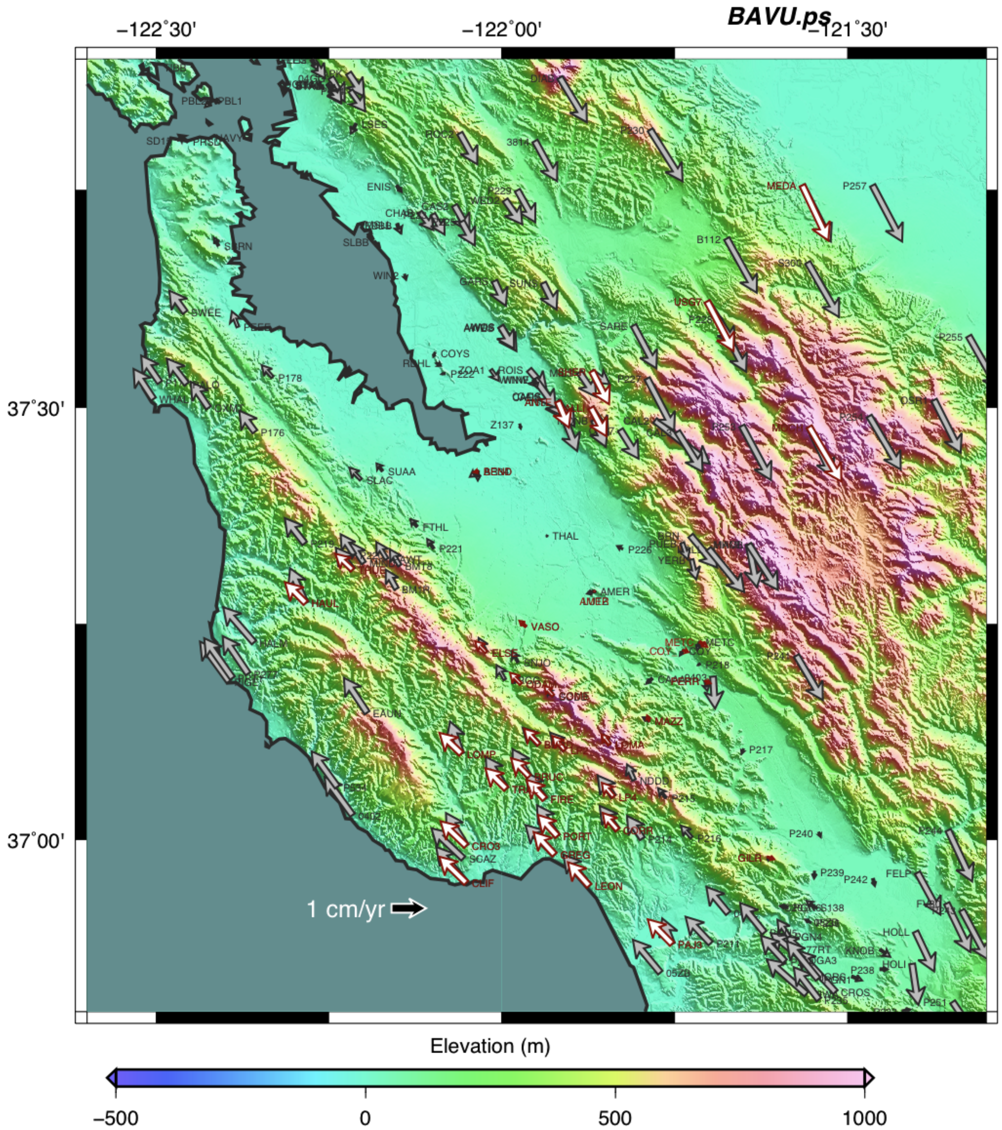

Figure 3.8: EDM and GPS measurements in the San Francisco Bay Area.

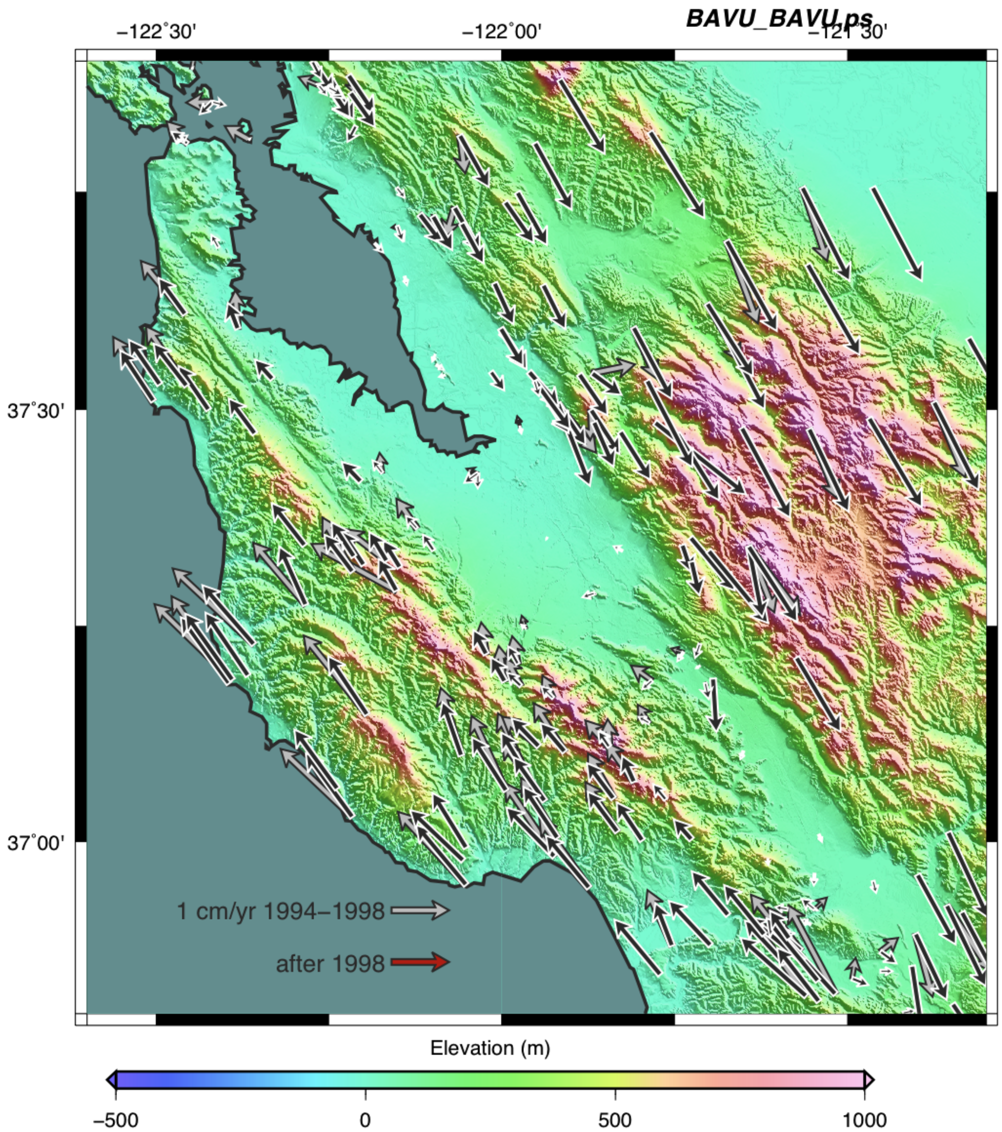

Figure 3.9: Early (1994-1998) and late (1997-2010) periods of BAVU measurements.

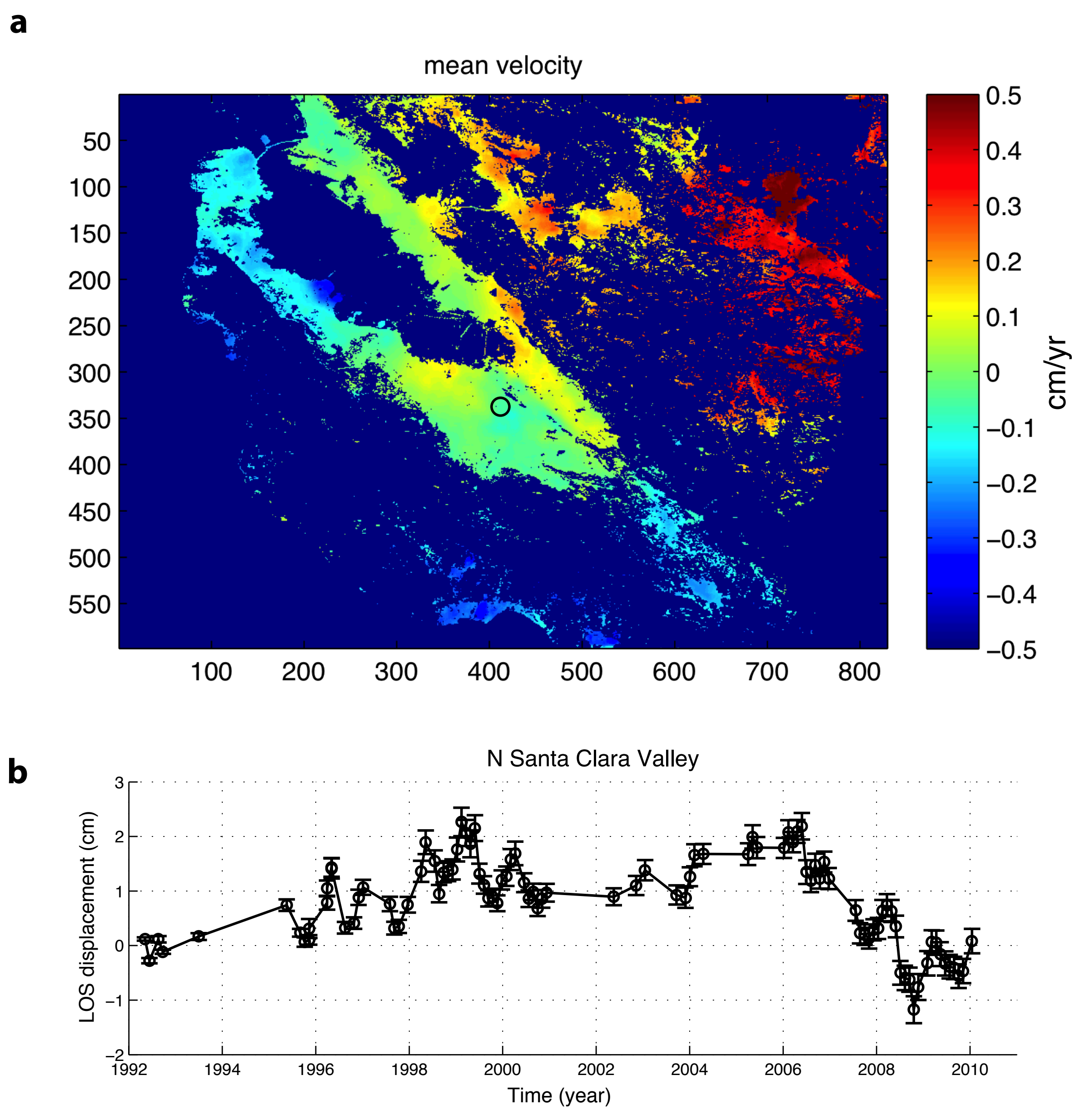

Figure 3.10: (a) The mean LOS annual velocity (cm/yr) between 1992 and 2010. (b) Time series of a point at the Santa Clara Valley.

Table 3.3: ERS-1/2 acquisitions (track: 70; frame: 2853) used in this study.

yymmdd	**yymmdd**	**yymmdd**
19920610	19980926	20011229
19920715	19981031	20020202
19920819	19981205	20020518
19920923	19990109	20020622
19930106	19990213	20020727
19950519	19990320	20021005
19950901	19990424	20021109
19951007	19990529	20021214
19951110	19990703	20030118
19951111	19990807	20040103
19951215	19990911	20051203
19960329	19991016	20060107
19960330	19991120	20060211
19960504	19991225	20060318
19960817	20000129	20060701
19961026	20000304	20060805
19961130	20000408	20060909
19970104	20000617	20061014
19970802	20000722	20061118
19970906	20000826	20061223
19971011	20000930	20070127
19971220	20001104	20071103
19980404	20001209	20071208
19980509	20010915	20080531
19980718	20011020	20080705
19980822	20011124	20080809

Table 3.4: Envisat acquisitions (track: 70; frame: 2853) used in this study.

yymmdd	**yymmdd**
20030118	20071208
20030503	20080112
20030920	20080216
20031129	20080322
20040103	20080426
20040207	20080531
20040417	20080705
20050402	20080809
20050507	20080913
20050611	20081018
20060211	20081122
20060318	20090131
20060422	20090307
20060527	20090411
20060701	20090516
20060805	20090620
20061014	20090725
20061118	20090829
20061223	20091003
20070721	20091107
20070825	20091212
20070929	20100116
20071103	20100220

Bibliography

[1] Arnadottir, T. and P. Segall (1994), The 1989 Loma Prieta earthquake imaged from inversion of geodetic data, *J. Geophys. Res.*, 99, 21,835-21,855.

[2] Berardino, P., G. Fornaro, R. Lanari, and E. Sansosti (2002), A new algorithm for surface deformation monitoring based on small baseline differential SAR interferograms, *IEEE Trans. Geosci. Remote Sensing*, 40, 2375-2383.

[3] Bürgmann, R., M. E. Ayhan, E. J. Fielding, T. J. Wright, S. McClusky, B. Aktug, C. Demir, O. Lenk, and A. Türkerzer (2002), Deformation during the 12 November 1999 Düzce, Turkey, Earthquake, from GPS and InSAR Data, *Bull. Seism. Soc. Am.*, 92, 161-171.

[4] Bürgmann, R., and G. Dresen (2008), Rheology of the lower crust and upper mantle: Evidence from rock mechanics, geodesy and field observations, *Ann. Rev. Earth Plan. Sci.*, 36, 531-567.

[5] Bürgmann, R., G. Hilley, A. Ferretti, and F. Novali (2006), Resolving vertical tectonics in the San Francisco Bay area from GPS and Permanent Scatterer InSAR analysis, *Geology*, 34, 221-224.

[6] Bürgmann, R., P. Segall, M. Lisowski, and J. Svarc (1997), Postseismic strain following the 1989 Loma Prieta earthquake from GPS and leveling measurements, *J. Geophys. Res.*, 102, 4933-4955.

[7] Chen, C. W. and H. A. Zebker (2002), Phase unwrapping for large SAR interferograms: Statistical segmentation and generalized network models, *IEEE Trans. Geosci. Remote Sensing*, 40(8), 1709-1719.

[8] Chaussard, E., Bürgmann, R., Shirzaei,, M. Fielding, E. and Baker, B. Predictability of hydraulic head changes and characterization of aquifer system and fault properties from InSAR-derived ground deformation. (in preparation)

[9] Colesanti, C., A. Ferretti, F. Novali, C. Prati, and F. Rocca (2003), SAR monitoring of progressive and seasonal ground deformation using the permanent scatterers technique, *IEEE Trans. Geosci. Remote Sensing*, 41, 1685-1701.

[10] d'Alessio, M. A., I. A. Johanson, R. Bürgmann, D. A. Schmidt, and M. H. Murray (2005), Slicing up the San Francisco Bay Area: Block kinematics and fault slip rates from GPS-derived surface velocities, *J. Geophys. Res.*, 110, doi:10.1029/2004JB003496.

[11] Ferretti, A., C. Prati, and F. Rocca (2001), Permanent scatterers in SAR interferometry, *IEEE Trans. Geosci. Remote Sensing*, 39, 8-20.

[12] Freed, A. M. and R. Bürgmann (2004), Evidence of power-law flow in the Mojave desert mantle, *Nature*, 430, 548-551, doi:10.1038/nature02784.

[13] Freed, A. M., R. Bürgmann, E. Calais, J. Freymueller, and S. Hreinsdóttir (2006a), Implications of deformation following the 2002 Denali, Alaska, earthquake for postseismic relaxation processes and lithospheric rheology, *J. Geophys. Res.*, 111, B01401, doi:10.1029/2005JB003894.

[14] Freed, A. M., R. Bürgmann, E. Calais, and J. Freymueller (2006b), Stress-dependent power-law flow in the upper mantle following the 2002 Denali, Alaska, earthquake, *Earth Planet. Sci. Lett.*, 252, 481-489, doi:10.1016/j.epsl.2006.10.011.

[15] Freed, A. M., R. Bürgmann, and T. Herring (2007), Far-reaching transient motions after Mojave earthquake require broad mantle flow beneath a strong crust, *Geophys. Res. Lett.*, 34, L19302, doi:10.1029/2007GL030959.

[16] Freed, A. M., T. Herring, and R. Bürgmann (2010), Steady-state laboratory flow laws alone fail to explain postseismic observations, *Earth Planet. Sci. Lett.*, 300, 1-10, doi:10.1016/j.epsl.2010.10.005.

[17] Freed, A. M., G. Hirth, and M. D. Behn (2012), Using short-term postseismic displacements to infer the ambient deformation conditions of the upper mantle, *J. Geophys. Res.*, 117, B01409, doi:10.1029/2011JB008562.

[18] Henstock, T. J., A. Levander, and J. A. Hole (1997), Deformation in the lower crust of the San Andreas fault system in northern California, *Science*, 278, 650-653.

[19] Hooper, A. (2008), A multi-temporal InSAR method incorporating both persistent scatterer and sall baseline approaches, *Geophys. Res. Lett.*, 35, L16302.

[20] Huang, M.-H., D. Dreger, R. Bürgmann, S.-H. Yoo, and M. Hashimoto (2013), Joint inversion of seismic and geodetic data for the source of the 2010 March 4, M_w 6.3 Jia-Shian, SW Taiwan, earthquake, Geophys. J. Int., 193, 1608-1626.

[21] Johanson, I. A., and R. Bürgmann (2005), Creep and quakes on the northern transition zone of the San Andreas fault from GPS and InSAR data, *Geophys. Res. Lett.*, 32, doi:10.1029/2005GL023150.

[22] Johnson, K. M., R. Bürgmann, and K. Larson (2006), Frictional properties on the San Andreas fault near Parkfield, California, inferred from models of afterslip following the 2004 earthquake, *Bull. Seism. Soc. Am.*, 96, 321-338.

[23] Jónsson, S., P. Segall, R. Pedersen, and G. Bjrnsson (2003), Post-earthquake ground movements correlated to pore-pressure transients, *Nature*, 424, 179-183.

[24] Kenner, S. J. and P. Segall (2003), Lower crustal structure in northern California: Implications from strain-rate variations following the 1906 San Francisco earthquake, *J. Geophys. Res.*, 108, doi:10.1029/2001JB000189.

[25] Lisowski, M., J. C. Savage, and W. H. Prescott, The velocity field along the San Andreas fault in central and southern California, *J. Geophys. Res.*, 96, 8369-8389, 1991.

[26] Marone, C. J., C. H. Scholz, and R. G. Bilham (1991), On the mechanics of earthquake afterslip, *J. Geophys. Res.*, 96, 8441-8452.

[27] Marshall, G. A., R. S. Stein, and W. Thatcher (1991), Faulting geometry and slip from co-seismic elevation changes: The 18 October 1989, Loma Prieta, California, earthquake, *Bull. Seism. Soc. Am.*, 81, 1660-1693.

[28] Okada, Y. (1985), Surface deformation due to shear and tensile faults in a half-space, *Bull. Seism. Soc. Am.*, 75, 1135-1154.

[29] Parsons, T. (1998), Haward fault extends into the lower crust of the San Francisco Bay area, California, *Bull. Seism. Soc. Am.*, 88, 1212-1223.

[30] Parsons, T. and P. E. Hart (1998), Dipping San Andreas and Hayward faults revealed beneath San Francisco Bay, California, *Geology*, 27, 839-842.

[31] Peltzer, G., P. Rosen, F. Rogez, and K. Hudnut (1996), Postseismic rebound in fault step-overs caused by pore fluid flow, *Science*, 273, 1202-1204.

[32] Poland, J. F. and R. L. Ireland (1988), Land subsidence in the Santa Clara valley, California, as of 1982, mechanics of aquifer suystems, U.S. Geol. Surv. Prof. Pap., 497-F, 61pp.

[33] Pollitz, F., R. Bürgmann, and P. Segall (1998), Joint estimation of afterslip rate and postseismic relaxation following the 1989 Loma Prieta earthquake, *J. Geophys. Res.*, 103, 26,975-926,992.

[34] Pollitz, F., C. Wicks, and W. Thatcher (2001), Mantle flow beneath a continental strike-slip fault: Postseismic deformation after the 1999 Hector Mine earthquake, *Science*, 293, 1814-1818.

[35] Pollitz, F. F. (2003), Transient rheology of the uppermost mantle beneath the Mojave Desert, California, *Earth Planet Sci. Lett.*, 215, 89-104, doi:10.1016/S0012-821X(03)00432-1.

[36] Pollitz, F. W. H. Bakun, and M. Nyst (2004), A physical model for strain accumulation in the San Francisco Bay region: Stress evolution since 1838, *J. Geophys. Res.*, 109, B11408, doi:10.1029/2004JB003003.

[37] Rosen, P. A., S. Hensley, and G. Peltzer (2004), Updated repeat orbit interferometry package released, *EOS, Trans. Am. Geophys. Un*, 85(5), 47.

[38] Savage, J. C., M. Lisowski, and J. L. Svarc (1994), Postseismic deformation following the 1989 (M = 7.1) Loma Prieta, California, earthquake, *J. Geophys. Res.*, 99, 13757-13765.

[39] Savage, J. C. and J. L. Svarc (2010), Postseismic relaxation following the 1989 Ms7.1 Loma Prieta earthquake, central California, *J. Geophys. Res.*, 115, B08404.

[40] Schmidt, D. A., and R. Bürgmann (2003), Time dependent land uplift and subsidence in the Santa Clara valley, California, from a large InSAR data set, *J. Geophys. Res.*, 108, doi:10.1029/2002JB002267.

[41] Segall, P., R. Bürgmann, and M. Matthews (2000), Time dependent deformation following the 1989 Loma Prieta earthquake, *J. Geophys. Res.*, 105, 5615-5634.

[42] Shirzaei, M. and R. Bürgmann (2013), Time-dependent model of creep on the Hayward fault from joint inversion of 18 years of InSAR and surface creep data, *J. Geophys. Res.*, 118, 1733-1746, doi:10.1002/jgrb.50149.

[43] Thatcher, W. (1983), nonlinear strain buildup and the earthquake cycle on the San Andreas fault, *J. Geophys. Res.*, 88, 5893-5902.

[44] Tse, S. T., and J. R. Rice (1986), Crustal earthquake instability in relation to the depth variation of frictional slip properties, *J. Geophys. Res.*, 91(B9), 9452-9472, doi:10.1029/JB091iB09p09452.

[45] Turner, R. C., R. M. Nadeau, and R. Bürgmann (2013), Aseismic slip and fault interaction from repeating earthquakes in the Loma Prieta aftershock zone, *Geophys. Res. Lett.*, 40, 1079-1083, doi:10.1002/grl.50212.

[46] USGS, `http://earthquake.usgs.gov/monitoring/gps/SFBayArea_SGPS/` (2014)

[47] Wang, K., Y. Hu, and J. He (2012) Deformation cycles of subduction earthquakes in a viscoelastic Earth, *Nature*, 484, 327-332.

[48] Wang, R., F. Lorenzo-Martin, and F. Roth (2006), PSGRN/PSCMP-A new code for calculating co- and post-seismic deformation, geoid and gravity changes based on the viscoelastic-gravitational dislocation theory. *Comput. Geosci.*, 32, 527-541.

Chapter 4

Probing the lithospheric rheology across the eastern margin of the Tibetan Plateau

4.1 Abstract

The fundamental geological structure, geodynamics, and rheology of the Tibetan Plateau have been debated for decades. Two end-member models have been proposed: (1) the deformation of Tibet is broadly distributed and associated with ductile flow in the mantle and middle or lower crust, (2) the Tibetan Plateau formed during interactions between rigid lithospheric blocks with localization of deformation along major faults. The nature and distribution of continental deformation is governed by the varying rheology of rocks and faults in the lithosphere. Insights into lithospheric rheology can be gained from observations of postseismic deformation, which represents the response of the Earths interior to coseismic stress changes. Here we use up to 2 years of InSAR and GPS measurements to investigate postseismic displacements following the 2008 M_w 7.9 Wenchuan earthquake in eastern Tibet and probe the differences in rheological properties across the edge of the Plateau. We find that near-field displacements can be explained by shallow afterslip on the Beichuan Fault, which is anti-correlated with the coseismic slip distribution. Far-field displacements cannot be explained with a homogeneous rheology, but instead require a viscoelastic lower crust (from 45-60 km depth) beneath Tibet with an initial effective viscosity of 4.4×10^{17} Pa s and a long-term viscosity of 10^{18} Pa s, whereas the Sichuan Basin block has a high-viscosity upper mantle ($> 10^{20}$ Pa s) underlying an elastic 35-km-thick crust. The inferred strong contrast in lithospheric rheologies between the Tibetan Plateau and the Sichuan Basin is consistent with models of ductile lower crustal flow that predict maximum topographic gradients across the Plateau margins where viscosity differences are greatest.

Keywords: Lithospheric rheology, 2008 Wenchuan earthquake, postseismic deformation, geodesy, finite element modeling

4.2 Introduction

The Himalayan-Tibetan orogen is a classic example of continent-continent collision resulting in a series of active mountain ranges, starting 50 million years ago [Thatcher, 2009; Royden et al., 2008; Tapponnier et al., 2001]. The tectonic evolution and geodynamics of the Tibetan Plateau, with its average elevation of 5 km and 60-to-80-km-thick crust, continue to be topics of debate. In the east, the Tibetan Plateau has collided with the Sichuan Basin since the Miocene and produced the Longmen Shan and its great topographic relief, rising 6 km over the Sichuan Basin within less than 40 km horizontal distance [Hubbard et al., 2010]. The low-lying Sichuan Basin is roughly circular, and seismic tomography suggests that a thick, cold mantle lithosphere underlies a 35-km-thick crust with 10 km of mostly undeformed Mesozoic and Paleozoic sediments [Li et al., 2009]. From east to west, the Pengguan fault (PGF) and the Beichuan fault (BCF) are the two major active northwest dipping fault zones of the Longmen Shan (Fig. 4.1) and represent reactivations of Mesozoic fold-and-thrust structures [Burchfiel et al., 2008]. The interseismic deformation across the Longmen Shan amounts to < 3 mm/yr shortening with an oblique right-lateral shear component [Shen et al., 2005; Shen et al., 2009]. Though many geophysical and geological studies have been carried out in eastern Tibet, the rheology of the lower crust and upper mantle is poorly constrained. Thus, the nature of the mountain building process and style of deep-seated deformation of eastern Tibet continue to be unresolved [Burchfiel et al., 2008].

On 12^{th} May, 2008, the M_w 7.9 Wenchuan earthquake occurred along the eastern Longmen Shan and caused more than 80,000 fatalities. The earthquake ruptured 235 km of the BCF and the entire PGF [Shen et al., 2009; Wang et al., 2011]. Several coseismic slip models have been proposed from seismic, geodetic, or combined inversions [Zhang et al., 2010]. All of the slip models show oblique thrusting along the southwestern BCF and a right-lateral slip component that gradually increases towards the northeastern end of the BCF (Fig. 4.1). The inferred deep geometry of the PGF and BCF, either shallowing into a sub-horizontal detachment [Hubbard et al., 2010] or a more steeply dipping localized shear zone to the Moho [Guo et al., 2013], is tested by coseismic slip models [Zhang et al., 2010]. Some rupture models prefer a moderate amount of coseismic slip on a shallowly-dipping detachment fault extending downdip below 20 km depth [Shen et al., 2009; Wang et al., 2011; Zhang et al., 2010].

The redistribution of stresses by the earthquake induce a variety of postseismic processes that result in observable surface displacements, which can then be used to constrain the rheologic properties of rocks and faults deep beneath the surface [Bürgmann and Dresen, 2008]. Postseismic mechanisms include aseismic afterslip, aftershocks, viscoelastic relaxation in the lower crust and/or upper mantle, and poroelastically induced fluid flow. The contributions from these mechanisms to observed postseismic deformation can, however, be difficult to separate, hence a major challenge lies in resolving the contributions of various postseismic

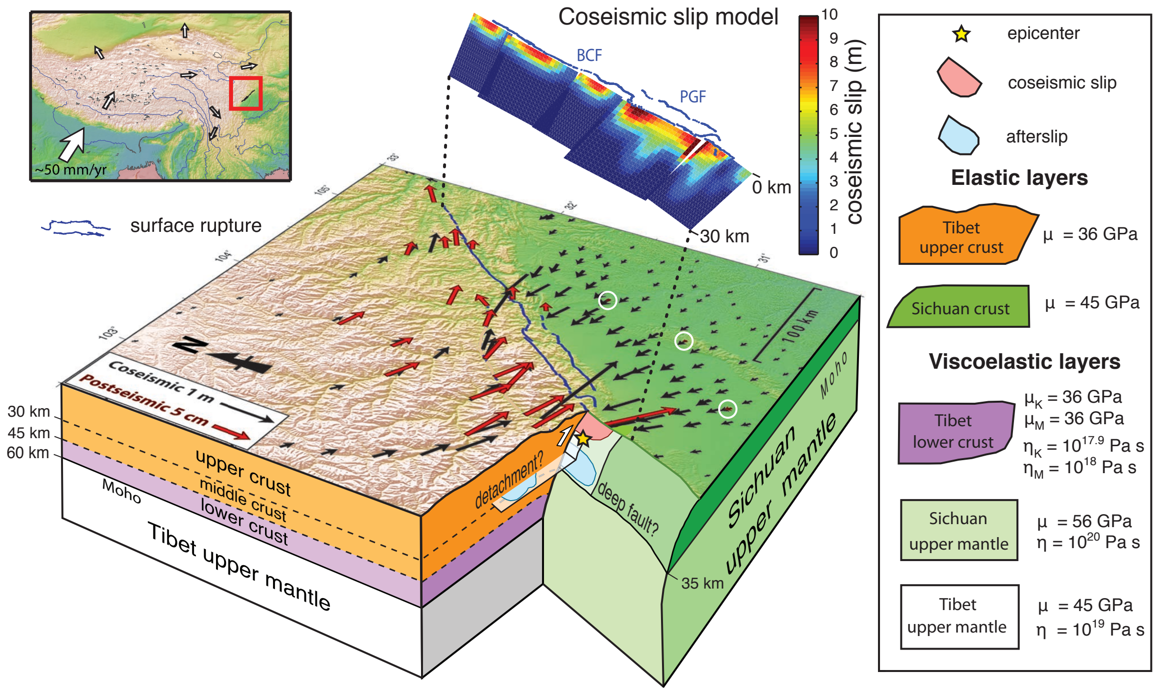

Figure 4.1: Three-dimensional representation of eastern Tibet. The upper left map shows the Tibetan Plateau, and the red square indicates the study area. The black and red arrows in the 3D block diagram are the co- and estimated first year postseismic GPS measurements. The white circles in the Sichuan Basin show stations that have < 5 mm postseismic measurements. The detachment and deep faults are based on Shen et al. [2009] and Wang et al. [2011]. The coseismic slip model is based on inversion of the coseismic GPS displacements. The rheologic properties of the viscoelastic relaxation model are given in the legend.

processes to the observed transient surface deformation [Hearn, 2003]. In this study, we incorporate two years of geodetic measurements after the Wenchuan earthquake and numerical modeling to isolate the individual contributions and use these constraints to probe the deep rheology of eastern Tibet and the adjoining Sichuan Basin.

4.3 Data

4.3.1 GPS

The GPS postseismic displacement data are from Shen et al. [2009] and Ding et al. [2013]. Both studies fit the early GPS horizontal data with a logarithmic function: D(t) = $D_{x,y}$ ln(1+t/τ), where $D_{x,y}$ is the amplitude of the postseismic displacement of each component. The logarithmic relaxation times (τ) of the functions are 8 and 38 days for Shen et al. [2009] and Ding et al. [2013], respectively. There are 37 stations from Shen et al. [2009] and 16 stations from Ding et al. [2013]. To compute the 1-year postseismic displacement, we use the amplitude terms ($D_{x,y}$) of each station and set t = 365.25 days.

4.3.2 InSAR and PSInSAR

We use Advanced Land Observation Satellite (ALOS) PALSAR L-band (23.6 cm) data from the Japan Aerospace Exploration Agency and Envisat ASAR C-band (5.6 cm) from the European Space Agency to observe the postseismic deformation starting a month after the mainshock until about 1.5 years afterward. The line-of-sight incidence angle at the center of the image track is 35° for ALOS and 23° for Envisat. There are up to 26 ALOS acquisitions from tracks 471-475 during the postseismic period, but the spatial baselines between acquisitions are often too large for producing interferograms (> 1,500 m), due to the orbital drift of the ALOS satellite (Supplementary Information S1). The selected interferograms are mostly 1.5-2 year pairs, similar to the period of the orbital drift. There are no SAR acquisitions of Envisat after April of 2012 and ALOS after April of 2011 due to the ends of the missions. All of the ALOS and Envisat acquisitions are from ascending and descending orbits, respectively (Tables 3.1-2). All SAR interferograms are generated using *ROI PAC 3.0* [Rosen et al., 2004]. The 90 m Shuttle Radar Topography Mission (SRTM) DEM is used to correct the phase due to topography. *Snaphu 1.4.2* [Chen and Zebker, 2002] is used for the phase unwrapping.

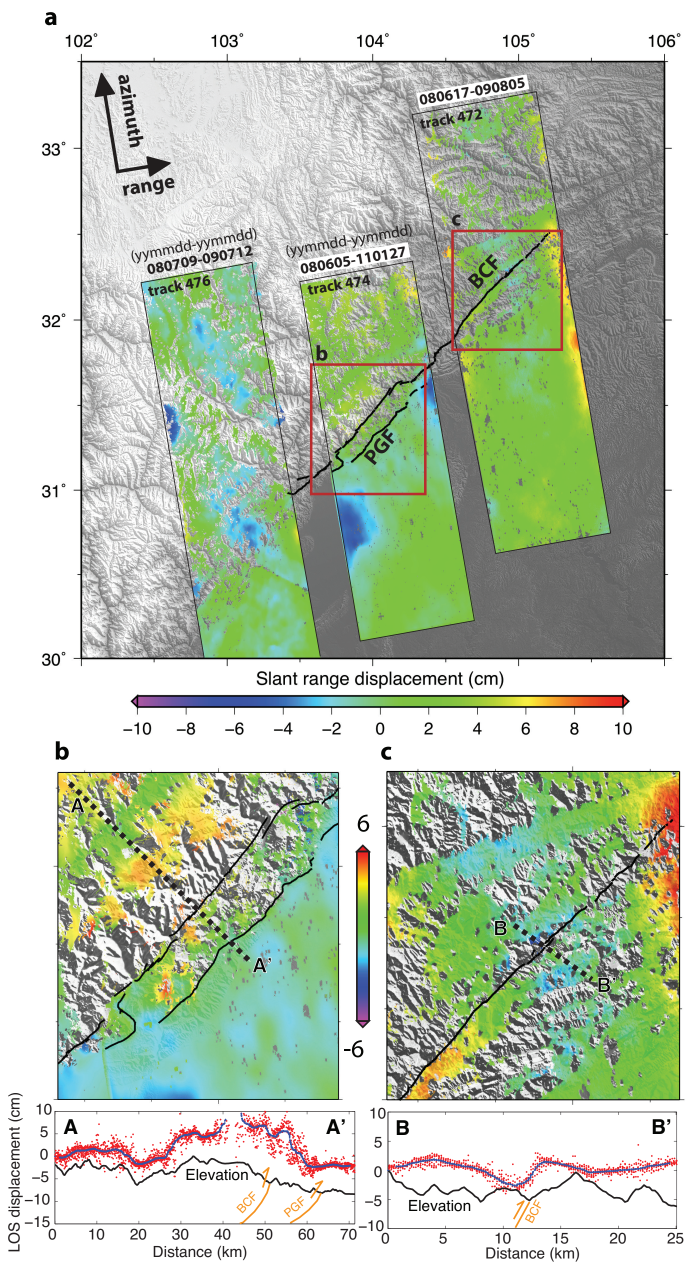

Figure 4.2: ALOS PALSAR 2-year postseismic displacement. (a) Interferograms of five ascending tracks (T471-475) showing about 2-year postseismic displacement (acquisition dates are shown above or below the interferograms (see Table 3.1 for a list of the interferograms). Warm and cold colors show range shortening and lengthening, respectively. The average look angle of ALOS at the center of the image track is 35°. (b) Close-up view of the SW section of the surface rupture. (c) Close-up view of the NE BCF. The profiles below (b) and (c) shows the elevation and the LOS displacement during the acquisitions. The black lines are the elevation and the red dots are the LOS displacements within 5 km along the profile. The blue lines are the mean LOS displacement.

4.4 The Wenchuan postseismic deformation

The GPS measurements of deformation following the Wenchuan earthquake show an overall NW-SE convergence along the southern BCF, transitioning into right-lateral strike-slip motion along the northern BCF (Fig. 4.1, data based on Shen et al., 2009 and Ding et al., 2013). The first-order patterns of the co- and postseismic displacements are similar (Fig. 4.1), but the peak postseismic motions occur about 40 km NW from the greatest coseismic displacement, which is located at the surface rupture [Shen et al., 2009]. Compared with the coseismic deformation, the spatial wavelength of the postseismic deformation is much greater, suggesting either deep-seated afterslip or viscoelastic relaxation in the deeper parts of a thick lower crust or upper mantle. In the footwall (to the SE of the fault), most of the displacements in the Sichuan Basin are toward the NW, but with much smaller amplitude ($<$ 5 mm in the first year) than in the hanging wall (Fig. 4.1).

Thirty-three ascending ALOS PALSAR acquisitions from tracks 471 to 475 cover the entire Wenchuan postseismic area (Table 3.1). The 1-2 year SAR interferograms (Fig. 4.2) show both near- and far-field postseismic deformation along the Longmen Shan. A sharp change in the line-of-sight (LOS) displacement in the line of sight appears across the northern BCF (Fig. 4.2c). This range change is consistent with shallow right-lateral strike slip of 3 cm in the first year (profile BB' in Fig. 4.2c). However, the full extent of creep on the northern BCF is unclear due to ionospheric and tropospheric noise that affects the interferograms (Fig. 4.7a). Along the southern BCF (Fig. 2b), there is no sharp range change across the surface rupture, but a 50-km-wide zone of range decrease extends from the PGF across the Longmen Shan (profile AA' in Fig. 2b). Due to low signal-to-noise levels and strong atmospheric perturbations (Supplementary Information S1), we choose to exclude the ALOS measurements as model constraints.

Fifteen Envisat ASAR acquisitions of descending track 290 are used to generate time series of postseismic displacement in the southern Longmen Shan (Table 4.2). The small baseline subset (SBAS) method (see Supplementary Information S2) is used to generate InSAR time series from June, 2008 to December, 2009. The result (Fig. 3a) shows a zone of range decrease of more than 10 cm in the southern Longmen Shan about 30-100 km NW of the surface rupture (green to red color in Fig. 3a). Time series of four selected groups of pixels illustrate the postseismic displacement in the near-, mid-, and far field of the hanging wall and footwall blocks (black lines in Fig. 3c). In eastern Tibet, the near- and mid-field measurements (2 and 3 in Fig. 3c) show a rapidly decaying trend, accumulating up to 12 cm of range decrease in 1.5 years. On the Sichuan Basin, the data show mostly insignificant range change. There is evidence for nearly 1 cm of subsidence near Chengdu (1 in Fig. 3c), but the range increase rate is not consistent over time and seems to have a seasonal variation during the 1.5-year period.

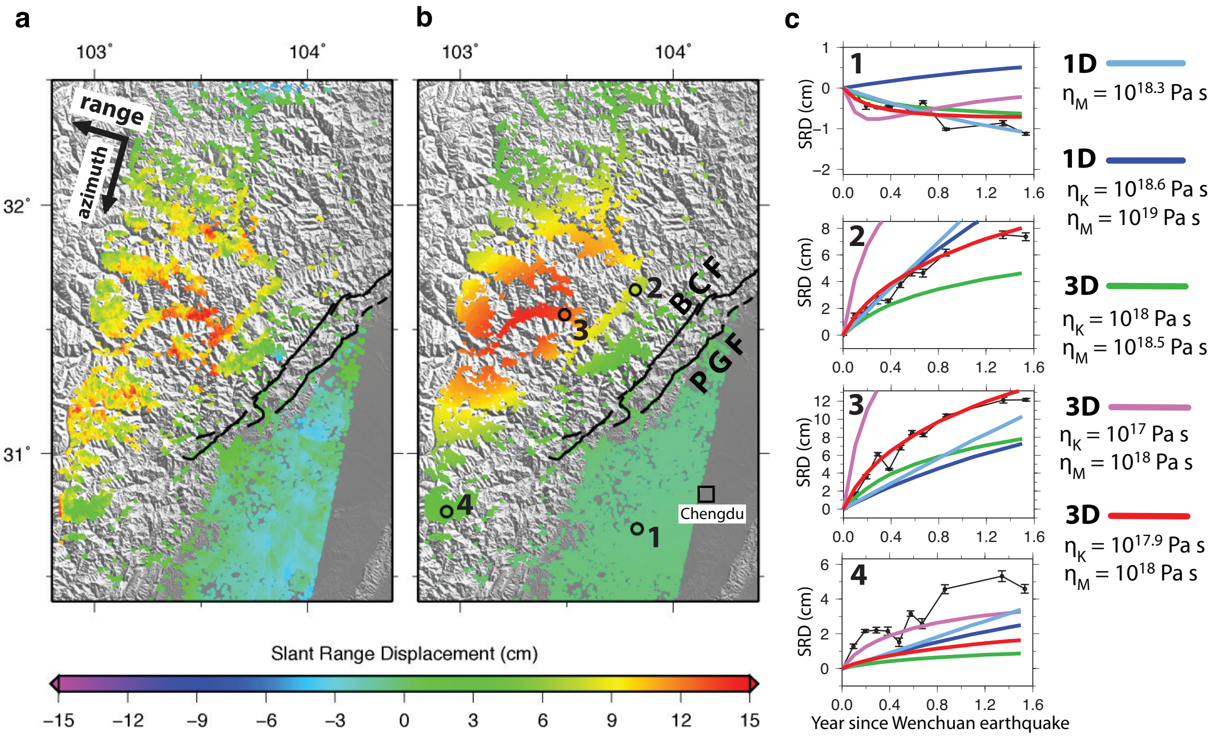

Figure 4.3: 1.5-year postseismic displacement from Envisat InSAR data. (a) The stable image points extracted with the SBAS algorithm (Supplementary Information S2) and the color represents the cumulative slant-range displacement. Warm colors indicate range shortening. The average look angle of Envisat at the center of the image track is 23°. (b) The predicted InSAR displacement from the preferred viscoelastic relaxation model. (c) Selected InSAR slant-range displacement (SRD) time series (black lines) at labeled points shown in (a) and predicted time series (red lines) based on the viscoelastic relaxation model in (b), as well as selected 1D and 3D model results.

4.5 Modeling approach

Shao et al. [2011] used the first 14 days of postseismic near-field GPS data to conclude that both afterslip and viscoelastic relaxation contributed to the deformation transients. Here we test models of these processes, as well as poroelastic rebound, constrained by one-year GPS displacements and 1.5-year Envisat time series.

4.5.1 Afterslip models

Afterslip describes the process when predominantly aseismic fault slip occurs on or beneath the rupture zone, in the days to years after the main shock. We consider inverse dislocation models with afterslip on either a straight down-dip extension of the coseismic rupture [Guo et al., 2013], or on a shallowly dipping detachment [Hubbard et al., 2010; Shen et al., 2009; Wang et al., 2011]. To evaluate if afterslip distributions found in the kinematic inversions are mechanically plausible, we also compute the distribution of afterslip from a model of slip on a friction-free fault driven by the coseismic stress changes. Such a stress-driven model predicts the maximum afterslip that can be expected based on the moment release of the earthquake.

The distributed slip models are calculated by the inversion of geodetic data (GPS and InSAR) for slip on a discretized dislocation model. We use the coseismic GPS data from Wang et al. [2011] and postseismic GPS and InSAR data for co- and post-seismic inversions. The geodetic Greens functions are computed using the programs *EDGRN*/*EDCMP* (Wang and Roth, 2006) for the coseismic and afterslip inversions. This allows for the calculation of the Greens functions relating unit slip on each subfault dislocation to surface displacements in a layered elastic model over a half-space. The weight between GPS and InSAR is chosen so that both datasets have similar variance reduction (see Huang et al., 2013 for detail about data weighting and smoothing factors). We use the eastern Tibet elastic structure from Li et al. [2011] to compute the Greens functions for the afterslip model. For the deep fault geometry, we keep the fault dip angle the same as Shen et al. [2009] and extend the fault width so it can reach the Moho depth (about 60 km) as the deepest location of afterslip. We also consider a fault geometry with a wide, shallowly dipping detachment fault 25-30 km below the Longmen Shan based on Qi et al. [2011].

4.5.2 Viscoelastic relaxation

Viscoelastic forward models explore the rheologic structure required to explain postseismic observations if they were driven solely by viscoelastic relaxation of coseismic stresses imparted to the lower crust and mantle. We also consider a multiple-mechanism model in which we first solve forward models of viscoelastic relaxation, then invert for a companion afterslip component required to satisfy the remaining displacement residuals.

We initially consider a 1D-layered structure [Pollitz, 1992] that is composed of two viscoelastic layers (lower crust and upper mantle) below an elastic lid representing the upper crust, with a crustal thickness of 60 km (Zhang et al., 2009). The shear moduli of the layers are estimated from regional shear-wave tomography models (Li et al., 2009; see Fig. 4.1). We evaluate a series of forward models to achieve a best fit to the Envisat time series and 1-year GPS displacements by varying the thickness and viscosity of the lower crust. The viscosity of the upper mantle is based on a series of tests varying viscosity from 10^{18} to 10^{20} Pa s, and is determined to be at least 10^{19} Pa s. The mantle viscosity is poorly constrained because the coseismic stress change below the Moho (> 60 km) is too small to produce significant relaxation.

We use the finite element model code Abaqus 6.12 (`http://www.simulia.com/products/abaqus_fea.html`) to construct a 3D geologic structure to better represent the lateral heterogeneity between eastern Tibet and the Sichuan Basin. This model extends 1,600 km in the horizontal dimension with the coseismic surface rupture at the center, and vertically to a depth of 1,000 km (Fig. 5a and b), so the fixed boundaries do not significantly affect the coseismic stress change and the relaxation. The fault geometry and the coseismic slip distribution are based on Shen et al. [2009] with some slip adjustments to accommodate the difference between 1D homogeneous and 3D heterogeneous models. Seismic tomography [Li et al., 2009] and receiver function studies [Zhang et al., 2009b] inform the first-order geologic structure. On the Sichuan side, the entire 35-km-thick crust is assumed elastic overlying a viscoelastic upper mantle. On the Tibetan side, the upper crust (0-30 km) is elastic. We assume that either the middle (30-45 km) or the lower (45-60 km) crust is viscoelastic (Fig. 5b), and we vary the viscosity for either layer to fit the geodetic observation. Note, the middle crust is assumed elastic when considering a viscoelastic lower crust and vise versa. The viscoelastic middle crust model is to test if eastern Tibet has similar structure as a weak middle crust overlaying stronger mafic crust beneath the southern Lhasa block in southern Tibet [Nelson et al., 1996]. The Tibetan upper mantle is also assumed viscoelastic.

4.5.3 Poroelastic rebound

Poroelastic rebound is the process in which coseismic pressure changes drive fluid flow in the crust, usually in the months following large earthquakes [Freed et al., 2006]. Postseismic pore fluid flow can be driven by coseismic changes in pressure. The resulting poroelastic rebound can contribute to the postseismic surface deformation. Peltzer et al. [1996] first proposed that poroelastic rebound can explain some of the near-field postseismic displacements following the 1992 M_w 7.3 Landers, California earthquake. While evidence for poroelastic

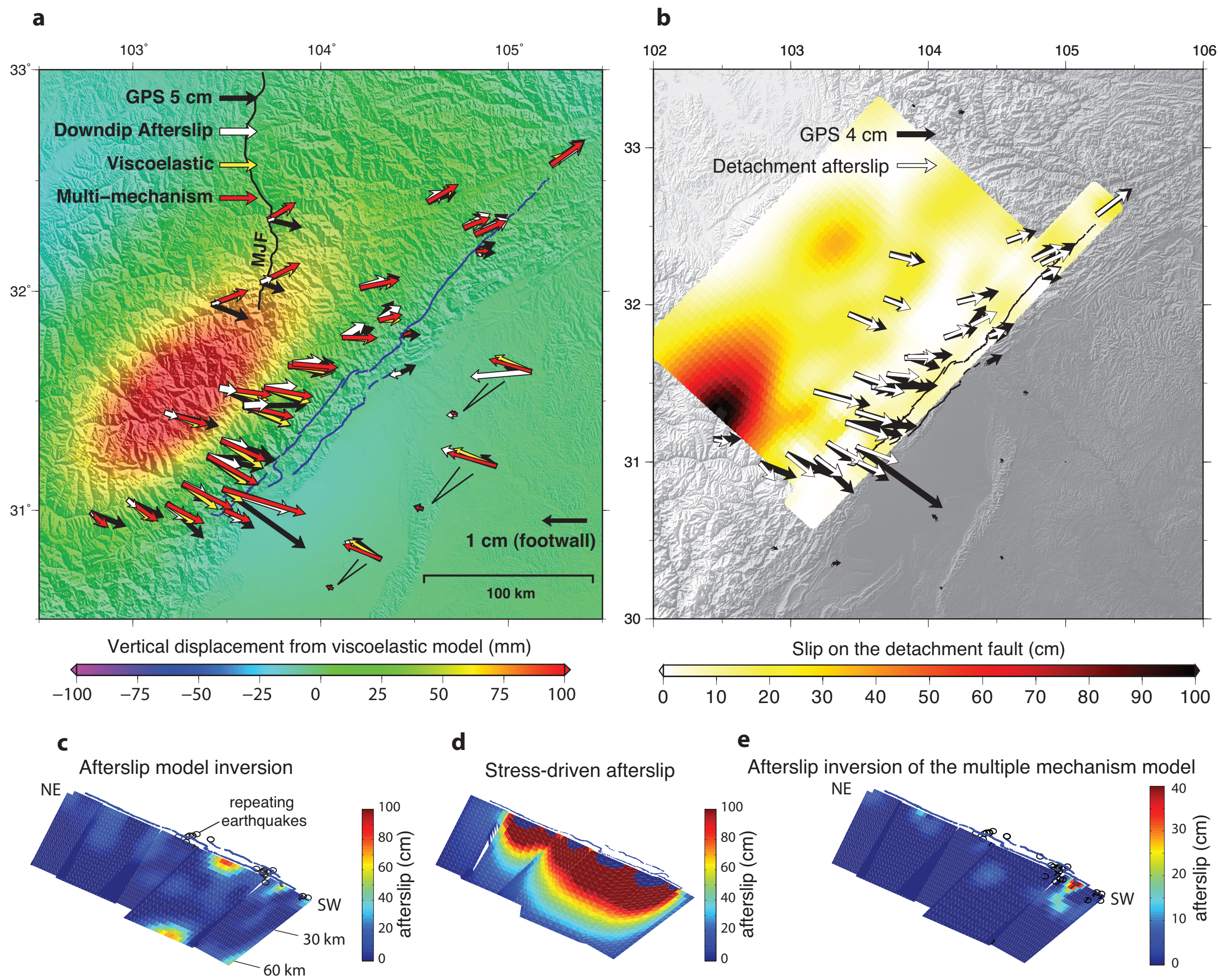

Figure 4.4: Postseismic model results. (a) One-year postseismic GPS measurement (black arrows), modeled postseismic displacement from afterslip-only inversion (white arrows), 3D viscoelastic relaxation model (yellow arrows and vertical color contoured values), and the multiple-mechanism model (red arrows). (b) Afterslip distribution on the sub-horizontal detachment underneath Longmen Shan. The fault geometry is based on Qi et al. [2011]. (c) The afterslip-only model inversion using the same fault geometry as the coseismic model but is extended to 60 km depth. Circles are repeating earthquakes (Li et al., 2011) observed from 2000 to 2008. (d) The stress-driven afterslip model relieving all coseismic shear-stress changes. (e) Afterslip distribution from the multiple mechanism model. Note the color scale of (c) and (d) is the same.

rebound is strong for some earthquakes [Peltzer et al., 1996; Jonsson et al., 2003] it has been ruled out in other cases [Barbot et al., 2008]. Deformation from poroelastic rebound can be estimated by the transition of the Poissons ratio of the deformed volumes of rock from undrained to drained conditions after the earthquake (typically within a few months). This process represents the return of pore pressure to hydrostatic equilibrium [Peltzer et al., 1996].

4.6 Results

4.6.1 Afterslip

We use a dislocation model in an elastically layered crust to invert the observed surface motions for the optimal smoothed afterslip distribution. We modify the fault geometry proposed by Shen et al. [2009] and extend the fault down dip to 60 km depth. In the best-fitting result, there are five main slip zones in the shallower part of the fault (Fig. 4b), which are anti-correlated with the coseismic peak slip areas. The peak afterslip is 82 cm on the southern BCF near the surface. The moment released by the afterslip is 4.09×10^{19} N m (M_w 7.07), about 5.4% of the main shock based on Shen et al. [2009] and about 8.5 times of the moment released by the first year of aftershocks (M_w 6.52, based on Jia et al., 2010). Similar to the coseismic slip, the inferred afterslip is mostly oblique thrusting in the SW and right-lateral strike slip in the NE. The afterslip in the deeper sections of the fault is distributed between 30 and 60 km depth with higher (> 60 cm) slip values near the bottom edge of the southern fault segments.

The fit to the geodetic measurements based on afterslip inversions is generally better in the near field (Fig. 4a). In the Tibetan far field, the afterslip model greatly underpredicts both GPS and InSAR displacements. Since the far-field displacement is directly related to the deeper slip (note the patch of deep afterslip in Fig.4c), to improve the fit would require afterslip that extends below the Moho of eastern Tibet (i.e. greater than 60 km), well separated from the inferred region of shallow afterslip.

Alternatively, we consider a fault geometry with a shallowly dipping detachment fault 25-30 km below the Longmen Shan based on Qi et al. [2011] for the afterslip-only inversion. We use the same method as in the deep afterslip inversion (see Section 4.4.1). In this model, slip can extend on the detachment fault for up to 170 km west of the coseismic surface rupture (Fig. 4b). In the best-fitting model, most of the afterslip is located in the SW part of the detachment fault, with peak amplitude of about 102 cm. This model fits the middle- to far-field horizontal GPS well, but cannot produce enough displacement in the near-field GPS and the Envisat measurements (Fig. 4.9a). Peak afterslip occurs far from the rupture and coseismic stress changes. The misfit (rms for 1-year GPS and InSAR displacements) of

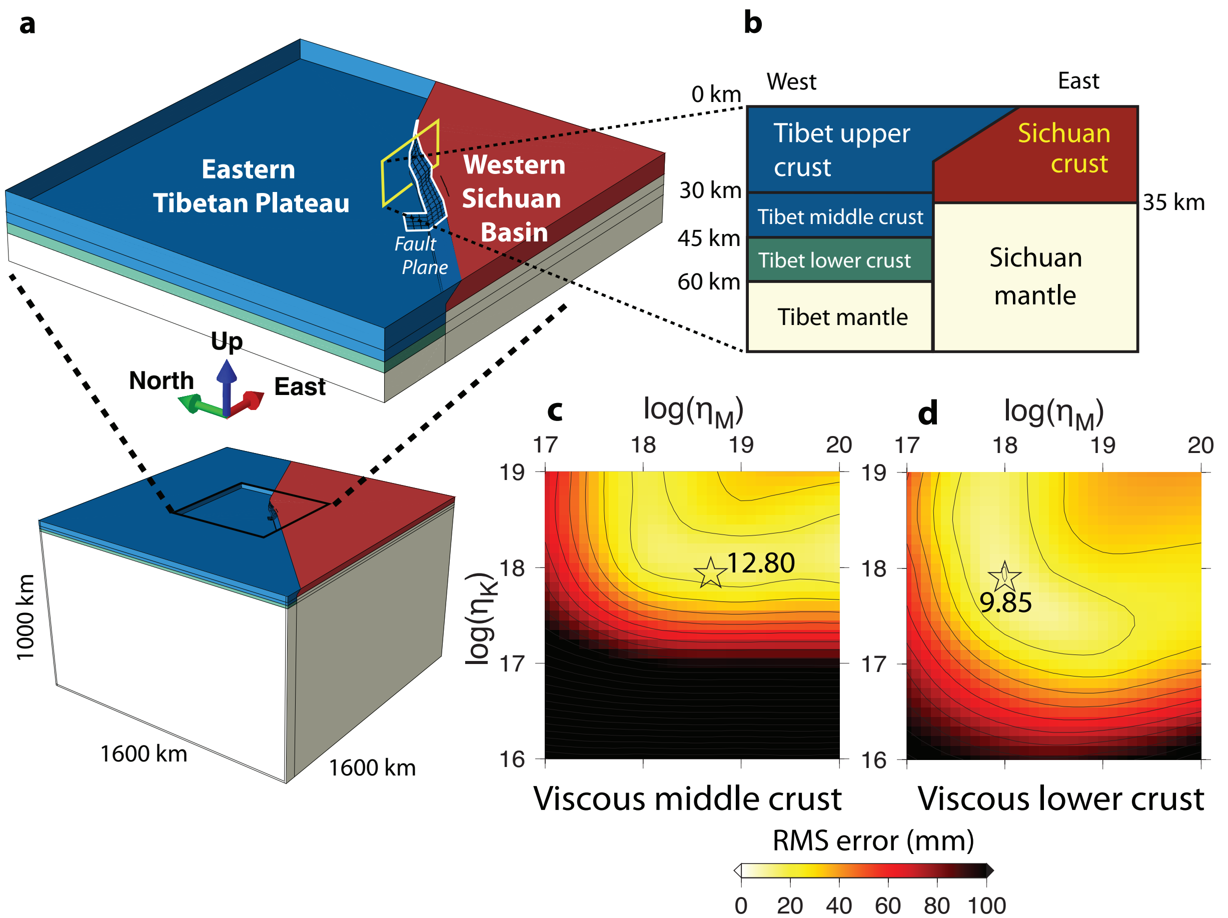

Figure 4.5: (a) The 3D block model and the fault geometry [Shen et al., 2009] constructed using ABAQUS in regional scale and in (b) detail around the boundary of Tibet and Sichuan blocks. (c) The estimation of viscosities of Kelvin and Maxwell components of the transient Burgers-body rheology, assuming viscoelastic relaxation in Tibets middle crust and in (d) Tibets lower crust. The stars indicate the locations of the preferred model viscosities for either case, and the numbers indicate the RMS error of the best-fitting models.

the detachment model is 14 mm versus 20 mm for the model inverting for afterslip on the steeper down-dip extension. The shallower (< 20 km) sections of the slip models with the two fault geometries are similar. The afterslip in the multiple-mechanism model with the deep fault geometry (Fig. 4d) is located mostly in the shallower part, so the afterslip in the multiple-mechanism model with detachment fault geometry would have similar distribution as the deep fault model.

To determine whether the afterslip inversions are mechanically plausible, we examine a stress-driven frictionless afterslip model [Freed et al., 2006; Johnson et al., 2012] to estimate the maximum possible afterslip distribution assuming full relaxation of coseismic stress changes on the BCF (Supplementary Information S3). We use the same coseismic slip distribution (Fig. 4.1) and allow afterslip away from the rupture down to 60 km depth. As shown in Fig. 4d, the stress-driven afterslip extends to the deeper sections of the southern BCF, and includes near-surface slip where the coseismic slip is smaller. While the stress-driven afterslip greatly exceeds the inverted values in the 10-km-wide zone below the coseismic rupture, the afterslip inversion predicts more than 50 cm of deep slip below 35 km, which exceeds the completely relaxed stress-driven afterslip of only up to 10 cm in this deep region. As a frictionless down-dip fault should enable the maximum afterslip that can be generated by coseismic stress changes, this suggests that the deep afterslip implied by the inversion is not plausible. To actually match the surface displacements with a stress driven model, it would be necessary to not allow for slip at intermediate depths, in which case even a further extended fault plane would not be able to produce a sufficient amount of deep slip.

4.6.2 Viscoelastic relaxation

Viscoelastic flow after a large earthquake results from the relaxation of coseismic stress changes in the lower crust and upper mantle, where high temperatures and pressures enable ductile flow of rocks [Bürgmann and Dresen, 2008]. Basic viscoelastic deformation relations can be represented by equations that consider various combinations of linear elastic and linear viscous components [Bürgmann and Dresen, 2008; Wang et al., 2012]. The initial 1D model composed of two Maxwell viscoelastic layers cannot predict the early fast displacements and their rapid decay in the Envisat time series (Fig. 3c). Early rapid transients are also seen in rock mechanics experiments [Chopra, 1997] and previous postseismic deformation studies [Pollitz, 2003; Ryder et al., 2007], and may reflect the transition from transient to steady-state rheologic properties following a stress perturbation. Hence, we use the bi-viscous Burgers model that is composed of a Kelvin solid (η_K) and a Maxwell fluid (η_M) to explain the two-stage displacements [Bürgmann and Dresen, 2008; Wang et al., 2012; Pollitz, 2003]. The best-fitting 1D bi-viscous model (Fig. 3c) with $\eta_K = 410^{18}$ Pa s and $\eta_M = 10^{19}$ Pa s in a layer extending from 20 to 60 km depth shows a general agreement with the observed deformation in the Longmen Shan, but fails to match the displacements in the

Sichuan Basin. However, the 1D models generally predict up to 3 cm uplift and 5 cm horizontal motions in the Sichuan Basin (Fig. 4.10), which greatly exceeds the geodetic observations.

The strong asymmetry of postseismic deformation across the Longmen Shan implies a rheologic contrast between the Tibetan Plateau and the Sichuan Basin. We therefore consider a 3D rheologic structure using a finite element model (Fig. 5a and b; see Section 4.4.2). In the Tibetan lower crust, the transient and steady-state viscosities of the crustal layers are varied from 10^{17} to 10^{20} Pa s. On the Sichuan, the upper mantle Maxwell viscosity below 35 km is allowed to vary from 10^{19} to 10^{21} Pa s. Fig. 4.11 demonstrates that the upper mantle below the Sichuan Basin must have an effective viscosity above 10^{20} Pa s, as a weaker mantle produces displacements that exceed those found to the SE of the Longmen Shan. A comparison of best-fit models for relaxation in the middle or lower crust can be found in Fig. 4.12 and plots of misfit as a function of transient and steady-state viscosity in the relaxing crustal layers are shown in Fig. 5c and d. The best fitting result was obtained with $\eta_K = 7.9 \times 10^{17}$ Pa s and $\eta_M = 10^{18}$ Pa s in Tibets lower crust (i.e., initial effective viscosity $= 4.4 \times 10^{17}$ Pa s and steady-state viscosity $= 10^{18}$ Pa s; see Supplementary Information S4) and viscosity $> 10^{20}$ Pa s in the upper mantle below Sichuan. This result fits the spatial and temporal pattern of the postseismic displacements well both to the NW and SE of the Longmen Shan thrust system (Figs 3 and 4a).

4.6.3 Poroelastic rebound

Poroelastic rebound can be modeled as the difference between two calculated coseismic displacement fields associated with different assumed Poissons ratios of the top 2-km-thick layer, from 0.25 (undrained) immediately following the earthquake to 0.21, representing drained conditions following fluid-pressure re-equilibration. In this model, fluid flow is assumed to occur only in the uppermost, most permeable section of the crust [Jonsson et al., 2003; Manning and Ingebritsen, 1999], but the pattern of poroelastic rebound is similar for drainage to greater depth. The coseismic input is the same as for the stress-driven afterslip model (Supplementary Information S3) and the viscoelastic relaxation models. The poroelastic rebound model with these parameters (Fig. 4.8a) predicts significant near-fault displacements of up to 4 cm in both horizontal and vertical components. However, the poroelastic rebound model cannot explain the postseismic displacement, or the misfits of afterslip and viscoelastic models (Fig. 4.8b). In order to further examine the possible contribution of poroelastic rebound, we subtract the poroelastic rebound model from the observed GPS measurement, and invert for afterslip on the fault. The inverted afterslip (Fig. 4.8c) is highly similar to the afterslip-only model, which implies that the poroelastic rebound model is not a significant contributor to the postseismic displacement. We rule out this mechanism as important in observed postseismic observations, as it only produces near fault displacements that are inconsistent with the observations (Fig. 4.8).

4.7 Discussion and conclusions

4.7.1 Multiple mechanisms

The afterslip model (Fig. 4a and b) can explain the postseismic displacements in the near field with up to 82 cm of afterslip in the shallower (above 20 km) part of the fault. However, the fitting to the far field, especially the vertical component, requires more than 60 cm of deep afterslip below 35 km (Fig. 4c), or $>$ 1.2 m on an isolated slip zone on a horizontal detachment (Fig. 4b). On the other hand, the viscoelastic relaxation model (Figs 3b-c and 4a) can explain middle- to far-field postseismic displacements with a 15-km-thick lower crustal layer below 45 km depth, but cannot fit the details of the near-field motions. Thus, a single mechanism cannot explain the observed postseismic displacement field. Following the exploration in the last section, we consider lower crustal relaxation of Tibet to be the main mechanism to explain the far-field measurements in eastern Tibet. If we invert the residual displacements from this model for afterslip (Fig. 4e), we find several $>$ 20 cm afterslip patches above 20 km and $<$ 10 cm afterslip deeper (25-40 km) on the southern BCF. The moment of afterslip in the multiple-mechanism is 6.56×10^{18} N m (M_w 6.54), only 16% of the moment of the afterslip-only model. The shallow model afterslip along the northern BCF can well explain the surface creep resolved in the ALOS InSAR data (Fig. 2c), as well as the near field GPS displacement along the BCF. To the northwest of the Longmen Shan close to 104°E and 32°N, none of the models accurately predict the displacement azimuths of three GPS stations (Fig. 4a). A possible cause of this misfit is triggered fault slip on the nearby Minjiang fault (MJF in Fig. 4a). Alternatively, the azimuthal error could be due to heterogeneous viscosity within the eastern Tibetan Plateau. Exploration of such possibilities is beyond the scope of this study. It is also worth noting that the shallow afterslip distribution is anti-correlated with the coseismic rupture asperities (Fig. 4c) with peaks near where repeating earthquakes were observed during 2000-2008 [Li et al., 2011]. Such identically repeating earthquakes are generally considered to represent repeated asperity failures driven by surrounding aseismic fault creep [Nadeau and McEvilly, 2004].

4.7.2 Heterogeneous rheology and the geodynamics of Tibet

Tomographic and receiver function studies [Li et al., 2009; Zhang et al., 2009; Li et al., 2009] find a reduced shear wave velocity and higher Poissons ratio in Tibets lower crust, which may reflect fluids or elevated temperatures. Magnetotelluric resistivity measurements also suggest elevated fluid content in eastern Tibets middle-to-lower crust [Zhao et al., 2012; Rippe and Unsworth, 2010]. Additionally, the temperature is estimated to be $>$ 800 °C at $>$ 30 km depth below the Lhasa block in central Tibet (Mechie et al., 2004) and in southern

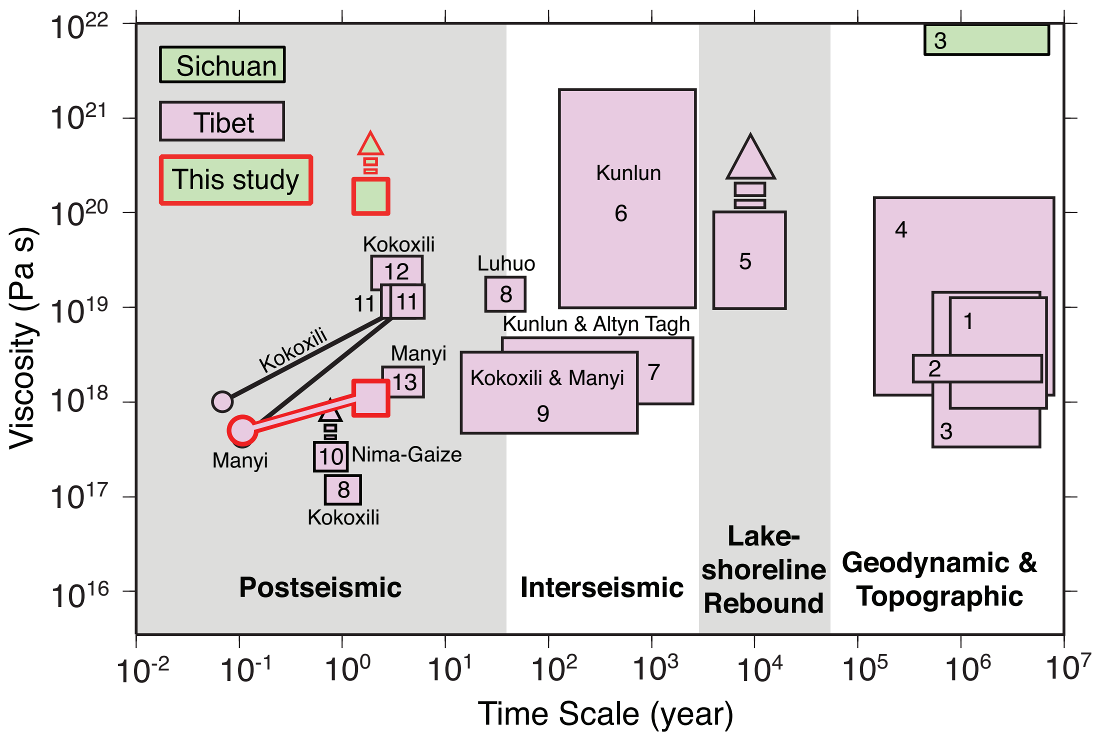

Figure 4.6: Viscosity estimates of Tibets lower crust for different time scales. The rectangles represent the range of viscosity of the lower crust estimated using constraints for different time scales. The circles represent the initial effective viscosity of a Burgers-type rheology. The arrows above the rectangles indicate that the estimated viscosity represents a lower bound. The estimated value for the Sichuan block (green square) is for the mantle below 35 km depth. The number in the rectangles refers to the cited references: 1, Beaumont et al. [2001]; 2, Clark et al. [2005]; 3, Cook and Royden [2008]; 4, Rippe et al. [2010]; 5, England et al. [2013]; 6, Hilley et al. [2005]; 7. Hilley et al. [2009]; 8, Zhang et al. [2009]; 9, DeVries and Meade [2013]; 10, Ryder et al. [2010]; 11, Ryder et al. [2011]; 12, Wen et al. [2012]; 13, Yamasaki and Houseman [2012].

Tibet (Wang et al., 2013), much higher than in the Sichuan Basin (500°C at 30 km depth, Wang, 2001). These thermal conditions suggest temperatures above the solidus of dry or wet granite while more mafic rock types that are likely to make up the lower crust of Tibet will deform by crystal plastic flow at these conditions [Klemperer, 2006]. The Sichuan Basin, on the other hand, has a thick, high-velocity lithospheric root [Li and van der Hilst, 2010] and a low geothermal gradient [Wang, 2001].

The strongly asymmetric distribution of postseismic deformation observed following the 2008 Wenchuan earthquake reveals viscous relaxation in the lower crust of Tibet, whereas little if any deformation occurred in the cratonic lithospheric block underlying the Sichuan Basin. A weak and viscous ($\eta_M = 10^{18}$ Pa s) lower crust beneath the Tibetan Plateau that relaxes the coseismic stress changes can explain the middle- to far-field postseismic displacements well (Figs 3 and 4). In Fig. 4.6, we compare viscosity estimates for Tibetan lower crust obtained using different types of constraints, including postseismic deformation (10^{17} 10^{19} Pa s; Ryder et al., 2011; Wen et al., 2012; Zhang et al., 2009; Yamasaki and Houseman, 2012; Ryder et al., 2010), GPS measurements of interseismic velocities (10^{18} 10^{19} Pa s; DeVries and Meade, 2013; Hilley et al., 2005; Hilley et al., 2009), paleo-lake shoreline rebound (10^{19}-10^{20} Pa s; England et al., 2013), magnetotelluric resistivity data (10^{18} 10^{20} Pa s; Rippe and Unsworth, 2010), and geodynamic models (3×10^{17}-1021 Pa s; Beaumont et al., 2001; Clark et al., 2005; Cook and Royden, 2008), involving time scales of up to a few Ma. Most of the viscosity estimates span a wide range from 3×10^{17} to 3×10^{19} Pa s across all time scales, which includes the value found in this study. On the other hand, we find that little if any viscous relaxation occurred in the Sichuan Basin lithosphere following the Wenchuan earthquake (upper mantle $\eta_M > 10^{20}$ Pa s).

The lower crustal viscosity inferred by postseismic deformation studies is about three to five orders of magnitude lower than the inferred lithosphere-averaged viscosities found in geodynamic deformation models by England and Houseman [1985], England and Molnar [1997], Flesch et al. [2001], and Copley and McKenzie [2007]. The main difference is that in postseismic studies, a depth dependent viscosity is necessary to produce reasonable near and far-field displacements in space and time, whereas the thin viscous sheet models of regional deformation assume a constant effective viscosity throughout the lithosphere, including the upper elastic crust that deforms by brittle faulting. Given these different model assumptions, these viscosity estimates should not be directly compared. Copley et al. [2011] use a two-layered viscosity structure in a model trying to explain the difference in tectonic deformation style between southern and northern Tibet by coupling to the underthrusting Indian crust. Their model requires a high-viscosity lower Tibetan crust (5×10^{23} Pa s) below southern Tibet, possibly due to an anhydrous, granulite lithology. This rheology structure and argument against channel flow below southern Tibet is inconsistent with our results from eastern Tibet.

A Maxwell fluid with a constant viscosity fails to explain the postseismic displacement rate changes, and shows the need of a model in which the effective viscosity increases with time. The change of effective viscosity implies either transient rheology or stress-dependent power-law rheology or both [Freed et al., 2012]. In this study we try to distinguish the main mechanism that contributes to the postseismic displacements and the contrasting rheology between Tibet and Sichuan, and thus adopt a simple bi-viscous Burgers rheology. As the viscoelastic relaxation model can explain most of the early postseismic transients in the middle field, we can rule out afterslip as being the major cause of the initial rapid displacements.

Models of Tibetan lower crustal channel flow predict that the Plateau margins are steepest where the viscosity of the surrounding blocks are highest, and thus impede and divert the flow [Royden et al., 2008; Beaumont et al., 2001; Clark et al., 2005; Cook and Royden, 2008]. These models predict the strongest viscosity contrasts with the Sichuan and Tarim Basin blocks ($\eta = 10^{16-18}$ Pa s in a 15-20 km thick lower crustal layer versus 10^{20-21} Pa s in adjacent crust), where topographic gradients are greatest. Our preferred viscosity structure deduced from the postseismic deformation transients across the Longmen Shan is consistent with such contrasting lithospheric rheology and deformation between eastern Tibet and the Sichuan Basin.

4.8 Supplementary information

4.8.1 S1. Correction for topography-correlated atmosphere delay ALOS PALSAR data

Most of the ALOS interferograms are strongly correlated with the topography, suggesting topography-correlated atmospheric perturbation (Fig. 4.7a). We use the 90-m resolution SRTM DEM to represent the topography, and perform the complex cross-correlation of DEM and each ALOS interferogram in the Fourier-domain. The complex cross-correlation can highlight the regions where the interferogram has higher similarity with the regional topography. We apply smoothing to adjust the wavelength of correlated topography. We estimate the spatial decorrelation by subtracting the correlation from 1, and then apply the inverse Fourier transform to produce the topographic-free interferogram, as shown in Fig. 4.7b. This method can remove most of the longer-wavelength topographic correlation, but the removal of the shorter wavelength features depends on the smoothing we apply in the complex cross-correlation. In addition, the long-wavelength topographic feathers are close to the wavelength of ionospheric correlations or the real postseismic deformation, so it is not easy to separate each component in a certain wavelength. As a result, this method may also remove some of the signal of the postseismic deformation that has a similar pattern as the regional topography. This may be the cause of the low amplitude of the hanging wall displacement in the Longmen Shan in Fig. 4.7b.

We simulate the one-year postseismic ALOS line-of-sight displacement in Fig. 4.7c from the best-fit viscoelastic relaxation model. Due to the direction of the postseismic deformation and the right-looking ascending orbit, the horizontal movement cancels out part of the vertical displacement. The peak line-of-sight displacement is about 6 cm in the SW Longmen Shan.

4.8.2 S2. Small Baseline InSAR time series analysis

We apply and modify the small baseline subset (SBAS) method based on Berardino et al. [2002]. We estimate the time series of 11 Envisat ASAR images (Table S2) from 15 unwrapped InSAR pairs. In this study, all interferograms are phase unwrapped using Snaphu 1.4.2 [Chen and Zebker, 2002]. SBAS relies on selecting an appropriate combination of differential interferograms with small temporal baselines and orbital separation (spatial baseline) in order to limit the spatial decorrelation. Given N SBAS InSAR pairs from M ASAR acquisition, one can link these pairs by an N by M matrix, and estimate the displacement between each ASAR acquisition by inverting the matrix using singular value decomposition (SVD). This method can also estimate the topographic errors of the DEM and the atmospheric perturbation in each acquisition, if there is a sufficient number of InSAR pairs (N). For details of the method see Berardino et al. [2002] and Hooper [2008].

In this study, after processing all of the SBAS pairs using *ROIPAC3.0* [Rosen et al., 2004], we select the stable scatterers following the method suggested by Hooper et al. [2007]. In general, a pixel of a SAR acquisition contains the sum of signals returned from many background scatterers. These background scatterers represent the physical condition of the surface (e.g., ocean, rock, vegetation, etc.). Hence, the variance in phase of the same pixel taken at different time may increase due to the change of the physical conditions. The stable scatterers are points in a region that are brighter than the background scatterers, and the variances in the phase are lower because the physical conditions are unchanged. As a result, the stable scatterers can dominate the signal of a pixel in all interferograms, so we may be able to extract the underlying deformation signal. In the Longmen Shan area, the high relief and abundant vegetation strongly impact the spatial correlation, so there are only 58,393 point scatterers left in the entire interferogram after this procedure. The stable point scatterers in the Longmen Shan are sparse, which may allow for significant phase unwrapping errors. As a result, the conventional SBAS method does not work unless some additional information is used to constrain long wavelength deformation and to avoid unwrapping errors. We apply the method provided by Dominquez et al. [2003] to constrain InSAR and to minimize phase unwrapping errors, using the cGPS data shown in Fig. 4.4 with additional vertical components from 31 stations. (Z. Shen, personal communication) and of 5 stations from Ding et al. [2013] as the constraints. To do this, we first use Dx,y,z and in the logarithmic function (see

Methods) to estimate the 3D displacement of GPS stations at each SAR acquisition time and project the displacement into Envisat line of sight [Huang et al., 2009]. We calculate the slant range displacement of each GPS station for the time spans of the 15 interferograms (Table 4.2). After this step, we interpolate the GPS slant range displacement using bicubic spline functions. We then apply a median filter with a 10 by 10 km moving window to the GPS simulated map that can remove higher spatial frequency. For each interferogram, we also apply a median filter with the same moving window to remove the short wavelength features. Finally, we compare the difference between the real and the GPS simulated interferograms and estimate the phase unwrapping errors (integer number of phase cycles).

After this procedure, we apply the SBAS method as suggested by Berardino et al. [2002]. This method assumes that the displacement of each stable scatterer is composed of a velocity, acceleration, and acceleration rate terms (i.e. the time series model) through the observation time. Besides, each pixel also has a topographic error term due to the uncertainty of the digital elevation model (DEM). The SVD can connect M interferograms and N SAR acquisitions by an M by N matrix (in our case M = 15 and N = 11) and minimize the misfit by finding the value of the velocity, acceleration, acceleration rate, and topographic error terms. After this process, we obtain the estimated time series model, a DEM error, and a residual phase. The residual phase contains part of the surface displacement that cannot be described by the model and other noises from the atmosphere and other sources (e.g. thermal noise). We use a spatial low-pass filter and a temporal high-pass filter to separate the atmospheric contribution to the phase and the surface displacement, assuming the atmospheric delay is spatially correlated and temporally uncorrelated. With the atmospheric correction, we then obtain final estimates of the DEM error, atmospheric noise contribution, and the postseismic displacement.

4.8.3 S3. Stress-driven afterslip

The stress-driven model estimates the slip on the fault away from the coseismic rupture, including the downdip extension, from the full relaxation of the coseismic stress changes. It is the maximum possible afterslip distribution because the model is assumed frictionless and the whole fault away from the coseismic rupture asperity is assumed to slip aseismically. The coseismic slip input is estimated from the geodetic inversion shown in Fig. 4.1. We drive afterslip with the coseismic slip areas with more than 7.5 m slip, in order to allow stress driven afterslip in low-slip zones of the coseismic model [Johnson et al., 2012], or alternatively only allow afterslip to occur below 20 km, similar to [Freed et al., 2006], in order to maximize the stress-driven afterslip. We extend the fault geometry down to 60 km, assuming that the slip is not extending below the Moho. We use the boundary element method as implemented in the poly3d code [Thomas, 1993] to estimate the resulting slip distribution. We allow slip in the along-strike and dip directions, but not fault-perpendicular motions. As shown in Fig.

4c and Fig. 4.9c, most of the afterslip occurred near the coseismic slip asperities. For both scenarios, more than 1 m afterslip occurs as deep as 40 km, and slip decays to zero at the bottom of the fault.

4.8.4 S4. The effective viscosity of the Burgers model

A Burgers model is composed of a Maxwell fluid connected in series with a Kelvin solid (Fig. 4.13a). As derived in Pollitz [2003], the strain (ε) of a Burgers model is,

$$\varepsilon(t) = \frac{\sigma_o}{2\mu_M} + \frac{\sigma_o}{2\mu_K}\left(1 - e^{-\frac{t}{\tau_K}}\right) + \frac{\sigma_o}{2\mu_M}\frac{t}{\tau_M}, \tag{4.1}$$

where σ_o is the initial stress, η_M and μ_M are the viscosity and shear modulus of the Maxwell fluid, η_K and η_K are the viscosity and the shear modulus of the Kelvin solid, and $\tau_M = \eta_M/\mu_M$ and $\tau_K = \eta_K/\mu_K$ are the characteristic relaxation times for the Maxwell and Kelvin components, respectively. The strain rate is the time derivative of ε,

$$\dot{\varepsilon(t)} = \frac{\sigma_o}{2\mu_K\tau_K}e^{-t/\tau_K} + \frac{\sigma_o}{2\mu_M\tau_M} = \frac{\sigma_o}{2\mu_M\tau_M}\left(\frac{\mu_M\tau_M}{\mu_K\tau_K}e^{-t/\tau_K} + 1\right), \tag{4.2}$$

and the effective viscosity is the stress divided by the strain rate, i.e.,

$$\eta(t) = \frac{\eta_M\eta_K}{\eta_M e^{-t/\tau_K} + \eta_K}, \tag{4.3}$$

which is a time dependent function of a combination of the Maxwell and Kelvin viscosities (M and K, respectively). In the E Tibetan Plateau, our best-fitting viscoelastic model finds $\eta_K = 7.910^{17}$ Pa s, $\eta_M = 10^{18}$ Pa s, and $\tau_K = 7.9 \times 10^{17}$ Pa s / 36 GPa = 0.7 year, so the effective initial viscosity is 4.4×10^{17} Pa s when t = 0, 9×10^{17} Pa s when t = 1.5 years, and 10^{18} Pa s when t $\approx \infty$ (also see Fig. 4.13b). However, due to the relatively short observational period (t = 1.5 years), we are not able to well constrain the Maxwell viscosity, so the long-term viscosity is only about 2 times larger than the transient viscosity, which is lower than the commonly found factor-of-10 difference. It is likely that the steady-state viscosity (or Maxwell viscosity) will be higher given a longer observational period, as it become more clear how surface displacements rates slow in the future.

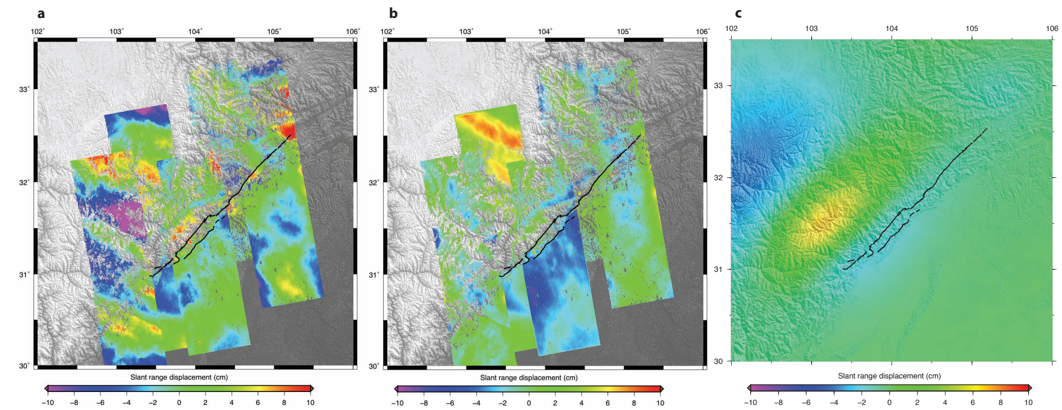

Figure 4.7: The ALOS postseismic images (a) before the topographic correction, (b) after the topographic correction, and c, the best fitting model prediction of the displacement in line of sight.

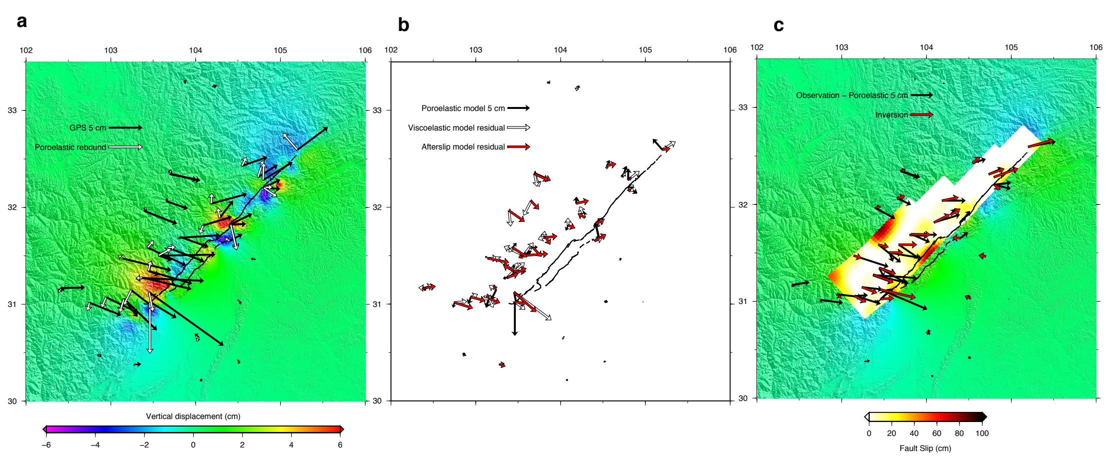

Figure 4.8: (a) Poroelastic rebound prediction. The response is calculated from assuming a Poissons ratio reduction (0.04) from undrained to drained conditions after the earthquake. (b) Inversion of displacements corrected for contribution of poroelastic rebound (observation poroelastic rebound, black arrows) for afterslip on extended fault plane. Red arrows show model prediction. (c) Comparison of predicted poroelastic rebound and the residuals of inverted afterslip-only and viscoelastic relaxation-only models.

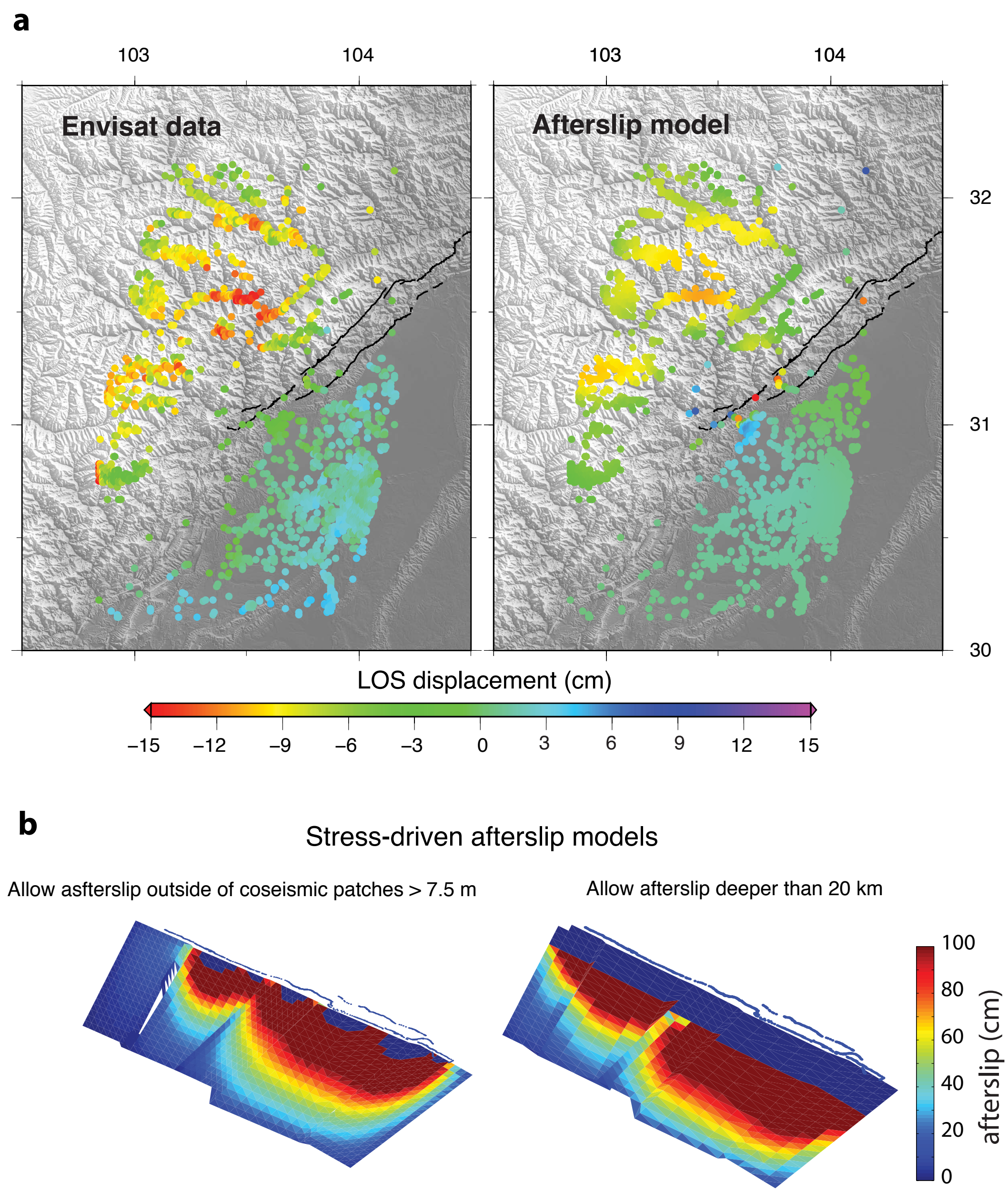

Figure 4.9: (a) Afterslip distribution on the sub-horizontal detachment underneath Longmen Shan. The fault geometry is based on Qi et al. [2011]. (b) Two stress-driven scenarios: the left hand one is the same as Fig. 4c; the right hand one assumes afterslip only occurs below 20 km deep.

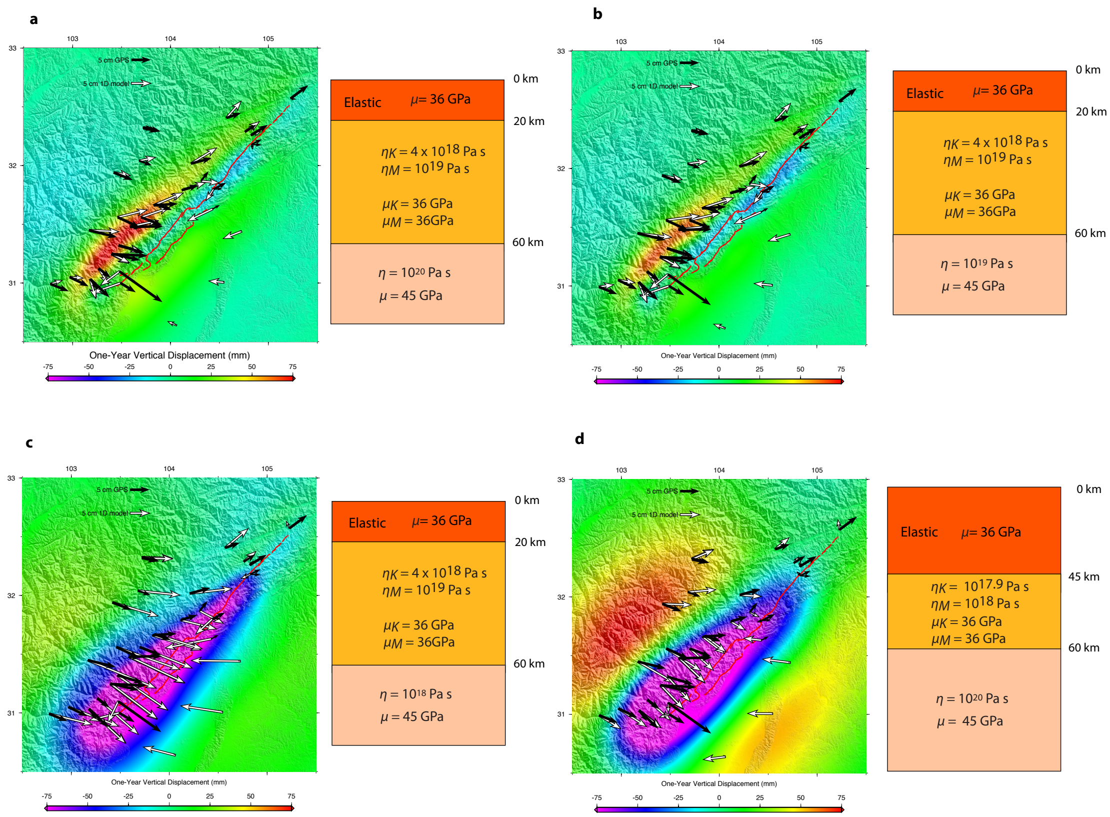

Figure 4.10: (a) One-year model prediction from the best fitting viscoelastic-relaxation-only model using a 1D layered structure. Note that the lower crust (20-60 km) has a bi-viscous Burgers rheology. (b) The same 1D layered as (a), but the viscosity of the upper mantle is 10^{19} Pa s. c, The same as (a), but the viscosity of the upper mantle is 10^{18} Pa s. (d) The viscoelastic-relaxation-only, 1D-layered model using Tibets rheologic structure from the 3D model (Fig. 4.1). Note that all 1D models predict more displacement (> 2 cm) in the footwall (Sichuan Basin) than the GPS measurements (< 5 mm).

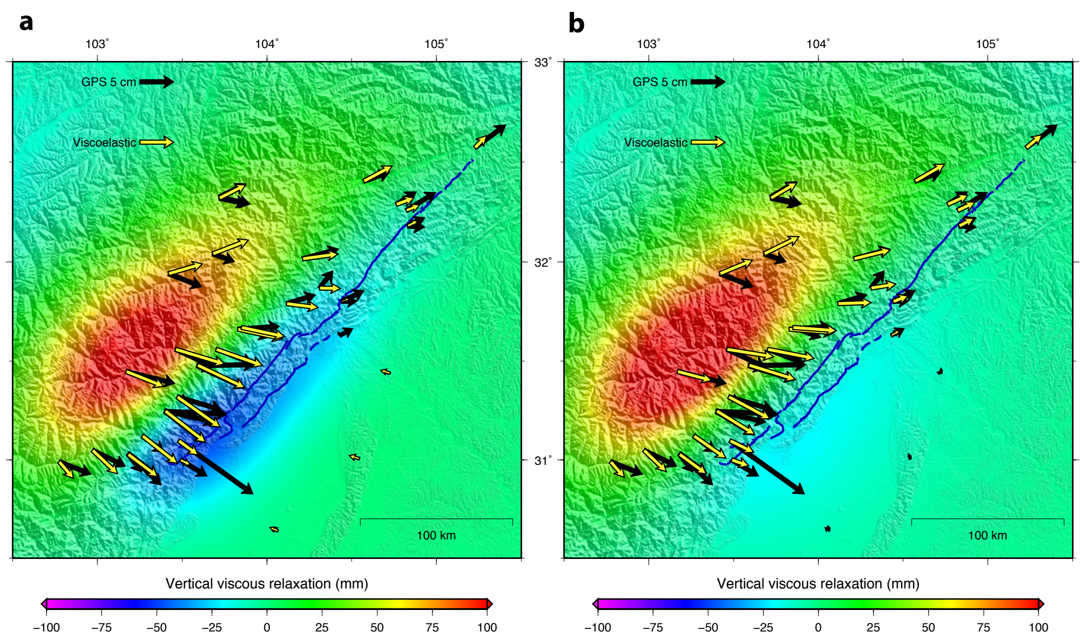

Figure 4.11: The postseismic deformation with (a) Weaker (10^{19} Pa s) Sichuan upper mantle and (b) Stronger (10^{20} Pa s) Sichuan upper mantle.

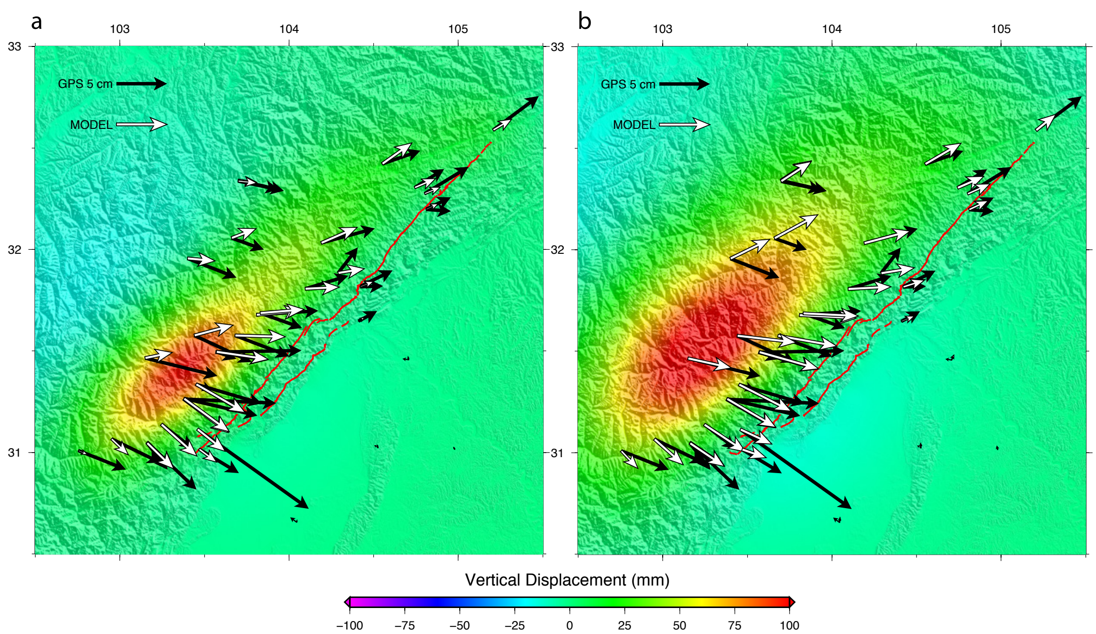

Figure 4.12: Best-fitting viscoelastic relaxation models of (a) Middle crust (30-45 km) and (b) Lower crust (45-60 km). The best-fitting transient and steady-state viscosities are 10^{18} and 10^{19} Pa s for (a) and 10^{17} and 10^{18} Pa s for (b), respectively.

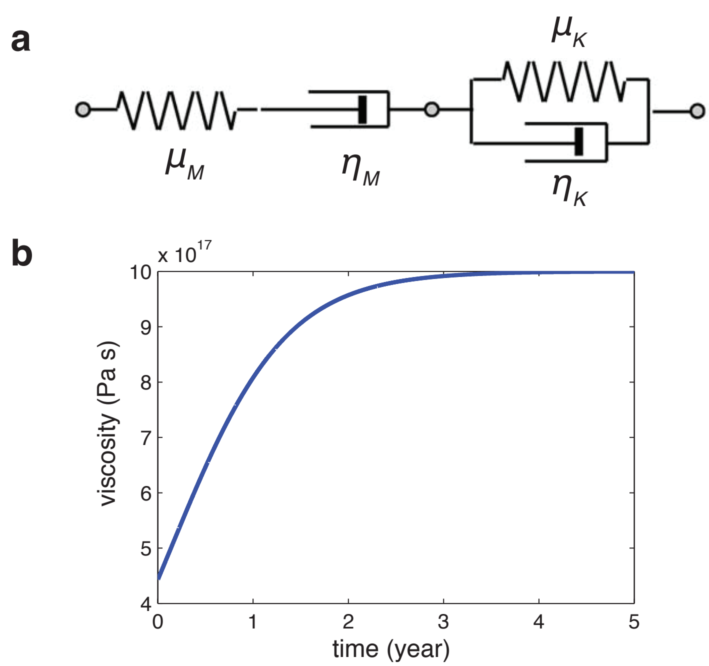

Figure 4.13: (a) The Burgers model (after Pollitz, 2003). (b) the effective viscosity versus time plot.

Table 4.1: ALOS interferograms on ascending orbit. The bold pairs are selected for Fig. 4.1 and Fig. 4.7

Track	**Frame**	**Master (YYYY/MM/DD)**	**Slave (YYYY/MM/DD)**	**Temporal baseline (year)**	B_{perp} **(m)**
472	610-640	2008/06/17	2009/02/02	0.63	-467
472	610-640	2008/06/17	2009/06/20	1.01	285
472	**610-640**	**2008/06/17**	**2009/08/05**	**1.14**	**-214**
472	610-640	2008/06/17	2009/09/20	1.26	367
473	620-640	2008/05/19	2010/08/25	2.27	-614
473	620-640	2008/05/19	2010/10/10	2.39	-300
473	**620-640**	**2008/05/19**	**2011/01/10**	**2.64**	**61**
473	620-640	2008/05/19	2011/02/25	2.77	708
473	620-640	2008/07/04	2009/02/19	0.62	-574
473	620-640	2008/07/04	2009/08/22	0.13	290
474	600-620	2008/06/05	2010/07/27	2.14	-835
474	600-620	2008/06/05	2010/10/27	2.39	-410
474	**600-620**	**2008/06/05**	**2011/01/27**	**2.64**	**201**
474	600-620	2008/07/21	2009/09/08	1.13	153
474	600-620	2008/07/21	2009/10/24	1.26	391
474	600-620	2008/10/21	2009/03/08	0.38	882
474	600-620	2009/09/08	2009/10/24	0.13	238
474	600-620	2010/07/27	2010/10/27	0.25	424
475	600-630	2008/06/22	2009/06/25	1.01	N/A
475	**600-630**	**2008/06/22**	**2009/11/10**	**1.39**	**-263**
475	600-630	2008/06/22	2009/12/26	1.51	124
476	590-620	2008/07/09	2009/02/24	0.62	-691
476	**590-620**	**2008/07/09**	**2009/07/12**	**1.01**	**281**

Table 4.2: Envisat interferograms for frame 2961-2997 on descending track 290

Master (YYYY/MM/DD)	**Slave (YYYY/MM/DD)**	**Temporal baseline (year)**	B_{perp} **(m)**
2008/06/16	2008/07/21	0.095824778	34
2008/06/16	2008/08/25	0.191649555	-32
2008/06/16	2008/11/03	0.38329911	-70
2008/07/21	2008/08/25	0.095824778	-67
2008/08/25	2008/11/03	0.191649555	-37
2008/08/25	2009/01/12	0.38329911	-27
2008/08/25	2009/02/16	0.479123888	-41
2008/09/29	2008/12/08	0.191649555	8
2008/09/29	2009/10/19	1.054072553	-26
2008/11/03	2009/01/12	0.191649555	10
2008/11/03	2009/02/16	0.287474333	-4
2008/12/08	2009/12/28	1.054072553	-20
2009/01/12	2009/02/16	0.095824778	-14
2009/02/16	2009/04/27	0.191649555	-49
2009/10/19	2009/12/28	0.191649555	12

Bibliography

[1] Barbot, S., Hamiel Y. and Fialko Y. Space geodetic investigation of the coseismic and postseismic deformation due to the 2003 M_w7.2 Altai earthquake: Implications for the local lithospheric rheology, *J .Geophys. Res.* 113, B03403 (2008).

[2] Beaumont, C. et al. Himalayan tectonics explained extrusions of low-viscosity crustal channel coupled to focused surface denudation. *Nature* 414, 738-742 (2001).

[3] Burchfiel, B. C. et al. A geological and geophysical context for the Wenchuan earthquake of 12 May 2008, Sichuan, Peoples Republic of China. *GSA Today* 18, 4-11 (2008).

[4] Bürgmann, R. and Dresen, G. Rheology of the Lower Crust and Upper Mantle: Evidence from Rock Mechanics, Geodesy and Field Observations. *Annu. Rev. Earth Planet. Sci.* 36, 531-67 (2008).

[5] Chen, C. W. and Zebker, H. A. Phase Unwrapping for Large SAR Interferograms: Statistical Segmentation and Generalized Network Models. *IEEE Trans. Geosci. Remote Sensing* 40(8), 1709-1719 (2002).

[6] Chopra P. N. High-temperature transient creep in olivine rocks. *Tectonophys.* 279, 93-111 (1997).

[7] Clark, K. M., Bush, J. W. M. and Royden, L. H. Dynamic topography produced by lower crustal flow against rheological strength heterogeneities bordering the Tibetan Plateau. *Geophys. J. Int.* 162, 575-590 (2005).

[8] Copley, A. and McKenzie, D. Models of crustal flow in the India-Asia collision zone, *Geophys. J. Int.* 169, 683-698 (2007).

[9] Copley, A., Avouac, J.-P. and Wernicke, B. P. Evidence for mechanical coupling and strong Indian lower crust beneath southern Tibet. *Nature* 472, 79-81 (2011).

[10] Cook, K. and Royden, L. H. The role of crustal strength variations in shaping orogenic plateaus, with application to Tibet. *J. Geophys. Res.* 113, B08407 (2008).

[11] DeVries, P. M. R. and Meade, B. J. Earthquake cycle deformation in the Tibetan plateau with a weak mid-crustal layer. *J. Geophys. Res.* 118, 3101-3111 (2013).

[12] Ding, K., Xu, C. and Wen, Y. Postseismic deformation associated with the 2008 Wenchuan earthquake by GPS data [in Chinese], *Geom. Inform. Sci. Wuhan Univ.* 38, 131-135 (2013).

[13] England, P. and Houseman, G. Role of lithospheric strength heterogeneities in the tectonics of Tibet and neighbouring regions, *Nature* 315, 297-301 (1985).

[14] England, P. and Molnar, P. Active deformation of Asia: From kinematics to dynamics, *Science* 278, 647-650 (1997).

[15] England, P. C., Walker, R. T., Fu, B. and Floyd, M. A. A bound on the viscosity of the Tibetan crust from the horizontality of paleolake shorelines. *Earth Planet Sci. Lett.* 375, 44-56 (2013).

[16] Flesch, L. M., Haines, A. J. and Holt, W. E. Dynaics of the India-Eurasia collision zone, *J. Geophys. Res.* 106, 16,435-16,460 (2001).

[17] Freed, A., Bürgmann, R., Calais, E., Freymueller, J. and Hreinsdottir, S. Implications of deformation following the 2002 Denali, Alaska, earthquake for postseismic relaxation processes and lithospheric rheology. *J. Geophys. Res.* 111, B01401 (2006).

[18] Freed, A., Hirth, G. and Behn, M. D. using short-term postseismic displacements to infer the ambient deformation conditions of the upper mantle, *J. Geophys. Res.* 117, B01409 (2012).

[19] Guo, X. et al. Imaging the crustal structure beneath the eastern Tibetan Plateau and implications for the uplift of the Longmen Shan range. *Earth Planet Sci. Lett.* 379, 72-80 (2013).

[20] Hearn, E. H. What can GPS data tell us about the dynamics of post-seismic deformation? *Geophys. J. Int.* 155, 753-777 (2003).

[21] Hilley, G. E., et al. Bayesian inference of plastosphere viscosities near the Kunlun Fault, northern Tibet. *Geophys. Res. Lett.* 32, L01302 (2005).

[22] Hilley, G. E., et al. Earthquake-cycle deformation and fault slip rates in northern Tibet. *Geology* 37, 31-34 (2009).

[23] Huang, M.-H., Dreger, D., Bürgmann, R., Yoo, S.-H. and Hashimoto, M. Joint inversion of seismic and geodetic data for the source of the 2010 March 4, M_w 6.3 Jia-Shian, SW Taiwan, earthquake. *Geophys. J. Int.* 193, 1608-1626 (2013).

[24] Hubbard, J., Shaw, J. H. and Klinger, Y. Structural setting of the 2008 M_w 7.9 Wenchuan, China, earthquake. *Bull. Seismol. Soc. Am.* 100, 2713-2735 (2010).

[25] Jia, D. et al. Structural model of 2008 M_w 7.9 Wenchuan earthquake in the rejuvenated Longmen Shan thrust belt, China. *Tectohophys.* 491, 174-184 (2010).

[26] Johnson, K. M., Fukuda, J. and Segall, P. Challenging the rate-state asperity model: Afterslip following the 2011 M9 Tohoku-oki, Japan, earthquake. *Geophys. Res. Lett.* 39, L20302 (2012).

[27] Klemperer, S. L. Crustal flow in Tibet: geophysical evidence for the physical state of Tibetan lithosphere, and inferred patterns of active flow. In: Law, R. D., Searle, M. P. and Godin, L. (eds) Channel flow, ductile extrusion and exhumation in continental collision zones, Geological Society, London, Special Publications, 268, 39-70 (2006).

[28] Li, C. and van der Hilst, R. D. Structure of the upper mantle and transition zone beneath South East Asia from travel time tomography, *J. Geophys. Res.* 115, B07308 (2010).

[29] Li, H., Su, W., Wang, C.-Y., Huang, Z. Ambient noise Rayleigh wave tomography in western Sichuan and eastern Tibet. *Earth Planet. Sci. Lett.* 282, 201-211 (2009).

[30] Li, L., Chen, Q.-F., Niu, F. and Su, J. Deep slip rates along the Longmen Shan fault zone estimated from repeating microearthquakes. *J. Geophys. Res.* 116, B09310 (2011).

[31] Manning, C. E. and Ingebritsen, S. E. Permeability of the continental crust: Implications of geothermal data and metamorphic systems. *Rev. Geophys.* 37, 127-150 (1999).

[32] Mechie J. et al. Precise temperature estimation in the Tibetan crust from seismic detection of the - quartz transition. *Geology* 32, 601-604 (2004).

[33] Nadeau, R. M. and McEvilly, T. V. Periodic pulsing of characteristic microearthquakes on the San Andreas Fault. *Science* 303, 220-222 (2004).

[34] Nelson, K. D. et al. Partially molten middle crust beneath southern Tibet; synthesis of Project INDEPTH results. *Science* 274, 1684-1688 (1996).

[35] Pollitz, F. F. Postseismic relaxation theory on the spherical Earth. *Bull. Seismol. Soc. Am.* 82, 422-453 (1992).

[36] Pollitz, F. F. Transient rheology of the uppermost mantle beneath the Mojave Desert, California, *Earth Planet. Sci. Lett.* 215, 89-104 (2003).

[37] Qi, W. et al. Rupture of deep faults in the 2008 Wenchuan earthquake and uplift of the Longmen Shan. *Nat. Geo.* 4, (2011).

[38] Rippe, D. and Unsworth, M. Quantifying crustal flow in Tibet with magnetotelluric data. *Phys. Earth Planet. Inter.* 179, 107-121 (2010).

[39] Royden, L. H., Burchfiel, B. C. and van der Hilst, R. The geological Evolution of the Tibetan Plateau. *Science* 321, 1054-1058 (2008).

[40] Ryder, I., Bürgmann R. and Pollitz F. Lower crustal relaxation beneath the Tibetan Plateau and Qaidam Basin following the 2001 Kokoxili earthquake. *Geophys. J. Int.* 187, 613-630 (2011).

[41] Ryder, I., Bürgmann, R. and Sun, J. Tandem afterslip on connected fault planes following the 2008 Nima-Gaize (Tibet) earthquake. *J. Geophys. Res.* 115, B03404 (2010).

[42] Ryder, I., Parsons B., Wright T. J. and Funning G. Postseismic motion following the 1997 Manyi (Tibet) earthquake: InSAR observations and modeling. *Geophys. J. Int.* 169, 1009-1027 (2007).

[43] Shao, Z., Wang, R., Wu, Y. and Zhang, L. Rapid afterslip and short-term viscoelastic relaxation following the 2008 M_w 7.9 Wenchuan earthquake. *Earthquake Sci.* 24, 163-175 (2011).

[44] Shen, Z.-K., Lu, J. N., Wang, M. and Bürgmann, R. Contemporary crustal deformation around the southeast borderland of the Tibetan Plateau. *J. Geophys. Res.* 110, 11409 (2005).

[45] Shen, Z.-K. et al. Slip maxima at fault junctions and rupturing of barriers during the 2008 Wenchuan earthquake. *Nat. Geosci.* 2, 718-724 (2009).

[46] Tapponnier, P. et al. Oblique stepwise rise and growth of the Tibet plateau. *Science* 294, 1671-1677 (2001).

[47] Thatcher, W. How the continents deform: The evidence from tectonic geodesy. *Annu. Rev. Earth Planet.* 37, 237-262 (2009).

[48] Wang, C.-Y., Chen, W.-P. and Wang, L.-P. Temperature beneath Tibet. *Earth Planet. Sci. Lett.* 375, 326-337 (2013).

[49] Wang, K., Hu Y. and He J. Deformation cycles of subduction earthquakes in a viscoelastic Earth. *Nature* 484, 327-332 (2012).

[50] Wang, R., Lorenzo-Martin, F. and Roth F. PSGRN/PSCMP-A new code for calculating co- and post-seismic deformation, geoid and gravity changes based on the viscoelastic-gravitational dislocation theory. *Comput. Geosci.* 32, 527-541 (2006).

[51] Wang Y. Heat flow pattern and lateral variations of lithosphere strength in China mainland: constraints on active deformation. *Phys. Earth Planet. Inter.* 126, 121-146 (2001).

[52] Wen, Y., Li Z., Xu C., Ryder I., Bürgmann, R. Postseismic motion after the 2001 M_w 7.8 Kokoxili earthquake in Tibet observed by InSAR time series. *J. Geophys. Res.* 117, B08405 (2012).

[53] Yamasaki, T. and Houseman, G. A. The crustal viscosity gradient measured from post-seismic deformation: A case study of the 1997 Manyi (Tibet) earthquake. *Earth Planet. Sci. Lett.* 351, 105-114 (2012).

[54] Zhang, C., Cao, J. and Shi Y. Studying the viscosity of lower crust of Qinghai-Tibet Plateau according to post-seismic deformation. *Sci. China* 52(3), 411-419 (2009).

[55] Zhao, G. et al. Crustal structure and rheolgy of the Longmenshan and Wenchuan M_w 7.9 earthquake epicentral area from magnetotelluric data. *Geology* 40, 1139-1142 (2012).

[56] Zhang, P.-Z., Wen, X.-Z., Shen, Z.-K. and Chen, J.-H. Oblique, high-angle, listric-reverse faulting and associated development of strain: The Wenchuan earthquake of May 12, 2008, Sichuan, China. *Annu. Rev. Earth Planet.* 38, 353-382 (2010).

[57] Zhang, Z. et al. Crustal structure across Longmenshan fault belt from passive source seismic profiling. *Geophys. Res. Lett.* 36, L17310 (2009).

Chapter 5

Exploring crustal rheology underneath eastern Tibetan using the 2008 M_w 7.9 Wenchuan postseismic deformation measurements

5.1 Abstract

Large earthquakes could cause a sudden change of stress in the lithosphere, and lead to viscous relaxation at depth. In eastern Tibetan Plateau, Huang et al. [2014] used ∼2 years observations following the 2008 M_w 7.9 Wenchuan earthquake to explore the postseismic mechanisms as well as the rheology underneath the plateau. They found a bi-viscous Burgers model including transient viscosity right after the main shock and a steady-state viscosity could explain the middle- to far-field observation. Here, with additional 18 GPS stations that continuously recorded ∼6 years of crustal deformation since the Wenchuan earthquake, we find that with longer geodetic observations, the transient viscosity is ∼2 times larger ($\eta_K = 10^{18}$ Pa s) and the steady-state viscosity is ∼10 times larger ($\eta_M = 10^{19}$ Pa s) than Huang et al. [2014]. This result implies that using short-term geodetic measurements to infer long-term viscosity may underestimate the steady-state viscosity. In addition, we apply the power law model with diffusion creep flow to estimate lithospheric viscosity and the postseismic deformation. For a diffusion type of creep, material parameters (mineral type, grain size, water content, etc.) and environmental parameters (temperature, pressure, etc.) would influence the material viscosity. Our best fitting model prefers a middle crust (30 – 45 km depth) composed of wet feldspar, a lower crust (45 – 60 km depth) composed of wet pyroxene, and an upper mantle (below 60 km depth) composed of wet olivine underneath the Tibetan Plateau. The steady-state viscosity of the middle crust is ∼10^{19} Pa s, and contributes most of the postseismic deformation. This result agrees with viscosity estimates for different time scales, including post- and interseismic studies, postglacial rebound, and dynamic topography analyses. However, to further understand the viscosity driven by background stress level changes we need to consider the stress-dependent dislocation creep models.

Keywords: Tibetan Plateau, rheology, postseismic deformation, 2008 M_w 7.9 Wenchuan earthquake, Burgers body, power law flow rheology

5.2 Introduction

Postseismic deformation after great earthquakes has been used for probing crustal and upper mantle rheology and the geologic structure. For example, Pollitz et al. [2001] and Freed et al. [2004, 2010, 2012] used viscoelastic relaxation model to explain postseismic deformation in the Mojave Desert in southern California after the 1992 M 7.3 Landers and 1999 M 7.1 Hector Mine earthquakes. Viscoelastic relaxation describes the coseismic stress changes to the viscous middle-to-lower crust and/or upper mantle, and the response of these viscous layers would cause surface deformation with time in terms of viscoelastic deformation. Pollitz [2003] and Freed et al. [2006, 2007] also used viscoelastic relaxation models to explain the 2002 M_w 7.9 Denali earthquake. Other possible mechanisms including Afterslip and Poroelastic rebound may also contribute to postseismic surface deformation. Afterslip describes the process when predominantly aseismic fault slip occurs on or beneath the rupture zone, in the days to years after the main shock [Huang et al., 2014]. Poroelastic rebound happens when the coseismic pressure changes drive fluid flow in the crust, and it usually would affect the regions near the fault surface rupture within months after the earthquake. In different earthquake cases different postseismic mechanism contribute the deformation with different spatial and temporal scales. For example, afterslips dominated both the 1999 M_w 7.0 Izmit earthquake and the 2004 M 6 Parkfield earthquake are dominated [Bürgmann et al., 2002; Freed, 2007], and Peltzer et al. [1996] stated that poroelastic rebound dominated the 1992 Landers earthquake. However, each possible mechanism can contribute about the same spatial scale, even though generally viscoelastic relaxation is thought to be in far-field scale and afterslip to be middle-to-near field scale, so the separation of viscoelastic relaxation from other possible mechanisms remains difficult even with high density of geodetic network [Hearn, 2003].

In the Tibetan Plateau, similar work has been done after several greater magnitude earthquakes including the 1997 M_w 7.6 Manyi earthquake [Ryder et al., 1997; Wen et al., 2012; DeVries and Meade, 2013], 2001 M_w 7.8 Kokoxili earthquake [Ryder et al., 2010; Yamasaki and Houseman, 2012; DeVries and Meade, 2013], 2008 M 6.4 Nima-Gaize earthquake [Ryder et al., 2010], and 2008 M_w 7.9 Wenchuan earthquake [Huang et al., 2014]. In a longer time scale, geologic and geodetic data can characterize crustal deformation at different time periods in the earthquake cycles. Hilley et al. [2005, 2009] used GPS measurements and geologic long-term slip rates on the Kunlun fault, to evaluate the crustal viscosity underneath northern Tibetan Plateau. In the geologic time scale (millions of years), the crustal and mantle interior properties would reflect to surface topography. This would allow us to

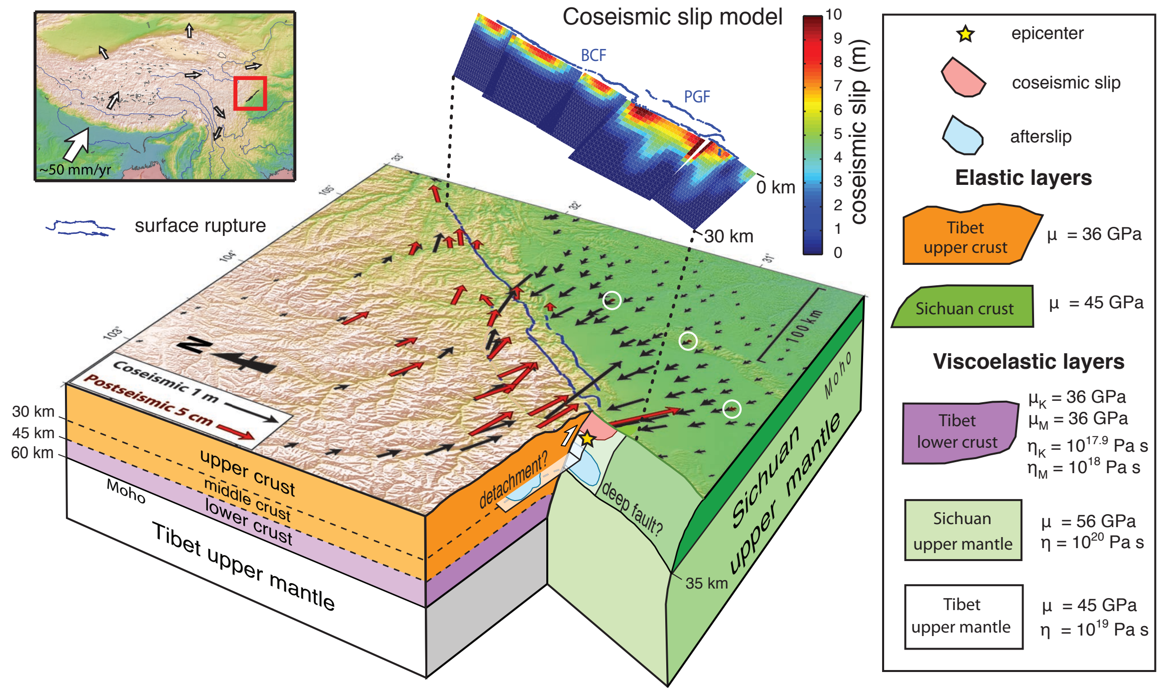

Figure 5.1: Three-dimensional representation of eastern Tibet. The upper left map shows the Tibetan Plateau, and the red square indicates the study area. The black and red arrows in the 3D block diagram are the co- and estimated first year postseismic GPS measurements. The white circles in the Sichuan Basin show stations that have < 5 mm postseismic measurements. The detachment and deep faults are based on Shen et al. [2009] and Qi et al. [2011]. The coseismic slip model is based on inversion of the coseismic GPS displacements. The rheologic properties of the viscoelastic layers are given in the legend.

probe the material and the environmental condition in depth as well as the history of the mountain orogeny. For example, Copley et al. [2011] use a two-layered viscosity structure model to explain the difference in tectonic deformation style between southern and northern Tibet by coupling to the underthrusting Indian crust. Their model requires a high-viscosity lower Tibetan crust below southern Tibet, possibly due to an anhydrous, granulite lithology.

In eastern Tibetan Plateau (Fig. 5.1), Huang et al. [2014] used GPS and InSAR measurements for ∼2-year period of surface displacement following the 2008 M_w 7.9 Wenchuan earthquake. They argued that a weak Tibetan lower crust composed of a bi-viscous Burgers rheology above a relatively stronger upper mantle could explain the far-field postseismic deformation. Based on their best fitting forward model, the transient viscosity is $\sim 4.4 \times 10^{17}$ Pa s and the steady-state viscosity is 10^{18} Pa s. In addition, a stronger Sichuan block with viscosity at least two orders of magnitude higher than the Tibetan lower crust is required to explain much smaller amount (<1 cm in the first 1.5 years) of the postseismic displacement in the Sichuan Basin (Figs 5.2 and 5.3). Near the coseismic surface rupture, they also found shallow (less than 10 km in depth) afterslip on the Beichuan fault. Based on their modeling, they proposed a multiple-mechanism model such that the postseismic deformation is fundamentally driven by viscoelastic relaxation, and shallow afterslip contributes the near-field postseismic deformation. The thickness and viscosity of Tibetan lower crust based on their study is consistent with what has suggested by Clark et al. [2005], Cook and Royden [2008], and Rippe and Unworth [2010] based on dynamic topography, numerical modeling for plateau morphology, and geophysical exploration.

In this study, we focus on using different rheologic models including viscoelastic rheology and power law flow rheology to predict postseismic relaxation after the Wenchuan earthquake. We use 6 years of time series data from 18 continuous GPS stations to test different rheologic models. We use a bi-viscous Burgers model as well as a power law flow rheology including diffusion and dislocation creeps to represent the Tibetan lower crust and upper mantle. For power low flow rheology, we compute effective viscosity as a function of pressure, temperature, grain size, background strain rate, and water content. Modeling postseismic viscoelastic relaxation with effective viscosities calculated from different material and environmental conditions would allow us to compare our result with other approaches in different time scales, including magnetotelluric (MT; e.g. Rippe and Unworth, 2010) and dynamic topography studies (e.g. Clark et al., 2005). Geology in eastern Tibetan Plateau indicates the Pengguan massif as the oldest stratigraphy in eastern Longmen Shan. The Precambrian Pengguan massif is mainly composed of granitic and meta-sedimentary rocks [Burchfiel et al., 1995, 2008] coming from the deeper crust, and hence provides insights to temperature or mineral composition underneath the Tibetan Plateau. Finally, low temperature geochronology dating methods provide surface exhumation information across the Longmen Shan and could reconstruct the orogenic history in eastern Tibet [Wang et al., 2012; Tian et al., 2013].

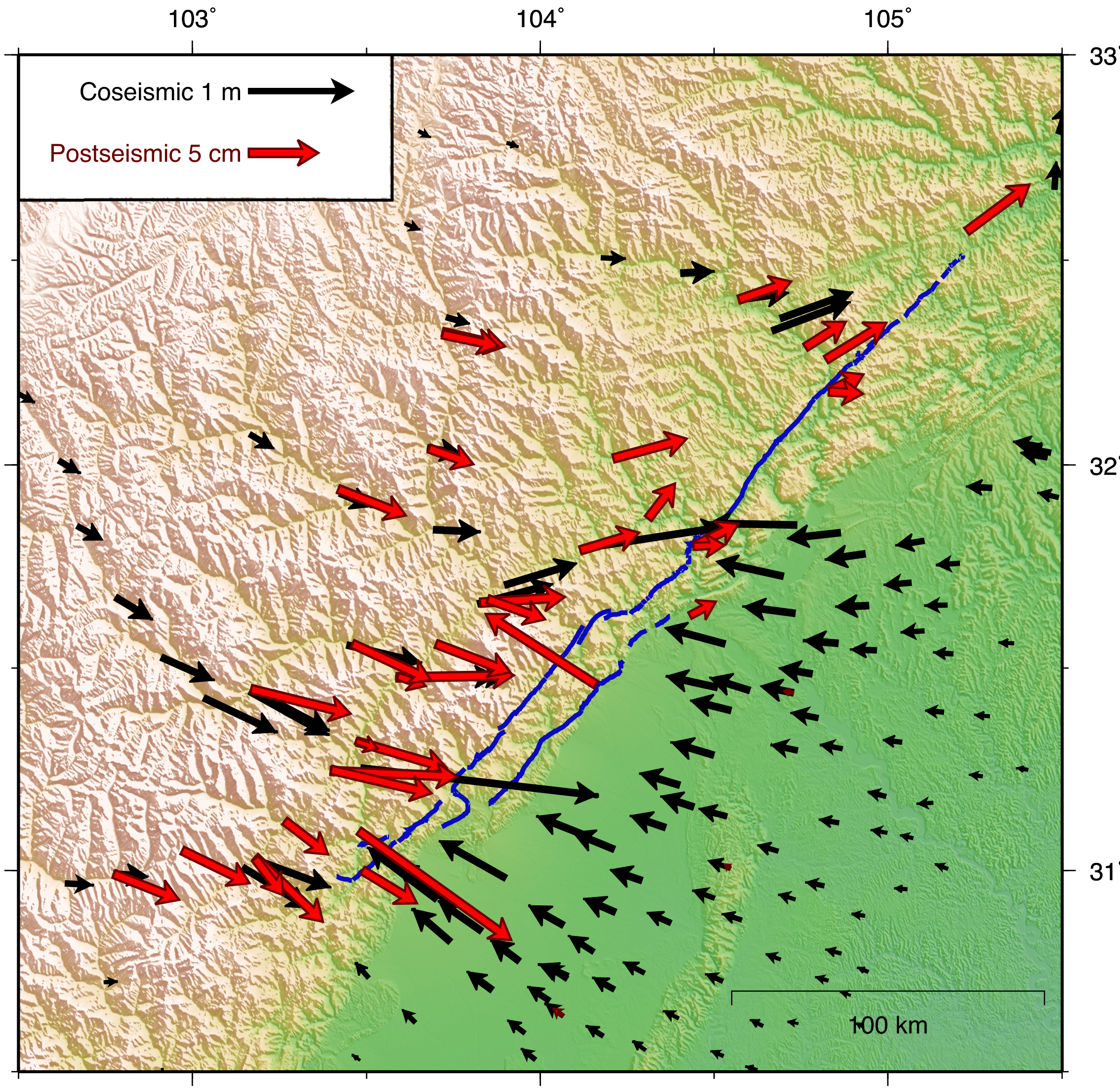

Figure 5.2: Co- and postseismic GPS displacement. The coseismic displacement is based on ∼400 GPS stations [Qi et al., 2011], and the postseismic displacement is based on 38 GPS measurements [Shen et al., 2010].

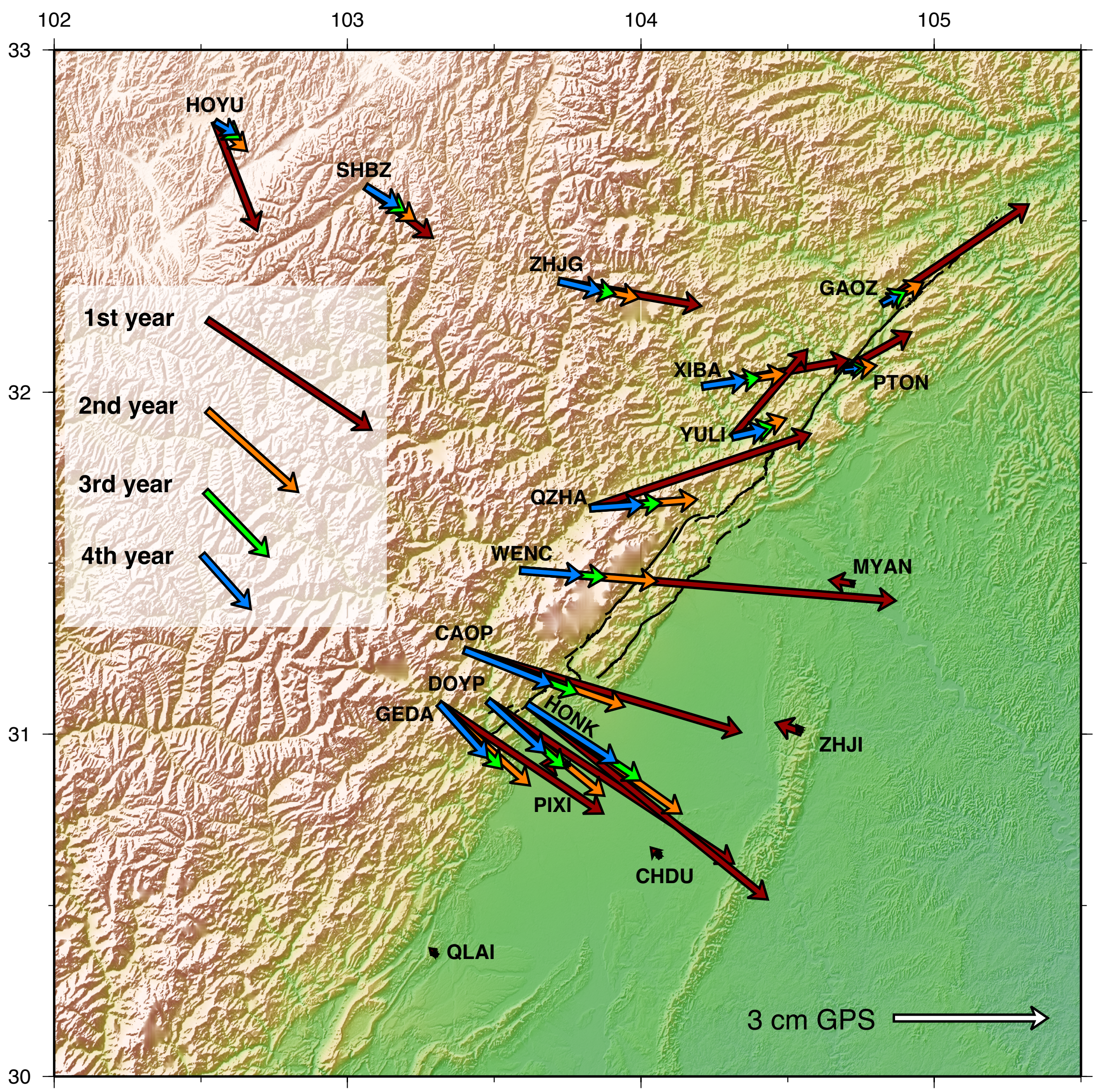

Figure 5.3: Postseismic displacement at different time periods based on 6 years of GPS time series after the Wenchuan earthquake. Red, orange, green, and blue are the 1^{st}, 2^{nd}, 3^{rd}, and 4^{th} year data, respectively. The magnitude and azimuth of each measurement is based on the logarithmic fit (Eq. 5.12) to the GPS time series.

5.3 Viscoelastic models: Maxwell and Burgers rheologies

Simple viscoelastic models with combinations of elastic and viscous elements can explain the postseismic relaxation [Pollitz, 2003; Ryder et al., 2007, 2011; Qi et al., 2012]. To visualize, the viscoelastic model is composed of several springs (elastic) and dashpots (viscous), as illustrated in Fig. 5.4. The most common viscoelastic models are Maxwell fluid and Burgers body. A Maxwell fluid connects a spring and dashpot in series (Fig. 5.4a), so the spring responds to the instantaneous stress change, whereas the dashpot can be accounted for the relaxation to this stress change. The constitutive relation of a Maxwell fluid is,

$$\dot{\varepsilon}_{total} = \dot{\varepsilon}_{spring} + \dot{\varepsilon}_{dashpot} = \frac{\dot{\sigma}}{2\mu} + \frac{\sigma}{2\eta}, \tag{5.1}$$

where $\dot{\varepsilon}$ is the strain rate, σ is stress, μ is shear modulus, and η is viscosity. To solve for the stress distribution for an earthquake like impulse, one can assume a instantaneously strain change ε_o, so stress σ is,

$$\sigma(t) = 2\mu\varepsilon_o e^{-\frac{\mu}{\eta}t}, \sigma(t) = 2\mu\varepsilon_o e^{-\frac{t}{\tau}}, \tag{5.2}$$

where τ is called characteristic relaxation time which describes how rapid the relaxation decays.

As described in (Eq. 5.1), the viscosity of the Maxwell fluid does not change with time. However, in several studies (e.g. Pollitz, 2003; Hetland and Hager, 2005; Ryder et al. 2007, 2011), they found that a Maxwell fluid model fails to explain the postseismic transient deformation that commonly occurred in the first few months following the earthquake. The bi-viscous Burgers body that has two relaxation modes is thus introduced to explain postseismic relaxation. A Burgers model is composed of a Maxwell fluid connected in series with a Kelvin solid (Fig. 5.4b). As derived in Pollitz [2003] and Segall [2010], the strain of a Burgers model is,

$$\varepsilon = \frac{\sigma_o}{2\mu_M} + \frac{\sigma_o}{2\mu_K}\left(1 - e^{-\frac{t}{\tau_K}}\right) + \frac{\sigma_o}{2\mu_M}\frac{t}{\tau_M}, \tag{5.3}$$

where σ_o is the initial stress, η_M and μ_M are the viscosity and shear modulus of the Maxwell fluid, η_K and μ_K are the viscosity and the shear modulus of the Kelvin solid, and $\eta_M = \eta_M/\mu_M$ and $\tau_K = \eta_K/\mu_K$ are the characteristic relaxation times for the Maxwell and Kelvin components, respectively. The strain rate is the time derivative of ε,

$$\dot{\varepsilon}(t) = \frac{\sigma_o}{2\mu_K\tau_K}e^{-t/\tau_K} + \frac{\sigma_o}{2\mu_M\tau_M} = \frac{\sigma_o}{2\mu_M\tau_M}\left(\frac{\mu_M\tau_M}{\mu_K\tau_K}e^{-t/\tau_K} + 1\right), \tag{5.4}$$

and the effective viscosity is the stress (σ) divided by the strain rate ($\dot{\varepsilon}$), i.e.,

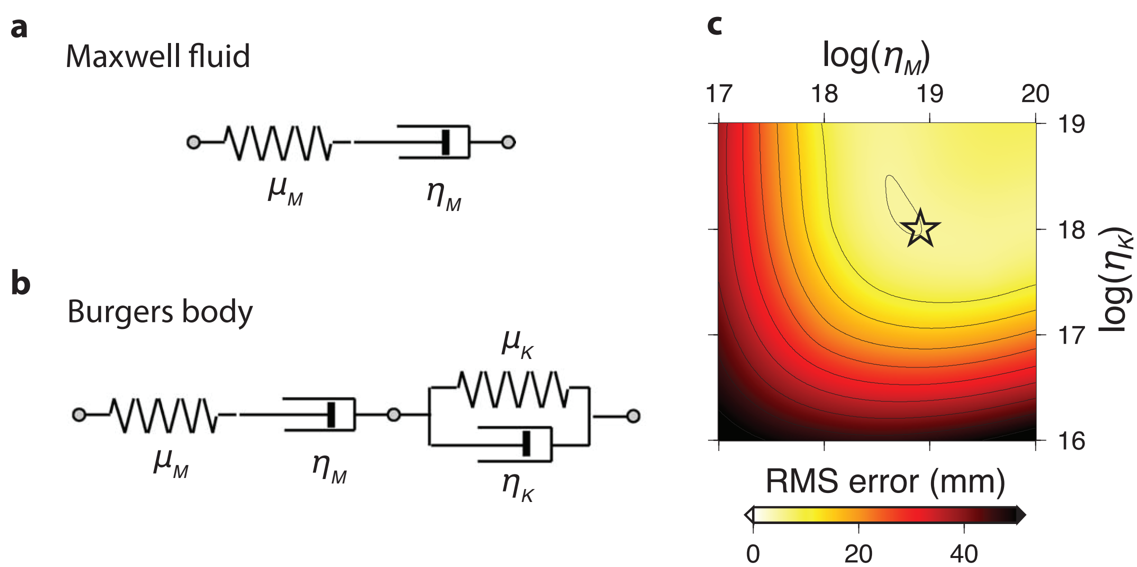

Figure 5.4: (a) A Maxwell fluid model. (b) A bi-viscous Burgers body model. (c) Forward modeling misfits assuming a bi-viscous Burges model for the Tibetan lower crust.

$$\eta(t) = \frac{\eta_M \eta_K}{\eta_M e^{-t/\tau_K} + \eta_K}, \tag{5.5}$$

which is a time dependent function of a combination of the Maxwell and Kelvin viscosities (η_M and η_K, respectively), and the value of $\eta(t)$ is controlled by η_M, η_K, and τ_K. Note that $e^{-t/\tau_K} \to 0$ when $t \to \infty$, so $\eta(t \gg) \approx \eta_M$. In other word, to better describe the long-term effective viscosity (i.e. Maxwell viscosity η_M) we would want to extend our observation as long as possible, otherwise we may underestimate the long-term viscosity.

5.4 Power Law Flow Rheology

The strength and viscosity of earth material is highly dependent on the mineral type and the ambient environmental conditions. Laboratory experiments find that the strain rate of mineral can be described as a function of temperature, background stress, grain size, stress, and water content [Hirth and Kohlstedt, 2003; Karato, 2008]. Each component has a power dependency to the total strength of the material. This can be simplified as a relation between the strain rate and other parameters such as,

$$\dot{\varepsilon} = Ad^{-p}C_{OH}^{r}\sigma^{n}e^{-(Q+PV)/RT}, \tag{5.6}$$

where A is a prefactor (MPa^{-n} s^{-1}), d is grain size (m), p is the grain size exponent, C_{OH} is water content (H/10^6 Si), r is the water content exponent, is the differential stress (Pa), n is the stress exponent, Q is activation energy (J/mol), P is pressure (Pa), V is activation volume (m^3), R is the universal gas constant (J/mol), and T is absolute temperature (°C). For dislocation creep, n is generally between 2.5 and 3.5 and p is 0 (no grain size dependency). For diffusion creep, n is 0 (no stress dependency) and p is generally between 2 and 3 [Karato, 2008; Bürgmann and Dresen, 2008; Freed et al., 2012]. Table 5.1 lists the power law parameters for dry and wet olivine, pyroxene, feldspar, and quartz (after Bürgmann and Dresen, 2008).

By definition, the effective viscosity is stress devided by strain rate, so the effective viscosity can be represented in terms of stress,

$$\eta = \frac{e^{(Q+PV)/RT}}{2Ad^{-p}C_{OH}^{r}}\sigma^{1-n}, \tag{5.7}$$

or in terms of strain rate,

$$\eta = \frac{e^{(Q+PV)/RT}}{2(Ad^{-p}C_{OH}^{r})^{1/n}}\dot{\varepsilon}^{(1-n)/n}. \tag{5.8}$$

For diffusion creep condition, the stress power $n = 1$ so the effective viscosity is independent of stress (the power term of σ is zero in Eq. 5.7). The effective viscosity is then,

$$\eta = \frac{e^{(Q+PV)/RT}}{2AC_{OH}^{r}}d^{p}. \tag{5.9}$$

In diffusion creep, the power term of grain size p is generally between 2 and 3, so plays a major role in this type of flow.

For dislocation creep condition, the power of grain size $p = 0$, so the effective viscosity is dependent on stress,

$$\eta = \frac{e^{(Q+PV)/RT}}{2AC_{OH}^{r}}\sigma^{1-n}, \tag{5.10}$$

where n is generally 2.7 – 5.5 for Earth materials [Bürgmann and Dresen, 2008]. Note that in the condition when $n = 1$ (diffusion creep), this type of flow is called Newtonian fluid, and when $n > 1$ the flow is called non-Newtonian fluid.

To obtain the parameter values in (Eq. 5.6), laboratory experiments simulate different environmental conditions by varying temperature and pressure, to represent different depth range in the lithosphere and their rheologic behavior. However, in the laboratory scale, strain rate of 10^{-4} to 10^{-6} s^{-1} is significantly smaller than that in natural shear zones of 10^{-9} to 10^{-13} s^{-1} [Bürgmann and Dresen, 2008]. In addition, centimeter-scale laboratory specimens are also much smaller than in natural scale and would contain different fracture or structural distributions. As a result, the values obtained from laboratory experiments may not directly apply for geologic conditions by using simple linear extrapolation. Nevertheless, Bürgmann and Dresen [2008] summarized common crustal and upper mantle minerals (olivine, pyroxene, feldspar, and quartz) rheology using the power law flow model based on previous works on different minerals in wet or dry condition under dislocation or diffusion creeps. Section 5.4 would focus on testing creep models under different environmental conditions based on these laboratory explored parameters.

Recent study by Freed et al. [2012] emphasized a possible transient state of the power law flow model to explain the postseismic deformation after the 1999 M 7.1 Hector Mine earthquake. This transient state relates to microcracks and cracks gliding along mineral boundries when a sudden change of applied stress [Karato, 2008]. Freed et al. [2012] modified Eq. 5.6 by adding a transient term similar to the Burgers model (Eq. 5.4). So Eq. 5.6 becomes,

$$\dot{\varepsilon} = Ad^{-p}C_{OH}^{r}\sigma^{n}e^{-(Q+PV)/RT}[1+(\beta-1)e^{-t/\tau}], \tag{5.11}$$

where β represents the ratio between transient and steady state viscosities. Note when $n = 1$ (diffusion creep or Newtonian fluid), Eq. 5.11 is equivalent to Eq. 5.4 because Ad^{-p} C_{OH}^{r} $e^{-(Q+PV)/RT} = \frac{1}{2\mu_M\tau_M}$, β -1 $= \frac{\mu_K\tau_K}{\mu_M\tau_K}$, and $\tau = \tau_K$. So diffusion creep with transient state can directly relate to Burgers model. By knowing the temperature and pressure conditions and the mineralogy of the bi-viscous layer, we can estimate water content and grain size based on the effective viscosity from the best-fitting model.

5.5 Estimating rheologic profile using laboratory rock mechanics data

In this section, we explore the viscosity of the most common crustal mineral – olivine, pyroxene, feldspar, and quartz using power law flow in different environmental conditions. We compare the viscosity under diffusion or dislocation creep with different grain size or background strain rate. We refer the mineral parameters to the list in the supplementary table S1 of Bürgmann and Dresen [2008]. We estimate the mineral rheology using power law flow under different conditions of temperature, pressure, water content, grain size, and strain rate. Table 5.1 lists mineral parameters for olivine, pyroxene, feldspar, and quartz used in this paper, including minerals in dry or wet conditions under diffusion or dislocation creep. Here we discuss viscosity under diffusion or dislocation creep.

5.5.1 Material viscosity under diffusion creep

For diffusion creep, we test mineral viscosity with different temperature, grain size, water content, etc. We use Eq. 5.9 to calculate effective viscosity with these parameters. Earlier work by Huang et al. [2014] shows lower crustal layer with lower viscosity at 35 – 50 km depth under eastern Tibet, so we consider pressure respectively at 50 km and density of rock = 3,000 kg/m^3 [Freed et al., 2012]. The geothermal gradient in eastern Tibet is not well known, so we consider temperature ranged from 700 to 1,000°C, representing temperature for a cold (cratonic environment) to hot (hot continental margins like Mojave Desert in California) continent at about 40 km depth.

Grain size (d) is varied from 10^{-2} to 10^{1} mm, representing the range of plutonic rocks from crust and upper mantle. We test water content (C_{OH}) from 5 (dry) to 3,000 (wet) H/10^{6}Si. Fig. 5.5 shows the viscosity as a function of temperature and grain size using Eq. 5.9 and mineral parameters from Table 5.1. It shows that for all minerals the viscosity is more sensitive to grain size than temperature. This is due to the higher power dependency in grain size (p = 2 – 3). Fig. 5.6 shows viscosity as a function of temperature and water content. In diffusion creep for all minerals, the power term (r) of water content is between 0 and 1.2, so the viscosity is more sensitive to temperature than water content. Note that when $r = 0$, the viscosity is independent of water content.

5.5.2 Material viscosity under dislocation creep

For dislocation creep, we do similar comparison of material viscosity at 50 km depth in different environmental conditions. In this condition, viscosity has power dependency on stress. For crustal and upper mantle minerals, the power of stress (n) is generally between 2.7 and 5.5 [Bürgmann and Dresen, 2008]. We calculate the effective viscosity using Eq. 5.10 for olivine, pyroxene, feldspar, and quartz with different temperature, strain rate, and water content. Fig. 5.7 shows the effective viscosity as a function of temperature and strain rate. We assume the same temperature range as in diffusion creep, and the strain rate is varied from 10^{-15} to 10^{-11} s^{-1}, which is ~0.03 - 316 μ-strain per year. The viscosity of the four minerals seems to be equally depended on temperature and strain rate. Based on Fig. 5.7, under the same environtal condition, olivine and feldspar have higher viscosity than pyroxene and quartz, so for a granitic lower crust the condition for viscosity of 10^{18-19} Pa s requires strain rate = 10^{-14} to 10^{-13} s^{-1} at lower temperature (700 - 850 °C). Fig. 5.8 shows

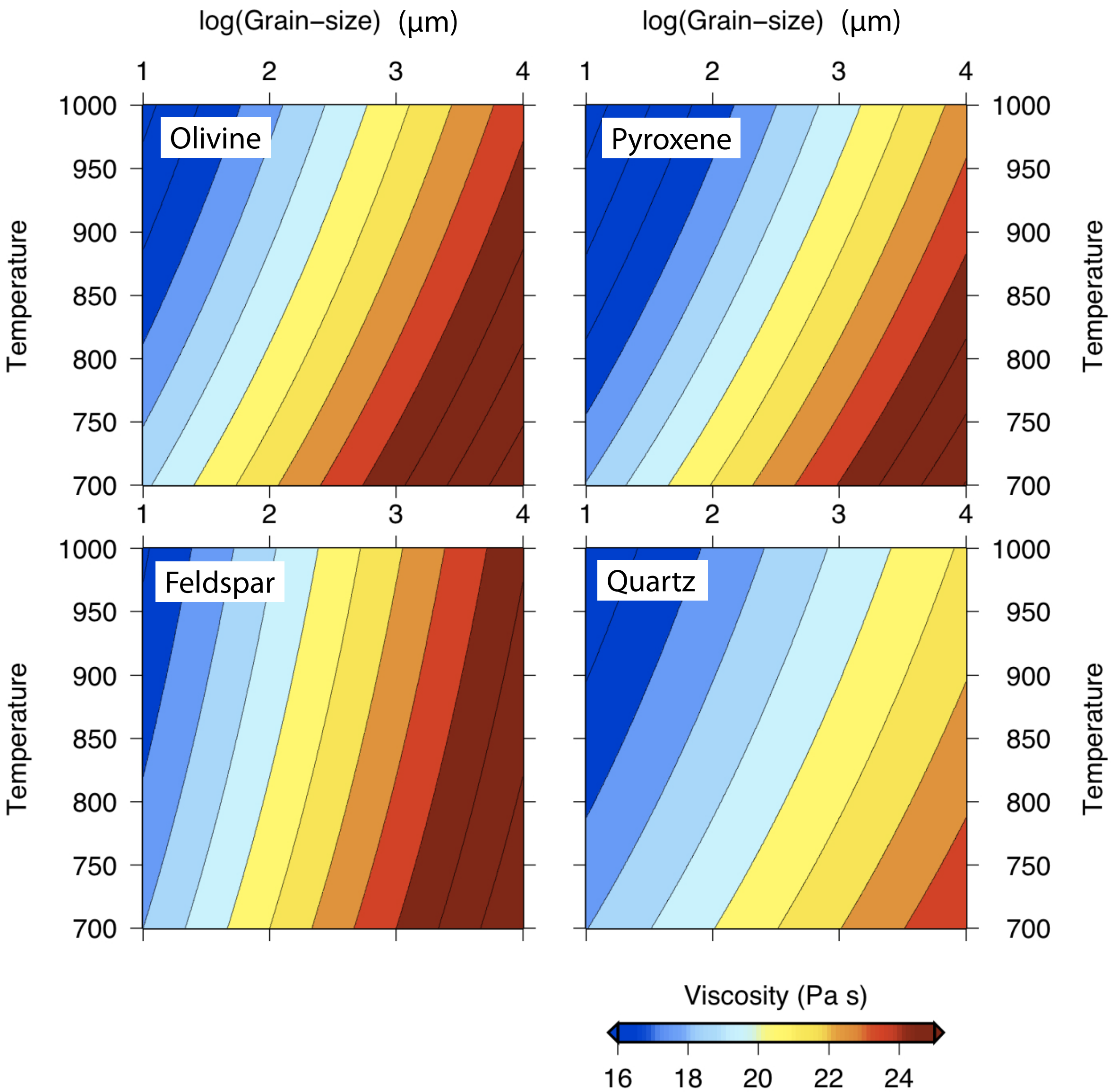

Figure 5.5: Estimated viscosity of olivine, pyroxene, feldspar, and quartz with different conditions of grain size (μm) and temperature (°C) assuming a diffusion creep power law flow model. The water content is assumed 1,000 H/10^6Si and the depth is 50 km. Power law parameters are from Bürgmann and Dresen [2008].

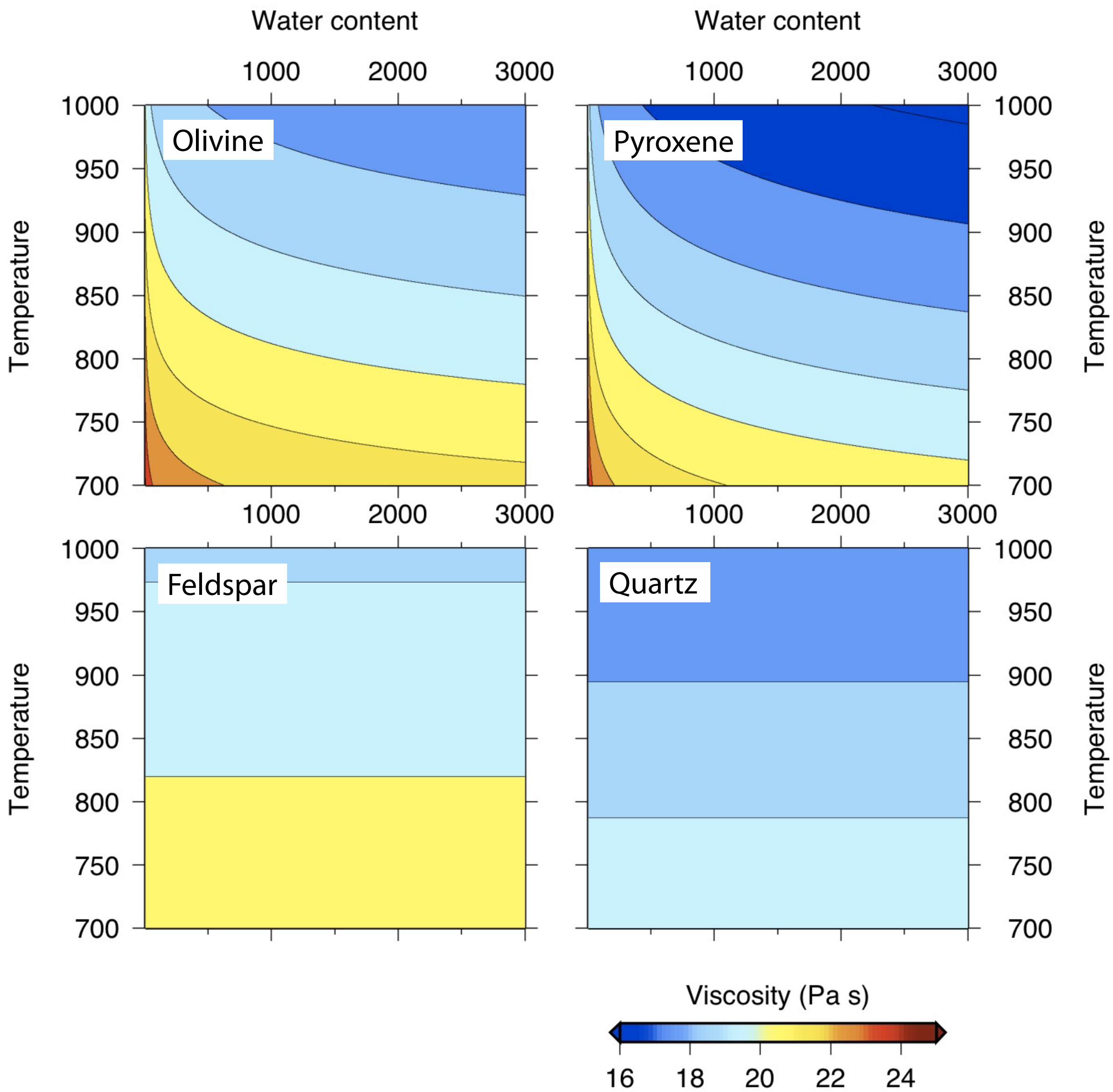

Figure 5.6: Estimated viscosity of olivine, pyroxene, feldspar, and quartz with different conditions of water content (H/10^6Si) and temperature (°C) assuming a diffusion creep power law flow model. The grain size is assumed 10-1 mm and the depth is 50 km. Power law parameters are from Bürgmann and Dresen [2008].

material viscosity as a function of temperature and water content. For feldspar the viscosity is independent of water content because r in Eq. 5.6 is 0 [Rybacki and Dresen, 2000; see Table 5.1]. For quartz, our preferred viscosity requires higher water content (2,000 - 3,000 $H/10^6Si$) when temperature is about 800 °C.

5.6 Geodetic data and the Wenchuan postseismic displacement

5.6.1 GPS data

We use 18 continuous GPS stations, 13 in hanging wall and 5 in footwall collected by Z. Shen. Most of the stations were deployed a few days to ∼3 months after the Wenchuan main shock. In the hanging wall (Longmen Shan), the measurements extend ∼3 – 6 years after the main shock, and ∼1.8 years in the footwall (Sichuan Basin). For most of the hanging wall near field GPS stations, the signal-to-noise ratio in both horizontal and vertical components is high, so we can use all three components (E-W, N-S, and vertical) to compare with the numerical models.

To better describe the postseismic displacement, we fit the GPS data with logarithmic functions with the logarithmic function,

$$D(t) = D_{xo,yo,zo} + D_{x,y,z} ln(1 + t/\tau), \tag{5.12}$$

where $D_{xo,yo,zo}$ is the displacement shift of each GPS record to account for the unknown postseismic displacement between the initiation of postseismic period and the first GPS record. $D_{x,y,z}$ is the amplitude of the postseismic relaxation of each component. Note here the postseismic relaxation refers to the amplitude of relaxation in Eq. 5.12, and is different from the viscoelastic relaxation from crustal or upper mantle. The logarithmic relaxation time (τ) describes the decay of postseismic displacement, and t is the observation time of each GPS record since the initiation of postseismic period.

For data fitting, we have no information between the initiation of postseismic displacement and the beginning of GPS records, so we use (Eq. 5.12) to forward calculate $D_{xo,yo,zo}$, $D_{x,y,z}$, and τ simultaneously based on the minimum misfit between the predicted time series and the GPS time series data. We assume the relaxation time τ can vary in different GPS stations but is the same in the three components of each GPS station. This simple relation does not consider periodic components of the time series such as seasonal groundwater level

Table 5.1: Mineral parameters (after Bürgmann and Dresen, 2008).

Mineral	**logA** **($Mpa^{-n}\mu m^{m}s^{-1}$)**	n	**Q** **(kJ/mol)**	m	r	**V** **(cm^3/mol)**	**Dislocation or diffusion creep**	**Reference**
Olivine (wet)	7.4	1	375	3	1	20	Diffusion	Hirth and Kohlstedt [2003]
Olivine (wet)	3.2	3.5	520	0	1.2	22	Dislocation	Hirth and Kohlstedt [2003]
Pyroxene (wet)	8.1	1	337	3	0	0	Diffusion	Dimanov and Dresen [2005]
Pyroxene (wet)	0.8	5.5	534	0	0	0	Dislocation	Dimanov and Dresen [2005]
Feldspar (wet)	-0.7	1	159	3	1	38	Diffusion	Rybacki et al. [2006]
Feldspar (wet)	0.2	3	345	0	1	38	Dislocation	Rybacki et al. [2006]
Quartz (wet)	-0.4	1	220	2	0	0	Diffusion	Rutter and Brodie [2004]
Quartz (wet)	-11.2	4	135	0	1	0	Dislocation	Hirth et al. [2001]

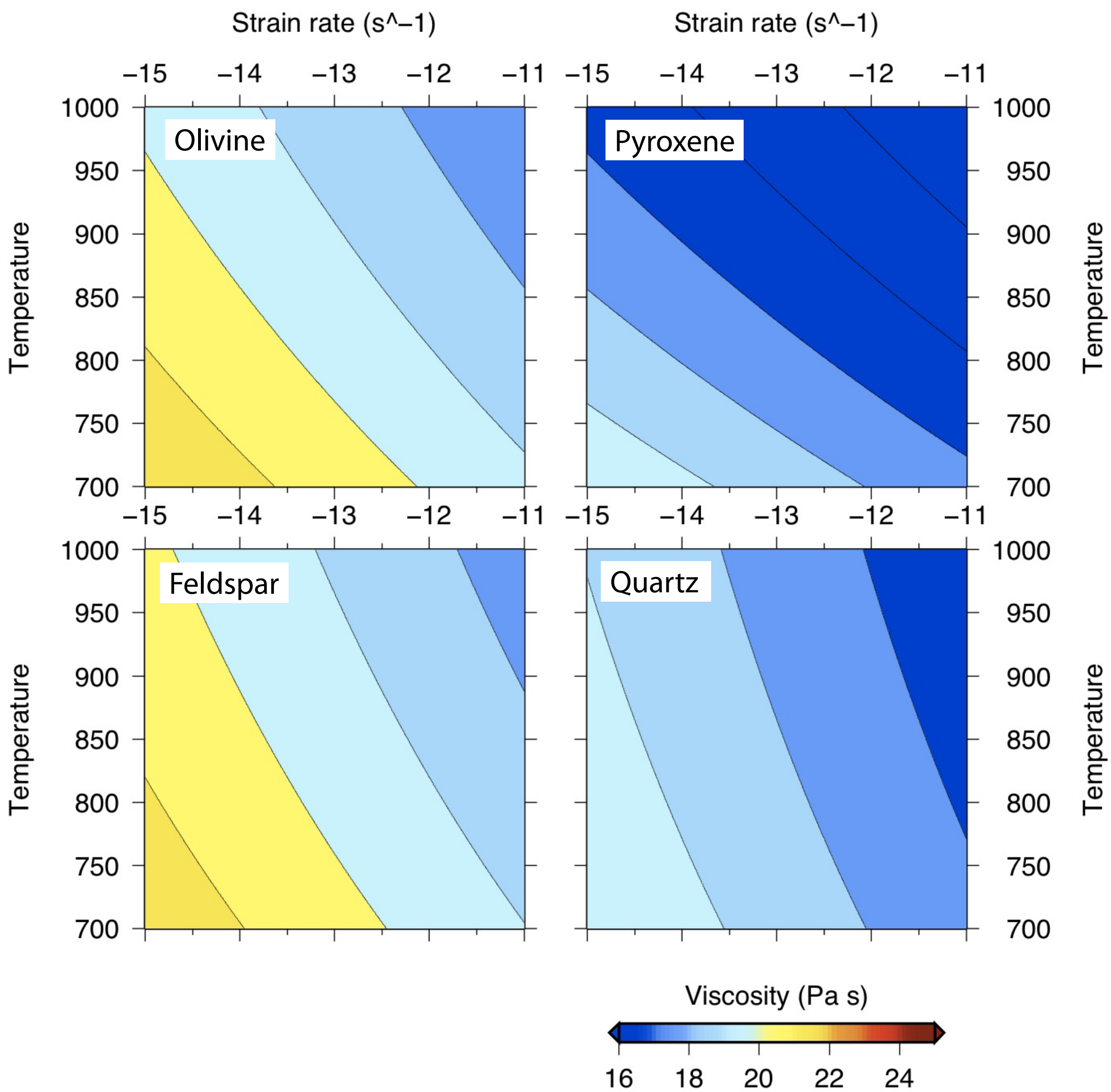

Figure 5.7: Estimated viscosity of olivine, pyroxene, feldspar, and quartz with different conditions of strain rate (s^{-1}) and temperature (°C) assuming a dislocation creep power law flow model. The water content is assumed 1,000 H/10^6Si, and the depth is 50 km. Power law parameters are from Bürgmann and Dresen [2008].

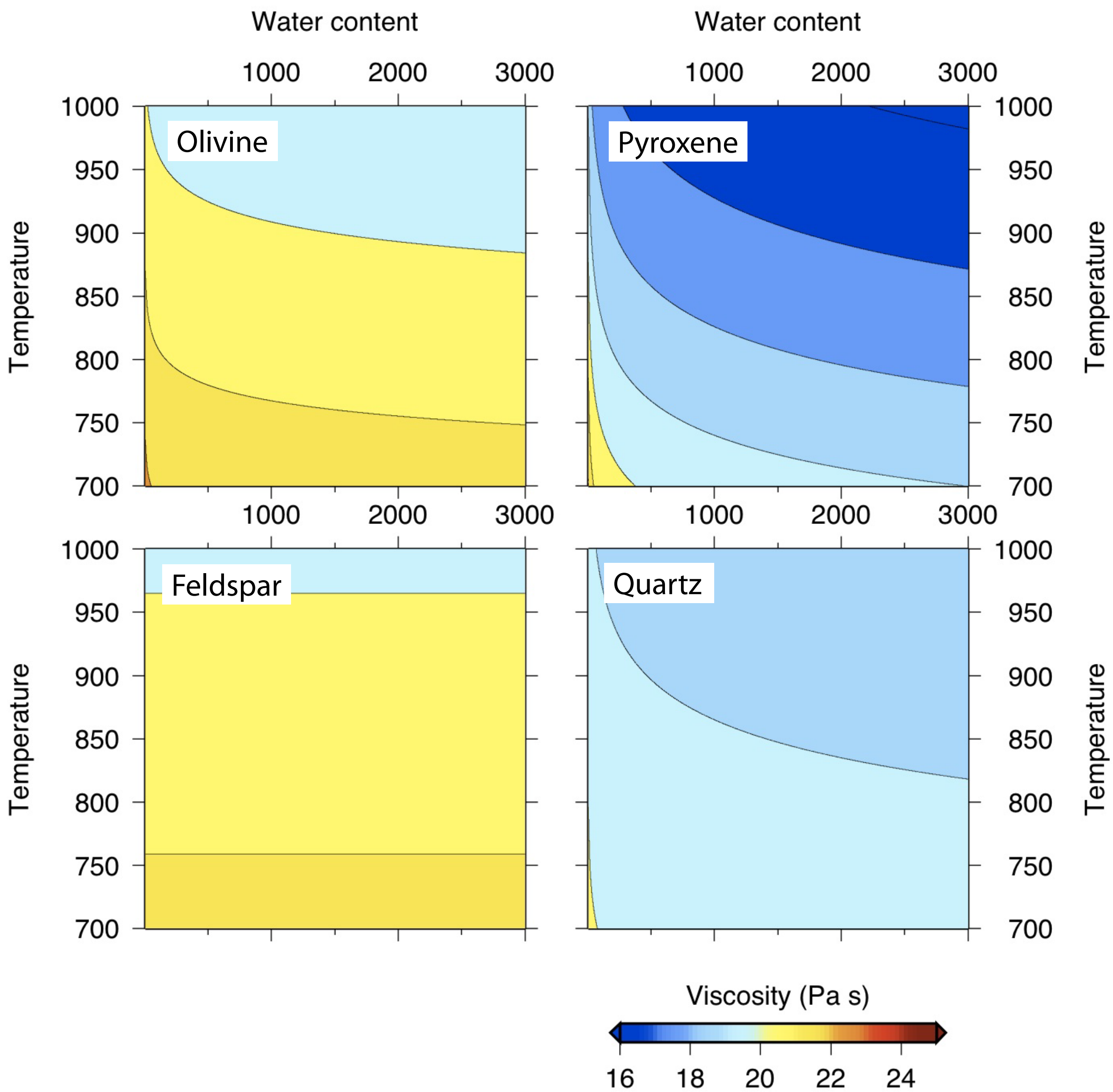

Figure 5.8: Estimated viscosity of olivine, pyroxene, feldspar, and quartz with different conditions of water content (H/10^6Si) and temperature (°C) assuming a dislocation creep power law flow model. The background strain rate is 10^{-14} s^{-1}, and the depth is 50 km. Power law parameters are from Bürgmann and Dresen [2008].

change or annual precipitation.

5.6.2 Postseismic deformation

The GPS measurements following the Wenchuan earthquake show an overall NW-SE convergence in the southern Longmen Shan, transitioning into right-lateral strike-slip motion in the northern Longmen Shan (Fig. 5.2, data based on Shen et al., 2009 and Ding et al., 2013). The first-order patterns of the co- and postseismic displacements are similar (Fig. 5.2), but the peak postseismic motions occur about 40 km NW from the surface rupture, where the greatest coseismic displacements were found [Shen et al., 2009]. Compared with the coseismic deformation, the spatial wavelength of the postseismic deformation is much greater. In the footwall (to the SE of the fault), most of the displacements in the Sichuan Basin are toward the NW, but with much smaller amplitude ($<$ 5 mm in the first year) than in the hanging wall (Fig. 5.1).

Eighteen continuous GPS stations show Wenchuan postseismic displacement west (hanging wall or eastern Tibet) or east (foot wall or Sichuan basin) of the Longmen Shan (Fig. 5.3). The GPS stations in the west side generally collect daily position solutions between 2008.5 and the end of 2009. In the Sichuan basin, we obtain 5 GPS stations with $\sim$2 years time series. In eastern Tibet, there are 13 GPS stations with 3 – 5 years long observations. Secular motion in eastern Tibet and the Sichuan basin has been subtracted from all of the GPS time series using the interseismic model based on Shen et al. [2005]. The red, orange, green, and blue arrows in Fig. 5.3 represent postseismic displacement in the first, second, third, and fourth year, respectively. In the hanging wall northeast of the Longmen Shan, all of the stations move toward northeast, and move toward southwest in the southwest of the Longmen Shan. In the far-field region (more than 100 km far away from the fault surface rupture), the stations from west to east move from southeastward to almost eastward. However, for stations SHBZ and HOYU, there is no measurement in the first year postseismic displacement so the first year postseismic displacement of the two stations is based on extropolations. In the footwall, all of the GPS stations move toward northwest and the first year postseismic displacement are all smaller than 1 cm.

In the Sichuan basin, the GPS data reveal $<$ 1 cm postseismic displacement in horizontal in the first 2 years. This value is essentially smaller than the seasonal variation in the Sichuan basin. In vertical displacement, most GPS stations (CHDU, QLAI, MYAN, and ZHJI) show 1.5 - 2 cm land subsidence in the first 2 years, even though the vertical component has strong seasonal change. These four Sichuan basin stations are all roughly 100 km away from the Wenchuan coseismic surface rupture, except station PIXI which is less than 10 km to the surface rupture shows uplift (about 1 cm) motion. Note that the uplift motion of station PIXI in the postseismic period is different from its coseismic subsidence (see the supplementary information in Qi et al., 2011).

In northeastern Longmen Shan, all of the GPS stations show a northeastward motion and the amplitude is 3 - 8 cm in 5.5 years (Fig. 5.3). In vertical it is generally 1 to 5 cm uplift. In central and southwestern Longmen Shan, there is a transition of horizontal displacement from northeastward to southeastward displacement. The amplitude of horizontal displacement near central Longmen Shan (stations QZHA, WENC, and CAOP) reaches 15 cm in 5 years. The horizontal displacement stays high in the southwestern Longmen Shan (> 8 cm) and is different from northeastern Longmen Shan. For vertical component, all GPS stations show 0 - 15 cm displacement in 5 years. For stations WENC, CAOP, and QZHA, the amplitude of the vertical displacement is about the same scale as of the horizontal displacement.

In the far-field region (stations ZHJG, SHBZ, and HOYU), all stations move southeastward with about 7 cm in the first 5 years. Similar to Shen et al. [2010] and Huang et al. [2014], the amount of postseismic displacement does not decay as rapidly as in coseismic displacement (Fig. 5.2).

5.7 Model setup

Earlier work by Huang et al. [2014] shows the evidence of transient and steady state viscosities, so here we start our initial model with using the bi-viscous Burgers rheology (Eqs 5.4 and 5.5) for the Tibetan lower crust. In addition, we apply power law flow model to construct viscosity profile in depth based on different environmental conditions such as pressure, temperature, and background strain rate, as well as material properties. In the following subsections we would describe the model setup, geometry, stress input, and the estimation of the viscosity in depth.

5.7.1 3D FEM model

We use the finite element model code Abaqus 6.12 (`http://www.simulia.com/products/abaqus_fea.html`) to construct a 3D geologic structure to better represent the lateral heterogeneity between eastern Tibet and the Sichuan Basin. This model extends 1,600 km in the horizontal dimension with the coseismic surface rupture at the center, and vertically to a depth of 1,000 km (Fig. 13a and b), so the fixed boundaries do not significantly affect the coseismic stress change and the relaxation. The fault geometry and the coseismic slip distribution are based on Shen et al. [2009] with some slip adjustments to accommodate the difference between 1D homogeneous and 3D heterogeneous models. Seismic tomography [Li et al., 2009] and receiver function studies [Zhang et al., 2009] inform the first-order geologic

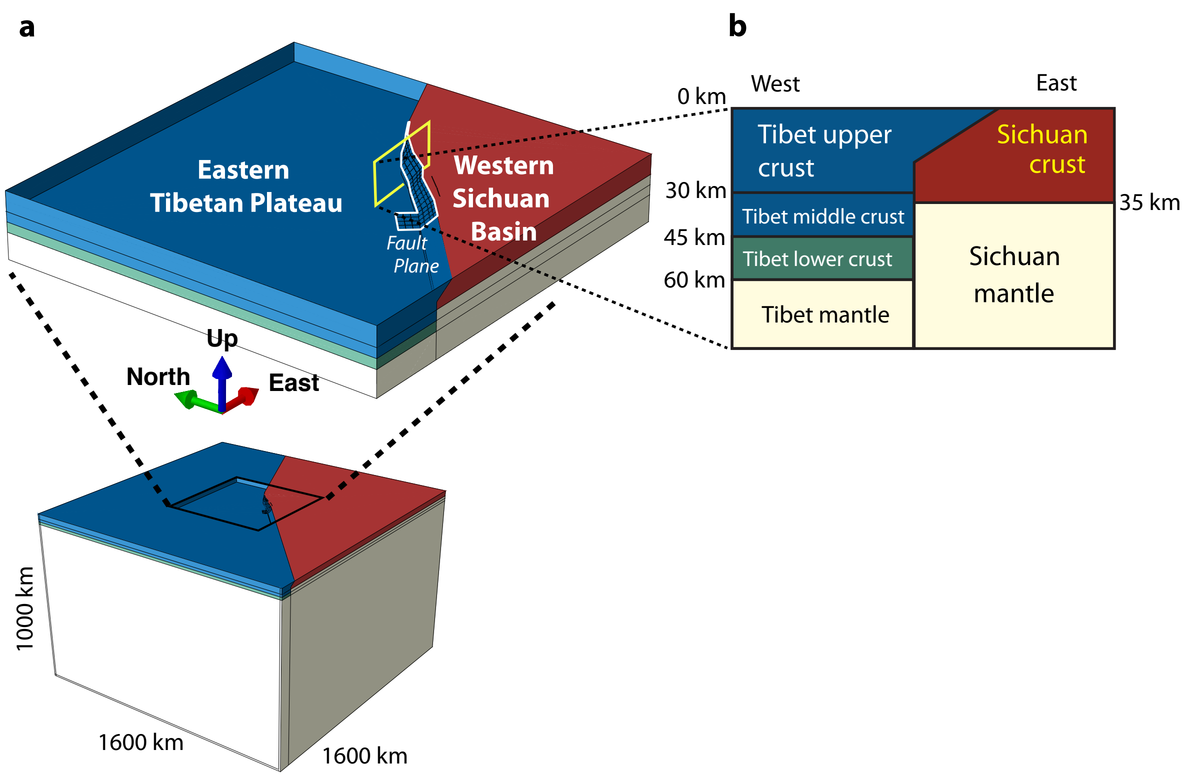

Figure 5.9: Model setup using 3D finite element modeling.

structure. On the Sichuan side, the entire 35-km-thick crust is assumed elastic overlying a viscoelastic upper mantle. On the Tibetan side, the upper crust (0 – 30 km) is elastic. We assume that either the middle (30 – 45 km) or the lower (45 – 60 km) crust is viscoelastic (Fig. 13b), and we vary the viscosity for either layer to fit the geodetic observation. Note, the middle crust is assumed elastic when considering a viscoelastic lower crust and vise versa. The Tibetan upper mantle is also assumed viscoelastic. For the boundary conditions we fix all walls on the sides and the bottom, and do not apply any boundary condition on the surface. The initial stress is based on the coseismic fault slip on the Beichuan fault and the Pengguan fault. The coseismic slip distribution is calculated based on the inversions of coseismic GPS measurements collected and processed by [Qi et al., 2011].

5.7.2 Elastic and viscoelastic layers

We assume that the Tibetan upper crust (0 – 30 km depth) and the entire Sichuan basin crust (0 – 35 km depth) are elastic. The elastic moduli (we use Young's Modulus and Poisson's ratio to represent isotropic materials) are based on laboratory experiments for granite and sandstone, representing Tibetan upper crust and Sichuan crust, respectively [Huang et al., 2014]. The Sichuan mantle is assumed viscoelastic using Maxwell rheology (Eq. 5.2) and the viscosity is 10^{20} Pa s, following previous work by Huang et al. [2014]. For Tibetan middle to lower crust, we try different approaches: [1] Assume the Tibetan middle crust as elastic and lower crust as a bi-viscous Burgers rheology (Eq. 5.4) based on Huang et al. [2014]. We vary the transient and steady state viscosities (η_K and η_M, respectively) and compare with the GPS time series measurements. The Tibetan upper mantle is assumed viscoelastic and the viscosity is 10^{19} Pa s based on Huang et al. [2014]. [2] We derive the viscosity of Tibetan middle-to-lower crust and upper mantle using power law flow rheology. Section 5.6.3 describes the detail in terms of the derivation of viscosity for different minerals and conditions.

5.7.3 Power law flow rheology

As described in Section 5.4, we can estimate the material viscosity by calculating the mineral type and properties, and the environmental conditions using power law flow equations. We assume the Tibetan upper mantle is mainly composed of wet olivine [Hirth and Kohlstedt, 2003; Karato, 2011; Freed et al., 2012], and the Tibetan middle-to-lower crust is mainly composed of quartz (see Section 5.8.4 for discussion of linking regional geology to inferred rock type in deeper crust). The transition zone is located at Moho, which is about 50 km depth [Zhang et al., 2009]. We use the flow law parameters from the laboratory experiments for wet olivine done by Hirth and Kohlstedt [2003], for wet pyroxene (diopside) by Dimanov and Dresen [2005], and for wet quartz by Rutter and Brodie [2004] (Table 5.1).

For diffusion creep, the system behaves as a Newtonian fluid ($n = 1$), so we can simply use flow law parameters in Eq. 5.11 and then calculate the effective viscosity. For dislocation creep, the effective viscosity varies with transient stress change (i.e. the coseismic slip in the Wenchuan main shock), so we first do not consider the transient viscosity (η_K in Eq. 5.5). In the following subsections we describe how we determine the geothermal gradient and the background strain rate. Even though the geothermal gradients are relatively well studied in southern Tibet (e.g. Chen et al., 1996; Mechie et al., 2004; Wang et al., 2013), such data in eastern Tibet are relatively sparse. Several borehole data constrain the thermal gradient in the shallower depth [Xu et al., 2011], but the temperature in the deeper part of eastern Tibet is still unknown. Godard et al. [2009] proposed a range of possible geothermal gradients for southern, northern, and eastern Tibetan Plateau near the adjacent low elevation basins.

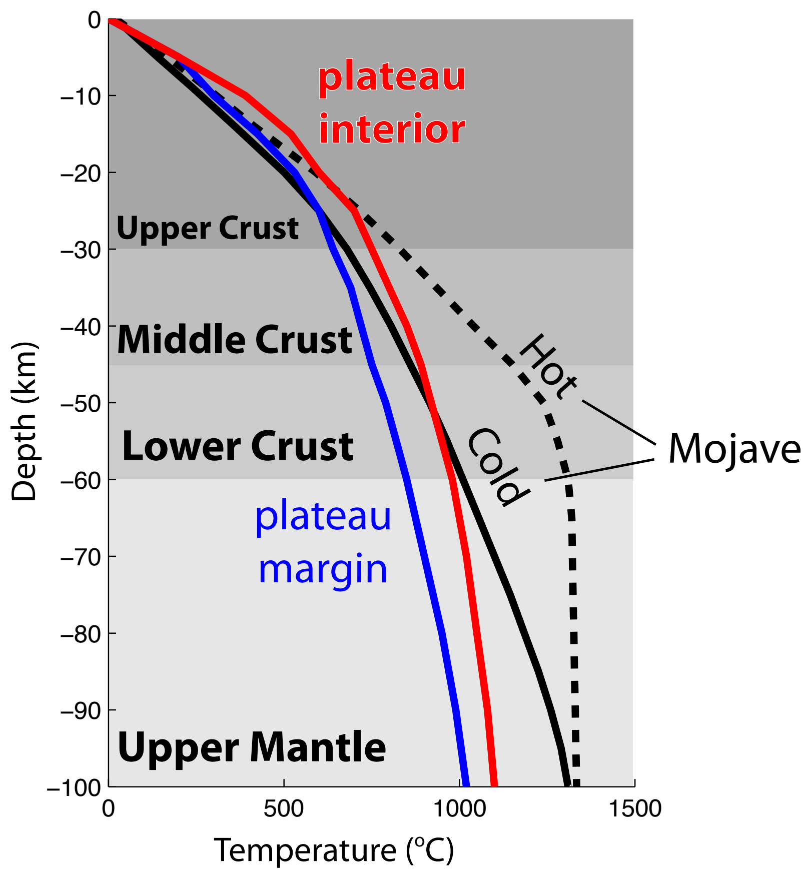

Figure 5.10: Geothermal gradients used in this study. The blue and red represent geothermal gradient at the plateau margin and 100 km away from the margin, respectively [Godard et al., 2009]. The solid and dashed black lines are based on the cold and hot geothermal gradients in Mojave Desert proposed by Freed et al. [2012].

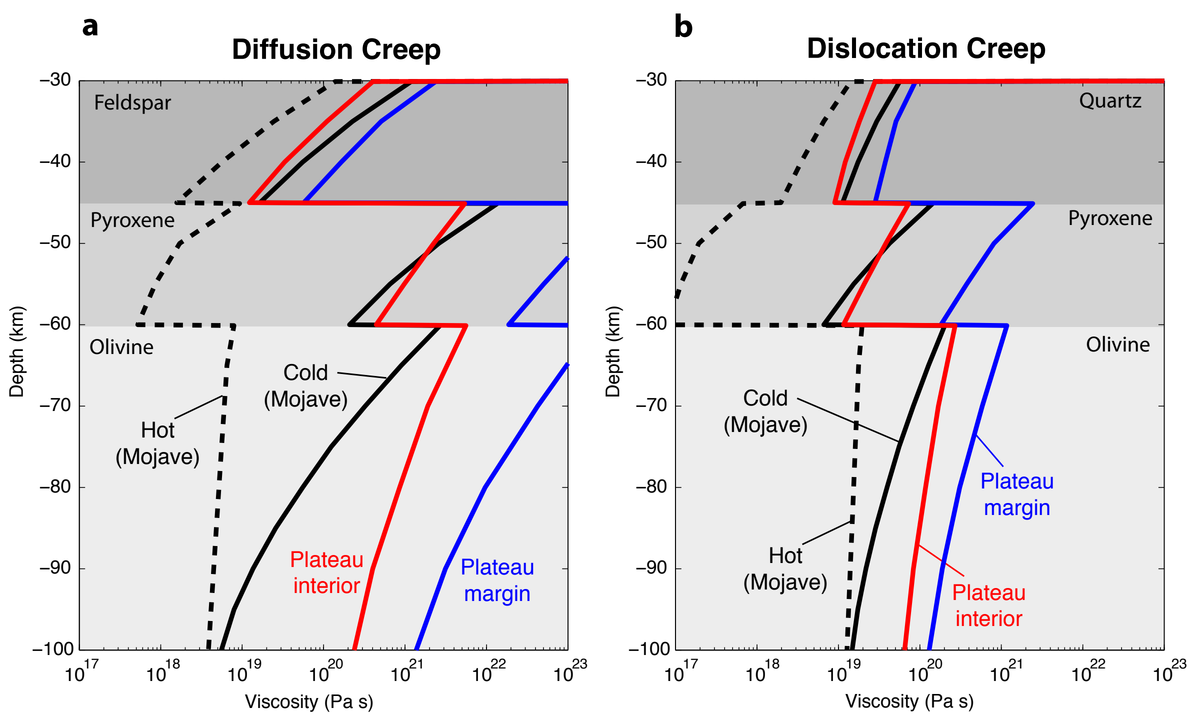

Figure 5.11: Viscosity as a function of temperature for (a) diffusion creep and (b) dislocation creep. Note that the power term (n) is 3.5 and the background strain rate is 10^{-6} yr^{-1} for the dislocation creep. The temperature of each depth is based on Fig. 5.10.

They imposed a constant temperature of 15 °C at the surface and a constant heat flow of 10 MW m^{-2} at the base of the model. In their thermal model, the temperature near the margin of the plateau at 50 km is about 700 °C and 800 °C about 100 km away from the plateau margin (Fig. 5.10). In Section 5.4, we find trade-offs between temperature versus grain size in diffusion creep and temperature versus background strain rate, so we cannot resolve temperature in depth solely from postseismic deformation data. For calculating viscosity profile, we use the geothermal gradients at plateau margin and 100 km away from the margin proposed by Godard et al. [2009], and we also consider the cold or hot geothermal gradients tested for Mojave Desert [Freed et al., 2012]. Fig. 5.10 shows all of the geothermal gradients used in this study.

Fig. 5.11a shows the viscosity profiles under diffusion creep with considering a middle crust (30 – 45 km) composed of wet feldspar, a lower crust (45 – 60 km) composed of wet pyroxene, and a upper mantle (below 60 km) composed of wet olivine. The mineral grain size for this setup is fixed in 4 mm, 1 mm, and 2 mm for middle crust, lower crust, and upper mantle, respectively (see Section 5.9.2 for the discussion). All of the minearl parameters are based on Table 5.1, so the four profiles in Fig. 5.11a show the difference in viscosity with different geothermal gradients. Fig. 5.11b shows the viscosity profiles under dislocation creep with the same geometric setup. Here we assume the background strain rate is 10^{-6} yr^{-1} in middle and lower crust and 10^{-7} yr^{-1} in upper mantle, so the viscosity only varies with different geothermal gradients.

5.8 Model result

5.8.1 Burgers rheology

We follow the model setup as in Huang et al. [2014] and test for Wenchuan postseismic GPS time series data. The Tibetan upper mantle and Sichuan upper mantle are fixed as 10^{19} and 10^{20} Pa s, respectively. In Tibetan lower crustal layer, we allow the steady state (Maxwell, η_M) viscosity to vary from 10^{17} to 10^{20} Pa s, and the transient (Kelvin) viscosity to vary from 10^{16} to 10^{19} Pa s. We calculate the model misfit of each time step for each GPS station for each component. The misfit is calculated as,

$$\chi^2 = \frac{1}{3NM} \sum_{k=1}^{M} \sum_{i=1}^{N} \sum_{j=1}^{3} \frac{(o_{k_{i,j}} - m_{k_{i,j}})^2}{\sigma_{i,j,k}^2}, \tag{5.13}$$

where $o_{ki,j}$ is the j^{th} component of the i^{th} time step for the k^{th} GPS observation, and $m_{ki,j}$ is the j^{th} component of the ith time step for the k^{th} model prediction. $\sigma_{i,j,k}$ is the standard deviation of the j^{th} component of the i^{th} time step for the k^{th} GPS observation.

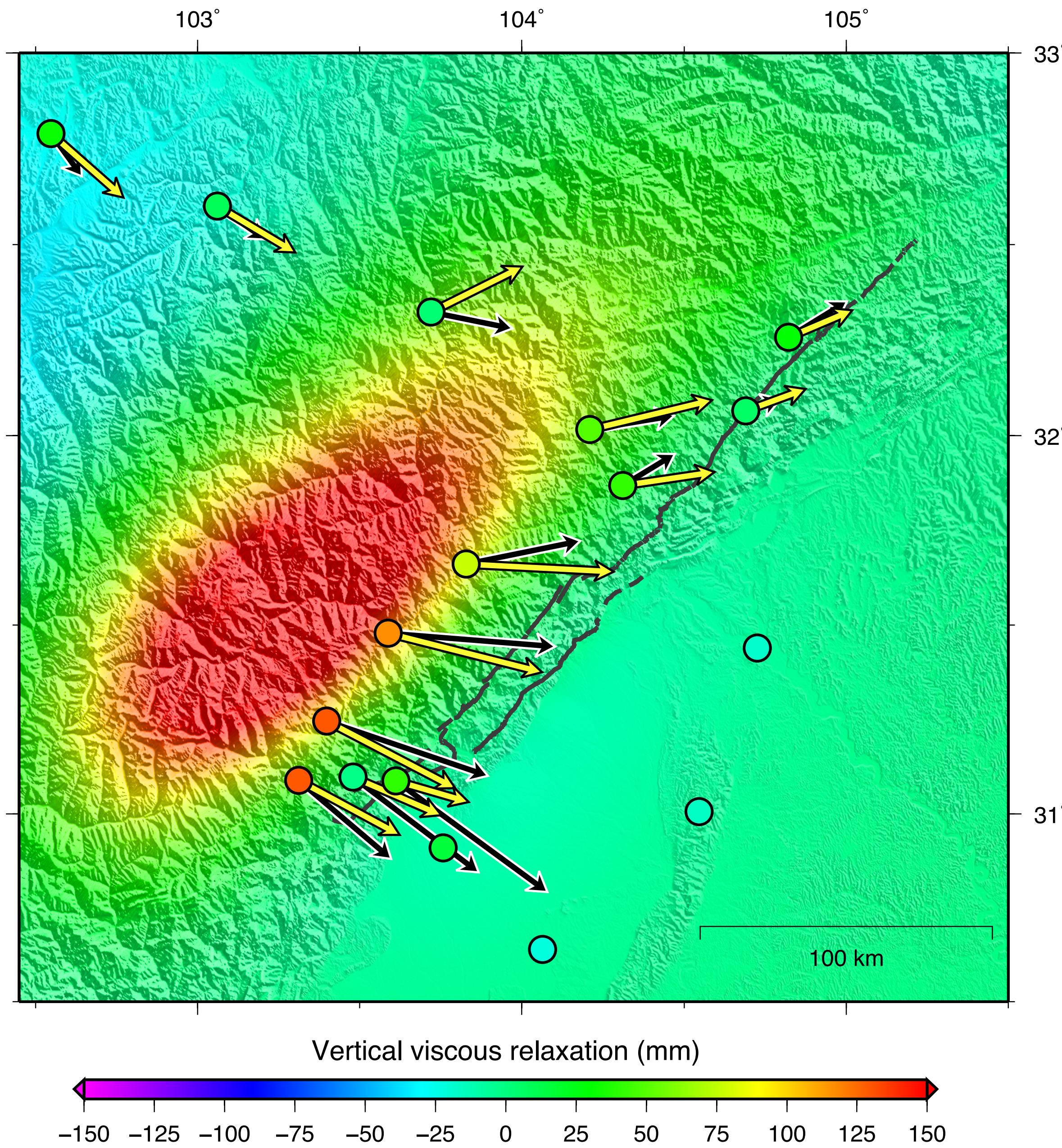

Figure 5.12: The predicted viscoelastic relaxation using a bi-viscous Burgers model.

Fig. 5.4c shows the model misfit with different transient (Kelvin solid, η_K) and steady state (Maxwell fluid, η_M) viscosity combinations in Tibetan lower crust. The forward results prefer a Tibetan lower curst with steady-state viscosity as 10^{19} Pa s and transient viscosity as 10^{18} Pa s. The transient viscosity estimated using the 6-year-long GPS data is about the same as estimated in Huang et al. [2014], but the steady-state viscosity is about 10 times higher.

5.8.2 Diffusion creep power law flow model

We consider the Tibetan upper mantle composed of wet olivine, and feldspar and pyroxene for the middle-to-lower crust (Fig. 5.11). As described in Section 5.3, a diffusion creep with transient creep is equivalent with a Burgers rheology (Eq. 5.11), so we can refer the Burgers rheology (Section 5.7.1) by using power law parameters to compute the steady-state viscosity (η_M) and β for the transient visocsity (η_K). Previous study by Huang et al. [2014] shows that the lower crustal layer between 45 and 60 km dominates the postseismic relaxation. Here we consider varying the middle crust, the lower crust, and the upper mantle viscosity to generate a lithospheric viscosity profile, and use these values as the steady-state viscosity (η_M) with a fixed transient viscosity as 10^{18} Pa s based on the result in Section 5.8.1. Eq. 5.9 shows the parameters that could change the effective viscosity: Grain size, temperature, and water content. We test power law flow relaxation with different geothermal gradients (Fig. 5.10), and estimate the viscosity using different water contents and grain size. We assume the upper mantle made of olivine, and consider quartz, feldspar, and pyroxene as major crustal minerals. Within the range of grain size as 0.1 mm and above, we find that a middle crust made of wet feldspar and a lower crust made of wet pyroxene can better obtain viscosity in the range of 10^{19-21} Pa s. Note that based on the power law flow model, the effective viscosity is the lowest at the base of the mineral layer due to the increase of temperature (Fig. 5.11). Based on a series of tests with different grain size and water content in the middle-to-lower crust, Fig. 5.13 shows the best fitting forward model when the grain size for the middle crust is 4 mm, 1 mm for lower crust, and 2 mm for upper mantle. The water content is 1,000 $H/10^6Si$ for middle-to-lower crust and 100 $H/10^6Si$ for upper mantle. As a result, the best fitting model (Fig. 5.13) shows that a weaker middle and a relatively stronger lower crust can best explain the GPS data. This result is different from Huang et al. [2014] and the result in Section 5.8.1.

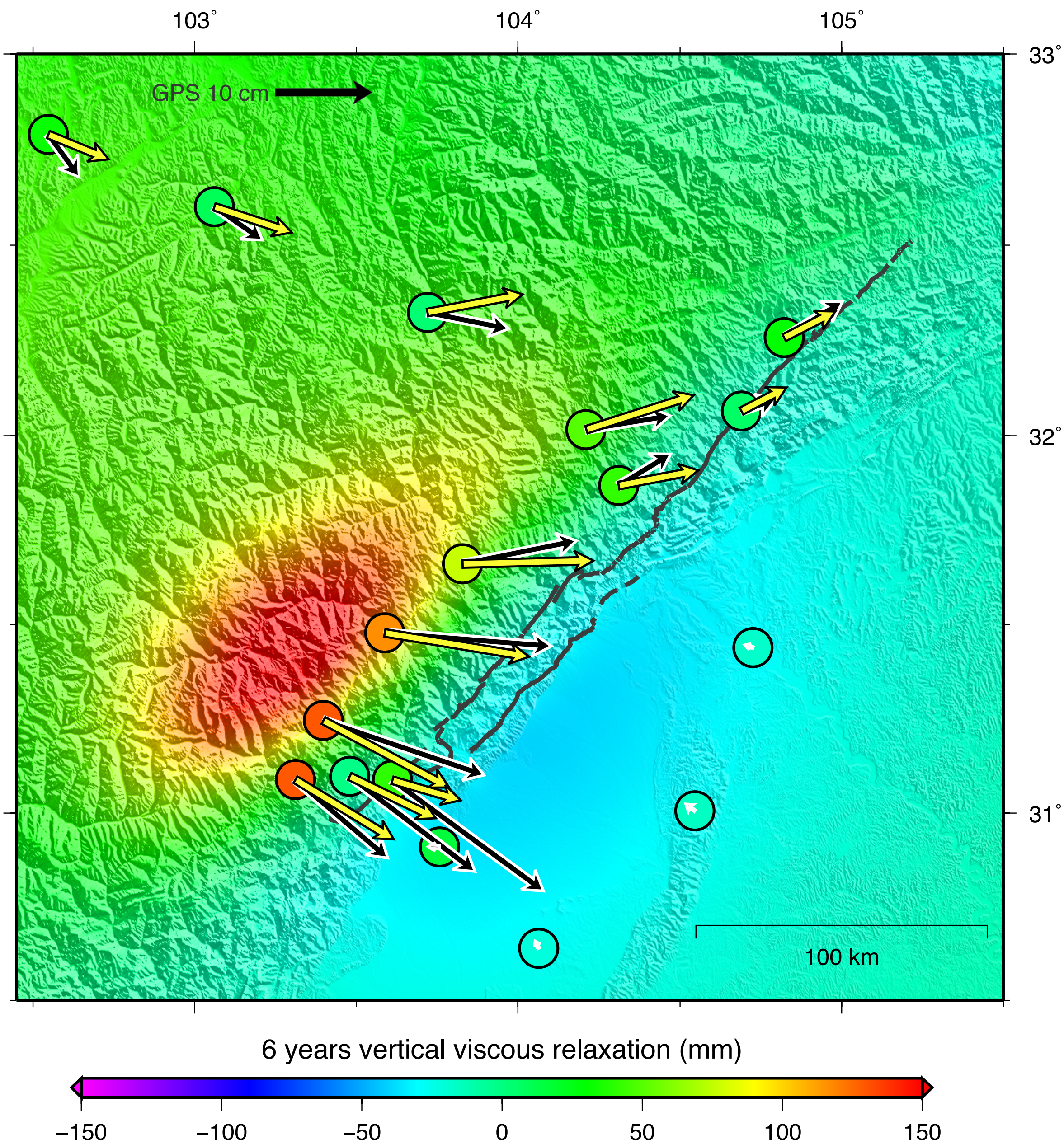

Figure 5.13: The preferred viscoelastic relaxation prediction assuming diffusion creep.

5.9 Discussion

5.9.1 Bi-viscous model fitting

Earlier work by Huang et al. [2014] using InSAR time series for the first 1.5 years shows that the transient viscosity of 4.4×10^{17} Pa s and steady-state viscosity of 10^{18} Pa s can fit the InSAR time series data well. In this study, with longer time scale and broader spatial coverage (Fig. 5.3), the transient viscosity is about 10^{18} Pa s and the steady state viscosity is about10^{19} Pa s. Fig. 5.14 shows different effective viscosity with different transient viscosity and steady state viscosity as a function of time (Eq. 5.5). In this figure, red line is the effective viscosity of the best fitting model by Huang et al. [2014], and the blue line shows the effective viscosity of the best fitting model in this study. The effective viscosity of both models is different by about a factor of 2 right after the main shock and 5 about 1.5 years later.

In Eq. 5.11, β describes the ratio between transient and steady state viscosities (β -1 = $\frac{\mu_K \tau_K}{\mu_M \tau_K}$). For postseismic with considering Burgers model, β is generally between 4 and 30 (4 – 10 for the 1999 M 7.6 Izmit and M 7.2 Düzce earthquakes, Hearn et al., 2009; 28 for the 1999 M 7.1 Hector Mine and the 2002 M 7.9 Denali earthquakes, Pollitz, 2003, 2005; 23 for the 2001 M 7.8 Kokoxili earthquake, Ryder et al., 2011). Similar with the result of Huang et al. [2014] using InSAR time series during 2008.5 - 2009, the steady-state viscosity of 10^{18} Pa s can fit geodetic data the best. However, the 2008.5 - 2014 time series prefers the transient viscosity about an order lower than the steady-state viscosity (in this case, 10^{18} to 10^{19} Pa s). This finding is of about the same order as most of the postseismic studies (e.g. 4 – 10 Hearn et al. 2009; 28 in Pollitz, 2003; 11 times in Ryder et al., 2011; 23 times in Freed et al., 2012).

5.9.2 Power law flow model fitting

In this type of modeling, the viscosity varied with depth instead of a single value for lower crust or for upper mantle. Besides, both Tibetan middle-to-lower crust and upper mantle are bi-viscous. The diffusion creep model produces similar result as the Burgers rheology, and the grain size of 2 mm for middle crust and 1 mm for lower crust, and water content of 1,000 H/10^6Si in the granitic Tibetan lower crust can explain postseismic deformation well. In this result, the upper mantle is composed of olivine with the grain size of 2 mm and water content of 200 H/10^6Si. At Moho depth, the change of material would produce a viscosity contrast up to an order of 4 (Fig. 5.11). Also similar to bi-viscous model test, the transient to steady state viscosities ratio $\beta = 11$. The model results show that the lowest viscosity in the lower crust dominates the postseismic surface displacement, and the depth of this lowest viscosity determines the spatial pattern of the surface displacement [Huang et al., 2014].

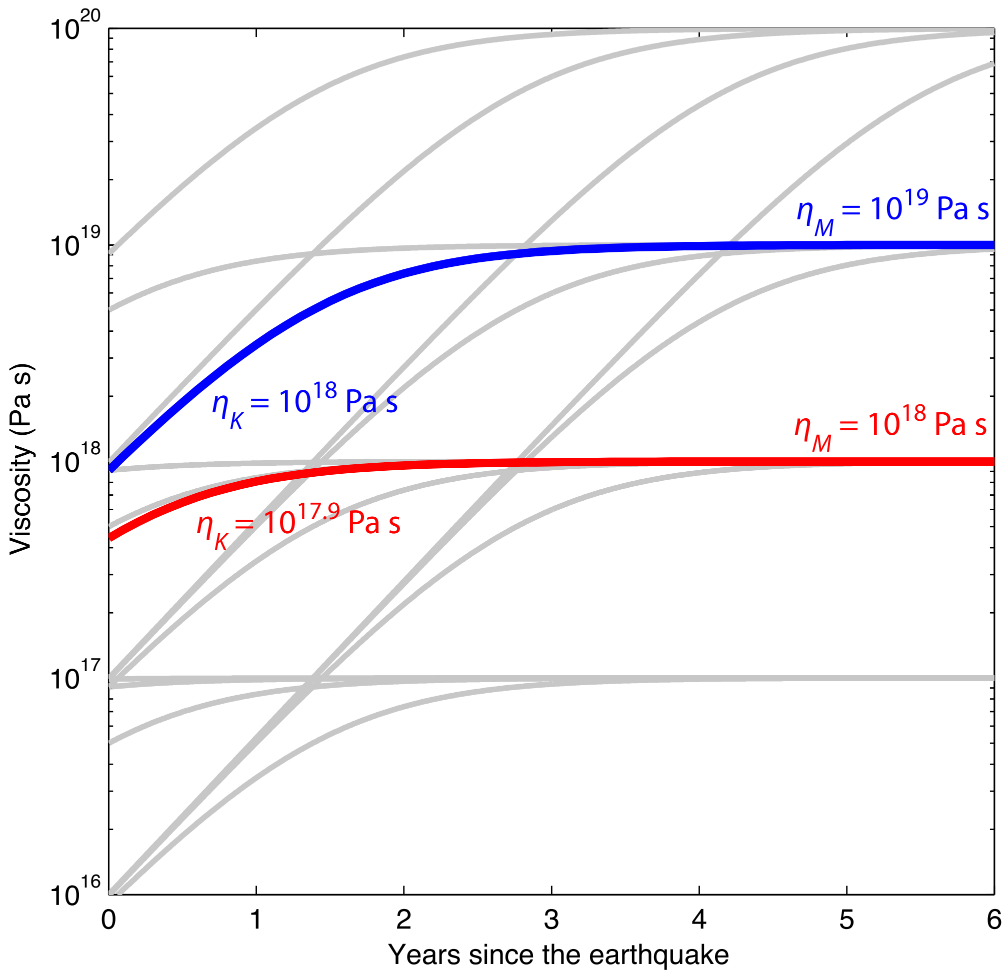

Figure 5.14: Effective viscosity as a function of time in bi-viscous Burgers rheology. The red line is the best fitting time dependent viscosity based on ∼2 years of InSAR time series [Huang et al., 2014], and the blue line is the best fitting viscosity based on ∼6 years of GPS measurements. The grey lines in the background show the viscosity evolution with time with different combinations of transient (η_K) and steady-state (η_M) viscosities. The characteristic relaxation time ($\tau = 0.6$ year).

Since the lowest crustal viscosity would occur at the base of the crust (Section 5.7.2), Moho depth of eastern Tibet would control the spatial pattern of the postseismic displacement. The best fitting model result indicates a transition between the middle- and lower crust at ∼45 km depth, and another transition at Moho (∼60 km depth). This result essentially agrees with the receiver function studies by Zhang et al. [2009] (50 km) and Robert et al. [2010] (60 km). Besides, based on ambient noise Love wave tomography study [Li et al., 2010], the lower shear wave velocity zone underneath eastern Tibetan Plateau (∼25 – 40 km depth) is roughly the same as our proposed weak middle crust (Fig. 5.11). In terms of the lower crustal thickness of weak layer, Clark et al. [2005], Rippe and Unworth [2010], and Huang et al. [2014] support a 15-km thick low viscosity zone at the lower crust with effective viscosity of $\sim 10^{18}$ Pa s. Although this study shows a shallower low viscosity layer, the viscosity roughly agrees with previous studies. In power law flow rheology, the viscosity of diffusion creep is mainly controlled by grain size, water content, and temperature. In order to obtain similar viscosity distribution in depth as in the layered structure in Section 5.8.1, we vary the grain size and water content, and also try different geothermal gradients (Fig. 5.10). The values of grain size and water content are the same in the same material layer (i.e. middle/lower crust and upper mantle), so the decrease of viscosity in depth is due to the increase of temperature (Fig. 5.11). To obtain a low viscosity channel, we could simply assume lower grain size or higher water content for a certain depth range. Besides, it seems like the spatial wavelength of the postseismic displacement (Figs 5.12 and 5.13) is more sensitive to the value and depth of the lowest viscosity than to the thickness of this low viscosity zone. On the other hand, current hypothesis of lower crustal flow assumes a change of flow velocity and partial melt at this layer [Clark et al., 2005; Cook and Royden, 2008; Royden et al., 2008; Rippe and Unworth, 2010] that would contribute to a lower viscosity under dislocation creep. Future work will focus on testing the thickness lower crust with different background strain rate in dislocation creep to represent different flow velocity in the lower crust.

5.9.3 Temperature and strain rate in Tibetan lower crust

We compare the viscosity of olivine, pyroxene, feldspar, and quartz under different temperature and grain size (diffusion creep; see Figs 5.5 and 5.6) or strain rate (dislocation creep; see Figs 5.7 and 5.8). From the bi-viscous model, we know that the middle-to-lower crust (∼30 – 60 km depth) has lower viscosity (from 10^{18} to 10^{19} Pa s) than upper crust. So for power law flow rheology we would expect to find similar effective viscosity value distribution (10^{18} to 10^{19} Pa s) for the crust, but the viscosity would vary at different depth due to the change of pressure and temperature. Besides, there may also be a change of dominating mineral at depth from middle to lower crust, and from lower crust to upper mantle [Behr and Hirth, 2014].

We test the temperature profile from Godard et al. [2009], which they imposed a constant temperature of 15 °C at the surfaceand a constant heat flow of 10 mW m^{-2} at the base of the model. They also assume different thermal conductivity, specific heat capacity, and radioactive heat production for upper crust, lower crust, and mantle. The blue and red lines in Fig. 5.10 show the geothermal gradient at the margin of the plateau (plateau margin in the figure) and ∼100 km far away from the marigin (plateau interior in the figure) based on their calculations. Alternatively we use the temperature profiles for Mojave Desert in California [Freed et al., 2012] in order to compare the effective viscosity for different tectonic regions. Fig. 5.11 shows the viscosity profiles with considering different geothermal gradients while the mineral parameters are the same. In diffusion creep (Fig. 5.11a), the effective viscosity with hot Mojave or plateau margin geothermal gradients would produce too low or too high viscosity. On the other hand, the cold Mojave and plateau interior geothermal gradients produce similar crustal viscosity, if temperature is the only changing parameter. Our best fitting model (Section 5.8.2) implies a plateau interior-like temperature profile, which also agrees with Godard et al. [2009]. For dislocation creep (Fig. 5.11b), it seems like the viscosity varies a lot more in the quartz layer than in the pyroxene layer when temperature is the only changing parameter. If we assume the background strain rate as 10^{-6} yr^{-1} and a similar effective viscosity as in diffusion creep, this model would also prefer a plateau interior geothermal gradient. In addition, the model also prefers a middle crust composed of quartz instead of feldspar in the diffusion creep model (Fig. 5.11a).

5.9.4 Geologic and geodynamic implication

In this section we try to relate our observation with the regional geology. Fig. 5.15a shows the geology in eastern Tibet and the Sichuan Basin by Cook et al. [2013], and Fig. 5.15b shows an E-W cross-section of the Longmen Shan [Burchfiel et al., 2008]. The geology of Longmen Shan includes Precambrian Pengguan massif, Paleozoic sediment, and Mesozoic sediments. The deep slip Wenchuan-Maowen fault separates the Paleozoic rocks from the Pengguan massif at west Longmen Shan (Fig. 5.15b), but the fault is considered either reverse [Tian et al., 2013] or normal [Burchfiel et al., 1995, 2008]. In the east Longmen Shan the Beichuan thrust fault separates the Mesozoic rocks from the Pengguan massif, and the Pengguan thrust fault cuts through the Mesozoic sediments. The Pengguan massif is composed of Precambrian igneous, meta-igneous and meta-sedimentary rocks [Burchfiel et al., 1995, 2008]. The thickening of eastern Tibet and the Longmen Shan appears to be younger than 15 Ma [Kirby et al., 2002; Burchfiel et al., 2008], which corresponds to one of the two rapid exhumation phases [Wang et al., 2012]. The Pengguan massif comes from the deeper part of the plateau (12 km in depth about 50 Myr ago), so we consider a granitic plutonic rock similar to the Pengguan massif that is mainly composed of quartz and feldspar for the Tibetan middle-to-lower crust. Section 5.4 describes viscosity of different minerals under diffusion or dislocation creep at different environmental conditions (also see Figs 5.5-8). In

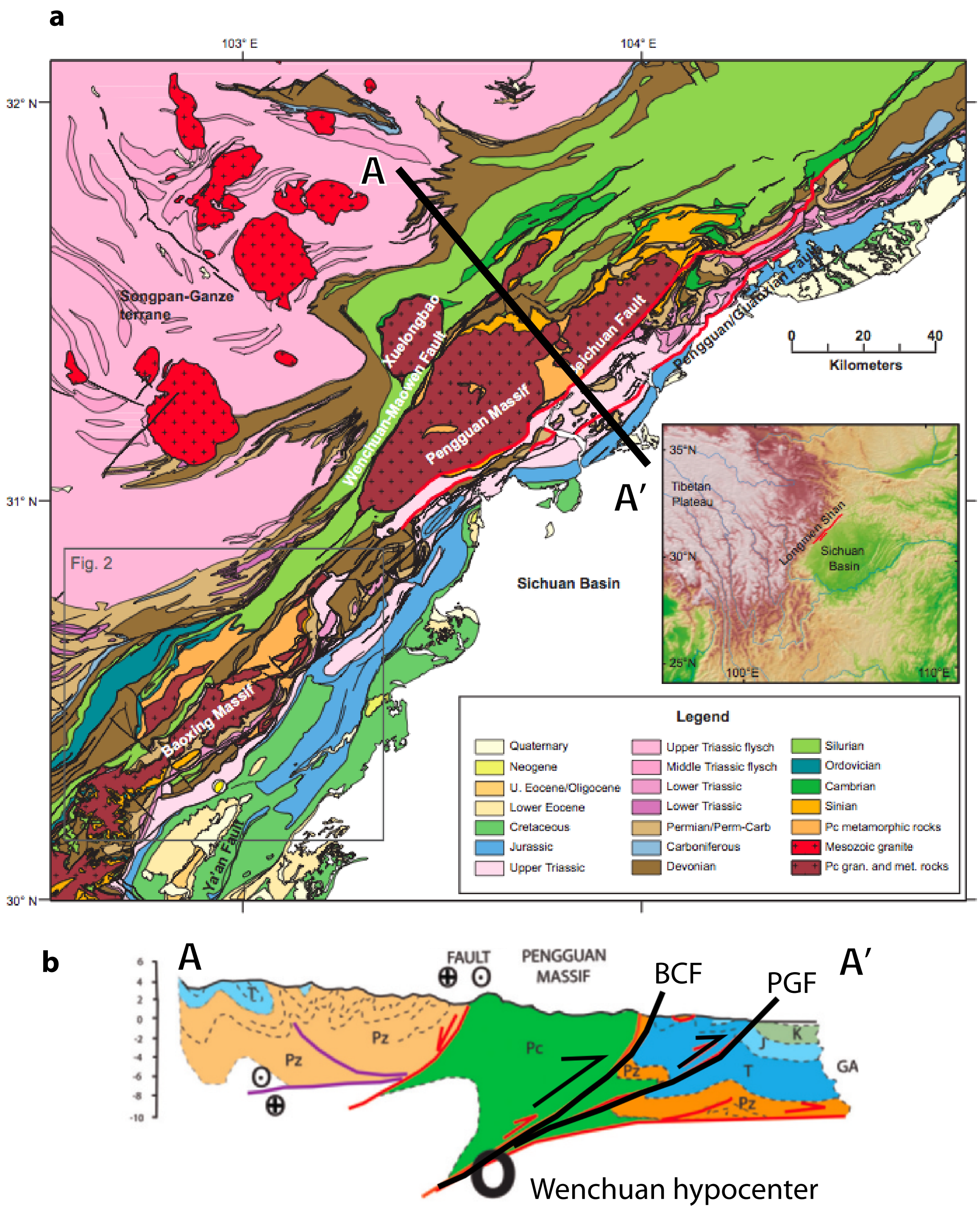

Figure 5.15: (a) Geologic map of eastern Tibet (after Cook et al., 2013). (b) A NW-SE geologic cross section in the central Longmen Shan (after Burchfiel et al., 2008). Pz – Paleozoic; Pc – Precambrian; T – Triassic; J – Jurassic; K – Cretaceous; BCF – Beichuan Fault; PGF – Pengguan Fault.

the bi-viscous Burgers model fitting (Section 5.7.1), the long-term viscosity in Tibetan lower crust is about 10^{19} Pa s. If the depth of the diffusion creep is 50 km, we can consider viscosity as a function of temperature, grain size, and water content (Eq. 5.8). If we consider the water content C_{OH} = 1,000 H/10^6Si, the range of temperature between 800 and 1000 and grain size = 0.1 - 1 mm, the material would have viscosity roughly = 10^{19} Pa s. On the other hand, if we fix the grain size = 1 mm and we vary water content from dry (C_{OH} = 0 H/10^6Si) to high water content (C_{OH} = 3,000 H/10^6Si), the viscosity does not change as much as the change of grain size (Figs 5.5 and 5.6).

Wang et al. [2012] used thermochronology to measure the cooling histories in the center part of Longmen Shan. They found a two phases of rapid exhumation about 30 – 25 Ma and 10 – 15 Ma, respectively. They stated that the significant crustal thickening in eastern Tibet during 30 – 25 Ma cannot be attributed to the lower crustal flow because it would take about 20 Myr for thermal weakening of the thickened crust to attain effective viscosities to permit the flow [Beaumont et al., 2004]. However, the second (10 – 15 Ma) rapid exhumation may reflect thickening of the lower crust that is consistent with timescales of crustal flow. Recently, Tian et al. [2013] used low temperature thermochronology to study two EW profiles in south and central part of Longmen Shan (Fig. 5.16a). They found an abrupt increase of exhumation from west to east when across the Beichuan fault, which suggests that the Beichuan fault is the main thrust boundary between the Longmen Shan and Sichuan basin, and the exhumation rate is the lowest in the Sichuan basin. Also, the exhumation rate decreases twofold over a short distance toward west (Fig. 5.16a). This result suggested thrusts in the Longmen Shan merge gradually into a gentle detachment around 20 – 30 km depth, and perhaps a modified lower crustal flow model that the ductile lower crust drags the upper crust eastward to thicken the crust in the Longmen Shan through high angle listric reverse faulting (Tian et al., 2013; see Fig. 5.16c). Besides, due to the higher exhumation rate west of the Wenchuan-Maowen fault (WMF in Fig. 5.16a), Tian et al. [2013] argued that this fault has a reverse sense, and hence violates the original lower crustal flow model [Clark and Royden, 2000; Clark et al., 2005; see Fig. 5.16b]. In our multiple-mechanism model, a weak and viscous middle-to-lower crust and afterslip on the shallower part of the Beichuan Fault can explain postseismic displacement well. This result agrees with the idea of the lower crustal flow connected to fault-propagation fold structure of the Longmen Shan [Burchfiel et al., 2008; Tian et al., 2013], but it cannot provide further evidences on fault slip on the Wenchuan-Maowen fault or how the faulting system in Longmen Shan links from the viscous middle-to-lower crust up to the upper crust.

In the geodynamic point of view, Rippe and Unworth [2010] used magnetotelluric (MT) data from eastern and southern Tibet estimate the lower crustal flow and the effective viscosity. In their model, they computed the percentage of partial molten of felsic rocks (e.g. Granite and Aplite) based on the conductance and bulk conductivity measured from MT, so they can estimate the material constant (i.e. A in Eq. 5.6). They assumed a power flow

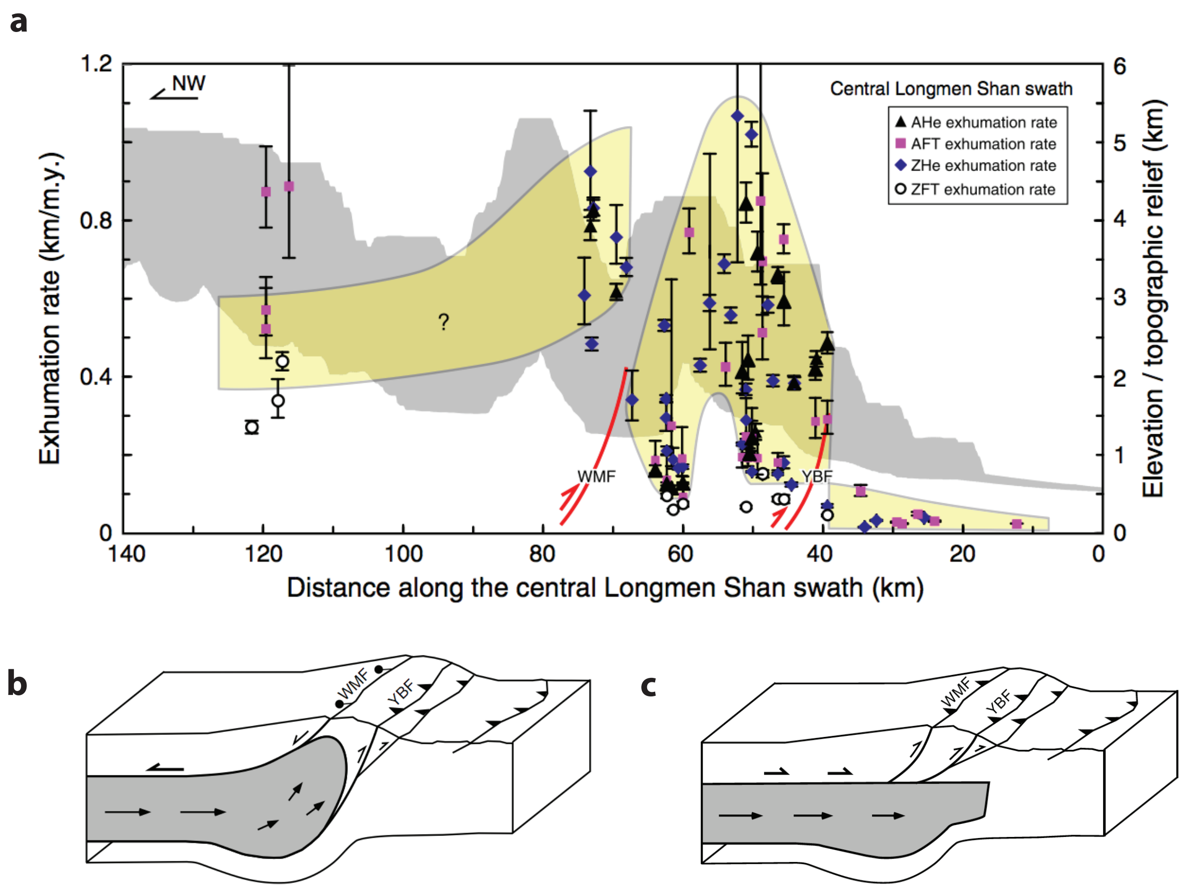

Figure 5.16: (a) Surface exhumation data in southern Longmen Shan. Location see Fig. 5.15a (b) Lower crustal flow model. (c) Modified lower crustal fallow model (after Tian et al., 2013).

model with dislocation creep ($n = 3$ in Eq. 5.6), so they can estimate the flow velocity based on the bulk resistivity, stress power (n), material constant (A), and the horizontal pressure gradient derived from the surface topographic gradients. The effective viscosity can then be calculated using

$$\eta_{eff} = \frac{-(\rho C)^2}{8(n+2)\bar{u}} \frac{dp}{dx}, \tag{5.14}$$

where ρ is the bulk resistivity, C is the conductivity, n is the stress power, $\bar{u}$ is the flow velocity, and dp/dx is the horizontal pressure gradient. They used this method to estimate the effective viscosity in Tibetan lower crust, and they suggested flow velocities of 0.07 - 192 cm/yr and effective viscosities of 1.7×10^{17} - 1.2×10^{20} Pa s, assuming a granitic lower crust. This result also agrees with the value based on dynamic topography (8 cm/yr and 2×10^{18} Pa s, Clark et al., 2005) and postseismic displacement (Huang et al., 2014; this study). However, this prediction shows a contradiction to our assumption that disffusion creeps dominate the power law flow ($n = 1$). Future work will focus on using dislocation creep model (Eq. 5.10) with flow velocity suggested by other studies, and then calculate the effective viscosity (similar to Fig. 5.11b).

Fig. 5.17 shows an updated version of the viscosity estimates of the lower viscosity underneath Tibetan Plateau for different time scales. In this version, the steady-state viscosity estimated from the Wenchuan postseismic deformation is $\sim$10 times higher than in the northern Tibet based on interseismic studies [Hilley et al., 2009; Devries and Meade, 2013], but agrees with longer-term time scale including post-glacial rebound [England et al., 2013] and dynamic topography [Beaumont et al., 2001; Cook and Royden, 2008; Rippe and Unsworth, 2010].

5.10 Conslusion

Longer time scale of postseismic displacement by GPS measurements can help constrain the steady state viscosity in eastern Tibetan lower crust. Compare with previous work by Huang et al. [2014], we find similar transient viscosity as 10^{18} Pa s and the steady state viscosity as 10^{19} Pa s (Fig. 5.17). This result is similar to northern Tibet also based on postseismic displacements [Zhang et al., 2009a; Ryder et al., 2011]. Besides, the viscosity of the Sichuan block is at least 10^{20} Pa s. Overall the effective viscosity is consistent with it in earthquake cycle, post glacial rebound, and geodynamic scales [Huang et al., 2014].

Power law flow model under diffusion creep (Eq. 5.9) behaves as a Newtonian flow, which can be described as a Maxwell fluid (Eq. 5.2). In this study we combine a diffusion creep with transient creep using Eq. 5.11, so we can calculate the effective viscosity of different major minerals in crust and upper mantle under different mineral parameters and environmental

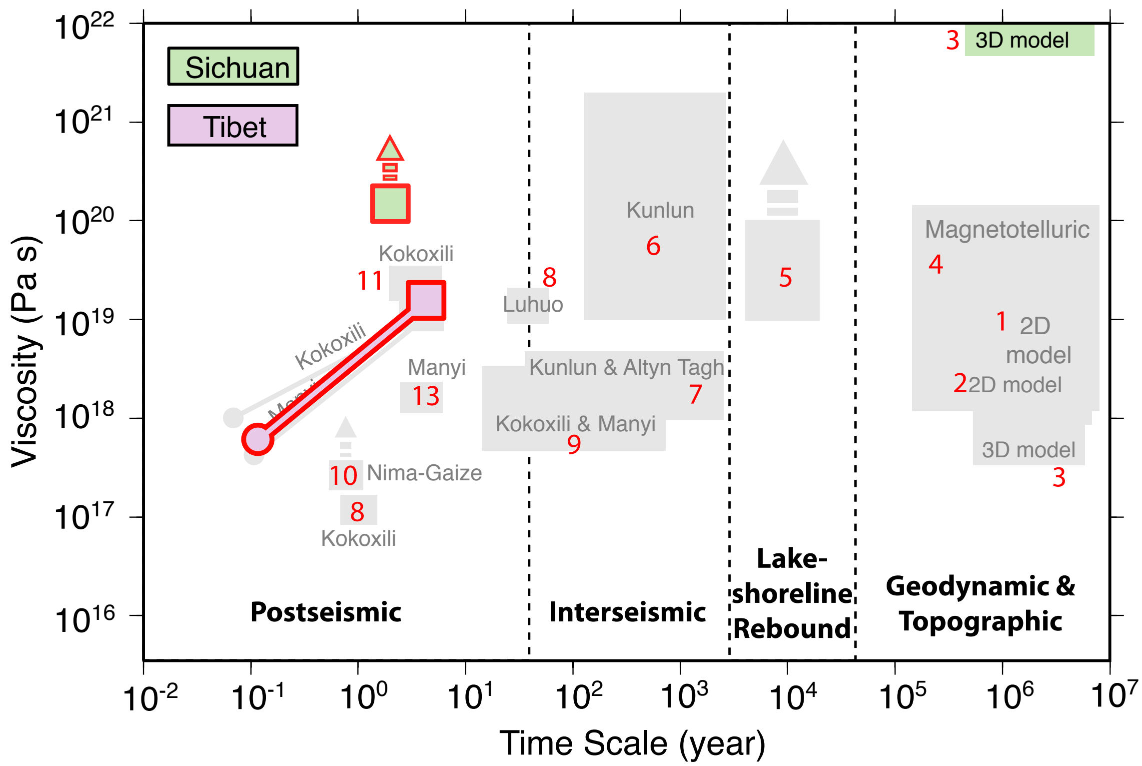

Figure 5.17: Viscosity estimates of Tibet's lower crust for different time scales (after Huang et al. [2014]). The number in the rectangles refers to the cited references: 1, Beaumont et al. [2001]; 2, Clark et al. [2005]; 3, Cook and Royden [2008]; 4, Rippe et al. [2010]; 5, England et al. [2013]; 6, Hilley et al. [2005]; 7. Hilley et al. [2009]; 8, Zhang et al. [2009]; 9, DeVries and Meade [2013]; 10, Ryder et al. [2010]; 11, Ryder et al. [2011]; 12, Wen et al. [2012]; 13, Yamasaki and Houseman [2012].

conditions. We find that the Tibetan middle crust composed mainly of wet feldspar of grain size of 4 mm and water content of 1,000 $H/10^6Si$, the lower crust composed of wet pyroxene of grain size of 1 mm and water content of 1,000 $H/10^6Si$, and the upper mantle composed manly of wet olivine of grain size of 2 mm and water content of 200 $H/10^6Si$ can explain 6 years of postseismic GPS measurements. However, the grain size of the middle-to-lower crust may not be compatible with rocks found in the Pengguan massif that came from the deep Tibetan crust. In the best fitting model, the temperature in the lowest viscosity layer is about 890 °C at 45 km depth, which represents the geothermal gradient underneath Tibetan Plateau 100 km away from the plateau margin. Future work will focus on testing crustal deformation under dislocation creep, and the effective viscosity with different background strain rate and the surface deformation due to the Wenchuan earthquake.

Bibliography

[1] Barbot, S., Hamiel Y. and Fialko Y. Space geodetic investigation of the coseismic and postseismic deformation due to the 2003 M_w7.2 Altai earthquake: Implications for the local lithospheric rheology, *J .Geophys. Res.* 113, B03403 (2008).

[2] Beaumont, C. et al. Himalayan tectonics explained extrusions of low-viscosity crustal channel coupled to focused surface denudation. *Nature* 414, 738-742 (2001).

[3] Burchfiel, B. C. et al. A geological and geophysical context for the Wenchuan earthquake of 12 May 2008, Sichuan, Peoples Republic of China. *GSA Today* 18, 4-11 (2008).

[4] Bürgmann, R. et al. Deformation during the 12 November 1999 Düzce, Turkey, Earthquake, from GPS and InSAR data. *Bull. Seismol. Soc. Am.*, 92, 161-171 (2002).

[5] Bürgmann, R. and Dresen, G. Rheology of the Lower Crust and Upper Mantle: Evidence from Rock Mechanics, Geodesy and Field Observations. *Annu. Rev. Earth Planet. Sci.* 36, 531-67 (2008).

[6] Chen, C. W. and Zebker, H. A. Phase Unwrapping for Large SAR Interferograms: Statistical Segmentation and Generalized Network Models. *IEEE Trans. Geosci. Remote Sensing* 40(8), 1709-1719 (2002).

[7] Chen et al. Electrically conductive crust in sourthern Tibet from IDEPTH magnetotelluric surveying. *Science* 274, 1694-1696 (1996).

[8] Chopra P. N. High-temperature transient creep in olivine rocks. *Tectonophys.* 279, 93-111 (1997).

[9] Clark, K. M., Bush, J. W. M. and Royden, L. H. Dynamic topography produced by lower crustal flow against rheological strength heterogeneities bordering the Tibetan Plateau. *Geophys. J. Int.* 162, 575-590 (2005).

[10] Cook, K. L. and Royden L. H. The role of crustal strength variations in shaping orogenic plateaus, with application to Tibet. *J. Geophys. Res.* 113, B08407 (2008).

[11] Cook, K. L., Royden, L. H., Burchfiel, B. C., Lee, Y.-H., and Tan, X. Constraints on Cenozoic tectonics in the southwestern Longmen Shan from low-temperature thermochronology. *Lithos.* (2013)

[12] Copley, A. and McKenzie, D. Models of crustal flow in the India-Asia collision zone, *Geophys. J. Int.* 169, 683-698 (2007).

[13] Copley, A., Avouac, J.-P. and Wernicke, B. P. Evidence for mechanical coupling and strong Indian lower crust beneath southern Tibet. *Nature* 472, 79-81 (2011).

[14] Cook, K. and Royden, L. H. The role of crustal strength variations in shaping orogenic plateaus, with application to Tibet. *J. Geophys. Res.* 113, B08407 (2008).

[15] DeVries, P. M. R. and Meade, B. J. Earthquake cycle deformation in the Tibetan plateau with a weak mid-crustal layer. *J. Geophys. Res.* 118, 3101-3111 (2013).

[16] Dimanov, A. and Dresen, G. Rheology of synthetic anorthite-diopside aggregates: Implications for ductile shear zones. *J. Geophys. Res.* 110, B07203 (2005).

[17] Ding, K., Xu, C. and Wen, Y. Postseismic deformation associated with the 2008 Wenchuan earthquake by GPS data [in Chinese], *Geom. Inform. Sci. Wuhan Univ.* 38, 131-135 (2013).

[18] England, P. and Houseman, G. Role of lithospheric strength heterogeneities in the tectonics of Tibet and neighbouring regions, *Nature* 315, 297-301 (1985).

[19] England, P. and Molnar, P. Active deformation of Asia: From kinematics to dynamics, *Science* 278, 647-650 (1997).

[20] England, P. C., Walker, R. T., Fu, B. and Floyd, M. A. A bound on the viscosity of the Tibetan crust from the horizontality of paleolake shorelines. *Earth Planet Sci. Lett.* 375, 44-56 (2013).

[21] Flesch, L. M., Haines, A. J. and Holt, W. E. Dynaics of the India-Eurasia collision zone, *J. Geophys. Res.* 106, 16,435-16,460 (2001).

[22] Freed, A. M. and Bürgmann, R. Evidence of power-law flow in the Mojave desert mantle. *Nature* 430, 548-551 (2004).

[23] Freed, A., Bürgmann, R., Calais, E., Freymueller, J. and Hreinsdottir, S. Implications of deformation following the 2002 Denali, Alaska, earthquake for postseismic relaxation processes and lithospheric rheology. *J. Geophys. Res.* 111, B01401 (2006a).

[24] Freed, A. M., Bürgmann, R., Calais, E., and Freymueller, J. Stress-dependent power-law flow in the upper mantle following the 2002 Denali, Alaska, earthquake. *Earth Planet. Sci. Lett.* 252, 481-489 (2006b).

[25] Freed, A., Hirth, G. and Behn, M. D. using short-term postseismic displacements to infer the ambient deformation conditions of the upper mantle, *J. Geophys. Res.* 117, B01409 (2012).

[26] Godard, V., Cattin, R. and Lave, J. Erosional control on the dynamics of low-convergence rate continental plateau margins. *Geophys. J. Int.* 179, 763-777 (2009).

[27] Guo, X. et al. Imaging the crustal structure beneath the eastern Tibetan Plateau and implications for the uplift of the Longmen Shan range. *Earth Planet Sci. Lett.* 379, 72-80 (2013).

[28] Hearn, E. H. What can GPS data tell us about the dynamics of post-seismic deformation? *Geophys. J. Int.* 155, 753-777 (2003).

[29] Hearn, E. H., McClusky, S., Ergintav, S. and Reilinger, R. E. Izmit earthquake post-seismic deformation and dynamics of the North Anatolian Fault Zone. *J. Geophys. Res.* 114, B08405 (2009).

[30] Hetland, E. A. and Hager, B. H. Postseismic and interseismic displacements near a strike-slip fault: A two-dimensional theory for general linear viscoelastic rheologies. *J. Gophys. Res.* 110, B10401 (2005).

[31] Hilley, G. E., et al. Bayesian inference of plastosphere viscosities near the Kunlun Fault, northern Tibet. *Geophys. Res. Lett.* 32, L01302 (2005).

[32] Hilley, G. E., et al. Earthquake-cycle deformation and fault slip rates in northern Tibet. *Geology* 37, 31-34 (2009).

[33] Huang, M.-H., Dreger, D., Bürgmann, R., Yoo, S.-H. and Hashimoto, M. Joint inversion of seismic and geodetic data for the source of the 2010 March 4, M_w 6.3 Jia-Shian, SW Taiwan, earthquake. *Geophys. J. Int.* 193, 1608-1626 (2013).

[34] Huang, M.-H., Bürgmann, R. and Freed A. M. Probing the lithospheric rheology across the eastern margin of the Tibetan Plateau. *Earth Planet. Sci. Lett.* 396, 88-96 (2014).

[35] Hubbard, J., Shaw, J. H. and Klinger, Y. Structural setting of the 2008 M_w 7.9 Wenchuan, China, earthquake. *Bull. Seismol. Soc. Am.* 100, 2713-2735 (2010).

[36] Jia, D. et al. Structural model of 2008 M_w 7.9 Wenchuan earthquake in the rejuvenated Longmen Shan thrust belt, China. *Tectohophys.* 491, 174-184 (2010).

[37] Johnson, K. M., Fukuda, J. and Segall, P. Challenging the rate-state asperity model: Afterslip following the 2011 M9 Tohoku-oki, Japan, earthquake. *Geophys. Res. Lett.* 39, L20302 (2012).

[38] Karato, S.-I. Deformation of Earth materials, Cambridge University Press (2008).

[39] Karato, S.-I. Water distribution across the mantle transition zone and its implications for global material circulation. *Earth Planet. Sci. Lett.* 301, 413-423 (2011).

[40] Klemperer, S. L. Crustal flow in Tibet: geophysical evidence for the physical state of Tibetan lithosphere, and inferred patterns of active flow. In: Law, R. D., Searle, M. P. and Godin, L. (eds) Channel flow, ductile extrusion and exhumation in continental collision zones, Geological Society, London, Special Publications, 268, 39-70 (2006).

[41] Li, C. and van der Hilst, R. D. Structure of the upper mantle and transition zone beneath South East Asia from travel time tomography, *J. Geophys. Res.* 115, B07308 (2010).

[42] Li, H., Su, W., Wang, C.-Y., Huang, Z. Ambient noise Rayleigh wave tomography in western Sichuan and eastern Tibet. *Earth Planet. Sci. Lett.* 282, 201-211 (2009).

[43] Li, L., Chen, Q.-F., Niu, F. and Su, J. Deep slip rates along the Longmen Shan fault zone estimated from repeating microearthquakes. *J. Geophys. Res.* 116, B09310 (2011).

[44] Manning, C. E. and Ingebritsen, S. E. Permeability of the continental crust: Implications of geothermal data and metamorphic systems. *Rev. Geophys.* 37, 127-150 (1999).

[45] Mechie J. et al. Precise temperature estimation in the Tibetan crust from seismic detection of the - quartz transition. *Geology* 32, 601-604 (2004).

[46] Nadeau, R. M. and McEvilly, T. V. Periodic pulsing of characteristic microearthquakes on the San Andreas Fault. *Science* 303, 220-222 (2004).

[47] Nelson, K. D. et al. Partially molten middle crust beneath southern Tibet; synthesis of Project INDEPTH results. *Science* 274, 1684-1688 (1996).

[48] Peltzer, G., Rosen, P., Rogez, F. and Hudnut, K. Postseismic rebound in fault step-overs caused by pore fluid flow. *Science* 273, 1684-1688 (1996).

[49] Pollitz, F. F. Postseismic relaxation theory on the spherical Earth. *Bull. Seismol. Soc. Am.* 82, 422-453 (1992).

[50] Pollitz, F. F. Transient rheology of the uppermost mantle beneath the Mojave Desert, California, *Earth Planet. Sci. Lett.* 215, 89-104 (2003).

[51] Pollitz, F., Wicks, C. and Thatcher, W. mantle flow beneath a continental strike-slip fault: postseismic deformation after the 1999 Hector Mine earthquake. *Science* 293, 1814-1818 (2001).

[52] Rippe, D. and Unsworth, M. Quantifying crustal flow in Tibet with magnetotelluric data. *Phys. Earth Planet. Inter.* 179, 107-121 (2010).

[53] Robert, A. et al. Crustal structures in the area of the 2008 Sichuan earthquake from seismologic and gravimeteric data. *Tectonophys.* 491, 205-210 (2010).

[54] Royden, L. H., Burchfiel, B. C. and van der Hilst, R. The geological Evolution of the Tibetan Plateau. *Science* 321, 1054-1058 (2008).

[55] Ryder, I., Bürgmann R. and Pollitz F. Lower crustal relaxation beneath the Tibetan Plateau and Qaidam Basin following the 2001 Kokoxili earthquake. *Geophys. J. Int.* 187, 613-630 (2011).

[56] Ryder, I., Bürgmann, R. and Sun, J. Tandem afterslip on connected fault planes following the 2008 Nima-Gaize (Tibet) earthquake. *J. Geophys. Res.* 115, B03404 (2010).

[57] Ryder, I., Parsons B., Wright T. J. and Funning G. Postseismic motion following the 1997 Manyi (Tibet) earthquake: InSAR observations and modeling. *Geophys. J. Int.* 169, 1009-1027 (2007).

[58] Shao, Z., Wang, R., Wu, Y. and Zhang, L. Rapid afterslip and short-term viscoelastic relaxation following the 2008 M_w 7.9 Wenchuan earthquake. *Earthquake Sci.* 24, 163-175 (2011).

[59] Shen, Z.-K., Lu, J. N., Wang, M. and Bürgmann, R. Contemporary crustal deformation around the southeast borderland of the Tibetan Plateau. *J. Geophys. Res.* 110, 11409 (2005).

[60] Shen, Z.-K. et al. Slip maxima at fault junctions and rupturing of barriers during the 2008 Wenchuan earthquake. *Nat. Geosci.* 2, 718-724 (2009).

[61] Tapponnier, P. et al. Oblique stepwise rise and growth of the Tibet plateau. *Science* 294, 1671-1677 (2001).

[62] Thatcher, W. How the continents deform: The evidence from tectonic geodesy. *Annu. Rev. Earth Planet.* 37, 237-262 (2009).

[63] Wang, C.-Y., Chen, W.-P. and Wang, L.-P. Temperature beneath Tibet. *Earth Planet. Sci. Lett.* 375, 326-337 (2013).

[64] Wang, Q. et al. Rupture of deep faults in the 2008 Wenchuan earthquake and uplift of the Longmen Shan. *Nat. Geo.* 4, (2011).

[65] Wang, K., Hu Y. and He J. Deformation cycles of subduction earthquakes in a viscoelastic Earth. *Nature* 484, 327-332 (2012).

[66] Wang, R., Lorenzo-Martin, F. and Roth F. PSGRN/PSCMP-A new code for calculating co- and post-seismic deformation, geoid and gravity changes based on the viscoelastic-gravitational dislocation theory. *Comput. Geosci.* 32, 527-541 (2006).

[67] Wang Y. Heat flow pattern and lateral variations of lithosphere strength in China mainland: constraints on active deformation. *Phys. Earth Planet. Inter.* 126, 121-146 (2001).

[68] Wen, Y., Li Z., Xu C., Ryder I., Bürgmann, R. Postseismic motion after the 2001 M_w 7.8 Kokoxili earthquake in Tibet observed by InSAR time series. *J. Geophys. Res.* 117, B08405 (2012).

[69] Xu, M., Zhu, C.-Q., Tian, Y.-T. Rao, S. and Hu, S.-B. Borehole temperature logging and characteristics of subsurface temperature in the Sichuan Basin. *Chinese J. Geophys.* 54, 224-233 (2011).

[70] Yamasaki, T. and Houseman, G. A. The crustal viscosity gradient measured from post-seismic deformation: A case study of the 1997 Manyi (Tibet) earthquake. *Earth Planet. Sci. Lett.* 351, 105-114 (2012).

[71] Zhang, C., Cao, J. and Shi Y. Studying the viscosity of lower crust of Qinghai-Tibet Plateau according to post-seismic deformation. *Sci. China* 52(3), 411-419 (2009).

[72] Zhao, G. et al. Crustal structure and rheolgy of the Longmenshan and Wenchuan M_w 7.9 earthquake epicentral area from magnetotelluric data. *Geology* 40, 1139-1142 (2012).

[73] Zhang, P.-Z., Wen, X.-Z., Shen, Z.-K. and Chen, J.-H. Oblique, high-angle, listric-reverse faulting and associated development of strain: The Wenchuan earthquake of May 12, 2008, Sichuan, China. *Annu. Rev. Earth Planet.* 38, 353-382 (2010).

[74] Zhang, Z. et al. Crustal structure across Longmenshan fault belt from passive source seismic profiling. *Geophys. Res. Lett.* 36, L17310 (2009).

Chapter 6

Conclusion

In the first part (Chapter 2) of the thesis, I combine seismic and geodetic observations to study the source of the 2010 M_w 6.3 Jia-Shian, SW Taiwan earthquake. In order to minimize the artifacts from the over-simplified 1-D velocity structure, I generate separate Green's functions for seismic stations in west and east Taiwan by fitting the waveforms of the largest aftershock (M_w 5.0) to calibrate the velocity structure and Green's functions. Independent inversions of each data set (i.e. seismic, GPS, and InSAR) show high consistency. The combined inversion with comprehensive tests of model smoothing and weighting between data sets obtain the total moment as 3.25×10^{18} N m (M_w 6.3). Rupture velocity tests suggest supershear propagating at $\sim$1.23 of the regional shear-wave velocity. The Jia-Shian event occured along the boundary between the western Foothills and the Central Range to the north and east and the sedimentary Pingtung Basin in the south. The youngest paleostress orientations and compression axes from seismic data are consistent with the kinematics of the Jia-Shian earthquake. However, the stress orientation in the upper crust around this region is inconsistent with the directions of the surface strain rate field derived form GPS measurements. The most recent large aftershock (M_w 5.7) where located $\sim$30 km away from this region reveals that the deep structure extends further to the southeast below the Central Range. As a result, the Jia-Shian event may represent the reactivation of pre-existing deep structures, and the orientation of stress locally deviates from the current orientation of plate collision.

In the second part (Chapters 3 – 5), I study postseismic deformation after smaller and greater earthquakes. For a smaller magnitude event such as the 1989 M_w 6.9 Loma Prieta earthquake in the San Francisco Bay Area, I first focus on the later period (5 years after the Loma Prieta earthquake) of postseismic deformation. One-D viscoelastic layer structure composed of an elastic upper crust, viscoelastic lower crust, and viscoelastic upper mantle can explain the geodetic measurements. In the best fitting model, a lower crust located at 16-to-30 km in depth composed of Maxwell fluid (viscosity = 10^{19} Pa s) and a upper mantle (below 30 km) composed of bi-viscous Burgers body (transient viscosity = 10^{17} Pa s; steady-state viscosity = 10^{18} Pa s), can predict $\sim$2 cm postseismic surface displacement near the Loma Prieta earthquake region between 1994 and 2013. In addition, the relaxation seems to relate to the repeating earthquakes on the nearby San Andreas Fault in San Juan Bautista region. I predict early postseismic relaxation based on this the viscoelastic model in order to discriminate the afterslip component from the relaxation. However, this early displacement residual does not improve the afterslip dislocation inversions. A higher resolved coseismic slip model might help refine viscoelastic relaxation component in early and late periods, and hence separates both mechanisms. However, difficulties still remind due to the lower magnitude of coseismic stress change to drive postseismic deformation, higher uncertainty in the early GPS observations, and the lack of the InSAR time series during early postseismic period.

For a larger magnitude event such as the 2008 M_w 7.9 Wenchuan earthquake in the Longmen Shan, eastern Tibetan Plateau, we can consider the coseismic stress changes as the source to probe the deep lithospheric rheology underneath eastern Tibetan Plateau. In the first part (Chapter 4) of this work, I incorporate $\sim$2 years of InSAR time series and the first few months of GPS measurements to test different end-member models for the Tibetan orogeny. The geodetic observations reveal postseismic transients for months after the Wenchuan main shock, which can be explained by a bi-viscous Burgers rheology with initial effective viscosity of 4.4×10^{17} Pa s and a steady-state viscosity of 10^{18} Pa s. A multiple-mechanism model including viscoelastic relaxation from the Tibetan lower crust at 35 – 50 km in depth and afterslip in the shallower part of the Wenchuan earthquake fault can predict $\sim$2-year-long geodetic measurements. The long-term effective viscosity of the Tibetan lower crust based on this study is within the range of the viscosity estimates for the Tibetan lower crust across years to million of years time scale. On the other hand, little viscous relaxation occurred in the Sichuan Basin lithosphere following the Wenchuan earthquake indicates a much higher viscosity (at least 10^{20} Pa s in the Sichuan upper mantle). The preferred viscosity structure deduced from the postseismic deformation across the Longmen Shan is consistent with a contrasting lithospheric rheology and deformation between eastern Tibet and Sichuan Basin, and also agrees with Tibetan lower crustal channel flow models.

In the second part (Chapter 5) of this work, I incorporate 18 GPS stations that continuously recorded 6 years of displacement since the Wenchuan earthquake. With these extended time series data, the bi-viscous Burgers model with the same viscoelastic geometry prefers the initial effective viscosity of 9×10^{17} Pa s and the steady-state viscosity of 10^{19} Pa s, which is $\sim$10 times higher than the steady-state viscosity derived from the previous work based on the 2-year-long data. Power law flow rheology derived from rock mechanics experiments is used to predict the Wenchuan postseismic deformation. By assuming a diffusion creep type rheology, forward calculations infer the Tibetan crust mainly composed of wet quartz and wet olivine for the upper mantle. The temperature at the lower crust is $\sim$800 – 900°C, which is consistent with the proposed geothermal gradient model $\sim$100 km away from the plateau margin. The boundary between the Tibetan lower crust and upper mantle (Moho) is $\sim$45 km in depth, which is slightly shallower than the previous work.

Future work will focus on the dislocation creep rheology. In this flow model, the material viscosity is dependent on the background stress level, and hence would be influenced by the coseismic stress change. However, the separation of this stress dependent viscosity and the initial effective viscosity would rely on more extensive network and a longer time span for the geodetic measurements.

To conclude, although challenges still exist in the separation of different poseismic mechanisms, this work has shown postseismic deformation as a robust tool to probe lithospheric rheology if dense networks and precise measurements are available. Cases study shows that afterslip and viscoelastic relaxation both contribute to postseismic deformation after smaller or greater earthquakes, but the ratio between both varies by events. Generally, afterslip and viscoelastic relaxation contribute to different spatial and temporal scales. For example, in Wenchuan event, the afterslip dominated the near-field whereas viscoelastic relaxation dominated the far-field regions; in Loma Prieta event, the afterslip contributed to the first 5 years postseismic deformation whereas the viscoelastic relaxation could continue for more than 20 years. The duration of the relaxation relates to the lithospheric viscosity of the layers and the coseismic stress changes. As a result, as demonstrated in Chapters 4 and 5, using short-term geodetic measurements to infer long-term viscosity would likely undereastimate the steday-state viscosity. Decades of continuous crustal deformation monitoring after greater earthquakes will allow us to better constrain rheology in the lithosphere.